CubeSat Antenna Design

CubeSat Antenna Design

Edited by

Dr. Nacer Chahat
*NASA Jet Propulsion Laboratory/California
Institute of Technology, Pasadena, CA, USA*

IEEE PRESS

WILEY

Contents

Preface

This book presents an overview of CubeSat antennas designed at the Jet Propulsion Laboratory (JPL). The objective of this book is to share the knowledge with undergraduate students, graduate students, and engineers all around the world. The Jet Propulsion Laboratory initiated a wave of innovation on deployable antennas for CubeSats enabling a new class of missions ranging from Low Earth Orbit to Deep Space missions.

The first chapter presents a brief introduction of CubeSats. It also provides an exhaustive overview of existing CubeSat antennas organized into three categories: low gain, medium gain, and high gain antennas. An emphasis on the selection of high gain antennas is provided for CubeSat missions depending on the requirements and constraints. As the reader might not be familiar with the design of spacecraft antennas, key information on the effect of space environment (i.e. radiation environment, material outgassing, temperature, and multipacting breakdown) on antennas is provided as these additional constraints drive the antenna design.

The second chapter describes the telecommunication subsystem of Mars Cube One (MarCO) mission with a focus on the antenna development. The requirements for each antenna is described and explained in the context of the mission, which helps the reader to understand the selection process of each antenna. Multiple antennas are described in this chapter: four X-band low gain patch antennas, an X-band high gain reflectarray antenna, and deployable circularly polarized UHF loop antenna. The performance of the reflectarray antenna and UHF antenna was demonstrated on-orbit. Details on the performance achieved on the ground and in space are provided in this chapter.

The third chapter describes the enabling technology of Radar in a CubeSat (Rain-Cube). The design steps of the deployable mesh reflector operating at Ka-band are thoroughly described from an electrical and mechanical point of view. The reader will appreciate through this chapter how mechanical and electrical designs are tightly related; one can affect the complexity of the other, and one can simplify the complexity of the other. The telecommunication challenge is also described briefly.

Chapter 4 describes the electrical and mechanical designs of the largest reflectarray compatible with a 6U-class CubeSat: OMERA (one meter reflectarray antenna). After providing a state of the art of deployable reflectarray, the electrical and mechanical designs of the deployable reflectarray are described in detail.

Chapter 5 describes the development of a one-meter mesh reflector for telecommunication at X- and Ka-band for deep space missions.

In Chapter 6, an inflatable antenna operating at X-band is described from an electrical and mechanical point of view with all the challenges associated with operation in space.

In Chapter 7, a novel patch array mainly made of metal is described for use on a CubeSat. This antenna demonstrates extraordinarily high efficiency (>80%) at both uplink and downlink X-band deep space network. It can also survive high radiation levels and extreme temperatures.

Finally, Chapter 8 describes the design of multiple metasurface antennas. While metasurface antennas have never flown in space, JPL is advancing the technology readiness of metasurface antennas with the objective of infusing this technology in future space missions. This chapter describes the advantage and drawbacks of these antennas. Innovative metasurface antenna concepts are described in detail.

Nacer Chahat
Pasadena, CA
January 2019

Editor Biography

Dr. Nacer Chahat (S'09–M'12–SM'15) received master's degree in electrical engineering from the École supérieure d'ingénieurs de Rennes (ESIR), Rennes, France, in 2009 and master's degree in telecommunication and PhD degree in signal processing and telecommunications from the Institute of Electronics and Telecommunications of Rennes (IETR), University of Rennes 1, Rennes, France, in 2009 and 2012, respectively. He is a senior antenna/microwave engineer with the National Aeronautics and Space Administration (NASA) Jet Propulsion Laboratory (JPL), California Institute of Technology, Pasadena, CA. Since 2013, he has been a microwave/antenna engineer with NASA's Jet Propulsion Laboratory, and he became the youngest technical section staff in 2018.

Since he joined NASA's Jet Propulsion Laboratory, he worked on several flight projects: Mars Perseverance and Mars Ingenuity, SWOT, NiSAR, Europa Clipper, Psyche, MarCO, NeaScout, Lunar Flashlight, RainCube, LunaH-map, Lunar Ice-Cube, BioSentinel, and CUSP.

To cite few of his major contributions, he enabled the first active radar in a CubeSat, Raincube, by co-inventing the Ka-band deployable mesh reflector. This patented technology was since then licensed and is now commercially available. He also co-invented the iconic deployable reflectarray antenna for the first interplanetary CubeSat, MarCO, which enabled real-time communication relay during Insight's Entry, Decent, and Landing. More recently, his patented metal-only high-gain antenna technology made it possible to have a direct-to-Earth communication channel from the Europa lander mission concept which otherwise would have not been possible. He also played a critical role in delivering the telecommunication subsystem for the Mars Perseverance and Mars Ingenuity

missions which will attempt the first helicopter flight on the red planet. From 2018 to 2020, he was Product Delivery Manager for the SWOT High Power Amplifier. Since January 2020, he is the Payload System Engineer lead on the SWOT mission.

He has authored and coauthored more than 100 technical journal articles and conference papers, has written four book chapters, and also holds 5 patents. His research interests include deployable antennas for CubeSat and small satellites, spacecraft antennas for telecommunications, RADAR, imaging systems, metasurface antennas, and metasurface beam steering antennas.

Dr. Chahat was the recipient of the 2011 CST University Publication Award, the 2011 Best Paper Award from the Bioelectromagnetics Society, and the IEEE Antenna and Propagation Society Doctoral Research Award in 2012. He was awarded the best PhD of University of Rennes by the Foundation of Rennes 1. In 2013, he received the best PhD thesis prize in France in electrical engineering awarded by club EEA (Enseignants et des chercheurs en Electronique, Electrotechnique et Automatique). In 2013, he was awarded the Airbus Group Foundation's Best Thesis Prize in France. In 2015, he received a French Early Career Award for Engineer and Scientist (Prix Bretagne Jeune Chercheur) for his significant scientific contribution in his early career.

In 2017, he received the IEEE A. Schelkunoff Transactions Prize Paper Award for his paper on the innovative deployable Ka-band mesh reflector which enabled the RainCube mission. In 2017, he also received the prestigious Lew Allen Award for Excellence awarded by NASA's Jet Propulsion Laboratory "for demonstrated unique talent as a leader in rapid spacecraft antenna development and telecom systems engineering." In 2018, he was awarded the Future Technology Leader Award by the Engineers' Council and the NASA Early Career Achievement Medal by the United States government and National Aeronautics and Space Administration (NASA).

Notes on Contributors

Dr. Manan Arya received his BASc in engineering science from the University of Toronto in 2011, and his PhD and MSc in space engineering from the California Institute of Technology in 2012 and 2016, respectively. His interests include the origami-inspired design of deployable spacecraft structures and ultralight ultrathin composite materials. He joined JPL in 2016 to support the Starshade technology development effort and has been involved in the development of deployable RF antenna reflectors for small satellites.

   Dr. Alessandra Babuscia received her BS and MS degrees from the Politecnico di Milano and her PhD degree from the Massachusetts Institute of Technology (MIT), Cambridge, in 2012. She is currently Telecommunication Engineer in the Flight Communications Section at the NASA Jet Propulsion Laboratory in Pasadena. She is PI for the Inflatable Antenna for CubeSat project; telecom system engineer for Mars2020 and Europa Lander missions; telecom lead engineer for ASTERIA, LunaH-Map, and RainCube missions; telecom chair lead for JPL TeamXc, and involved in many CubeSat mission design concepts and proposals. Her current research interests include communication architecture design, statistical risk estimation, inflatable antennas, and communication system design for small satellites and CubeSats.

   Dr. Goutam Chattopadhyay is a Senior Research Scientist at the NASA's Jet Propulsion Laboratory, California Institute of Technology, and a Visiting Associate at the Division of Physics, Mathematics, and Astronomy at the California Institute of Technology, Pasadena, USA. He received his PhD degree in electrical engineering from the California Institute of Technology (Caltech), Pasadena, in 2000. He is a Fellow of IEEE (USA) and IETE (India) and an IEEE Distinguished Lecturer. His

research interests include microwave, millimeter-wave, and terahertz receiver systems and radars, and applications of nanotechnology at terahertz frequencies. He has more than 300 publications in international journals and conferences and holds more than 15 patents. He has also received more than 35 NASA technical achievement and new technology invention awards. He received the IEEE Region 6 Engineering of the Year Award in 2018 and Distinguished Alumni Award from the Indian Institute of Engineering Science and Technology (IIEST), India, in 2017. He was the recipient of the best journal paper award in 2013 by IEEE Transactions on Terahertz Science and Technology, best paper award for antenna design and applications at the European Antennas and Propagation Conference (EuCAP) in 2017, and IETE Prof. S. N. Mitra Memorial Award in 2014.

Dr. Tom Cwik leads the space technology development at NASA's Jet Propulsion Laboratory, as well as leading tech development for the exploration of ocean worlds. He was formerly Associate Chief Technologist at JPL. He received his bachelor's, master's, and doctorate in electrical engineering from the University of Illinois, Urbana-Champaign. He joined JPL in 1988 working in a range of advanced engineering and project activities including antenna design, instrument development, and high-performance computing focused on high-fidelity modeling of instrument and electromagnetic systems.

His previous position includes leading the JPL Earth Science Instruments & Technology Office. He led proposal development of the Earth-observing mission Aquarius/SAC-D NASA Earth System Pathfinder mission to measure sea surface salinity. Tom has supervised the High-Performance Computing Group at JPL and has worked in engineering positions across a range of tasks and projects starting with the Cassini Mission, the Deep Space Network, and a long-term funded effort from the Special Projects Office of the Air Force that originated the field of large-scale parallel computing in computational electromagnetics and design.

Tom is an IEEE Fellow, an Associate Fellow of the AIAA, a Principal Member at JPL, and an Affiliate Professor at the University of Washington, Department of Electrical Engineering, Seattle, WA. He was named a 2012 Distinguished Alumni of the University of Illinois, ECE Department, Urbana, IL. He has written 8 book chapters and over 30 refereed journal papers. He holds two US patents. He has consulted with industry and has been cofounder and part of start-up companies in a variety of fields.

Dr. Emmanuel Decrossas received the BS and MS with honors in materials science and electrical engineering from the université Pierre et Marie Curie Paris-6, Paris, France, in 2004 and 2006, respectively. In 2012, he received his PhD from the University of Arkansas, Fayetteville, in electrical engineering. He has authored and coauthored over 40 technical journal articles, conference papers, and invited talks; has written one book chapter; and holds over five patents. Emmanuel Decrossas was awarded the NASA postdoctoral fellowship given annually to only 60 postdoctoral candidates worldwide, based on the scientific merit of proposed research, academic, and research record in 2012. Although he joined JPL only in

2015, he has already delivered a large amount of flight hardware for Mars CubeSat One (MARCO), Sentinel-6 (ex JASON-CS), and Cold Atom Laboratory (CAL). He is currently developing the high-power feed absorber cover for SWOT Karin instrument (2000 W peak) and the antennas for EUROPA REASON radar-sounder instruments. Dr. Decrossas is a member of the electrical engineering honor society Eta Kappa Nu, IEEE. In 2017, he received the Charles Elachi award for outstanding early-career achievement in the development of innovative antenna designs making missions successful. Dr. Decrossas also received the prestigious NASA early career medal in 2018 for early-career achievement developing innovative spacecraft antennas, enabling novel space instruments and telecom systems in support of NASA's research mission.

Gregg Freebury received his MS degree in Aero-Astro Engineering from Stanford University in 1985. He is the founder and CEO of Tendeg and has over 30 years of experience in aerospace, satellite and aircraft vehicle design, analysis, and test. Before starting Tendeg, he held senior engineering positions in Northrop and consulted specifically in the space deployable field for over 20 years. He has designed and developed numerous commercial products and been awarded six patents related to space deployables.

M. Michael Kobayashi received his BS in Electrical Engineering (2006) and MS in Electrical and Computer Engineering (2007) from the University of California, Irvine, and joined the Jet Propulsion Laboratory in 2007 as an RF Microwave Engineer. He has worked on various microwave flight hardware deliveries such as the Ka-band up/down converter for the Terminal Descent Sensor of the Curiosity Mars Rover and the 550 W L-band transmitter for the Soil Moisture Active Passive mission. Recent work focuses on space-borne software-defined radio and transponder development including the Iris Deep-Space Transponder, the Universal Space Transponder, and the high-rate Ka-band Modulator for the NASA/ISRO SAR (NISAR) mission. He has been involved in various telecom and radio support activities for JPL CubeSat projects such as INSPIRE, MarCO, and the EM-1 CubeSat missions. Currently, he serves as the payload system engineer for the NISAR project to develop the high-rate Ka-band communications system to downlink 26 Terabits/day of science and engineering data from low-Earth orbit.

Dr. David González-Ovejero was born in Gandía, Spain, in 1982. He received the telecommunication engineering degree from the Universidad Politécnica de Valencia, Valencia, Spain, in 2005, and the PhD degree in electrical engineering from the Université catholique de Louvain, Louvain-la-Neuve, Belgium, in 2012. From 2006 to 2007, he was as a Research Assistant with the Universidad Politécnica de Valencia. In 2007, he joined the Université catholique de Louvain, where he was a Research Assistant until 2012. From 2012 to 2014, he worked as Research Associate at the University of Siena, Siena, Italy. In 2014, he joined the Jet Propulsion Laboratory, California Institute of Technology, Pasadena, CA, USA, where he was a Marie Curie Postdoctoral Fellow until 2016. Since then, he has been a Research Scientist with the French National Center for Scientific

Research (CNRS), appointed at the Institut d'Électronique et de Télécommunications de Rennes, France. Dr. González-Ovejero was a recipient of a Marie Curie International Outgoing Fellowship from the European Commission 2013, the Sergei A. Schelkunoff Transactions Prize Paper Award from the IEEE Antennas and Propagation Society in 2016, and the Best Paper Award in Antenna Design and Applications at the 11th European Conference on Antennas and Propagation in 2017.

Dr. Jonathan Sauder received a BS majoring in Mechanical Engineering from Bradley University in 2009, a MS in Product Development Engineering from the University of Southern California in 2011, and a PhD in Mechanical Engineering from the University of Southern California in 2013. Prior to joining JPL, he worked in R&D roles for companies including Mattel, Microsoft, Monsanto, and technology startups. He began his career at JPL in 2014 as a technologist. Dr. Sauder is currently a senior mechatronics engineer at Jet Propulsion Laboratory, in the Technology Infusion Group, which seeks to bridge the Technology Readiness Level (TRL) "Valley of Death" for innovative concepts. He is the Principle Investigator on a Phase I and Phase II NIAC study "Automaton Rover for Extreme Environments" and also an inventor of several patent pending deployable antennas and the Principle Investigator on several deployable antenna research projects. He was the Mechanical Engineering Lead on the RainCube Spacecraft, and responsible for infusing a new antenna technology, taking it from prototype to flight. He is also a member of NASA Engineering and Safety Center (NESC) Mechanical Systems Technical Discipline Teams (TDT) and lectures at the University of Southern California on Advanced Mechanical Design.

Mark Thomson is an inventor and technology development PI in the field of very large precision deployable structures for space. As Chief engineer in the JPL Division 35 Instrument and Small Spacecraft Mechanical Engineering Section, he has been consulted lab-wide since 2006 as a deployable structures subject matter expert for mission formulation, development, and implementation. JPL projects include the main radar and radiometer antennas for SMAP, SWOT, NiSAR, Europa, and numerous CubeSats including RainCube. He is currently developing a 40 m diameter class optical Starshade for imaging Earth-like Exoplanets. Mr. Thomson spends a great deal of his time mentoring the next generation of mechanical engineers at JPL in low-cost rapid prototyping of large structures and mechanical space systems. At Northrop Grumman Aerospace Systems from 1988 to 2006, Mr. Thomson invented and developed the AstroMesh antenna of which 10 have been flown, deployed, and operating on-orbit with apertures to 12-m. At NGAS, he also developed the telescoping booms that will deploy the James Webb Space Telescope sunshield and the RadarSat 15-m deployable L-band synthetic aperture radar antenna. Mark holds a BS Mechanical Engineering, University of Southern California, 1981, with a minor in Architectural Design.

Dr. Okan Yurduseven received the BSc and MSc degrees in electrical engineering from Yildiz Technical University, Istanbul, Turkey, in 2009 and 2011, respectively, and the PhD degree in electrical engineering from Northumbria University, Newcastle upon Tyne, the United Kingdom in 2014. He is currently a Senior Lecturer (Associate Professor) at the Centre for Wireless Innovation (CWI), The Institute of Electronics, Communications and Information, Technology (ECIT), School of Electronics, Electrical Engineering and Computer Science (EEECS), Queen's University Belfast, UK. He is also an Adjunct Assistant Professor at Duke University, USA. From 2018 to 2019, he was a NASA Postdoctoral Fellow at the Jet Propulsion Laboratory, California Institute of Technology. From 2014 to 2018, he was a Postdoctoral Research Associate within the Department of Electrical and Computer Engineering at Duke University, working in collaboration with the U.S. Department of Homeland Security. His research interests include microwave and millimeter-wave imaging, multiple-input-multiple-output (MIMO) radar, wireless power transfer, antennas and propagation, antenna measurement techniques, and metamaterials. He has authored more than 100 peer-reviewed technical journal and conference articles. He has organized and chaired numerous sessions in international symposiums and conferences, including IEEE International Symposium on Antennas and Propagation (AP-S) and European Conference on Antennas and Propagation (EuCAP). Dr. Yurduseven was the recipient of an Academic Excellence Award from the Association of British – Turkish Academics (ABTA) in London in 2013. He also received a best paper award at the Mediterranean Microwave symposium in 2012 and a travel award from the Institution of Engineering and Technology (IET). In 2017, he was awarded a NASA Postdoctoral Program (NPP) Fellowship administrated by Universities Space Research Association (USRA) under contract with NASA. In 2017, he received an Outstanding Postdoctoral Award from Duke University and a Duke Postdoctoral Professional Development Award. He is a senior member of the Institute of Electrical and Electronics Engineers (IEEE) and a member of the European Association on Antennas and Propagation (EurAAP).

Dr. Min Zhou was born in 1984 in Beijing, China. He received the MSc degree in electrical engineering from the Technical University of Denmark (DTU), Lyngby, Denmark, in 2009, and the PhD degree in 2013 at the same university. In fall 2007, he spent 5 months at the University of Illinois, Urbana-Champaign, USA. Since 2009, he has been with the Danish company TICRA, Copenhagen, Denmark, where he performs research and development for computational techniques and antennas for space applications as well as software development for TICRA's software packages. His research interest includes computational electromagnetics, antenna theory, and analysis and design techniques for quasi-periodic surfaces such as reflectarrays and frequency selective surfaces. Dr. Min Zhou received DTU's Young Researcher Award for his PhD work on reflectarrays in 2013. He was also the recipient of the Best Innovative Paper Award at the 36th ESA Antenna Workshop on Antennas and RF Systems for Space Science in 2015.

1

Introduction

Nacer Chahat

NASA Jet Propulsion Laboratory/California Institute of Technology, Pasadena, CA, USA

1.1 Description of CubeSats

1.1.1 Introduction

Our understanding of the universe, solar system, and Earth has significantly changed thanks to the revolution of space-based observations using large spacecraft such as Voyager, Galileo, and Cassini, to name only a few. Although the science achievement of these missions cannot be presently matched with small satellites, smaller platforms could address targeted science questions in a rapid, and more affordable manner.

A new era for CubeSats has started with the success of Radar In a CubeSat (Raincube) [1] and Mars Cube One (MarCO) [2]. Raincube is the first active radar in a CubeSat. It has successfully demonstrated that an active precipitation radar can fit in a 6U form factor CubeSat and collect valuable atmospheric science. The Raincube CubeSat was released on July 13, 2018 from a NanoRacks deployer outside the International Space Station (ISS). As an example of its accomplishments, Raincube successfully observed typhoon Trami. Tempest-D, another NASA Cube-Sat, also observed Trami within 5 minutes. RainCube nadir Ka-band reflectivity are shown overlaid on TEMPEST-D 165 GHz brightness temperature in Figure 1.1. This illustrates the capabilities of these small satellites that could potentially be

(a)   (b)
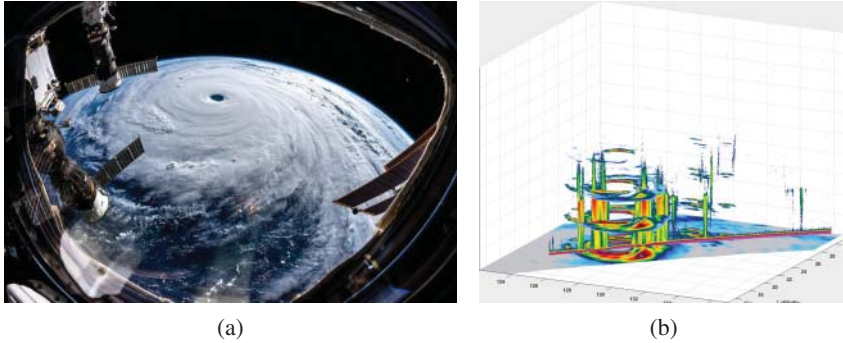
Figure 1.1   *(a) Photography of Trami Typhoon taken from the ISS. (b) RainCube nadir Ka-band reflectivity overlaid on TEMPEST-D 165 GHz brightness temperature of Typhoon Trami.*

launched in a constellation to unlock unprecedented temporal resolution (i.e. minutes) necessary to observe the evolution of weather phenomena. A potential Raincube Follow-on mission, intends to launch a constellation of 12U CubeSats, to accommodate a larger deployable antenna for a small radar footprint with increased resolution.

The 2018 launch of the InSight lander to Mars, included two 6U twin CubeSats called MarCO. These two CubeSats successfully provided real-time telecommunication relay during the Entry, Descent, and Landing (EDL) of the lander. This is also the first CubeSat to travel to another planet, Mars, and operate in Deep Space. Millions of people all over the world witnessed the successful landing of InSight thanks to these two mighty but small spacecraft. Indeed, the first image of Mars landing site taken by Insight (see Figure 1.2) was relayed in real time from the Mars surface to the Earth via the MarCO CubeSat. Without MarCO CubeSats, this picture and play-by-play real time EDL events would have not been possible and reconstruction of EDL event data would have been delayed by 2–3 hours.

MarCO and RainCube have paved the way for future small Earth Science and Deep Space spacecraft making interplanetary space science and high performance Earth Science much more affordable and accessible.

In 2021, 13 CubeSats will launch as secondary payloads on the Exploration Mission 1 test flight. Two examples of these missions are Lunar Flashlight [3] and Near-Earth Asteroid Scout (NeaScout) [4]. They will utilize mostly commercial-off-the-shelf components. Lunar Flashlight uses reflected sunlight to determine whether water ice is exposed on the surface in permanently shadowed lunar polar craters. It uses a four-band spectrometer to observe the reflected light to detect exposed water ice. NeaScout will perform reconnaissance of an asteroid. Propelled by sunlight using a large solar sail, it will make accurate measurement of the asteroid ephemeris, shape, rotation state, spectral class, local dust and debris field, regional geomorphology, and regolith properties. They are both science driven missions using much of the same communication capability as MarCO (Figure 1.3).

Figure 1.2 *Photography of Insight landing site taken shortly after its successful landing was relayed by MarCO-A and MarCO-B 3 hours before the Mars Reconnaissance Orbiter (MRO). Courtesy of NASA.*

1.1.2 Form Factors

Mass of small satellites ranges from 0.1 to 500 kg including microsatellites (10–100 kg), nanosatellites (1–10 kg), and picosatellites (0.1–1 kg). Cube-Sats belong to the nanosatellite category. Standard CubeSats are made up of $10 \times 10 \times 11.35 \, \text{cm}^3$ units designed to provide $10 \times 10 \times 10 \, \text{cm}^3$ of useful volume while weighing no more than 1.33 kg per unit. CubeSats come in different form factor ranging from 1 to 12U as illustrated in Figure 1.4.

Most missions described in this book utilize 6U-class CubeSats ($10 \times 20 \times 30 \, \text{cm}^3$ or $12 \times 24 \times 36 \, \text{cm}^3$). To extend the capabilities of CubeSats, future missions are already exploring the possibility of using larger platform such as 12U ($20 \times 20 \times 30 \, \text{cm}^3$ or $24 \times 24 \times 36 \, \text{cm}^3$). Examples of NASA CubeSats in 3U, and 6U form factors are illustrated in Figure 1.5.

1.1.3 Brief Introduction to CubeSat Subsystems

1.1.3.1 Attitude Control

The in-flight orientation of a CubeSat is of uppermost importance for many aspects of operation. For example, a radar instrument needs to be accurately pointed to take

(a)   (b)
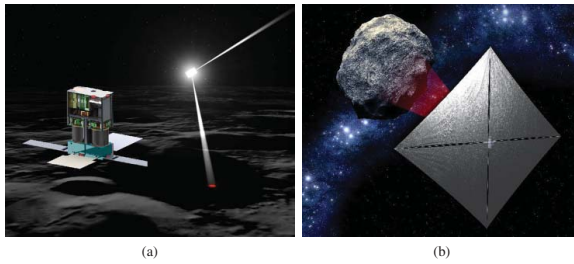
Figure 1.3   (a) *Lunar Flashlight* [3] *uses reflected sunlight to determine whether water ice is exposed on the surface in permanently shadowed lunar polar craters. (b) NEA Scout* [4] *pioneers close-up observation of asteroids and their environments during fly-by encounters, to pave the way for human exploration of such destinations.*
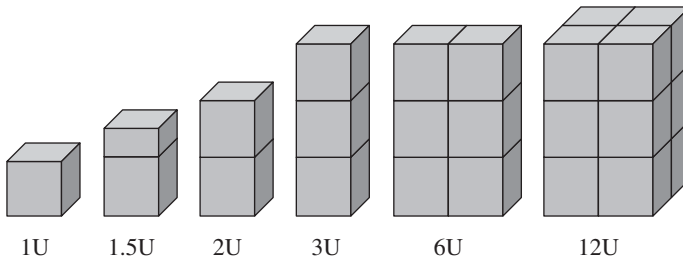
Figure 1.4   *Different form factors of CubeSat.*

1U   1.5U   2U   3U   6U   12U
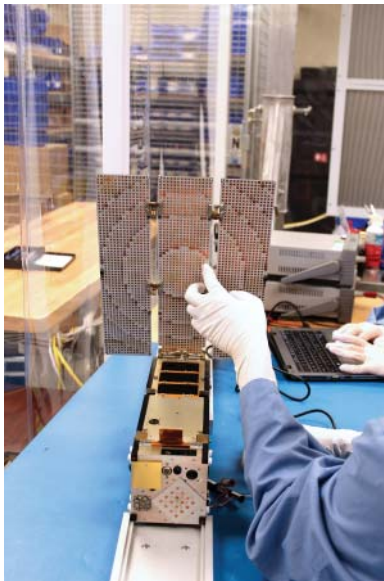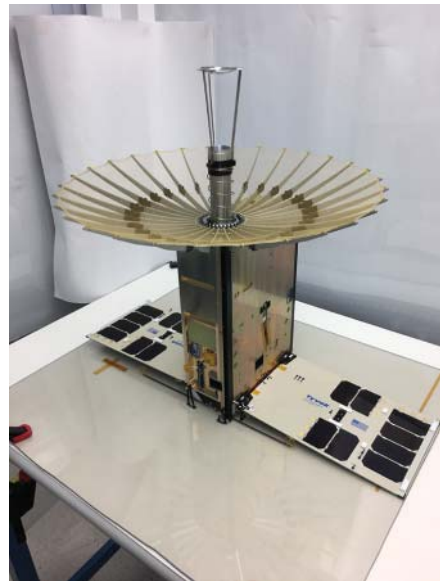
(a)   (b)

Figure 1.5   *Examples of 3U and 6U CubeSats. (a) ISARA (3U). (b) Raincube (6U).*

accurate measurements. This is an example of application that requires a CubeSat's attitude and pointing to be carefully controlled throughout operation.

CubeSat deployment mechanisms are typically low-cost ejection system. If the CubeSat tumbles due to the asymmetric deployment forces, they need to be detumbled.

Systems that perform attitude determination and control include reaction wheels, magnetorquers, thrusters, star trackers, sun sensors, and GPS receivers. Combinations of these systems are usually used to leverage advantages of each methods and mitigate their individual shortcomings.

(a)   (b)
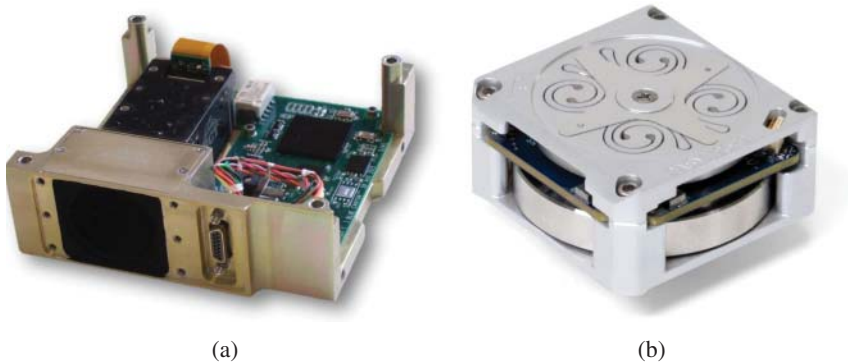
Figure 1.6   *(a) Sun sensor. (b) Reaction wheel. Courtesy of Blue Canyon Technologies.*

NeaScout and MarCO CubeSats use a Blue Canyon Technologies XACT attitude-control unit (see Figure 1.6) that includes a star tracker, gyro, coarse sun sensors, and three-axis reaction wheels. The star tracker is used for fine orientation and sun sensors are used for course orientation. Gyroscopes are employed to sense rotation speed and the three-axis reaction wheels adjusts orientation.

1.1.3.2   Propulsion

Propulsion systems are luxury for CubeSats that need to save their limited volume and mass for science instruments. CubeSat propulsion has made rapid advancements in the following technologies: cold gas, chemical propulsion, electric propulsion, and solar sails. Propulsion systems can be used for attitude control or trajectory correction maneuvers (TCMs).

As an example, MarCO CubeSat uses cold gas with four reaction wheel thrusters and two axial thrusters fitting in a 2U volume and providing a nominal thrust of 50 mN and a total impulse of 755 N-s. It uses R-236FA as the propellant; it is a cold-gas propellant used terrestrially in fire extinguishers. Propulsive force is stored as pressurized gas. The attitude control unit commands thruster firing both for reaction-wheel desaturation and TCMs. For safety, the control and data handling (C&DH) subsystem maintains power control of the propulsion system. The propulsion unit employed on MarCO is shown in Figure 1.7.

NASA's CubeSat NeaScout, currently under development, employs both cold gas reaction control system and a large solar sail (Figure 1.8). Solar sails are made of ultrathin and highly reflective material. When a photon from the sun hits the mirror-like surface, it bounces off the sail and transfers its momentum.

Figure 1.7 *MarCO micro propulsion system. Courtesy of VACCO.*

Figure 1.8 *NeaScout solar sail fully deployed. Courtesy of NASA.*

1.1.3.3   Power

To date, CubeSats have used solar cells to convert solar light to electricity then stores the power in rechargeable lithium-ion batteries that provide power during planetary eclipse, during any operations that point solar panels away from the sun and provide extra power during peak load times. The solar cells can either be located on the CubeSat bus or they can be deployed. A dedicated electrical power system (EPS) controls the battery charging and discharging and monitors and manages battery health. Other CubeSat power system options could be possible in the future.

Missions with higher power requirements can make use of attitude control to ensure the solar panels remain in their most effective orientation toward the Sun, and further power needs can be met through the addition and orientation of deployed solar arrays. This also implies tradeoff that involves more than one subsystem. For instance, the pointing of a telecommunication antenna may compete with optimum solar array pointing toward the sun and both solar array and this competition/optimization will change over the long term trajectory of the CubeSat itself. This is where system engineering tradeoff needs to be made early on in a project as it defines critical constraints on multiple subsystems.

Deployable solar arrays compatible with 3U or 6U CubeSats are commercially available. For example, MarCO uses two deployable solar arrays for a total of 42 cells folding in a stowed volume of 1U × 3U with a dual-axis deployment providing 36 W beginning of life (BOL) (Figure 1.9).
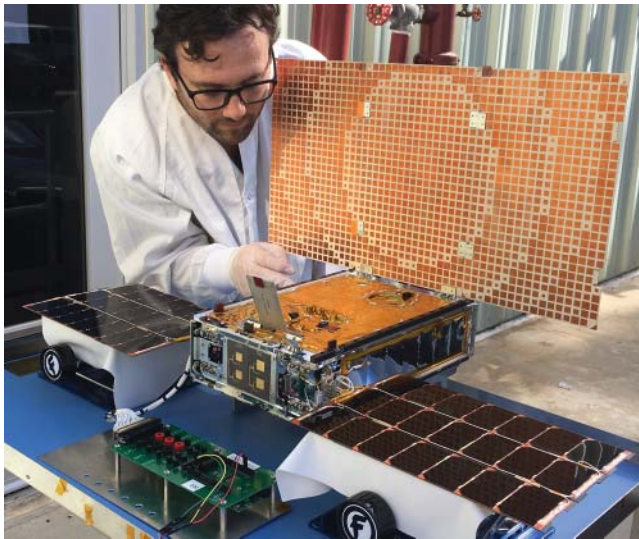
Figure 1.9   *Two dual-axis deployment 36 W BOL deployable solar arrays on MarCO each folding on a 1U × 3U stowage volume. Courtesy of NASA.*

   Important requirements are imposed on CubeSats that fly as secondary payloads. Under current policies, no electronics may be active during launch to prevent any electrical or RF interference with the launch vehicle and primary payloads. Cube-Sats with rechargeable batteries must be fully deactivated during launch or launched with discharged batteries. A remove before flight (RBF) pin is required to deactivate the CubeSats during integration outside the Poly-Picosatellite Orbital Deployer P-POD. The pin is removed once the CubeSats are placed inside the P-POD.

1.1.3.4   Telecommunication

The telecommunication challenges for Low Earth Orbit (LEO) missions vs. deep space missions are very different. In LEO, ground-antenna gain can compensate for limited onboard antenna gain and radio power and CubeSats can manage limitations of power generation and thermal dissipation by duty-cycling high-power components. Most radios commercially available for CubeSats operate at UHF [5] or S-band [5, 6].

   Most LEO CubeSats rely on UHF and/or S-band radios to receive commands or transmit telemetry back to Earth's ground station. For instance, the Raincube radar utilizes both a UHF and an S-band telecommunication system to relay data to the ground (see Figure 1.10).
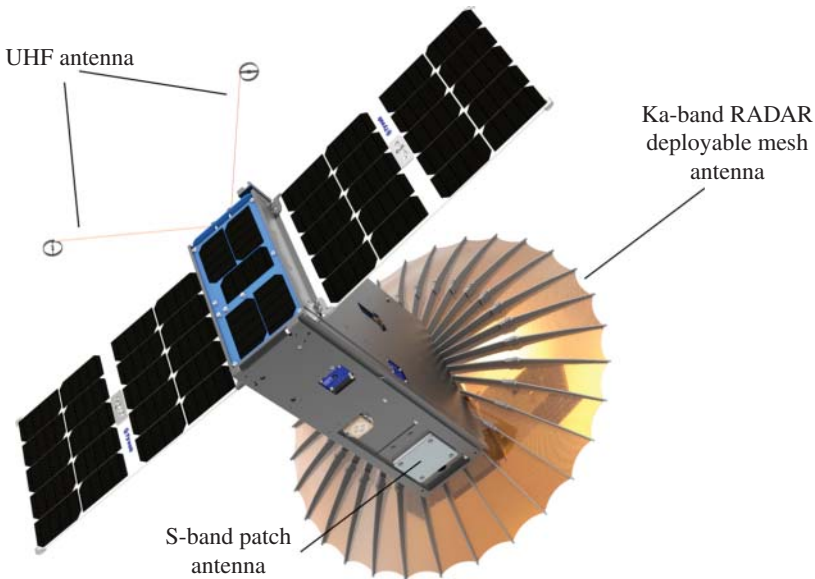
Figure 1.10   *Raincube LEO CubeSat uses both UHF and S-band telecommunication system.*

There are only few radios available at X-band [7] or Ka-band [8]. The Iris radio is the only CubeSat radio that provides interoperability with NASA's Deep Space Network (DSN) at X-Band frequencies for command, telemetry, and navigation (i.e. ranging and delta-differential one-way ranging). Iris was launched for the first time in deep space with MarCO in May 5, 2018. The radio was successfully demonstrated in the two MarCO Cubesats at X-band and UHF. The Iris software-defined, radiation-tolerant radio with 5 W RF output at X-band frequencies, has four receive and four transmit ports, and an external solid-state power amplifier and low-noise amplifier. The details of the Iris radio are covered in Chapter 2.

The Artemis CubeSat missions follow the lead of MarCO. Most of the Artemis deep space CubeSats use two X-band low-gain patch antennas (Tx and Rx) on each side of the CubeSat for near-Earth communications with wide beamwidth or safe-mode communications, and medium- or high-gain antenna for high-data-rate communication at larger distance. This is the case of NeaScout as shown in Figure 1.11.

A CubeSat using these low-gain antennas with a 5 W solid state power amplifier (SSPA) can transmit telemetry at 62.5 kbps to a 70 m DSN ground station with a misalignment of 90° at distances up to 0.15 AU and it can tolerate a misalignment of up to ±1° at 1 AU using the transmitting-low gain antenna (Tx-LGA). The alignment required to close the link with a 70 m DSN ground station at 62.5 kbps is shown in Figure 1.12b as a function of distance.

A Cubesat can receive commands at 62.5 kbps, on its LGAs (i.e. 7 dBi patch), from a 34 m DSN ground station with a misalignment of 90° off boresight at a maximum distance of 0.338 AU. The spacecraft can tolerate a misalignment of up to ±62° at 1 AU (see Figure 1.12a). Using a 70 m DSN, the uplink link can close
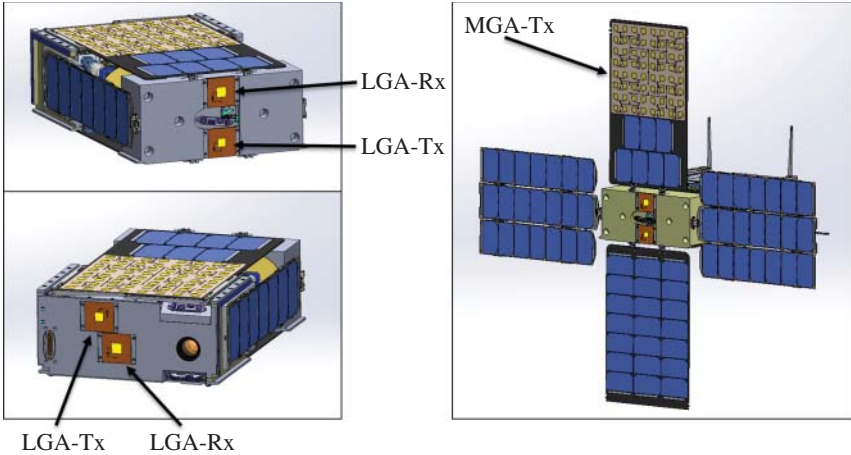
Figure 1.11   *Near-Earth Asteroid Scout (Nea Scout) CubeSat employs four LGAs and one MGA.*
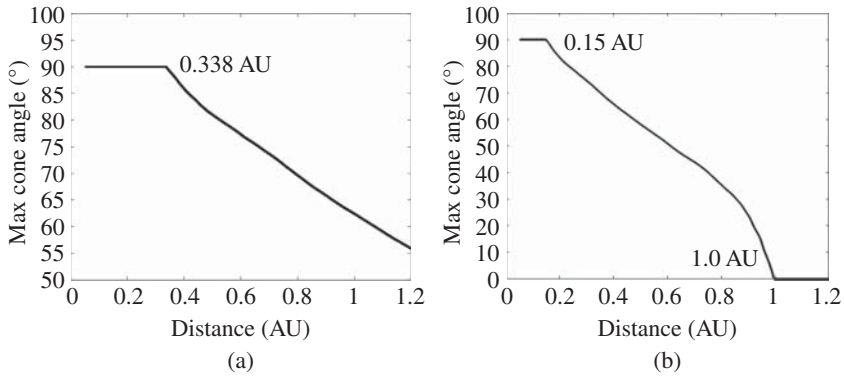
Figure 1.12 *Maximum antenna misalignment to close the link at 62.5 kbps. (a) Uplink in safe mode with a 34 m DSN ground station. (b) Downlink in safe mode with a 70 m DSN ground station.*

with a misalignment of $\pm 90°$ at distances up to 0.67 AU. The uplink link can tolerate a misalignment of up to $\pm 80°$ at 62.5 kbps using a 70 m DSN.

1.1.4 CubeSat Antennas

To cover existing antenna technologies for CubeSats, we will classify them in the following categories: LGAs (<8 dBi), medium gain antennas (MGAs) (<25 dBi), and high-gain antennas (>25 dBi). This section provides an overview of the different type of antennas used for CubeSats.

1.1.4.1 Low Gain Antennas

LGAs are primarily used to receive data or transmit telemetry without requiring a precise pointing. Their larger beamwidth comes in handy when the science payload or the solar cells dominate the spacecraft pointing requirement forcing the telecommunication antennas to be off-pointed. Also, in safe mode, if the pointing is unknown, LGAs enable communication link at low data rate.

In LEO, an omnidirectional antenna allows the spacecraft to always be in contact with the ground station without the need for rotating or re-pointing the spacecraft. Traditionally UHF or S-band LGAs are employed in LEO. An example of a LEO mission is provided in Chapter 3, Raincube, where both UHF and S-band is employed to relay the science data to the ground station.

Dipole Antennas Dipole antennas are mainly used at VHF or UHF. The most commonly used UHF CubeSat antenna is the commercially available deployable dipole antenna. It consists of four tape spring antennas of up to 55 cm length [9]
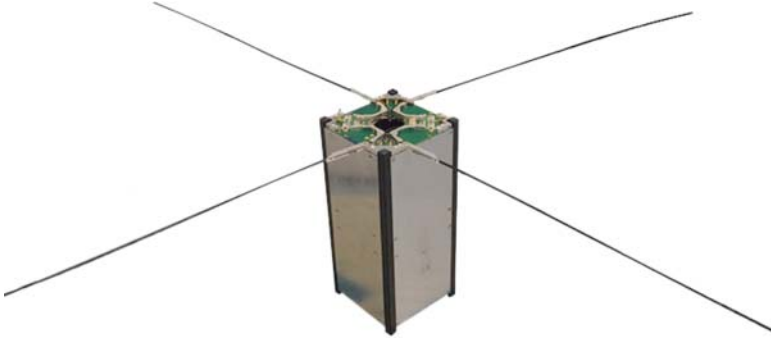
Figure 1.13   *Turnstile UHF deployable dipole antenna. Courtesy of ISIS.*

(Figure 1.13). Various antenna configurations are available (monopole, dipole, or turnstile) allowing to obtain linear or circular polarizations with an omnidirectional pattern and a gain of about 0 dBi with an output power of 2 W.

Patch Antennas   Circular polarization is typically employed for space communication to minimize (1) polarization loss due to misalignment between antennas, (2) de-polarization caused by the atmosphere, and (3) signal degradation due to atmospheric conditions.

   Circular polarization can easily be obtained from a patch antenna. Circular polarization is obtained by exciting two orthogonal linear polarizations. The two modes must be excited with equal power and with a 90° phase difference. Examples of techniques to achieve circular polarization with a patch are shown in Figure 1.14. A patch with single feed and with truncated corners is often preferred due to avoidance of combining network.

   LEO CubeSats often use commercially available S-band circularly polarized patch antennas. The antenna shown in Figure 1.15 is designed to operate in the 2.4–2.5 GHz ISM band. A conventional corner truncated microstrip patch antenna
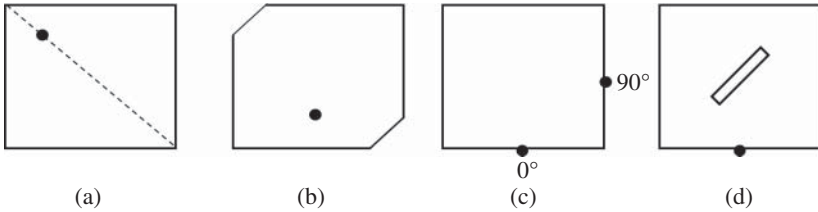
Figure 1.14   *Examples of techniques to design circularly-polarized patch antennas. (a) Nearly square patch fed on the diagonal. (b) The corners truncated patch antenna. (c) Dual feed edge fed patch. (d) Square patch with thin slot.*
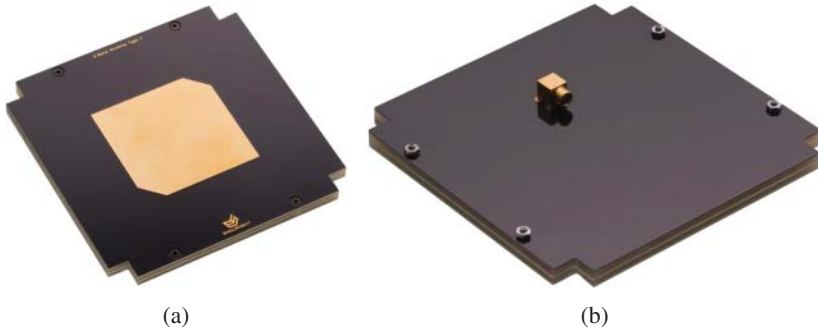
Figure 1.15   *Low gain corner truncated circularly-polarized patch array operating at S-band. Courtesy of EnduroSat.*
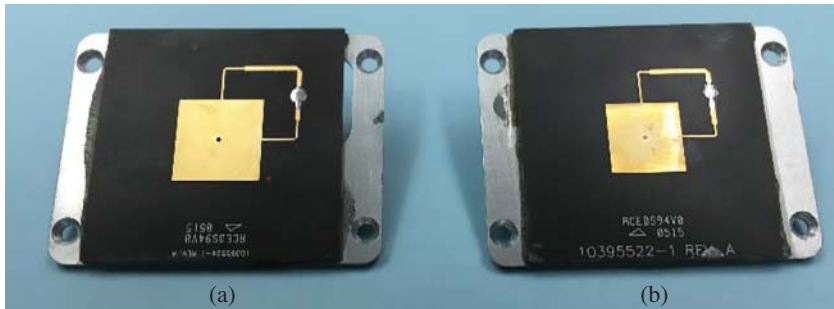
Figure 1.16   *MarCO low gain circularly-polarized patch array compatible with the deep space network. (a) Rx-LGA. (b) Tx-LGA.*

is used to obtain circular polarization. It provides a gain of 8.3 dBic with a half power beam width of 71°.

All current deep space CubeSats utilize Jet Propulsion Laboratory (JPL's) X-band circularly-polarized Rx and Tx patch antennas. For instance, the X-band LGAs flown on MarCO are shown in Figure 1.16. They consist of dual feed edge-fed circularly polarized patch antenna to cover a wider bandwidth. The two right-hand circular polarization (RHCP) patch antennas are printed on RT Duroid 5880 ($\varepsilon_r = 2.2$ and thickness $= 0.787$ mm). They demonstrate a boresight gain of more than 7 dBic and more than -8 dBic at $\pm 90°$. While the antenna design is relatively simple, the bonding process between the aluminum plate and the antenna substrate is very critical to avoid delamination over time caused by thermal changes. The process needs to be well-controlled and flight qualified. Critical parameters are the epoxy selection, the bondline thickness, and surface preparation. Testing needs to be performed on all flight hardware to reduce risks of failure due to process variability.
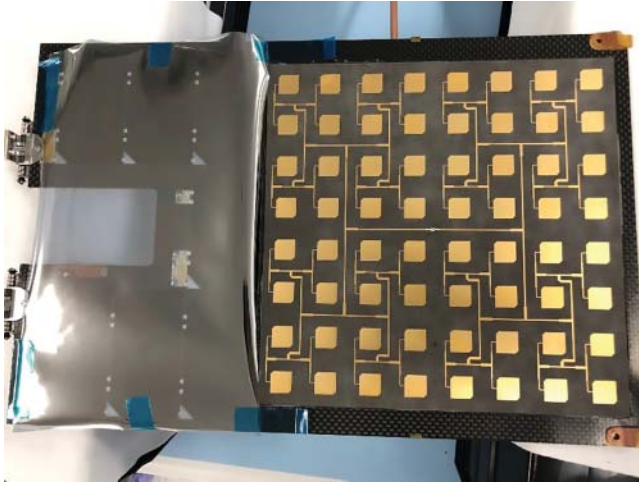
Figure 1.17 *NeaScout X-band medium gain antenna located near solar cells. The 8 × 8 patch array is mounted on a carbon fiber deployable wing. The same antenna is used on other Deep Space missions (Biosentinel, CuSP) at different locations.*

1.1.4.2   Medium Gain Antennas

Medium antennas showcase gain ranging from 12 to 25 dBi. They are mainly used on deep space CubeSats where higher gain is required for long range or higher data rate communications.

Patch arrays are very attractive antennas for CubeSats if they can fulfil the gain requirement within the allocated volume without involving any complex mechanical deployment. They are constrained to the maximum size of the CubeSat. On a 6U CubeSat, a 8 × 8 patch array can easily fit within 19 cm × 19 cm.

Missions such as NeaScout, Biosentinel, CuSP, are all using a transmit-only 8 × 8 circularly polarized patch array providing more than 23.4 dBic. This enables 1 kbps at 1 AU using a 34 m DSN antenna or 4 kbps using a 70 m DSN antenna. The MGA developed for NeaScout is shown in Figure 1.17. It is bonded onto the solar array fixture made of carbon fiber. A new bonding process was developed to accommodate for the coefficient of thermal expansion (CTE) mismatch between the Rogers 5880 (i.e. 31 and 48 ppm/°C in *x*- and *y*-direction) and carbon fiber (0 ppm/°C). The antenna survived thermal cycling from −55 to 110 °C.

Table 1.1 summarizes the gain and half power beamwidth achieved for multiple array configuration.

More recently, a new all-metal patch array was developed for a potential Europa Lander [10] (see Chapter 7). This antenna demonstrates unprecedented efficiency of more than 80% and achieving a gain of 25.3 dBic for an 8 × 8 patch array. In addition, this antenna can operate at both uplink and downlink frequency bands.

Table 1.1   *Performance of patch array with different configuration.*

Array	Size (cm × cm)	Gain (dBic)	HPBW (°)
2 × 2	4.8 × 4.8	13.2	39.5
2 × 4	4.8 × 9.5	16.2	39.5/19.4
4 × 4	9.5 × 9.5	17.0	19.4
8 × 4	19 × 9.5	20.0	9.5/19.4
8 × 8	19 × 19	23.4	9.5

This is a 2 dB improvement compared to the previous array, which translates into a 1.6 times data rate improvement. One drawback of this antenna is the mass increase but one can consider using the bus as the ground plane.

The first metal-only metasurface (MTS) antenna was fabricated using metal additive manufacturing [11] (see Chapter 8). It is operating at Ka-band in the downlink DSN frequency band (i.e. transmit only). The 10 cm-diameter MTS antenna achieves 26.1 dBic. Such an antenna can be printed on the bus surface using the largest side of the CubeSat as a radiating aperture. Unfortunately, metal-only MTS are still low efficiency ($\sim$<40%). However, it was recently published that MTS antennas can possibly achieve up to 70% efficiency [12]. This would make them good solutions for transmit-only MGA antennas at X- or Ka-band, particularly because they can be designed to achieve any radiation pattern (i.e. directive, isoflux, etc.). MTS antennas printed on dielectric could also be used as MGAs similarly as patch arrays assuming higher efficiencies can be achieved.

1.1.4.3   High Gain Antennas

Selection Criteria Guidelines   Selecting a high gain antenna (HGA) for deep space communication or remote sensing instruments is not an easy task and is of the utmost importance for mission success. A guideline highlighting the advantages and drawbacks of each HGA technologies is provided to help in the selection process in Figure 1.18.

The available HGA technologies developed for Cubesats are abundant: patch arrays [10], deployable reflectarrays [13–15], mesh reflector [16–18], inflatables [19–21], and membrane [22, 23]. Few potential new technologies applicable to CubeSats are MTSs [11, 12] and slot arrays [24, 25].

The selection criteria typically includes: (1) stowage volume, (2) frequency band, (3) bandwidth, and (4) performance.

Example 1:
For instance, if one mission requires a HGA at X-band with no stowage volume available inside of the bus, the first choice is patch array. If the largest side of the CubeSat does not provide the required gain (i.e. gain > 26 dBic; reference
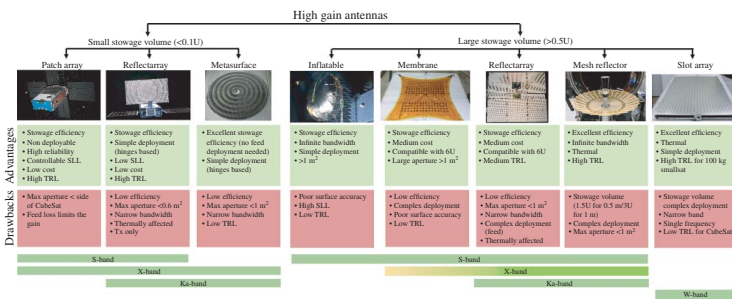
Figure 1.18 High gain antenna selection guidelines for CubeSats high gain antennas.

to Table 1.1), the obvious choice becomes a deployable reflectarray. This is the case of MarCO discussed in Chapter 2.

Example 2:

As another example, if one is looking for a Ka-band highly efficient antenna (i.e. >50%), with available stowage volume, the options are deployable reflectarray or mesh reflector. However, mesh reflectors are more efficient and they are also less sensitive to thermal variation; so they are the natural choice. This was the case of Raincube discussed in Chapter 3.

Example 3:

Lastly, for a mission requiring a gain of 23 dBic to transmit telemetry to a 34-m DSN antenna at 1 AU at 1 kbps, the choice is more straightforward for a 6U CubeSat. A 8×8 patch array does not require any deployment and fits on one side of the CubeSat (see Figure 1.17). This was the case of NeaScout.

Reflectarray In 1996, Dr. John Huang at NASA JPL introduced the idea of using deployable reflectarray composed of flat panels that could also potentially be combined with solar cells in the back of the reflectarray [26, 27]. This concept takes advantage of flat reflecting surface relying on a simple mechanical deployment with spring loaded hinges [26]. His concept was implemented for the first time for the technology demonstration CubeSat ISARA (Integrated Solar Array & Reflectarray Antenna) [13]. ISARA was the first reflectarray in space. It was designed to achieve a gain of 33.0 dBic at 26 GHz for LEO communication, which translates into an efficiency of 26%. It suffers from a low efficiency feed, large gaps between panels and bulky hinges causing both side lobe level increase and gain reduction. The antenna was successfully deployed in orbit as witnessed by the photography of the deployed antenna taken in-orbit (Figure 1.19).

(a)   (b)
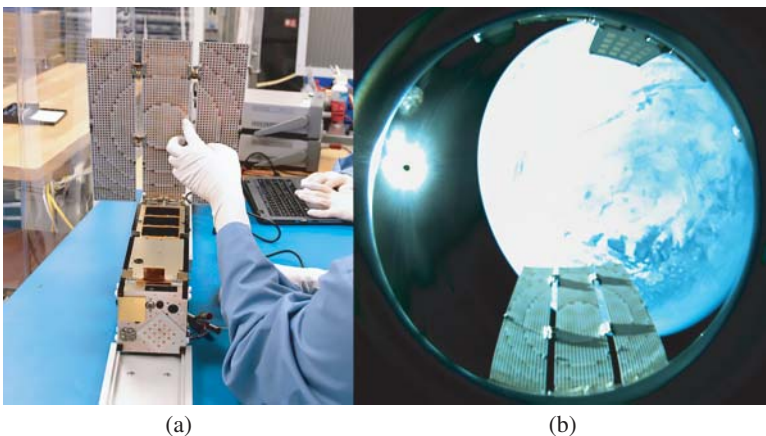
Figure 1.19 *(a) NASA's JPL ISARA CubeSat* [13] *during Integration and Testing. (b) Photography of ISARA successfully deployed in-orbit.*

(a)   (b)
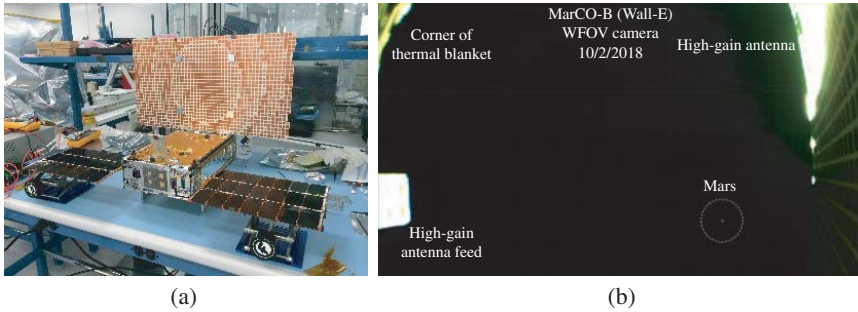
Figure 1.20   *(a) NASA's JPL MarCO CubeSat during Integration and Testing. (b) Photography of MarCO in deep space on its way to Mars* [2].

This work was extended to an X-band telecommunication system using a reflectarray deployed from a 6U CubeSat jointly launched with the NASA InSIGHT Mars lander mission to provide auxiliary telecommunications during the entry descent and landing portion of that mission [2, 14]. The transmit-only reflectarray demonstrates a gain of 29.2 dBic (i.e. 42% efficiency). Higher efficiency was achieved by (1) removing the gaps between the panels, (2) using low profile hinges, and (3) improving significantly the feed efficiency. MarCO near-real time bent pipe communication (i.e. 8 kbps) at Mars distance (∼156 million km) would have not been possible without its X-band deployable reflectarray as its SSPA is limited to 5 W [2, 14]. For MarCO, the choice of HGA technology is obvious as very limited volume was available inside the bus and the antenna aperture to meet the gain requirement could not be reached with a non-deployable patch array. A photography of the deployed antenna is shown in Figure 1.20 while the CubeSat is approaching Mars. The antenna gain of MarCO reflectarray was measured within 0.4 dB during Insight EDL and providing flawless near-real-time coverage. More details regarding the design of this reflectarray are provided in Chapter 2.

To achieve smaller footprint for remote sensing, a highly constrained deployable reflectarray antenna compatible with 6U-class CubeSat was developed (see Figure 1.21) [15]; it is currently the largest Ka-band CubeSat antenna. While this antenna was designed primarily for Earth Science remote sensing [15], it can easily be redesigned for Ka-band Deep Space communication. The Ka-band high gain reflectarray antenna employs Cassegrainian optics to accommodate a deployment mechanism that stows the reflectarray panels and feed assembly into a highly constrained volume. Despite the stringent mechanical constraints, the linearly-polarized antenna demonstrated excellent performance at 35.75 GHz with a gain of 47.4 dBi [15]. More details regarding the design is provided in Chapter 4.

The adjustable hinges developed for OMERA allows to deploy accurately six panels from one side of the bus at frequency bands up to Ka-band. For this reason, it was easy to extrapolate the MarCO design to a larger X-band antenna. A six-panels
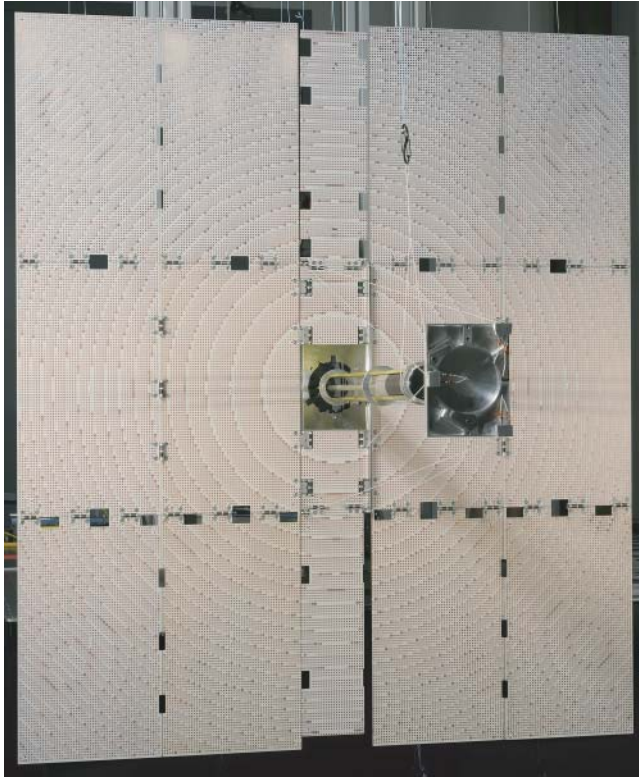
Figure 1.21 *One meter reflectarray (OMERA) compatible with 6U-class CubeSat* [15].

deployable reflectarray operating at 8.4–8.45 GHz DSN band was designed for a 6U-class CubeSat (see Figure 1.22). This antenna provides a gain of 33.0 dBic at X-band. Similarly to MarCO, the feed folds against the CubeSat bus. It is a 2×2 circularly polarized patch array (see Figure 1.23a) with only 0.4 dB of insertion loss.

The same six-panels deployable reflectarray was also designed at Ka-band (see Figure 1.23a). The feed is a simple Ka-band multiflare horn. The DSCKa antenna offers a gain of 33 dBic at Ka-band downlink frequency band (i.e. 31.8–32.3 GHz).

One can combine X- and Ka-band operation using two collocated feeds. A six-panels reflectarray operating at X- and Ka-bands was achieved using a feed horn and a X-band 2×2 patch array. The beam pointing was adjusted by the reflectarray design itself to obtain the same beam direction at both frequency bands; the spacecraft can communicate at X- or Ka-band without adjusting its attitude. The unit cell covering X- and Ka-band is shown in Figure 1.23b, where square patches are used as unit cells at Ka-band and cross-dipoles are used as unit cells at X-band.

(a)   (b)
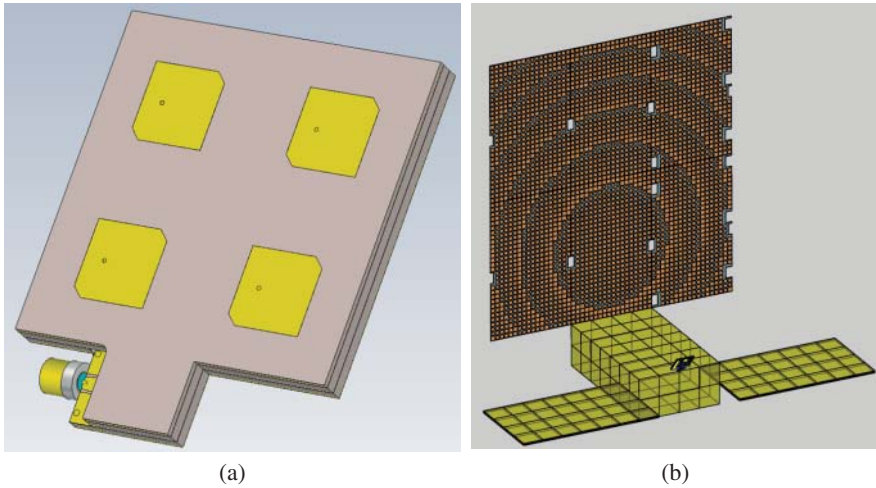
Figure 1.22   *Deep Space CubeSat Antenna operating at X-band (DSCX). (a) Transmit only X-band feed. (b) Six-panels deployable reflectarray on the CubeSat Bus simulated using Ticra GRASP and QUPES tools.*

The thickness of the reflectarray panels needs to remain small while supporting the required bandwidth. The cross-dipole is narrow-band and therefore sensitive to the fabrication tolerance. Hence, the thickness of the cross-dipole layer was chosen to meet the bandwidth requirement taking into account the achievable fabrication tolerance.

Critical characteristics of all available deployable reflectarray antennas are compared in Table 1.2.

Mesh Reflector   Multiple deployable mesh reflector for CubeSats were developed at S-band [28, 29], X-band [18], or Ka-band [16, 17]. A Ka-band 0.5 m deployable mesh reflector compatible with 6U-class CubeSat was introduced for deep space communication [17] and Earth science mission [16]. Although the antenna fits in a constrained volume of 1.5U (i.e. $10 \times 10 \times 15 \, cm^3$) a gain of 42.4 dBi and a 56% efficiency were demonstrated. The antenna was successfully deployed in LEO on July 28, 2018 (see Figure 1.24). The RF design and mechanical deployment is thoroughly described in Chapter 3.

An offset mesh reflector compatible with 12U-class CubeSats is currently under development at Tendeg [18]. The offset configuration allows reaching higher efficiency (no feed blockage), achieving lower side lobe levels, and redesigning the antenna at other or multiple frequencies. The antenna was designed at X- and Ka-band for deep space communication [30] (Figure 1.25). For X-band, a gain of 36.1- and 36.8-dBic is achieved at uplink and downlink frequency bands, respectively (i.e. ~72 and 62% efficiency, respectively). At Ka-band, a
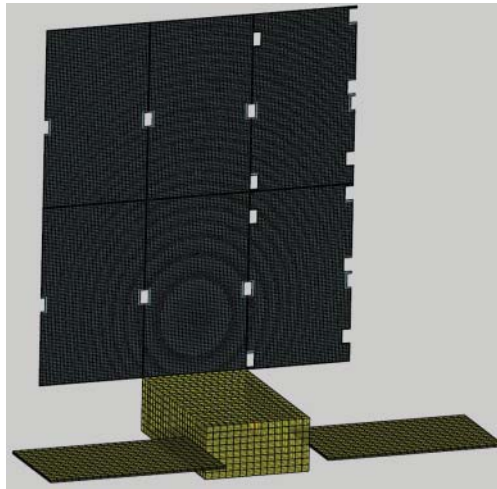
(a)
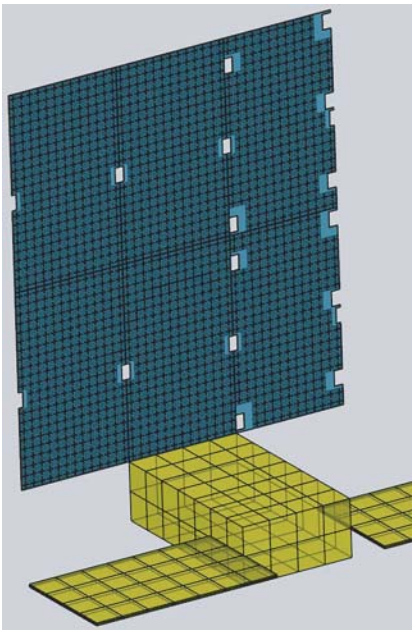
(b)
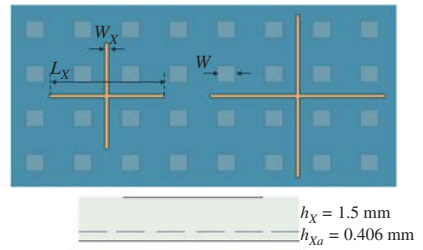
Figure 1.23 *Deep Space CubeSat Antenna operating at (a) Ka-band (DSCKa) and (b) X-/Ka-bands (DSCXKa).*

Table 1.2   *Deployable reflectarray performance for CubeSats.*

Name	Type	Aperture size (m × m)	Frequency	Gain	Efficiency [a] (%)	CubeSat size (U)
ISARA [13]	Reflectarray	0.33 × 0.27	26	33.0 dBic	26	3
MarCO [14]	Reflectarray	0.60 × 0.33	8.4–8.45	29.2 dBic	42	6
OMERA [15]	Reflectarray	1.05 × 0.91	35.75	47.4 dBi	32	6
DSCX	Reflectarray	0.60 × 0.67	8.4–8.45	33.0 dBic	50	6
DSCKa	Reflectarray	0.60 × 0.67	31.8–32.3	43.5 dBic	40	6
DSCXKa	Reflectarray	0.60 × 0.67	8.4–8.45	32 dBic	40	6
			31.8–32.3	43.0 dBic	35	

[a]The efficiency is defined as the ratio of the realized gain of the antenna to its standard directivity. The standard directivity is $10 \cdot \log_{10}(4\pi A/\lambda_0^2)$, where A the area of the antenna aperture and λ_0 is the free space wavelength. This defines how efficiently the area of an antenna is used.
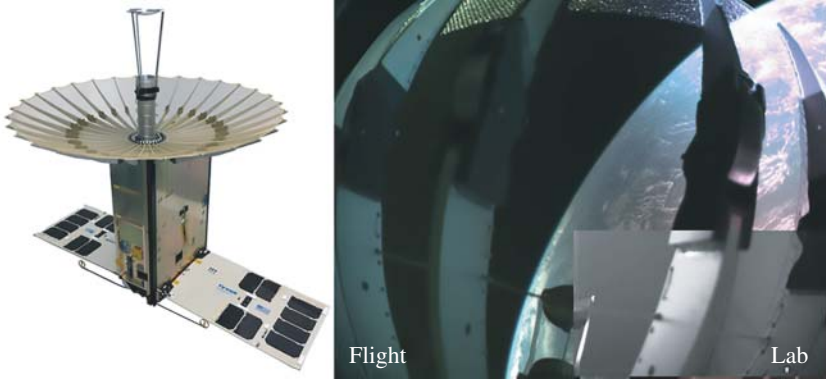
Figure 1.24   *One NASA's JPL 0.5-m mesh reflector antenna on Raincube CubeSat [16] was successfully deployed and operated in-orbit.*

gain of 48.4-dBic is obtained at downlink frequency band (~62% efficiency). The mechanical deployment is still in progress but the results are promising. The antenna mechanical and RF design are is detailed in Chapter 5.

The performance of these two mesh reflectors are summarized in Table 1.3. Compared to reflectarray deployable antennas (Table 1.2), mesh reflectors achieve higher efficiency at the expense of larger stowage volume and higher complexity.

Inflatables   Inflatable antennas were developed and comprehensively tested at S-band [19] and X-band [20] for Deep space communication. Additional work was also reported by another team at W-band [21]. Although the spherical surface aberration can be compensated by adjusting the feed location [20, 21] or using a corrective lens [31], it is unlikely that the surface accuracy can be maintained at frequencies above S-band.

(a)   (b)
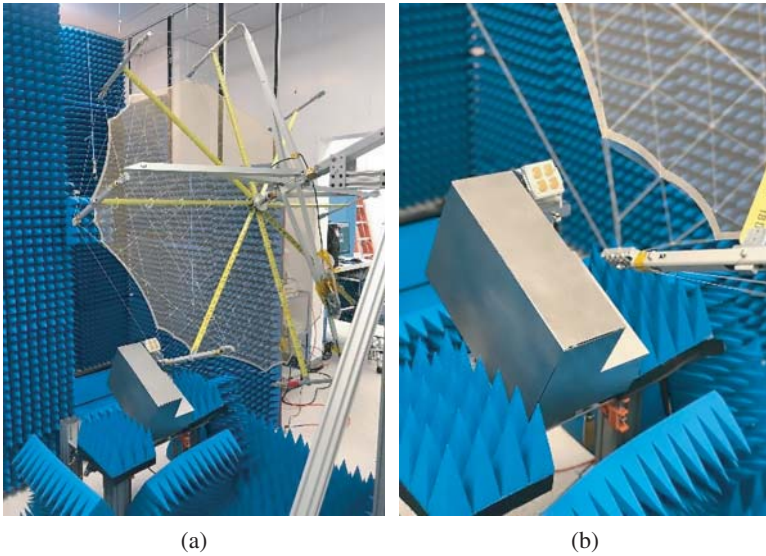
Figure 1.25 *One-meter deployable mesh reflector for deep space communication at X-, Ka-, or X/Ka-band* [30]. *The mesh reflector mechanical deployment is described in* [18].

Table 1.3 *Deployable mesh reflector performance for CubeSats.*

Name	Type	Aperture size (m diam.)	Frequency (GHz)	Gain (dBic)	Efficiency (%)[a]	CubeSat size (U)
KapDA [17]	Mesh reflector	0.5	32	42.0	57	6
			34	42.4	55	
KaTENna [18, 30]	Mesh reflector	1	8.4	36.8	62	12
			36	48.4	62	

[a]The efficiency is defined as the ratio of the realized gain of the antenna to its standard directivity. The standard directivity is $10 \cdot \log_{10}(4\pi A/\lambda_0^2)$, where A the area of the antenna aperture and λ_0 is the free space wavelength. This defines how efficiently the area of an antenna is used.

Membrane Antennas   Membrane antennas were extensively investigated by John Huang [32–34] at NASA JPL for small satellites as they allow achieving large aperture with excellent stowage efficiency. Membrane antennas can be patch arrays [32] or reflectarrays [33, 34]. Membrane antennas are a natural option for CubeSats. A large patch array operating at S-band was recently introduced for 6U-class CubeSat [22] (Figure 1.26). A $1.53\,m^2$ linearly-polarized patch array deploys from a 2U stowage volume. After multiple deployments, a 28.6 dBi gain was measured which translates into an 18% efficiency.

Figure 1.26   *S-band 1.5 m² aperture deployable membrane antenna after its first deployment* [22].

An X-band reflectarray membrane antenna is under development at the JPL [23] (Figure 1.27). It deploys into a 1.5 m² aperture with a 0.5 mm surface rms from a canister of 20 cm diameter and 9 cm height. A gain of 39.6 dBi was measured using a feed horn located at its focal point. Although the antenna is not yet completed, the achieved efficiency is about 40% (Table 1.4). The feed deployment inaccuracy, feed loss, and feed blockage will contribute to additional loss.

Slot Arrays   The concept of deployable slot array was presented for 100 kg small satellites [24]. It consists of six deployable panels folding around the spacecraft (Figure 1.28). Slot arrays are good solutions for single-band and narrow-band applications with linear or circular polarization. The concept introduced in [24] can be implemented for CubeSats at Ka-band or above. Reference [25] presents the development of an S-band slot array able to produce three operating modes: omnidirectional, multibeam, or directive.

Metasurface Antennas   MTS antennas could potentially also be a good solution for HGAs. They provide the ability to deploy a large aperture antenna without deploying a feed at a focal distance from the antenna aperture; this is the biggest challenge as the antenna aperture increases [15, 35]. Similar deployment approach as deployable reflectarrays can be applied. From 6U- or 12U-class CubeSats, the maximum aperture achievable is about 1 m². The effect of small gaps between the panels remain to be assessed. As mentioned earlier, MTS antennas are narrow band. A methodology to achieve dual-frequency operation from the same aperture was recently reported [36, 37].

In Chapter 8, the design process of MTS antennas is described in details throughout multiple examples.
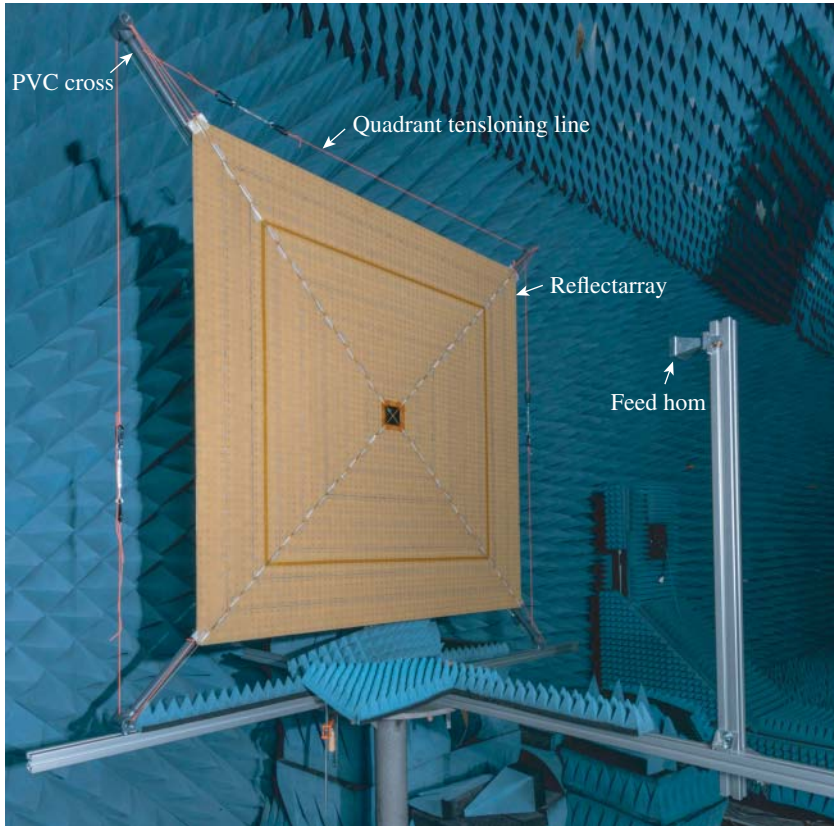
Figure 1.27 *X-band 1.5 m² aperture deployable membrane antenna in an anechoic chamber* [23].

Table 1.4 Deployable high gain antenna performance for CubeSats.

Name	Type	Aperture size (m × m)	Frequency (GHz)	Gain (dBi)	Efficiency (%)	CubesSat size (U)
Membrane [22][a]	Membrane	1.24 × 1.24	3.6	28.6	18	6
LaDeR [23][a]	Membrane	1.5 × 1.5	8.4	39.6	40	6

[a]Not fully completed – with missing elements that will affect the gain and efficiency.
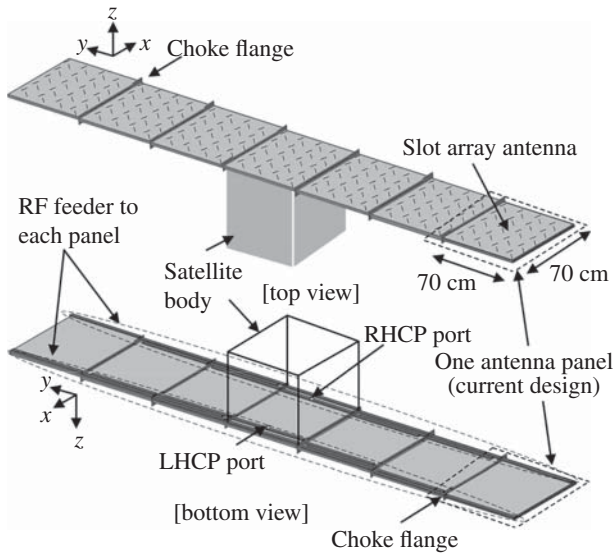
Figure 1.28   *X-band deployable slot array for small satellites. Source: From Akbar et al.*
[24]. © 2015 IEEE.
.

1.1.5   Effect of Space Environment on Antennas

When an antenna is used in space, particular attention needs to be made to four
major effects related to space environment: radiation exposure, material outgassing,
temperature change, and multipacting or ionization breakdown.

1.1.5.1   Radiation

Cosmic radiations, such as beta, gamma, and X-rays, are similar to nuclear radia-
tion in many aspects. As a result, cosmic high-energy radiation is a critical design
constraint in space applications and the choice of material is critical when designing
an antenna for spacecraft.

Cosmic radiations can damage materials after long term or short term exposure
to space. It can alter their electrical properties such as dielectric constant and loss
tangent. During irradiation, the dielectric constant and loss factor will be temporar-
ily increased. They are affected by electrical charge distributions in the resin which
decays with time, and thus, the radiation dose rate is important.

Cosmic radiations can also damage the mechanical properties of the material; this
is due to the reduction of molecular weight caused by breaking the large polymer
molecule into smaller parts. The effect of molecular weight reduction is primarily
on mechanical properties: there will be an increase in brittleness and reduction in
tensile strength, modulus, and elongation.

Table 1.5 Radiation doses in rads for damage to PTFE material.

	In air	In vacuum
Threshold	$2-7 \times 10^4$	$2-7 \times 10^5$ or more
50% tensile strength	10^6	10^7 or more
40% tensile strength	10^7 or more	8×10^8 or more
Retain 100% elongation	$2-5 \times 10^5$	$2-5 \times 10^6$

Due to the very low conductivity of the dielectrics, electrons can accumulate in dielectrics over the time. Once excessive charge has accumulated within the dielectric, electrostatic discharge (ESD) events such as arcing or discharge will occur if the resultant electric field strength exceeds the material's breakdown limit, dielectric strength. It worthwhile to note that the damage due to radiation is minimized in an oxygen free environment such as space.

Most of the dielectric used in our Cubesat patch antennas are PTFE-based composites (e.g. Rogers 5880). The mechanical changes in PTFE appear to depend on the total radiation dose and to be independent of the dose rate. The degree to which PTFE is affected is essentially a function of the amount of the energy absorbed regardless of the identity of the radiation. Table 1.5 summarizes the radiation does in rads related to damage levels for PFTE in air and vacuum.

As CubeSat missions are meant to be quick turnaround and lower cost, it is highly recommended to use material already tested.

1.1.5.2 *Material Outgassing*

Material outgassing is another phenomenon to take into account when flying new antenna designs in space. It refers to the release of gas trapped within a material. Outgassing causes a material to lose its mass in the form of gases or volatile condensable matter when in vacuum, especially at hot temperature. Losing mass can potentially affect the material's mechanical and electrical properties.

In space-based equipment, released gas can condense on critical equipment such as camera lenses or other optical systems, rendering them inoperative. As such, rigorous test should be performed to select a material with the lowest outgassing properties.

NASA test procedure SP-R-0022A is used to test composite materials. ASTM International, a well-respected materials standards organization, has developed procedures, such as ASTM E595-84 [38], to gauge key material parameters such as total mass loss (TML) and collected volatile condensable materials (CVCM) for the purpose of evaluating the changes in mass of different materials in a vacuum environment as would occur due to outgassing. ASTM E595-84 [38] outlines a test method for evaluating the changes of mass in a test specimen under vacuum at a

Table 1.6   Outgassing test results of Rogers 5880 and 4003C.

Material	Rogers 5880	Rogers 4003C
Material composition	PTFE with glass microfiber	Hydrocarbon ceramic woven glass
Nominal dielectric constant	2.2	3.38
% TML	0.03	0.06
% CVCM	0.00	0.00
% WVR	0.02	0.02

temperature of $+125\,°C$ for 24 hours. NASA's target number for acceptable TML is less than 1% and for CVCM is less than 0.1%.

The outgassing test does not have to be done at the vacuum levels of deep space, which are typically 10^{-14} Torr. According to the ASTM the vacuum, for performing TML and CVCM testing, should be less than 7×10^{-5} Torr for 24 hours at $+125\,°C$. An additional test, for water vapor recovered (WVR), can be performed after measurements of TML and CVCM.

The outgassing properties of the composites used in our patch antennas (see Chapters 2 and 7) are summarized in Table 1.6. More outgassing data for spacecraft materials can be found in [39]. In general, materials with TML over 1.0% or VSCM over 0.10% should be avoided in spacecraft application.

1.1.5.3   *Temperature Change*

The effect of temperature in space on electrical and physical properties of any antennas should be taken into consideration when designing spacecraft antennas. Since space is a vacuum without conduction medium, the temperature of an object in space could be extremely cold, when it is not exposed to the sunlight, or it could be very hot, when it is illuminated by the Sun.

The choice of material is also critical to mitigate CTE mismatch or change of dielectric properties over a wide thermal range. The effect of these temperatures could cause change of physical dimensions, affect bond lines, and also dielectric properties of a material.

- The physical dimension changes due to thermal is captured by the CTE of a material, which is provided in x-, y-, and z-axis in ppm/°C. For instance, Rogers 4003C, they were measured to be 11, 14, and 46 ppm/°C in x-, y-, and z-axis, respectively. The CTE of aluminum and aluminum alloys varies from 19 to 25 ppm/°C.
- The process for bonding are extremely well documented and carefully inspected to avoid any delamination during thermal cycling. Over time, NASA has created an inventory of bonding process given for specific material.

- The thermal coefficient of the dielectric constant is also provided ppm/°C. For instance, the dielectric constant Rogers 4003C exhibits a thermal coefficient of 40 ppm/°C.

Simulation with applied CTE changes are usually performed to make sure the antenna will perform adequately. They are also designed with sufficient thermal guard (i.e. larger bandwidth) to mitigate a drop of performance over thermal variation.

Sometimes, performance metrics are measured over a specified operational thermal range, for example, antenna reflection coefficient variation with temperature is measured in a thermal chamber. Less commonly, the radiation pattern of an antenna can also be measured at hot and cold.

When dealing with deployable antennas, if the antenna is small enough, a deployment can be performed at hot and cold in a thermal vacuum chamber. This was done for the Raincube antenna (see Chapter 3).

1.1.5.4   Multipaction Breakdown

The requirements in terms of microwave breakdown (multipaction or corona discharge) of spacecraft components are becoming more restrictive due to the generalized power increase in remote sensing or telecommunication components which is less of an issue for CubeSats.

The multipaction breakdown occurs when electrons accelerated by radiofrequency fields are self-sustained in a vacuum (or near vacuum) via an electron avalanche caused by secondary electron emission. The impact of an electron to a surface can, depending on its energy and angle, release one or more secondary electrons into the vacuum. These electrons can be accelerated by the electric fields and impact with the same or another surface. The phenomenon can grow exponentially causing potential damage and ultimate destruction to the RF devices and antennas.

A few important properties of multipaction breakdown should be pointed out. First, it is not dependent on the type of gas in which the breakdown takes place as multipaction relies only on secondary electron emission from the electrodes. Second, the breakdown mechanism of multipaction is independent of pressure. The only requirement on pressure is that it is sufficiently low so that the mean free path will be longer than the electrode separation distance.

The author recommends the NASA technical report written by R. Woo on RF voltage breakdown in coaxial transmission lines [40] which provide all the curves required to perform breakdown voltage calculation and a thorough description of the phenomenon.

The author also recommends the ECSS multipaction tool which uses the ESTEC multipaction pre-calculated susceptibility charts for the five materials defined (Alodine, Silver, Gold, Copper, and Aluminium) and computes breakdown levels according to them.

Another commonly used software, allowing to perform full numerical simulation of the multipaction effect considering the 3D EM field distribution, is Spark3D. Spark3D is a unique simulation tool for determining the RF breakdown power level in a wide variety of passive devices, including those based on cavities, waveguides, microstrip and antennas. Field results from CST Studio Suite or HFSS simulations can be imported directly into Spark3D to analyze vacuum breakdown (multipaction) and gas discharge. From this, Spark3D calculates the maximum power that the device can handle without causing discharge effects.

Please note corona discharge or ionization breakdown will not be addressed in this book as this phenomenon only occurs at lower pressure and CubeSat antennas are used in the vacuum of space.

1.2   Conclusion

As small spacecraft venture from LEO to Deep Space to explore our solar system, new antennas with quick turnaround and lower cost are crucial to enable this historical space advancement. This introduction provides a brief description of CubeSats (form factor and key subsystems) and summarizes the innovative work on CubeSat antennas ranging from low-gain to high-gain antennas operating at UHF, S-, X-, Ku-, and Ka-band. The choice of HGA technologies is not straightforward when planning a new mission and this introduction provides clear examples of HGA choices to achieve mission goals and constraints. On-going research concepts are summarized with promising results (e.g. membrane antennas and larger mesh and reflectarray designs).

Finally, four major effects related to space environment are described in details (radiation exposure, material outgassing, temperature change, and multipacting breakdown) as they are crucial when designing spacecraft antennas.

Acknowledgments

References

1. E. Peral, S. Tanelli, Z. S. Haddad, G. L. Stephens, and E. Im, "RaInCube: a proposed constellation of precipitation profiling radars in CubeSat," *Proceedings of the AGU Fall Meeting*, San Francisco, CA, Dec. 2014.
2. N. Chahat, "A mighty antenna from a tiny CubeSat grows," *IEEE Spectrum*, vol. **55**, no. 2, pp. 32–37, Jan. 2018.

3. B. A. Cohen, P. O. Hayne, D. A. Paige, and B. T. Greenhagen, "Lunar flashlight: mapping lunar surface volatiles using a CubeSat," *Annual Meeting of the Lunar Exploration Analysis Group*, vol. **35812**, p. 3031, 2014.

4. L. McNutt, L. Johnson, P. Kahn, J. Castillo-Rogez, and A. Frick, "Near-earth asteroid (NEA) scout," *AIAA SPACE 2014 Conference and Exposition*, San Diego, CA, 4–7, Aug. 2014.

5. "Syrlinks products lines for cube & nano satellites," Available: online: https://www.syrlinks.com/en/produits/all/space/nano-satellite

6. "SpaceQuest: TX-2400 S-band transmitter," Available: online: http://www.spacequest.com/radios-and-modems/tx-2400

7. C. B. Duncan, *Iris V2 CubeSat Deep Space Transponder. X-, Ka-, S-Band, and UHF Deep Space Telecommunications and Navigation*. Available: online: https://deepspace.jpl.nasa.gov/files/dsn/Brochure_IrisV2_201507.pdf, Jan. 7, 2016.

8. "Tethers Unlimited Ka-band re-programmable radio," Availbale: online: http://www.tethers.com/SpecSheets/Brochure_SWIFT_KTX.pdf

9. "Deployable UHF and VHF antennas," Available: online: http://www.isispace.nl/brochures/ISIS_AntS_Brochure_v.7.11.pdf

10. N. Chahat, B. Cook, H. Lim, and P. Estabrook, "All-metal dual-frequency RHCP high-gain antenna for a potential Europa lander," *IEEE Transactions on Antennas and Propagation*, vol. **66**, no. 12, pp. 6791–6798, Dec. 2018.

11. D. González-Ovejero, N. Chahat, R. Sauleau, G. Chattopadhyay, S. Maci, and M. Ettorre, "Additive manufactured metal-only modulated metasurface antennas," *IEEE Transactions on Antennas and Propagation*, vol. **66**, no. 11, pp. 6106–6114, Nov. 2018.

12. G. Minatti, M. Faenzi, M. Mencagli, F. Caminita, D. G. Ovejero, C. D. Giovampaola, A. Benini, E. Martini, M. Sabbadini, and S. Maci, "Chapter 9: Metasurface antennas," in *Aperture Antennas for Millimeter and Sub-Millimeter Wave Applications*, Springer International Publishing, ISBN: 978-3-319-62772-4, 2018.

13. R. Hodges, D. Hoppe, M. Radway, and N. Chahat, "Novel deployable reflectarray antennas for CubeSat communications," *IEEE MTT-S International Microwave Symposium (IMS)*, Phoenix, AZ, May 2015.

14. R. E. Hodges, N. Chahat, D. J. Hoppe, and J. Vacchione, "A deployable high-gain antenna bound for mars: developing a new folded-panel reflectarray for the first CubeSat mission to mars," *IEEE Antennas and Propagation Magazine*, vol. **59**, no. 2, pp. 39–49, Apr. 2017.

15. N. Chahat, E. Thiel, J. Sauder, M. Arya and T. Cwik, "Deployable One-Meter Reflectarray For 6U-Class CubeSats," *2019 13th European Conference on Antennas and Propagation (EuCAP)*, Krakow, Poland, 2019, pp. 1–4.

16. N. Chahat, J. Sauder, M. Thomson, R. Hodges, and Y. Rahmat-Samii, "CubeSat deployable Ka-band reflector antenna development for earth science mission," *IEEE Transactions on Antennas and Propagation*, vol. **64**, no. 6, pp. 2083–2093, June 2016.

17. N. Chahat, R. E. Hodges, J. Sauder, M. Thomson, and Y. Rahmat-Samii, "The Deep space network telecommunication CubeSat antenna: using the deployable Ka-band mesh reflector antenna," *IEEE Antennas and Propagation Magazine*, vol. **59**, no. 2, pp. 31–38, Apr. 2017.

18. G. E. Freebury and N. J. Beidleman, "Deployable reflector," Patent WO 2017/131944 A4, Jan. 2016.

19. A. Babuscia, M. Van de Loo, Q. J. Wei, S. Pan, S. Mohan, and S. Seager, "Inflatable antenna for CubeSat: fabrication, deployment and results of experimental tests," *Proceedings of the IEEE Aerospace Conference*, 2014.

20. A. Babuscia, T. Choi, J. Sauder, A. Chandra, and J. Thangavelautham, "Inflatable antenna for CubeSats: development of the X-band prototype," *IEEE Aerospace Conference*, Big Sky, MT, 2016.

21. M. Alonso-DelPino, P. Goldsmith, C. Elmaleh, T. Reck, and G. Chattopadhyay, "Efficiency optimization of spherical reflectors by feed position adjustments," *IEEE Antennas and Wireless Propagation Letters*, vol. **16**, pp. 2865–2868, 2017.

22. P. A. Warren, J. W. Steinbeck, R. J. Minelli, and C. Mueller, "Large, deployable S-band antenna for a 6U CubeSat," *Proceedings of the 29th Annual American Institute of Aeronautics and Astronautics/Utah State University Conference on Small Satellites*, 2015.

23. M. Arya, J. Sauder, and R. Hodges, "Large-area deployable reflectarray antenna for CubeSats," Scitech, San Diego, CA, Jan. 7–11, 2019.

24. P. R. Akbar, H. Saito, M. Zang, J. Hirokawa, and M. Ando, "X-band parallel-plate slot array antenna for SAR sensor onboard 100 kg small satellite," *2015 IEEE International Symposium on Antennas and Propagation & USNC/URSI National Radio Science Meeting*, Vancouver, BC, 2015, pp. 208–209.

25. J. Padilla, G. Rosati, A. Ivanov, F. Bongard, S. Vaccaro, and J. Mosig, "Multi-functional miniaturized slot antenna system for small satellites," *Proceedings of the 5th European Conference on Antennas and Propagation (EUCAP)*, Rome, 2011, pp. 2170–2174.

26. J. Huang, "Microstrip reflectarray and its applications," *Proceedings of the ISAP*, vol. **96**, pp. 1177–1180, 1996.

27. M. Zawadzki and J. Huang, "Integrated RF antenna and solar array for spacecraft application," *IEEE International Conference on Phased Array Systems and Technology*, Dana Point, CA, 2000, pp. 239–242.

28. M. Aherne, T. Barrett, L. Hoag, E. Teegarden, and R. Ramadas, "Aeneas – Colony I meets three-axis pointing," *AIAAUSU Conference Small Satellite*, Aug. 2011.

29. C. "Scott" MacGillivray, "Miniature high gain antenna for cubeSats," presented at the 2011 CubeSat Developers Workshop, California Polytechnic State University, San Luis Obispo, CA, Apr. 22, 2011.

30. N. Chahat, J. Sauder, M. Mitchell, N. Beidleman, and G. Freebury, "One-meter deployable mesh reflector for deep-space network telecommunication at X- and Ka-band," *IEEE Transaction on Antennas and Propagation*, vol. **68**, no. 2, pp. 727–735, Feb. 2020.

31. P. F. Goldsmith and M. Alonso-DelPino, "A spherical aberration corrective lens for centimeter through submillimeter wavelength antennas," *IEEE Antennas and Wireless Propagation Letters*, vol. **17**, no. 12, pp. 2228–2231, Dec. 2018.

32. J. Huang, G. Sadowy, C. Derksen, L. Del Castillo, P. Smith, J. Hoffman, T. Hatake, and A. Moussessian, "Aperture-coupled thin-membrane microstrip array antenna for beam scanning application," *2005 IEEE Antennas and Propagation Society International Symposium*, vol. 1A, Washington, DC, 2005, pp. 330–333.

33. J. Huang and A. Feria, "Inflatable microstrip reflectarray antennas at X and Ka-band frequencies," *IEEE Antennas and Propagation Society International Symposium. 1999 Digest.*, vol. 3, Orlando, FL, 1999, pp. 1670–1673.

34. S. Hsu, C. Han, J. Huang, and K. Chang, "An offset linear-array-FedKu/KaDual-band reflectarray for planet cloud/precipitation radar," *IEEE Transactions on Antennas and Propagation*, vol. **55**, no. 11, pp. 3114–3122, Nov. 2007.

35. J. Sauder, M. Arya, N. Chahat, E. Thiel, S. Dunphy, M. Shi, G. Agnes, and T. Cwik "Deployment mechanisms for high packing efficiency one-meter reflectarray antenna (OMERA)," *6th AIAA Spacecraft Structures Conference*, 2019.

36. A. Tellechea, J. C. Iriarte, I. Ederra, R. Gonzalo, E. Martini and S. Maci, "Characterization of a dual band metasurface antenna with broadside and isoflux circularly polarized radiation patterns," *11th European Conference on Antennas and Propagation (EUCAP)*, Paris, 2017, pp. 3408–3411.

37. M. Faenzi, D. González-Ovejero, F. Caminita, and S. Maci, "Dual-band self-diplexed modulated metasurface antennas," *12th European Conference on Antennas and Propagation (EuCAP 2018)*, London, 2018.

38. A. Designation, "Standard test method for total mass loss and collected volatile condensable materials from outgassing in a vacuum environment," *American Society for Testing and Materials, Annual Book of Standards*, E595-93, 1993.

39. W. A. Campbell, Jr, R. S. Marriott, and J. J. Park, "Outgassing data for spacecraft materials", *NASA Reference Publication 1124*, Goddard Space Flight Center, Greenbelt, MD, June 1984.

40. R. Woo, "Final report on RF voltage breakdown in coaxial transmission lines," *NASA Technical Report 32–1500*, Oct. 1970.

2

Mars Cube One

Nacer Chahat, Emmanuel Decrossas and M. Michael Kobayashi

NASA Jet Propulsion Laboratory/California Institute of Technology, Pasadena, CA, USA

2.1 Mission Description

In the last decade, CubeSats have grown from university graduate projects, best suited for training students given their limited capabilities, to highly capable small satellites. Advances in technology have expanded their capabilities in areas as diverse as Earth surveillance, Earth science remote sensing, planetary exploration, and military communications, attracting greater interests from scientists and engineers. This was also possible because CubeSats have grown from their original 1U 10-centimeter-cubed form factor to the now common 6U ($\sim 12 \times 24 \times 36 \, \text{cm}^3$) class CubeSat [1].

While to date, CubeSats are only launched into Low Earth Orbit (LEO), scientists and engineers have started to explore CubeSat missions targeting lunar, asteroid, and planetary destinations in which a telecom system must contend with very large free space attenuation to achieve even a relatively low data rate of few kilobits per second. Meeting these communication system requirements in a CubeSat is a significant challenge for two main reasons: (1) limited transmit power and (2) insufficient antenna gain.

The X-band radio frequency (RF) transmit power for most CubeSats is limited to a few watts (up to 5 W at X-band) due to solar panel power limits, significant thermal management issues, and electronics packaging density [2]. As far as the antenna

gain is concerned, the goal is to produce maximum antenna area and efficiency for a given frequency band. However, the limited mass and volume available in a CubeSat present a tremendous design challenge. This challenge needed to be solved even before thinking of sending any CubeSat to Deep Space and to enable the first interplanetary CubeSat mission: Mars Cube One (MarCO).

MarCO focuses on an engineering goal rather than a scientific investigation. The InSight mission has placed a lander on the Martian surface that is studying the Mars interior. During its Entry, Decent, and Landing (EDL) sequence, the lander sent real time telemetry data of the EDL flight progress and informed us on its expected successful touchdown. The Mars Reconnaissance Orbiter (MRO) listened to InSight's data stream, but its design prevents it from simultaneously listening to the lander and relaying that data back to Earth. MRO then disappeared behind Mars, as seen from Earth, before it could relay Insight's data. MRO was able to receive confirmation of a successful landing more than three hours before it was able to relay that information to Earth.

National Aeronautics and Space Administration's (NASA's) Jet Propulsion Laboratory (JPL) engineers proposed to send two identical CubeSats (MarCO-A and MarCO-B) to capture and relay InSight data to earth in real time, AKA "bent pipe relay" (i.e. data is transmitted as it is received at the same data rate) (Figure 2.1). The MarCO spacecraft will flyby Mars at an altitude of 3,500 km. Each MarCO is equipped with a deployable circularly polarized (CP) loop antenna that will listen to the InSight lander's UHF broadcast while an X-band deployable reflectarray antenna relays the data in real time to Earth.
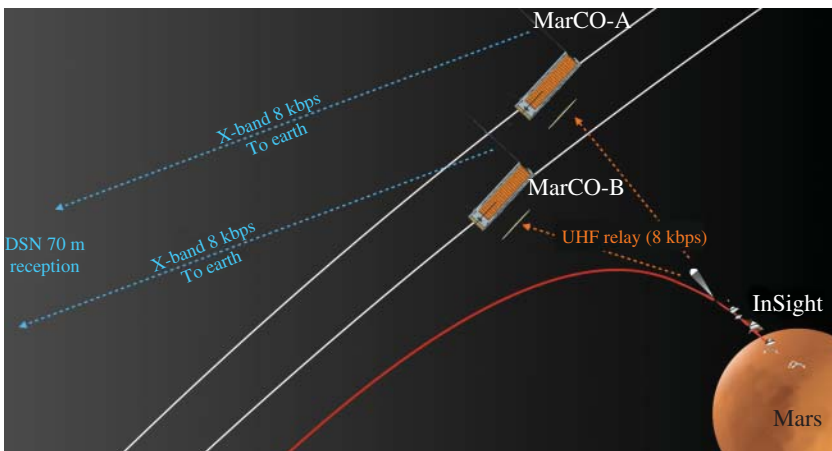
Figure 2.1 *MARCO mission consists of two CubeSats flying alongside the InSight lander to Mars to provide bent-pipe telecommunication link to transmit Insight's Entry, Descent, and Landing (EDL) data to Earth.*

The MarCO spacecraft is carried into space on the same upper stage that is sending the InSight lander to Mars. Following its release from the booster stage, each CubeSat becomes an independent spacecraft. Each of the spacecraft then unfolds their solar panels, their X-band high gain antenna (HGA) [3, 4], and their UHF antenna, in preparation for six and a half months' cruise to Mars. When Insight gets to Mars, it goes through its EDL sequence. Each of the MarCO spacecraft relays data to the NASA's Deep Space Network (DSN). The twin spacecrafts must perform up to five trajectory correction maneuvers to correctly pass over the InSight landing zone.

A detailed description of MarCO's CubeSat is illustrated in Figure 2.2. It consists of a 6U CubeSat which includes attitude determination and control system technology (Blue Canyon Technology, BCT), cold gas thrusters, a telecommunication subsystem (IRIS radio with UHF and X-band capabilities, solid state power

(a)

(b)
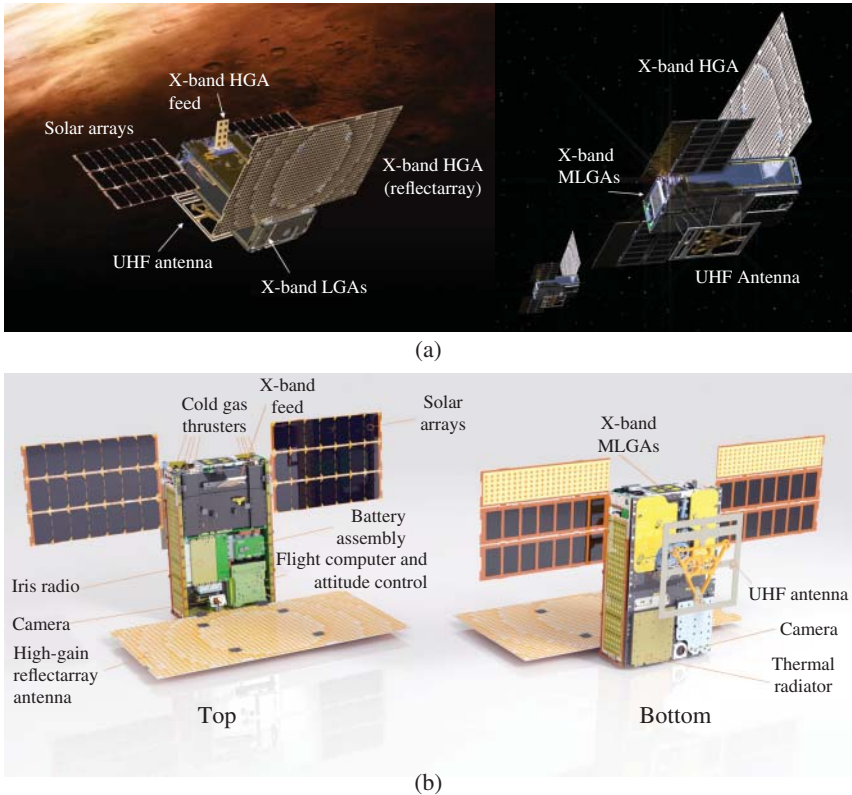
Figure 2.2 *(a) MarCO CubeSat with emphasis on telecom subsystem; (b) MarCO CubeSat description.*

amplifier – SSPA, low noise amplifier – LNA, and antennas), command and data handling (CDH), two cameras, batteries, solar panels, and electrical power subsystem (EPS), and more.

MarCO A and B were launched along with NASA's InSight Mars lander at 4:05 a.m. Pacific Daylight Time (PDT) (7:05 a.m. Eastern Daylight Time (EDT)) on May 5, 2018 from Vandenberg Air Force Base in Central California. Both spacecraft have successfully carried out their tasks and became the first interplanetary CubeSats.

All X-band antennas Rx and Tx LGAs, Tx and Rx MLGAs, and HGA and the UHF antenna were successfully tested in space on both spacecraft. This chapter will provide detailed information on the antenna development at X-band and UHF that made this mission possible.

2.2   Iris Radio

The information-coded electromagnetic waves received by the spacecraft antenna must be sampled and decoded so that the CDH subsystem can process the commands sent from Earth. Conversely, the telemetry data must be encoded and modulated so that the spacecraft antenna can radiate the data back to Earth. For many CubeSats in LEO, this transmit and receive function is performed by the radio transceiver, typically operating in the VHF and UHF RF bands [4–7]. For an interplanetary mission such as MarCO, a ground station with large antennas such as NASA's DSN is necessary to overcome the large free-space path loss. For standard deep-space operations, X-band frequencies (7.2 GHz uplink, 8.4 GHz downlink) are often used to take advantage of the nearly transparent transmission of microwave signals through the Earth's atmosphere in the absence of weather effects [8]. All three Deep Space Communication Complexes of the DSN (Goldstone, Canberra, and Madrid) supports X-band uplink and downlink on the 34 m and 70 m antennas [9].

In addition to the basic telecommunication system, a separate Global Positioning System (GPS) receiver is often employed to determine the precise position of the CubeSat in flight [10–12]. However, for spacecraft going beyond the reach of GPS signals (e.g. lunar, interplanetary, and deep space), a separate scheme for measuring the spacecraft velocity, distance, and angular position relative to Earth is necessary for orbit determination. Radiometric tracking techniques such as sequential ranging and delta differential one-way ranging (delta-DOR) provides the means for generating navigational products at the DSN [13]. However, the on-board oscillator on a typical radio does not have adequate frequency stability for precise radiometric measurements. A phase-coherent radio architecture, where the downlink carrier signal has the same frequency stability as the uplink signal (the DSN uses a hydrogen maser as the main reference clock with Allan deviation $\sigma(\tau) < 10^{-14}$ at 10,000 seconds [9]) has been proven to demonstrate precise tracking of spacecraft by many years of deep-space exploration at the JPL. The so-called two-way

coherent transponder, along with the use of special navigational tones, are required for any deep-space mission.

In order to fill the needs of deep-space communications and navigation for CubeSats and small satellites, the Iris V1 Deep-Space Transponder was developed at the JPL [14] starting with the interplanetary nanospacecraft pathfinder in relevant environment (INSPIRE) "first CubeSat to deep space" mission [15]. The Iris software-defined radio largely inherits the designs and knowhow from JPL's flight transponders including the Electra Proximity Operations UHF Transceiver, the Small Deep-Space Transponder (SDST), and the now-in-development Universal Space Transponder (UST). The hardware architecture of Iris follows the same phase-locked loop based receiver and in-phase/quadrature modulator as its larger sisters, which allows synergistic development of existing code base for the digital signal processor. During the hardware design phase of Iris, not only was miniaturization a key driver, but modularity was also an important feature for the transponder. As such, Iris is a highly capable transponder, allowing configurability to various mission requirements and modular extension to other operating bands such as Ka, S, and UHF.

The prime mission requirement for MarCO is to provide the telecommunication relay for InSight's EDL sequence [16]. It was quickly identified that the MSP430-based CDH subsystem, with its 8 kB of RAM and 128 kB of flash memory, would not have enough processing power to decode and packetize the 8 kbps EDL data stream from InSight (8 kbps over 20 minutes of EDL equates to roughly 10 Mbits of data volume). The Xilinx Virtex family of Field Programmable Gate Array (FPGA) used as the main digital processor for the Iris transponder was identified to have enough resources to perform the modem processing functions alongside the data processing functions. However, the Iris V1 design for the INSPIRE mission did not incorporate software functionality, and was hence missing a processor and RAM for program memory and execution. In addition, a new UHF receiver is now necessary to capture the InSight transmission. These new requirements resulted in the development of the Iris V2 Deep-Space Transponder [17].

The Iris V2 Transponder for MarCO consists of three units as depicted in Figure 2.3. The main transponder unit shown in Figure 2.3a is a bolted modular assembly consisting of the UHF Receiver, X-Band Receiver, X-Band Exciter, Power Supply Board, and the Radiation-tolerant Digital slice with Xilinx (RaDiX) from bottom to top. The X-Band LNA unit (Figure 2.3b) provides the front-end RF amplification of the received DSN uplink signal for the X-band Receiver slice, and is intended to be placed physically close to the receiving antenna to reduce the induced noise from the system cable loss. The X-band SSPA unit (Figure 2.3c) provides the RF amplification of the modulated signal to be radiated from the transmit antenna. A simplified top-level block diagram is provided in Figure 2.3.

A typical spacecraft telecom system incorporates a diplexer so that one antenna can be used for both the transmission and reception of commands and data. This allows for two-way communications with the ground station without adding
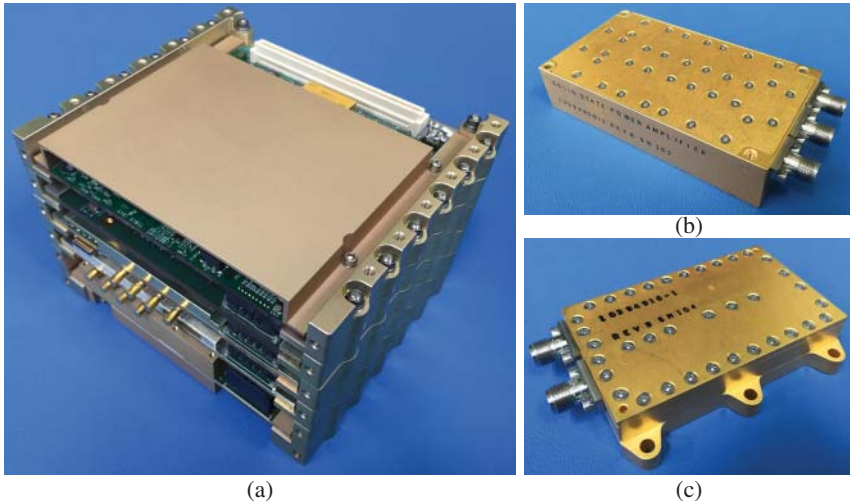
Figure 2.3 *MarCO flight hardware. (a) Photograph of the Iris V2 Deep-Space Transponder with UHF Receiver; (b) Photograph of the X-Band Low Noise Amplifier unit; (c) Photograph of the X-Band Solid State Power Amplifier unit.*

extra physical constraints to the spacecraft bus design, or adding operational constraints during the mission phase. However, X-band diplexers with sufficient channel-to-channel isolation are typically constructed of bulky cavity resonators in waveguide, which are not very well suited for CubeSat applications. As with any active RF system, the powerful transmitter may interfere with nominal operations of the sensitive receiver, and this transmit rejection is an important specification. The Iris LNA unit is designed to accept up to +15 dBm while keeping the receiving amplifiers linear. With a 5 W (37 dBm) transmitter, at least 22 dB of transmit-receive isolation must be maintained. It has been shown that patch antennas for a CubeSat application can achieve greater than 35 dB isolation with the use of separate transmit and receive antennas [18], and the design of such CubeSat antennas is the focus of this book. In addition to the high isolation, the removal of a lossy diplexer is beneficial for both the uplink and downlink space paths.

The Iris V2 Transponder receiver architecture is a shared-IF design in order to save mass and volume. Both X-band and UHF receivers are single-downconverter super heterodyne receivers modeled greatly after the Iris V1 design [18]. A power combiner was added before the IF chain so that the downconverted IF signal from either the X-band or UHF slice can be fed to the shared amplifiers, filters, and voltage-variable attenuators (VVA) for the automatic gain control (AGC) circuitry (Figure 2.4). A limitation of this topology is that simultaneous dual-frequency receive (UHF and X-band) cannot be performed at the sacrifice of volume. The IF signal is then sampled by the 12-bit analog-to-digital converter (ADC) on the
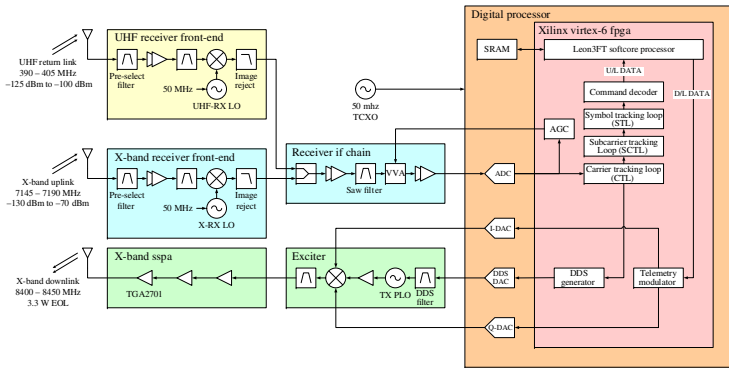
Figure 2.4 *Simplified transponder block diagram.*

digital processor board, and is then fed to the modem processor in the FPGA where the digital carrier-tracking loop (CTL) obtains frequency lock to the uplink carrier. In two-way coherent mode, this frequency tuning information is fed to the direct digital synthesizer (DDS) to produce the proper downlink carrier at the 880/749 turn-around ratio for the DSN. The configuration of the CTL loop-filter bandwidth is a key design parameter to control the behavior of the transponder. A larger bandwidth is necessary to maintain carrier lock in challenging Doppler dynamics, but a narrow bandwidth is necessary to reduce the stochastic effects for increased receiver sensitivity. The configurability of a software-defined radio provides the adaptability to different mission phases and needs. For instance, the MarCO receiver loop bandwidth is nominally set to approximately 75 Hz for most of the mission, but in EDL mode, the bandwidth is increased to 200 Hz to be able to maintain carrier lock throughout the Doppler dynamics of InSight's parachute deployment and other dynamic effects during EDL.

Downlinking telemetry data from the spacecraft can be performed in both one-way and two-way modes. In a transmit-only mode, the DDS frequency is set constant and a nominal downlink carrier is generated at the desired channel frequency. It should be noted that the downlink carrier will drift in frequency due to the limited stability of the on-board oscillator as mentioned previously. The MarCO Iris unit uses a 50 MHz temperature compensated crystal oscillator (TCXO) with 0.001 ppm short-term stability over 1 second, but as this frequency is multiplied up to X-band, the stability degrades to 0.5 ppm, or roughly ± 4 kHz. Telemetry data is encoded and modulated onto this carrier by use of an in-phase/quadrature mixer driven by independent 10-bit digital-to-analog converters (DAC) on the digital board. For the modulated signal to reach the ground stations on Earth, the SSPA unit amplifies the signal. MarCO's SSPA units provide a nominal 5 W of RF power.

Significant upgrades were made to the digital processor board from the first incarnation of Iris to the MarCO Iris V2 unit. Many complementary metal oxide semiconductor (CMOS) devices with unknown radiation effects were replaced with radiation-tolerant devices, the main processing element was upgraded to the Xilinx Virtex-6 FPGA to provide more computing resources with lower power consumption, and radiation-tolerant memory elements were added for program memory and execution. A dedicated central processing unit (CPU) could not be populated on the highly real estate constrained board, so an embedded softcore processor was implemented on the FPGA. The Leon3-FT softcore SPARC processor was chosen primarily to maintain synergistic code compatibility with JPL flight transponders that also use SPARC-based processors. This processor compatibility will allow for incorporating features such as the Consultative Committee for Space Data System (CCSDS) Proximity-1 Protocol [19] and adaptive data rate modules [20] for future Iris units.

The Iris software for MarCO is responsible for basic configuration of the transponder, command processing, telemetry framing, and EDL data handling. A register-based modem interface allows programmatic control of the data rate, encoding scheme, receiver loop bandwidth, etc. Downlink telemetry is framed per

the Advanced Orbiting Systems (AOS) space data link protocol of the CCSDS [21], in 8920-bit frames for Turbo-1/6 encoding. In EDL mode, the software is also responsible for managing the InSight EDL data stream by storing the decoded bits into memory and reshipping AOS-framed data for bent-pipe retransmission.

The Iris DSN-compatible CubeSat-platform transponder for communications and navigation that is presented has been used on the INSPIRE and MarCO missions. The modular design and software-defined nature of the transponder provides the flexibility to adapt to various mission requirements with relative ease. Currently at the JPL, several research tasks are underway to develop the hardware modules for a Ka-band high-rate version for near-earth communications, S-band version for exploration of Venus, and further X-band development with higher efficiency power amplifiers for potential use at Europa. The 2018 Space Launch System EM-1 launch of the Orion spacecraft intends to deploy eleven secondary payload CubeSats, to which most missions are targeting lunar or deep space exploration [22]. The Iris Deep-Space Transponder will be a key technology device for many CubeSat missions of the coming era.

2.3   X-Band Subsystem

2.3.1   Frequency Allocation

As MarCO is venturing to Mars, it is considered as a Deep Space mission. The DSN's "deep-space" frequency bands are allocated for spacecraft at distances greater than 2 million kilometers from Earth: 7.145–7.190 GHz for Uplink (i.e. Earth to Space) and 8.400–8.450 GHz for Downlink (i.e. Space to Earth). MarCO essentially communicates at X-band with the DSN stations and all antennas are optimized across the deep-space frequency bands.

2.3.2   Near Earth Communications Using Low Gain Antennas

2.3.2.1   *Antenna Requirements*

On one end of the spacecraft (i.e. behind the reflectarray panels), two LGAs are included for emergency communication near earth ($\sim$<0.1 astronomical unit–AU) at a data rate of 62.5 bps (i.e. minimum data-rate handled by Iris V2 [1]). They are placed so that no part of the spacecraft can interfere with their broad beams. A 34 m diameter DSN antenna will be used for non-EDL communications to receive command from Earth and to transmit telemetry to Earth.

Although it is technically possible to design an LGA with both transmitting and receiving capabilities, the Iris V2 radio was designed to accommodate distinct transmitting and receiving antennas [1]. Hence, two LGAs were designed:

- Rx-LGA: a right-hand circular polarization (RHCP) receiving (Rx) antenna,
- Tx-LGA: a RHCP transmitting (Tx) antenna.

For downlink, the antenna gain and cross polarization discrimination (XPD) requirements were selected to be able to transmit telemetry to Earth at a distance of 0.1 AU (astronomical distance – 1 AU $\sim$ 150 million kilometers), using the 34 m DSN antenna, with an off-pointing angle of $\pm 80°$ at the emergency data-rate. Hence, the gain of Tx-LGA should be greater than or equal to -5 dBic with a XPD higher than 3 dB within $\pm 80°$ off boresight. The reflection coefficient should be smaller than -14 dB to avoid power to reflect back into the radio and to avoid losing any significant amount of power or damaging the SSPA.

For uplink, the same requirements allow to receive commands from Earth at a distance as far as 0.1 AU with an off-pointing angle of $\pm 80°$ at the emergency data-rate using the 34 m DSN antenna. The isolation between Tx-LGA and Rx-LGA at uplink frequency band should be higher than 30 dB. The main requirements for Tx- and Rx-LGA are summarized in Table 2.1.

2.3.2.2   Antenna Solution and Performance

A dual edge-fed CP patch antenna (Figure 2.5) meets the aforementioned requirements. The two RHCP patch antennas are printed on RT Duroid 5880 ($\varepsilon_r = 2.2$ and thickness = 0.787 mm).

The reflection coefficient is measured using an Agilent 8510XF vector network analyzer (VNA). The measurement setup is calibrated using a Short Open Load (SOL) calibration procedure. The calculated and measured reflection coefficients of both LGAs are shown in Figure 2.6. The achieved antenna bandwidth exceeds the required value. To maximize the isolation between the transmitting and receiving antennas to relax the filtering requirement at the receiving frequency band, the antennas are rotated to maximize the distance between the feeding points of each antenna. The isolation is greater than 40 dB.

The radiation patterns at the center frequency of each antenna are shown in Figures 2.7 and 2.8. Measured and simulated results are in good agreement. The

Table 2.1   *Low-gain antenna requirements.*

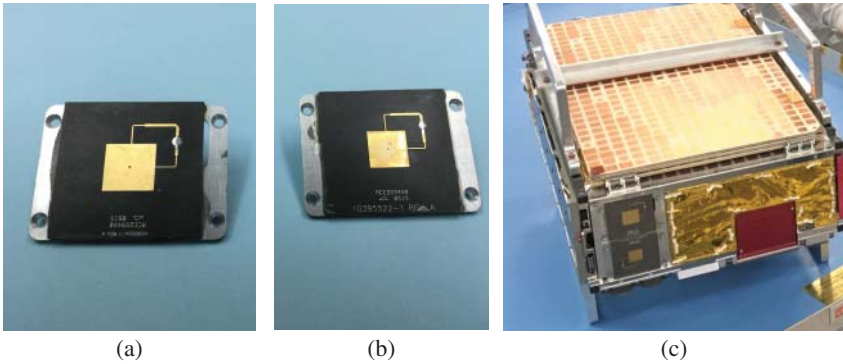| Property	Value
Frequency band (MHz)	7145–7190 (Rx-LGA)
	8400–8450 (Tx-LGA)
Gain between $\pm 80°$	>-5 dBic
XPD between $\pm 80°$	>3 dB
Boresight El. angle	$0 \pm 2°$
Boresight Az. angle	$0 \pm 2°$
Polarization	RHCP
Return loss	≥ 14 dB
Isolation	≥ 30 dB

Figure 2.5 *Low gain antennas: (a) Rx-LGA; (b) Tx-LGA; (c) LGAs fixed on MarCO Flight Model.*
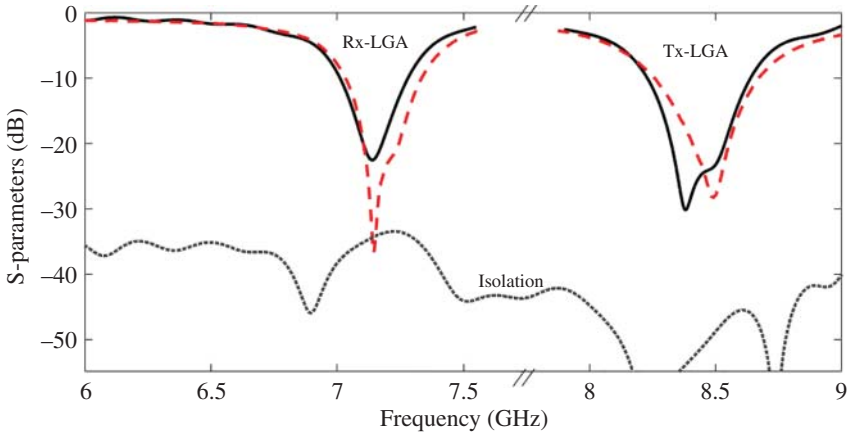

Figure 2.6 *Reflection coefficient of the two low gain antennas (Rx-LGA and Tx-LGA) and isolation between the two antennas. — (black) calculated. (gray) measured.*

gain is greater than −5 dBic within ±80° off boresight with an XPD higher than 3 dB. It allows closing the link at a distance of 0.1 AU at a data rate of 62.5 bps with sufficient margin.

Using the Rx-LGAs, the spacecraft can receive commands at 62.5 bps from a 34 m DSN ground station with a pointing of ±90° at a maximum distance of 0.3 AU (Figure 2.9). Using the Tx-LGAs, the spacecraft can transmit telemetry to a 70 m DSN ground station at 62.5 bps, with a pointing of ±90° at a maximum distance of 0.15 AU (Figure 2.10). Figure 2.9 illustrates the pointing requirement imposed to the spacecraft to receive commands from a 34 m DSN ground station. Figure 2.10
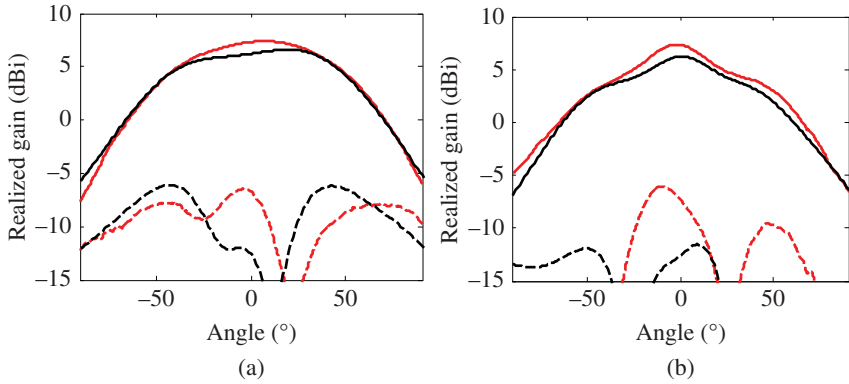
Figure 2.7   *Radiation pattern of Rx-LGA at 7.1675 GHz. (a) Elevation; (b) Azimuth. – (grey) Measured. – (black) Calculated.*
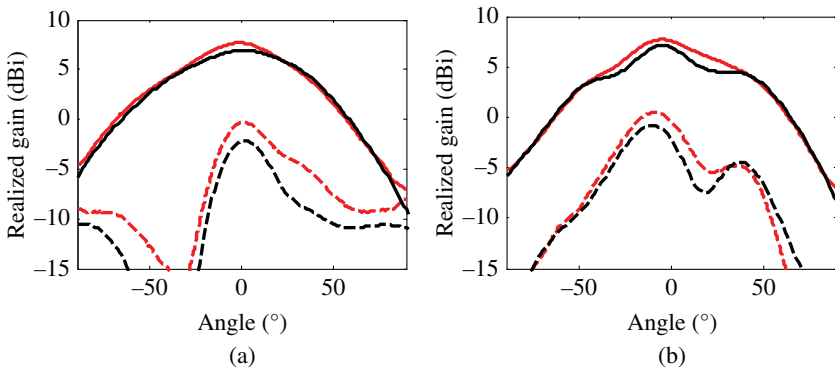
Figure 2.8   *Radiation pattern of Tx-LGA at 8.425 GHz. (a) Elevation; (b) Azimuth. (black) Calculated. (grey) Measured.*

illustrates the pointing requirement imposed to the spacecraft to transmit data to a 70 m DSN ground station.

2.3.3   Mars-to-Earth Communications

2.3.3.1   *Telecommunication Description: Uplink and Downlink from Mars*

While landing, Insight transmits to MRO on a UHF link at 8 kbps. MarCO CubeSats are also receiving the EDL data using their UHF deployable circularly-polarized loop antenna at 8 kbps. To provide a bent pipe system, MarCO CubeSat must be designed to send data to Earth at 8 kbps at 1.07 AU (i.e. 157 million km). Using the

Figure 2.9 *Pointing required to receive commands at 62.5 bps using the Rx-LGAs using a 34 m Deep Space Network ground station.*

Figure 2.10 *Pointing required to transmit telemetry at 62.5 bps using the Tx-LGAs using a 70 m Deep Space Network ground station.*

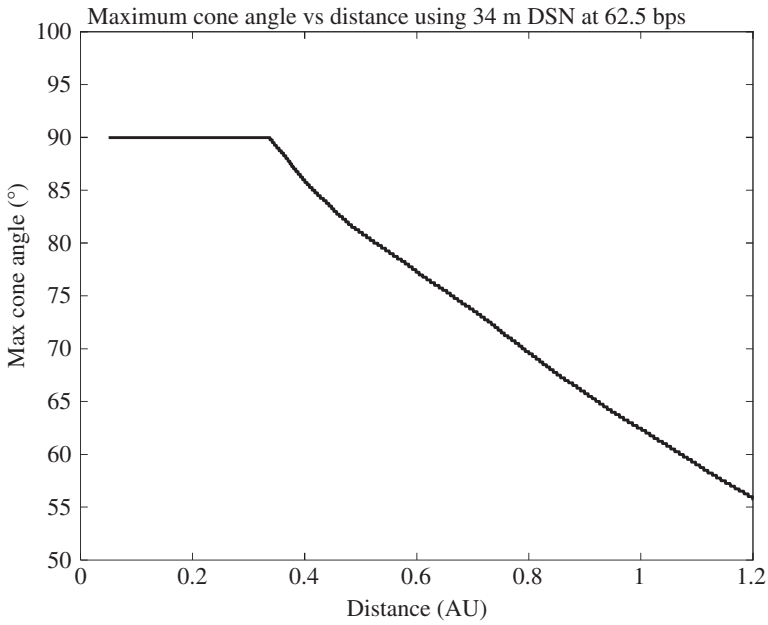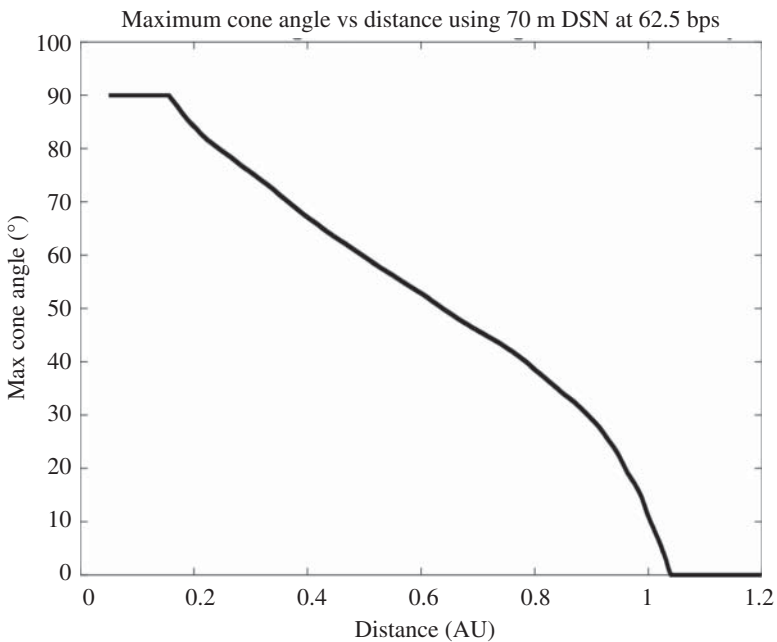**Table 2.2**   *Mars low-gain antenna requirements.*

Property	Value
Frequency band (MHz)	7145–7190 (Rx-MLGA)
	8400–8450 (Tx-MLGA)
Gain within ±8° off boresight	>7 dBic
XPD within ±8° off boresight	>7 dB
Boresight El. angle	22.7 ± 1°
Boresight Az. angle	0 ± 1°
Polarization	RHCP
Return loss	≥14 dB
Isolation	≥30 dB

70 m DSN antenna, 8 kbps can be achieved with a 28.0 dBi-gain antenna at X-band for downlink assuming the spacecraft can maintain a pointing accuracy of ±2°.

As far as the HGA is concerned, a reflectarray antenna is a natural choice as the available antenna stowage volume is very limited (refer to Chapter 1 for HGA selection guidelines). Because of volume constraints and IRIS V2 radio limitations [1], the reflectarray only operates as a transmitting antenna. Hence, a complementary low-gain receiving antenna (Rx-MLGA for receiving Mars Low-Gain Antenna) is employed for uplink. As opposed to downlink, the link margin for uplink is much larger for two reasons: (1) lower data rate is required (i.e. 62.5 bps) and (2) the output power from the DSN is several orders of magnitude higher than the IRIS output power (i.e. 20 kW vs. 4 W). Therefore, a LGA with a broader beamwidth and lower gain is suitable to close the link at Mars.

As a result, a transmitting 1 × 2 patch array LGA (Tx-MLGA for transmitting Mars Low-Gain Antenna) is employed. Because its larger beamwidth provides telemetry capability without the precise pointing required by the narrow beam HGA, the Tx-MLGA is also used for emergency situations when spacecraft pointing may not be correct.

First, the low-gain antennas are described in terms of requirement and performance. Second, the high-gain antenna is discussed in details including its requirements, feed and panel design, and overall performance.

2.3.3.2   Mars Low Gain Antennas

Two LGAs are located on the other side of the spacecraft as shown in Figure 2.11:

- Rx-MLGA: an RHCP receiving antenna,
- Tx-MLGA: an RHCP transmitting antenna.

The MLGAs pointing requirement is driven by the HGA pointing angle of 22.7° from the bus axis. For downlink, the antenna gain and XPD requirements were
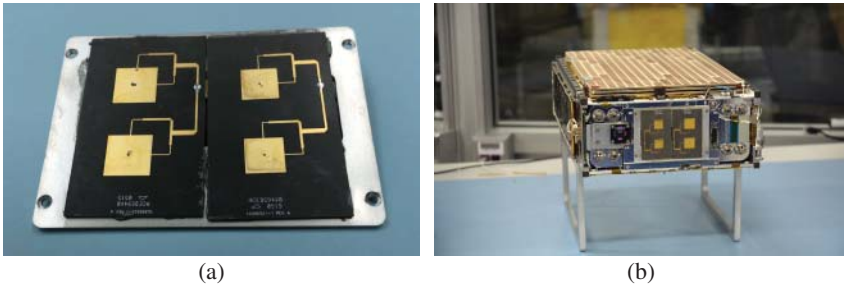
(a)   *(b)*

Figure 2.11 *(a) Rx-MLGA (left) and Tx-MLGA (right);(b) MLGAs fixed on MarCO Flight Model.*

selected to be able to transmit telemetry to Earth from Mars with an off-pointing angle of $22.7° \pm 8$, using the 70 m DSN antenna, at the emergency data rate of 62.5 bps. Hence, the gain of Tx-MLGA should be greater than or equal to 7 dBic with an XPD higher than 7 dB within $22.7° \pm 8$ from the bus axis. For uplink, the same requirements allow to receive commands at 62.5 bps from Earth to Mars, using the 34 m DSN antenna, with an off-pointing angle of $22.7° \pm 8$ from the bus axis. The return loss should be better than 14 dB and the isolation between Tx-MLGA and Rx-MLGA at uplink frequency band should be higher than 30 dB. The requirements for Tx- and Rx-MLGAs are summarized in Table 2.2.

The off-pointing angle of $22.7° \pm 8$ from the bus axis can is easily achievable using a 1×2 patch array with a phase difference of $75°$. The 1×2 patch array (Figure 2.11) consists of two RHCP patch elements printed on RT Duroid 5880 ($\varepsilon_r = 2.2$ and thickness $= 0.787$ mm). The calculated and measured reflection coefficients of both MLGAs are shown in Figure 2.12. Overall antenna bandwidth exceeds the required value which provides a useful thermal guard. The isolation between Rx-MLGA and Tx-MLGA is higher than 30 dB within the uplink frequency band.

The radiation patterns of Rx-MLGA and Tx-MLGA calculated and measured at the center frequency are shown in Figures 2.13 and 2.14. Measured and calculated results are in good agreement. The effect of the solar panels and reflectarray panels were numerically studied. While the solar panels do not affect the antenna performance, the reflectarray can cause up to 0.3 dB interference. This remains too small to be an issue as the gain from 14.7 to $30.7°$ from the bus axis remains higher than 8 dBi (requirement is 7 dBi).

2.3.3.3   High Gain Antenna

HGA Description   The reflectarray antenna is designed to achieve a gain greater than 28.0 dBi within the 8.4–8.45 GHz frequency band with an XPD higher than 10 dB. The HGA should satisfy an elevation pointing angle of $22.76°$ from the
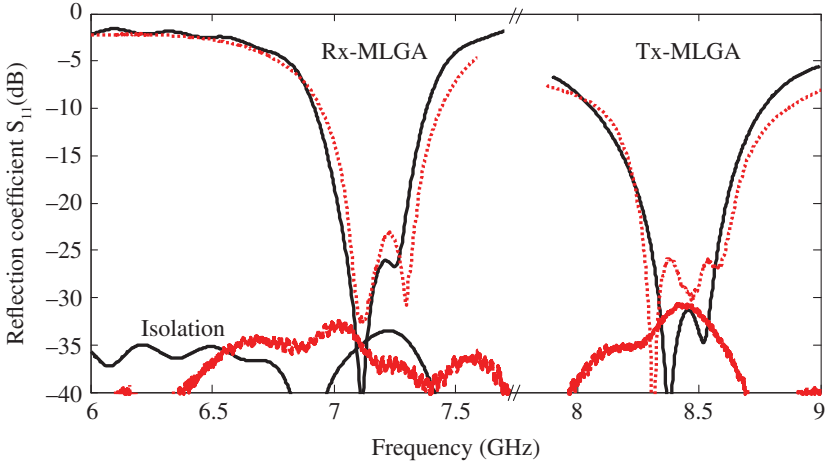
Figure 2.12   *Reflection coefficient of the two MLGAs (Rx-MLGA and Tx-MLGA) and isolation between the Tx and Rx antennas (black) Calculated. (gray) Measured.*
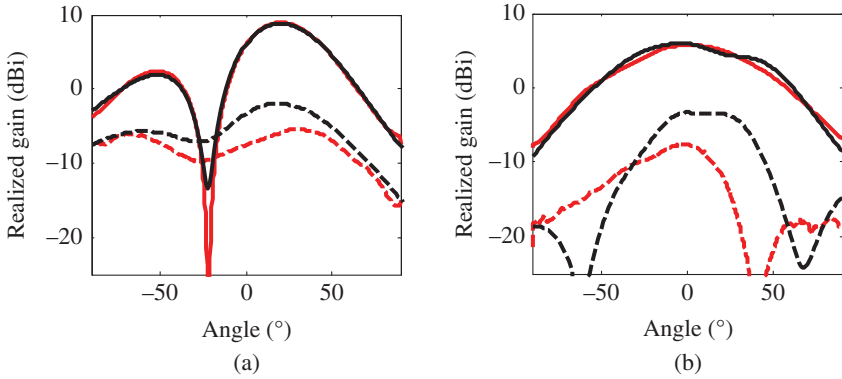
Figure 2.13   *Radiation pattern of Rx-MLGA at 7.1675 GHz. (a) Elevation; (b) Azimuth. (black) Calculated. (gray) Measured.*

bus axis. In addition, the side-lobe-level should remain under −15 dB. The HGA requirements are summarized in Table 2.3.

The MarCO high-gain antenna consists of a medium gain patch array antenna feeding a 33.5 cm × 59.7 cm assembly of three reflectarray panels. The deployment of the reflectarray antenna is illustrated in Figure 2.15. The feed is mounted to a spring-loaded hinge which enables it to fold flat against the spacecraft body. The three reflectarray panels are connected via spring loaded hinges which enable them to be folded down against the MarCO Spacecraft. At launch, the Feed and
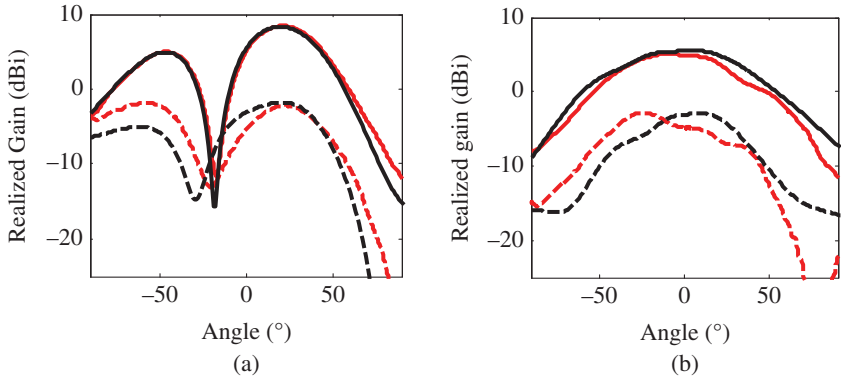
Figure 2.14   *Radiation pattern of Tx-MLGA at 8.425 GHz. (a) Elevation; (b) Azimuth. (black) Calculated. (grey) Measured.*

Table 2.3   *High-gain antennas requirements.*

Property	Value
Frequency band (MHz)	8400–8450
Gain	>28.0 dBic
XPD (in 3 dB BW)	>10 dB
AZ 3 dB beamwidth	>3.5°
EL 3 dB beamwidth	> 6.5°
Boresight Az. angle	$0 \pm 0.1°$
Boresight El. angle	$22.76 \pm 0.35°$
Azimuth peak SLL	≤ -15 dB
Elevation peak SLL	≤ -15 dB
Polarization	RHCP

reflectarray panels are folded down against the spacecraft body. The three reflectarray panels are folded against each other and are down atop the feed. The arrays are tied to the spacecraft body for launch. During the early phase of the cruise to Mars, the reflectarray and feed are deployed using a burn-wire mechanism. As the panels deploys, the feed is released and deploys. The reflectarray panels deploy perpendicular to the side of the bus so that the main beam is scanned 22.76° from the bus axis to satisfy MARCO's mission pointing requirement.

The previously reported Integrated Solar Array and Reflectarray Antenna (ISARA) CubeSat reflectarray [23] suffered from large panel gaps due to the size of the hinges resulting in high side lobe levels (SLL) and extra gain loss. Hence, we designed custom-made hinges at NASA's JPL to reduce the large panel gaps
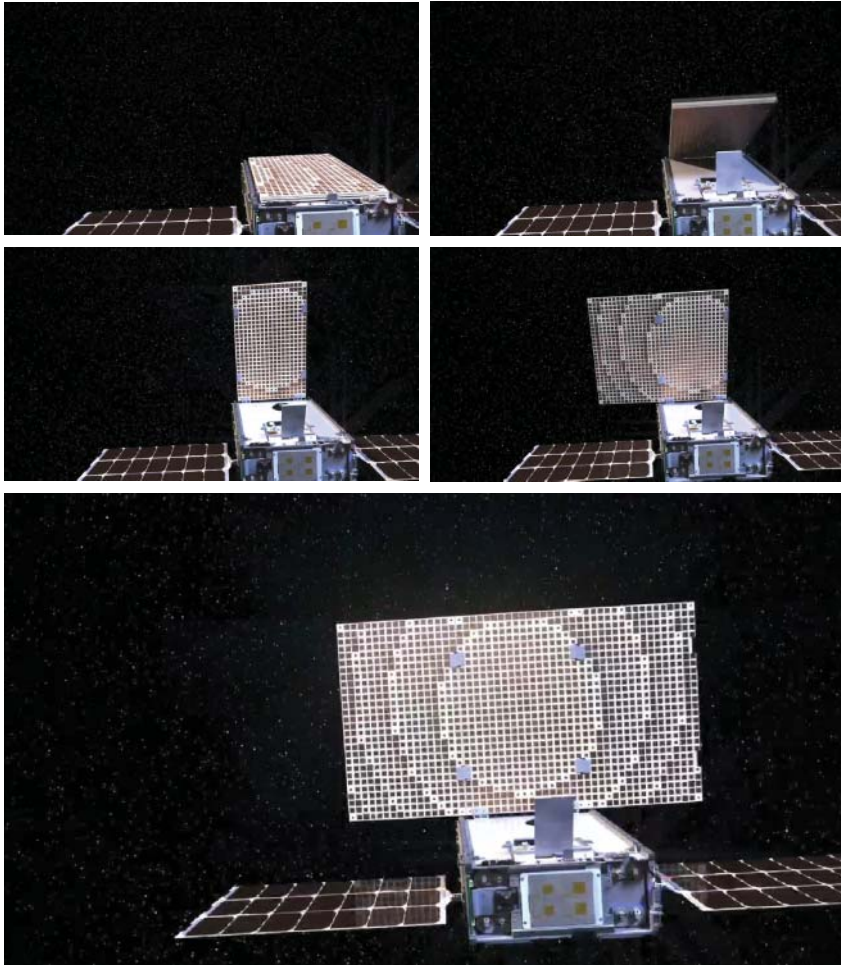
Figure 2.15   *MarCO High-Gain Antenna deployment.*

(Figure 2.16). As a result, this strongly reduces the SLL and increases the overall gain. The gaps between the three panels are reduced to 0.254 mm (Figure 2.19). The most challenging task in designing the high-gain deployable antenna is to comply the tight stowage volume requirement: 12.5 mm × 210 mm × 345 mm. These custom hinges also minimize the overall thickness of the folded panels (Figure 2.16c).

To fit within the 12.5 mm × 210 mm × 345 mm volume allocation, the panel thickness is minimized. The three reflectarray panels consists of two 0.813 mm fiberglass reinforced hydrocarbon ceramic laminate circuit boards co-cured with

Figure 2.16 *MarCO custom made hinge. (a) CAD model of the folded hinge; (b) CAD model of the deployed hinge; (c) Photography of MarCO flight spacecraft with its HGA folded. The gaps between each panel is apparent.*

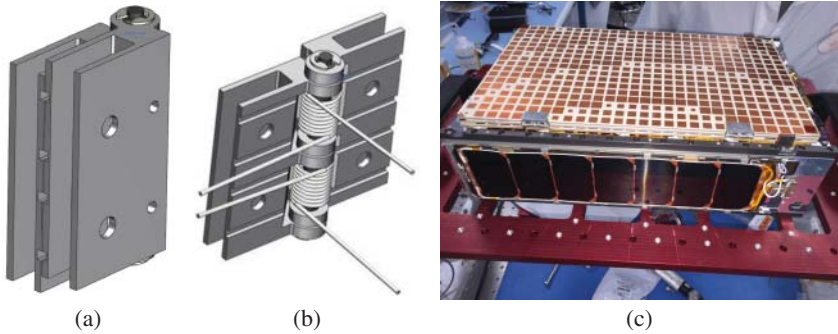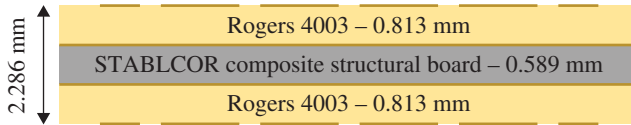**Figure 2.17** *MarCO reflectarray panel configuration. It consists of three layers. Layer 1: a 0.813 mm-thick Rogers 4003 printed with the reflectarray patches on one side. Layer 2: a 0.589 mm-thick STABLCOR layer providing the required flatness over temperature. Layer 3: another 0.813 mm-thick Rogers 4003 printed with the reflectarray patches on the opposite side of layer 1 to provide structural rigidity over larger temperature range (symmetry avoids large temperature gradients).*

a 0.589 mm central core of graphite composite. The symmetrical panel with a thickness of 2.286 mm results in a very high structural rigidity (Figure 2.17).

The MarCO reflectarray design uses variable square patches arranged on a rectangular grid [24]. The required phase of each element is determined from the reflectarray design equation:

$$\phi_i + \phi_0 - k_0(r_i + \bar{r}_i \cdot \hat{r}_0) = 2\pi N \tag{2.1}$$

where r_i is the distance from the feed to the ith array element, ϕ_i is the phase of the field reflected from the ith element, ϕ_0 is an arbitrary phase constant, $\bar{r}_i$ is a vector from the center of the array to the ith array element and $\hat{r}_0$ is a unit vector in the main beam direction. A unit cell Floquet mode Moment Method technique [25] is used to design the patch elements and perform radiation pattern calculations.

This design methodology assumes that each patch is surrounded by identical patches which is an acceptable assumption for this application. However, reflectarrays are aperiodic by nature due to the need to compensate for the spatial

phase delay from the feed. Hence, the local periodicity assumption can lead to discrepancies between simulated and measured radiation patterns and other methods have been investigated to account for this aperiodicity [26, 27]. The surrounded element approach does not account for periodicity and includes the actual neighboring elements that surrounds the element under consideration, thus accounting for mutual coupling. Mutual coupling will mainly affect the SLL and cross polarization at a level that does not affect the telecommunication link. Therefore, the design methodology used here is sufficient.

This S-parameter calculation can also be performed with a full-wave software such as HFSS and CST MWS assuming an infinite periodicity. The S-curve of the reflectarray unit cell is shown in Figure 2.18. It gives the reflection phase as a function of patch size at an incident angle of 22.76° for *V*- and *H*-polarizations. To achieve the best performance out of this reflectarray, the angle of incidence for each patch element should be taken into account.

Since the MarCO aperture is electrically small ($9.4 \lambda \times 16.8 \lambda$), it is important to minimize the element spacing in order to maximize the number of patches and create a more uniform environment surrounding each patch. The phase wrap pattern was adjusted to place hinges and other discontinuities in non-resonant patch locations (Figure 2.19) by varying the value of ϕ_0 [4]. This minimizes the impact of the hinges and other discontinuities on the overall performance of the antenna.

It is worthwhile to mention that a multitude of solutions could lead to similar performance. One could optimize the performance with different optimization goals (e.g. max gain, max XPD, or larger bandwidth, etc.).

However, most of the performance are driven by the feed. The directivity could be improved by improving the feed illumination reducing spillover and taper loss. The

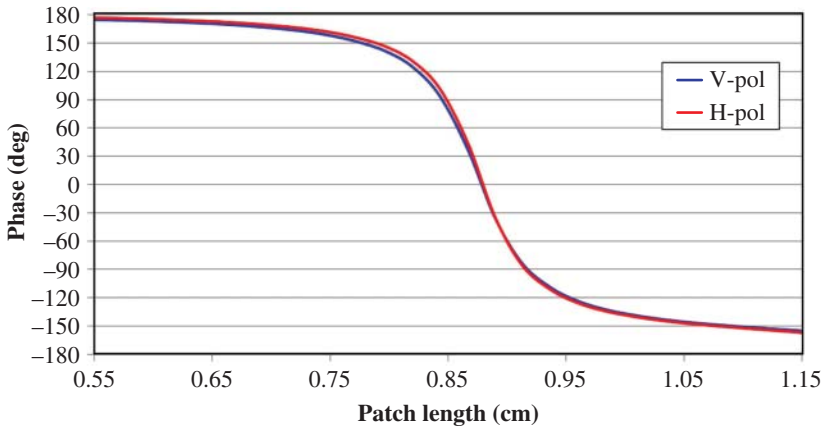**Figure 2.18**   *MarCO reflectarray S-curve of the reflection phase vs patch size in cm for V- and H-polarization. Source: From Hodges et al. [4]. © 2017 IEEE.*
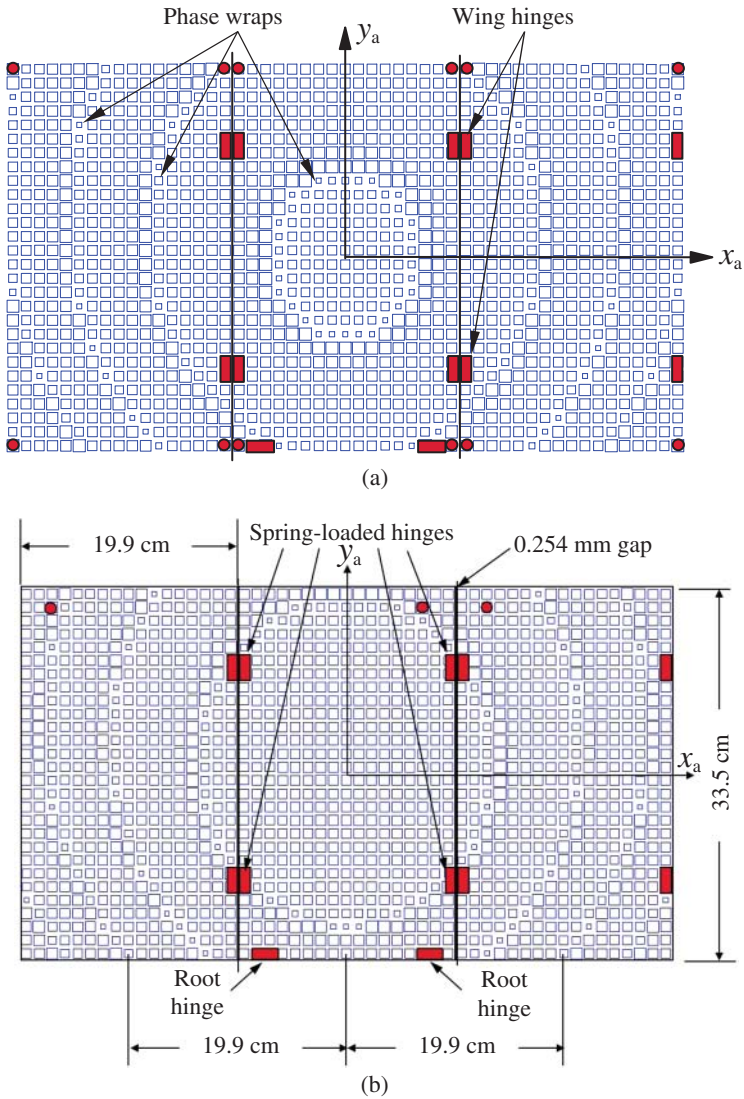
Figure 2.19 *MarCO reflectarray panel layout. (a) Panel layout before adjusting the phase; (b) Panel layout after adjusting the phase wrap with $\phi_0 = 240°$. Source: From Hodges et al. [4]. © 2017 IEEE.*
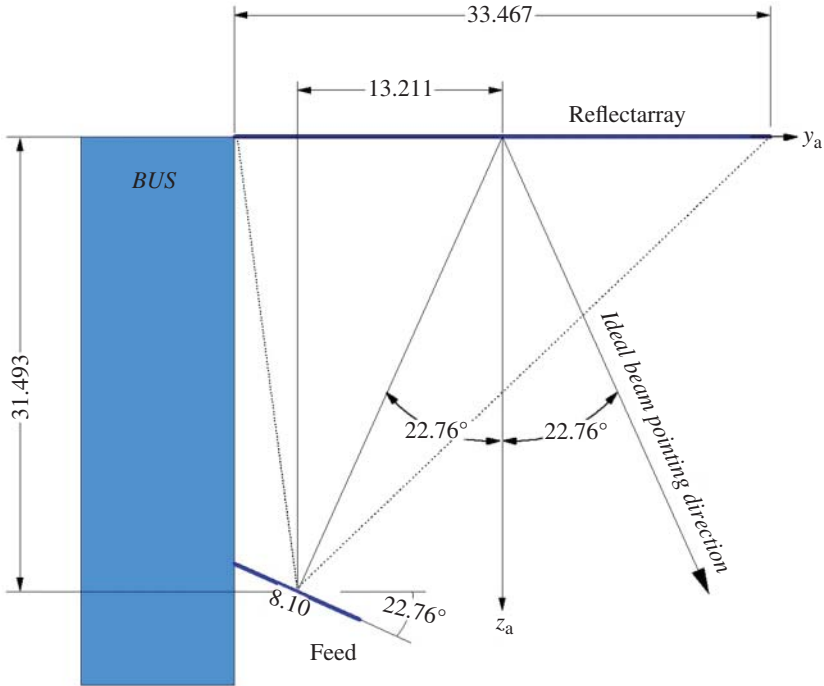
Figure 2.20   *MarCO reflectarray antenna optic design. Source: From Hodges et al.* [4]. © 2017 IEEE.

feed is mounted at the bottom of the bus (Figure 2.20) to maximize the *f/D* which results in a more efficient design. Maximizing the *f/D* also minimizes the angle of incidence variation. The *f/D* is also a critical parameter driving the feed directivity. The higher the *f/D*, the higher the feed directivity will be, which in turn will require a larger feed.

High-Gain Feed Antenna Array   The reflectarray circular polarization is formed by the feed patch array design. For communication, RHCP is employed; hence, the feed should be left-handed circularly polarized (LHCP). The feed covers the whole downlink frequency band (8.4–8.45 GHz).

The feed is a 4×2 microstrip patch array designed to create approximately -10 dB edge taper. The edge taper angle in azimuth and elevation are set by the reflectarray antenna optic design (Figure 2.20). To minimize spillover and edge taper loss, a -10 dB elevation beamwidth of $47.1 \pm 2°$ and a -10 dB azimuth beamwidth of $84.1 \pm 2°$ are required.

This is achieved using a 4×2 patch array with the right spacing between each patch elements (Figure 2.21). To minimize the fabrication complexity, corner
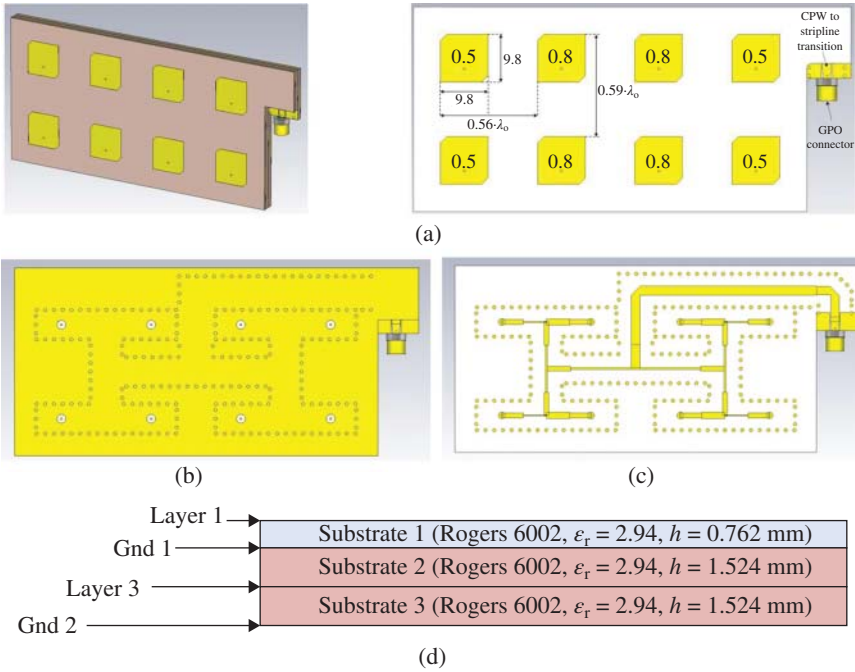
(a)

(b)

(c)

(d)

Figure 2.21   *Patch antenna array model. (a) Top layer with Taylor distribution; (b) Ground layer of substrate 1; (c) Layer 3: strip-line corporate feed with a Taylor distribution; (d) Feed layout.*

truncated patches are employed to generate LHCP within the 8.4–8.45 GHz band. In addition, to avoid any spurious radiation generated by corporate feed lines, the antenna consists of probe fed patch element excited by a stripline corporate feed (Figure 2.21).

In addition, the SLL in the direction of the CubeSat bus should be controlled and minimized. Analysis performed on Ticra GRASP using Physical Optics (PO), have shown that the SLL should be lower than −20 dB to avoid multipath issues. Therefore, a Taylor distribution is employed to reach SLL of −20 dB. Reducing the SLL helps minimizing spillover loss. The Taylor distribution is shown in Figure 2.21a.

It is worthwhile to underline that each patch is excited perpendicularly to its E-plane, which causes an asymmetry in the SLL in the elevation plane. This allows to reduce further the SLL on one side of the feed and therefore the radiation toward the CubeSat.

For the feed deployment, a SMP (sub miniature push-on) Full Detent connector is acting as a rotary joint (Figure 2.22). The feed is deployed with a spring-loaded hinge. It is restrained in its stowed position by the reflectarray panels and deploys automatically when the panels deploy. The SMP connector is connected to a
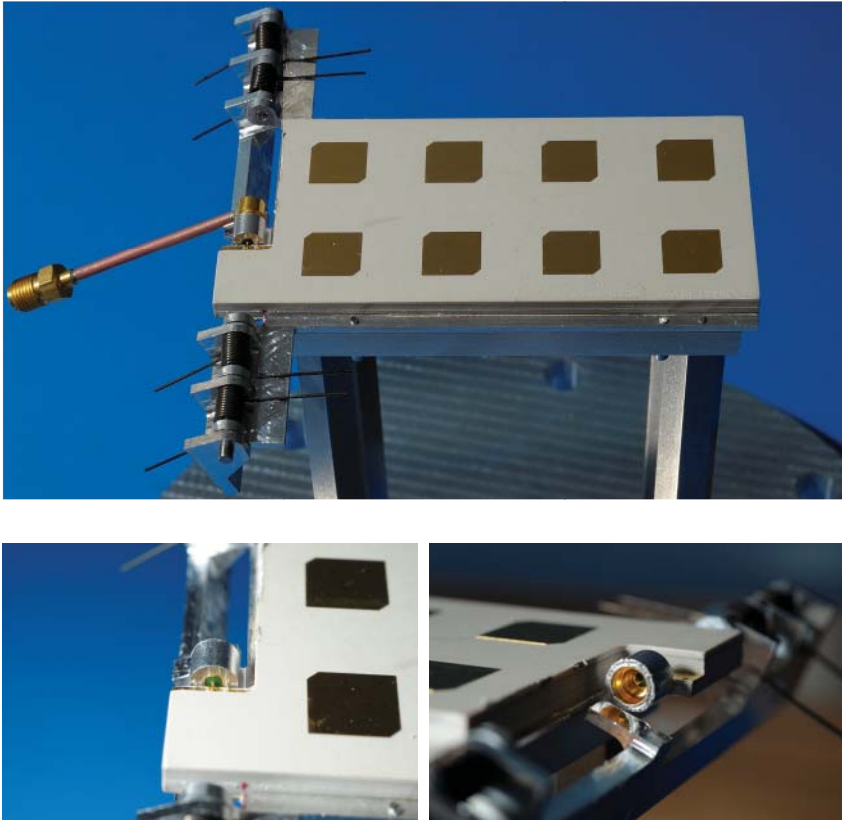
Figure 2.22 *Photographies of the feed antenna.*

CPW (co-planar waveguide) line. The CPW-to-stripline transition is optimized to minimize the insertion loss (~0.1 dB). The reference point for all measurements (i.e. reflection coefficient and radiation patterns) is taken at the end of the 4 cm-long coaxial cable (Figure 2.22a). The measured insertion loss in this cable equals 0.25 dB. Measurements have shown that the rotation around the SMP shroud does not affect the reflection coefficient or the antenna gain.

The reflection coefficient was optimized to be below −15 dB from 8.3 to 8.5 GHz to withstand temperatures ranging from −55 to +80 °C. The measurement and simulated reflection coefficient is shown in Figure 2.23. The measured reflection coefficient is below −10 dB from 8.20 to 8.82 GHz.

The radiation pattern is measured in a far-field anechoic chamber at NASA's JPL, Pasadena, CA. The feed radiation pattern is shown in Figure 2.24 at 8.4, 8.425, and 8.45 GHz. The measured and calculated co- and cross-polarization components are in excellent agreement in both elevation and azimuth planes. The gain is measured

Figure 2.23   *Reflection coefficient of the reflectarray feed.*
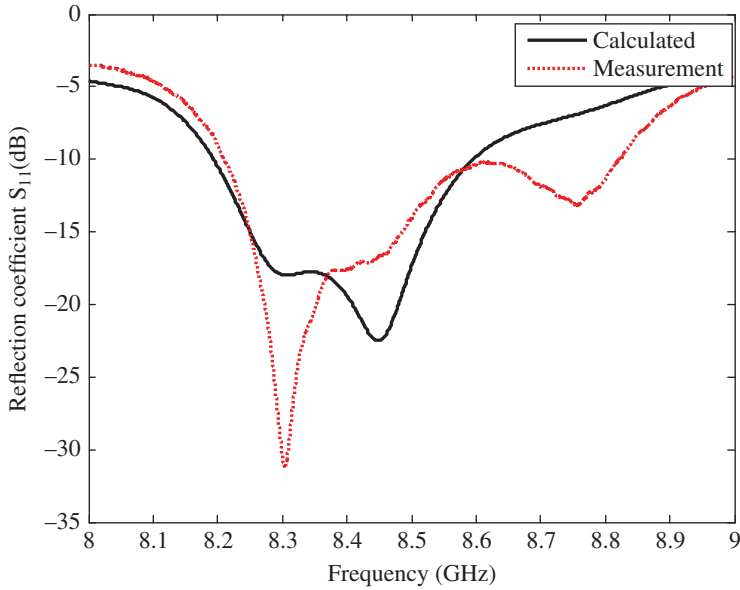
by substitution method using a standard horn. The calculated and measured gains are shown in Table 2.4. They are in excellent agreement.

   The deployment of the feed was tested and a total of 20 deployments were performed. The results led to a mean deployment angle of 22.82°. The maximum deviation angle was found to be up to 0.1°. Such a small deviation will not affect the reflectarray pointing.

   The CP feed proved to be one of the greatest challenges for this antenna as it drives the HGA performances:

- minimizes taper and spillover loss affecting the antenna directivity,
- controls the XPD,
- mitigates multipath interference caused by the CubeSat bus (achieved by reducing the SLL).

HGA Calculated and Measured Results   Two Flight Models (FM) MarCO reflectarray and feed mounted on a representative bus were built to perform antenna deployment and radiation pattern tests (Figure 2.25). Figure 2.26 shows the FM antenna mounted on the flight spacecraft. Table 2.5 gives the gain budget for the reflectarray antenna. The predicted MarCO antenna gain corresponds to an overall efficiency of 42% (i.e. 3.81 dB of loss). There is little room for improvement but if
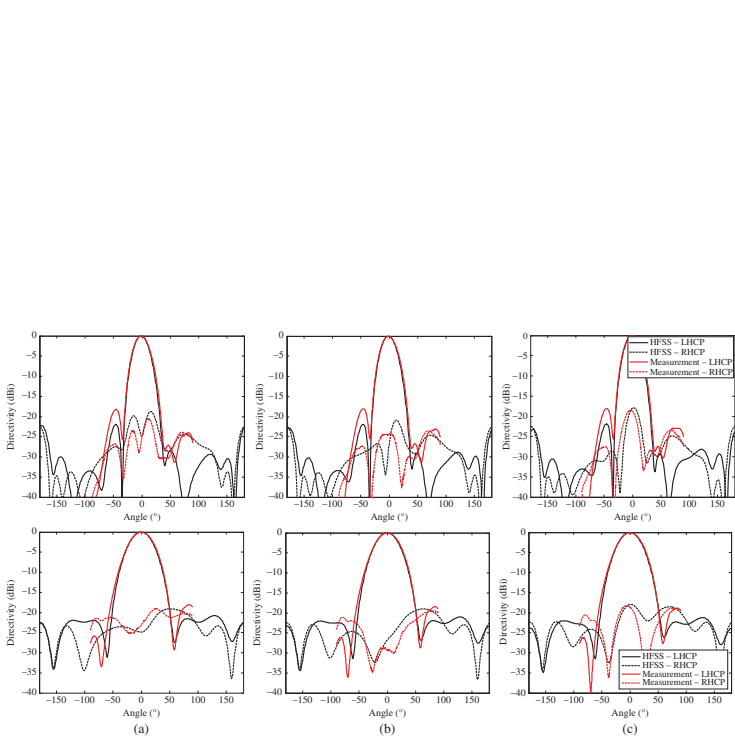
Figure 2.24 *Radiation pattern of the feed. (Top) Elevation. (Bottom) Azimuth. (a) f = 8.4 GHz; (b) f = 8.425 GHz; (c) f = 8.45 GHz.*

Table 2.4   *Simulated and measured realized gain of the feed.*

Frequency (GHz)	Gain (dBi)		Axial ratio (dB)	
	Calculated	**Measured**	**Calculated**	**Measured**
8.375	13.8	13.90	2.0	2.76
8.400	13.96	13.96	1.2	1.53
8.425	13.97	13.93	0.3	0.55
8.450	13.87	13.92	1.6	1.33
8.475	13.78	13.87	3.0	2.60

(a)   (b)

Figure 2.25   *(a) Reflectarray prototype folded and deployed; (b) Photograph of the HGA with its feed mounted on the CubeSat.*

Figure 2.26   *Two MarCO flight spacecrafts.*

Table 2.5   *Marco antenna gain budget.*

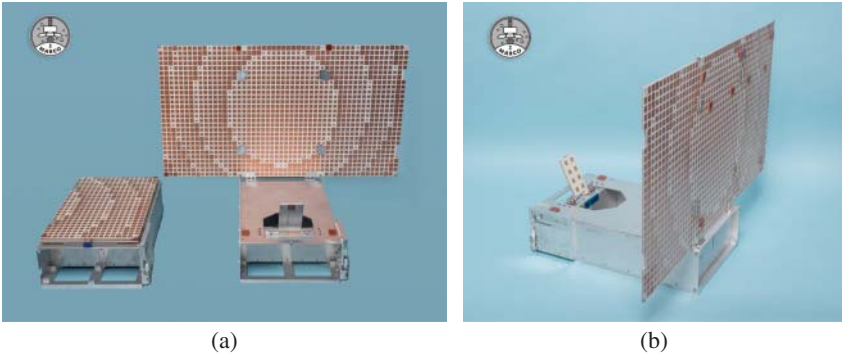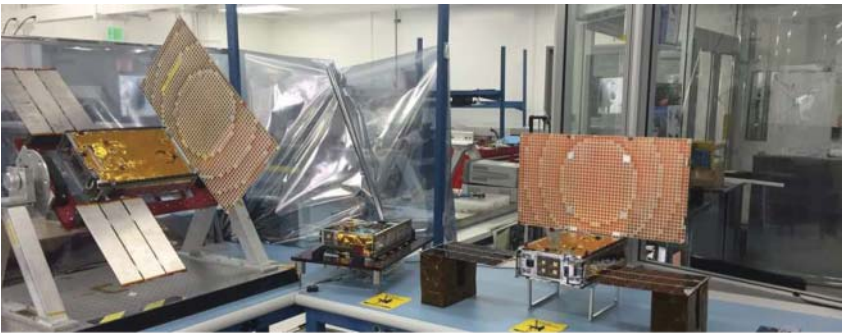|	Gain	Loss
Max directivity (aperture)	32.97	—
Spillover loss	31.46	1.51
Taper loss	30.48	0.98
Feed loss	29.74	0.74
Patch diel loss	29.49	0.25
Patch conductivity loss	29.45	0.04
Mismatch loss	29.31	0.14
Hinge mounting area loss	29.16	0.15
Total	**29.16**	**3.81**

one wanted to achieve a higher efficiency, the focus would be on reducing taper and spillover loss. It should be noted that the feed, in terms of efficiency, has achieved maximum performance.

While the reflectarray hinges were designed to achieve the best deployment accuracy, it is critical to assess the impact of the deployment error. These hinges do not have tuning features. An effort to characterize the deployment accuracy and repeatability was carried out using dummy panels made of aluminum as shown in Figure 2.27. The maximum deployment angle error between the center panel and the right and left panels is about 0.65° and −0.06°, respectively. The impact of having both side of the panels deployed within ±1° (with margin) was assessed. The gain is reduced by 0.3 dB and the azimuth pointing can be as large as 0.4°. It is worthwhile to note that the deployment repeatability is excellent (i.e. within 0.03°). A deviation of 0.03° will not affect the gain or pointing. Hence, the effect of the panel deployment deviation is captured during the RF measurements and the pointing angle of the radiation pattern and gain will be well known in space. The root
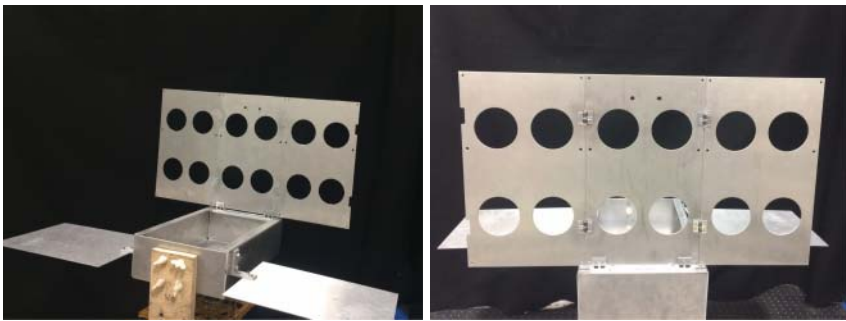

Figure 2.27   *MarCO deployment test setup to determine the deployment angle repeatability.*

hinges (i.e. between the CubeSat bus and the center panel) also show good repeatability of about 0.03° with a maximum error of 0.22°. Our calculation predict a gain loss of 0.01 dB, which is negligible. In conclusion, at X-band the hinges requirement is not as stringent as Ka-band where tuning features are required on hinges (see Chapter 4). At X-band, good repeatability can be obtained and the deployment accuracy can easily be achieved.

The effect of the feed deployment accuracy also needs to be assessed. It was shown that the feed is deployed within ±0.1°. The radiation pattern of the reflectarray was calculated with a feed deployment error of ±0.1° and the gain and pointing of the reflectarray is not affected.

The HGA flight model was validated on a simplified CubeSat mockup entirely made of aluminum (Figure 2.28). The radiation pattern of the reflectarray was measured in a cylindrical near field chamber at NASA's JPL, Pasadena, CA (Figure 2.28a).

An accurate knowledge of the beam pointing is required for the MarCO's mission success. A series of measurements was performed in the metrology laboratory at NASA's Jet Propulsion, Laboratory, Pasadena, CA (Figure 2.28b). First, four tooling ball nests located on the test fixture surface are employed to provide a convenient reference for laser metrology on the antenna near field range. Second, the reflectarray panel surface flatness is assessed using photogrammetry. Finally, a theodolite is employed to determine the physical center and orientation of feed, and to locate the four corners of each panel. This measurement permits to determine the best fit plane of the reflectarray antenna coordinate system (x_A, y_A, z_A) relative to the four tooling ball nests.

To accurately determine the HGA beam pointing relative to the best fit plane of the reflectarray antenna coordinate system (x_A, y_A, z_A), two additional measurements were performed in the near field chamber. First, laser tracker measurement of the four tooling ball locations is used to establish the coordinate system reference of the
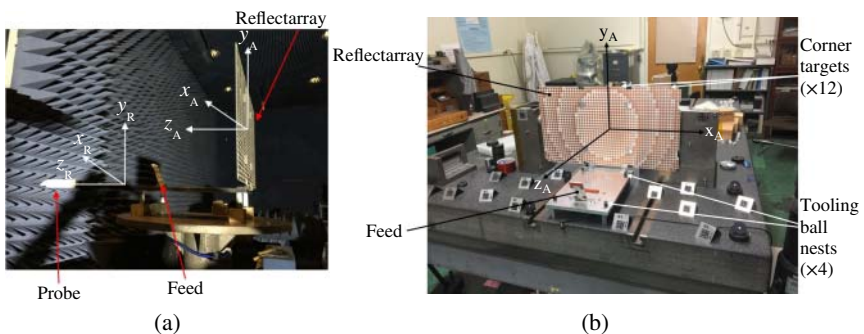

Figure 2.28 *(a) Measurement set-up of the HGA in the cylindrical near field chamber at NASA's JPL, Pasadena, CA; (b) Lab metrology set-up used to measure surface flatness and determine best fit plane.*

Table 2.6 *HGA radiation pattern performances.*

Frequency (GHz)	8.400		8.425		8.450	
	Calc.	Meas.	Calc.	Meas.	Calc.	Meas.
Gain (dBi)	29.3	29.2	29.2	29.2	29.2	29.0
Az beam pointing (°)	−0.08	0.10	−0.06	0.10	−0.05	0.10
El beam pointing (°)	22.52	22.14	22.53	22.15	22.54	22.17

measurements performed in the metrology laboratory. Second, the near field antenna range coordinate system (x_R, y_R, z_R) is determined using laser tracker measurements. These two datasets allow to accurately determine the beam pointing relative to best fit plane of the reflectarray antenna coordinate system.

The elevation and azimuth beam pointing are summarized in Table 2.6 at 8.4, 8.425, and 8.45 GHz. While the deviation between predicted and measured azimuth pointing angle remains under 0.18°, the deviation of the elevation pointing angle can be as large as 0.4°. Such misalignment would result in up to 0.45 dB loss which could be mission critical. Measured radiation patterns are shown in Figure 2.29. The antenna gain remains greater than 29 dBi within the entire downlink bandwidth. The XPD is greater than 15.2 dB across the band. It is important to note that the HGA is deployed shortly after the release of the CubeSat and remains deployed during the long trip to Mars. The antenna radiation pattern is fully characterized shortly after deployment near Earth to verify the successful deployment of the antenna and to characterize its performance and its optimal beam pointing. This is a critical phase of the mission that should not be omitted.

Prior to the radiation pattern characterization in space, a photography of the antenna is taken shortly after its deployment. The photography is transmitted back to Earth using the LGA-Tx and is compared with a photography taken in the lab prior to launch. This allows to rule out any major deployment error.

Performances obtained for this high-gain antenna meet the mission requirements in all aspects. This high-gain antenna, involving different innovative technologies, was designed by two RF engineers and two mechanical engineers in a short period of 6 months to meet the tight and unforgivable interplanetary launch window. Another innovative aspect of this mission, is the deployable UHF antenna discussed in Section 2.4.

On-Flight Performance of the X-Band HGA   On May 5, 2018, NASA launched InSight to Mars. The MarCO satellites made the journey alongside NASA's InSight lander. The lander successfully touched down on Mars just before 3 p.m. Eastern Time (ET) on Monday, November 26, 2018. MarCO A and B transmitted flawlessly the EDL data from Insight to the 70 m DSN ground station. The received carrier power from both MarCO CubeSats at the 70 m DSN antenna (DSS-63 in Madrid, Spain) as a function of ERT (Earth-Received Time) is shown in Figure 2.30. During EDL, DSS-63 operated in MSPA (Multiple Spacecraft Per Aperture) mode, where downlinks from more than one spacecraft can be achieved simultaneously as long
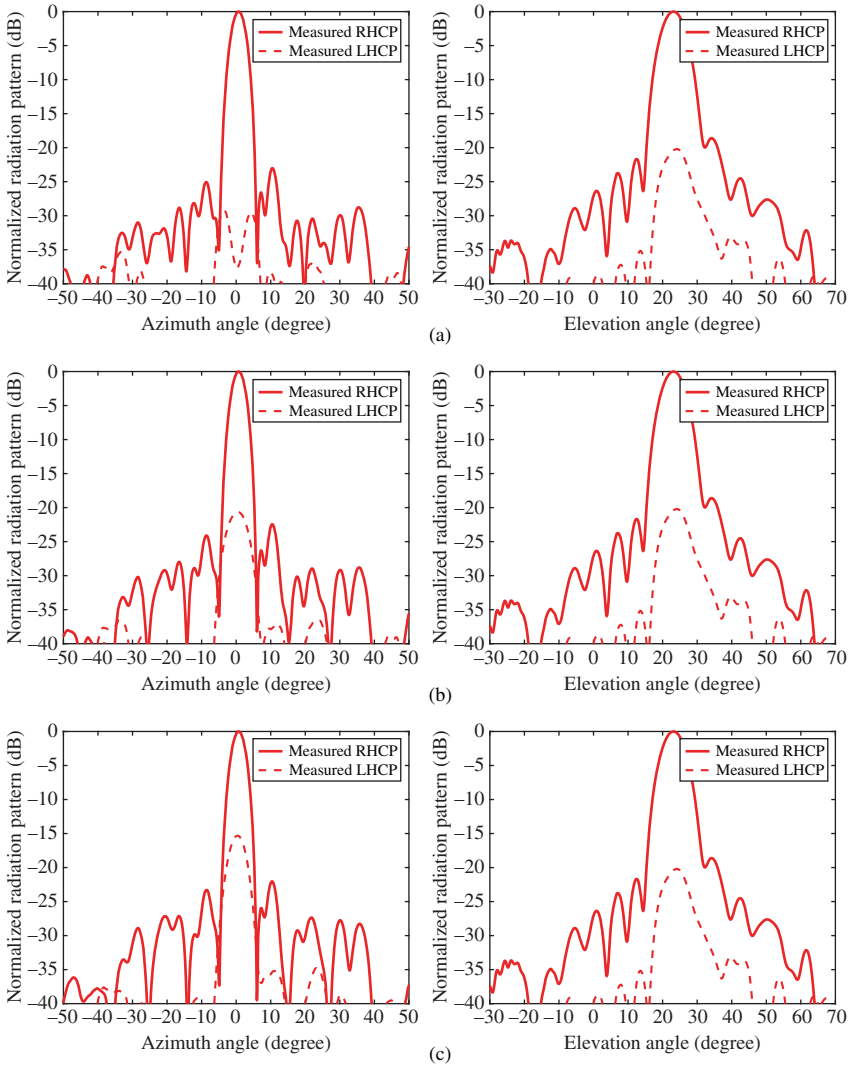
Figure 2.29 *Normalized measured HGA radiation pattern at (a) 8.4 GHz; (b) 8.425 GHz; and (c) 8.45 GHz.*

as the transmitted beam is within the same view of the ground-station antenna. The received carrier power from the two spacecraft could have some variation in power, which arises from one spacecraft being off-point relative to the other in MSPA. In addition, variations between the two spacecraft (unit-to-unit, thermal, etc.) can compound to 1–2 dB of power difference as seen at the station. During InSight's EDL, the carrier power varied approximately 0.6 dB for MarCO-A and 1.0 dB for MarCO-B at a distance of 0.977947 AU. The predicted carrier power at this distance is about −148 dBm ± 2 dB.
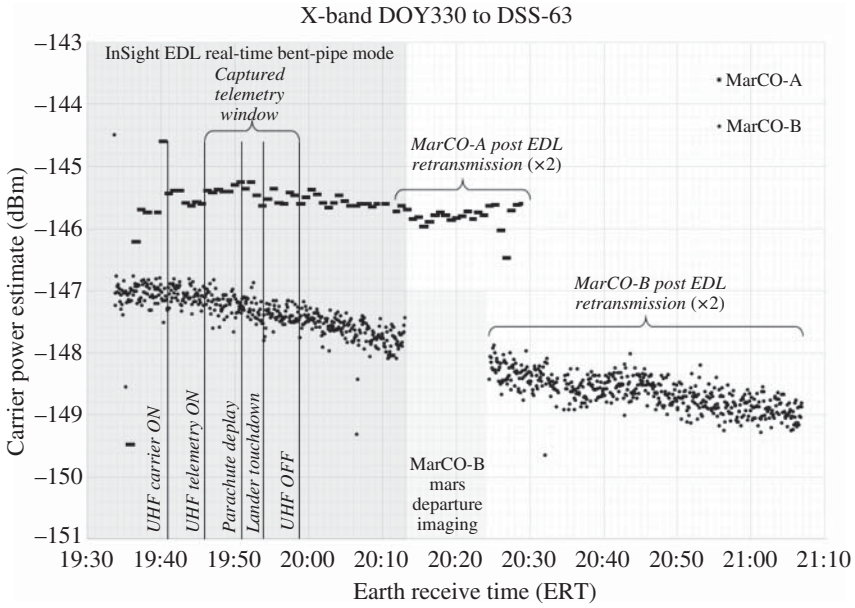
Figure 2.30   Carrier power during and post EDL from MarCO A and B at 0.977947 AU range.
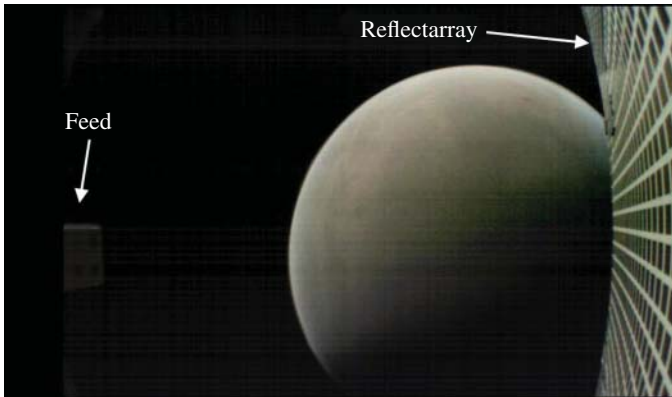

Figure 2.31   Photography taken by MarCO B while approaching Mars.

As MarCO was approaching the red planet, few minutes before carrying out its duty, the spacecraft took multiple historical pictures of Mars (see Figure 2.31).

2.4 Entry, Descent, and Landing UHF Link

One of the major challenges to design a UHF system in such a small spacecraft is to accommodate the size of the antenna. Typical CubeSat UHF antennas consist of four deployable monopoles fed in phase quadrature and placed at the bottom, top and/or sides of the CubeSat [28]. However, the MarCO mission antenna gain requirement cannot be met using monopoles.

In addition, the UHF antenna must be positioned on only one side of the CubeSat in order to keep InSight spacecraft in line of sight. Although different UHF antenna tradeoffs were considered (e.g. patch and unifilar, bifilar, and quadrafilar helices), the loop antenna proposed here offers the best performance in terms of stowage factor, required gain, XPD and simple deployment mechanism. Additionally, because the loop antenna has extensive material cutouts, it offers a favorable spacecraft thermal view-factor which provides the radiative cooling performance needed to meet system thermal requirements.

The single resonant linearly polarized loop antenna, one wavelength around, is well known and different designs can be found in the literature for circular, square, triangular, rectangular, and rhombic loops. It was shown that a reactively loaded loop antenna with a reflector can radiate CP waves if a gap is introduced in the loop [29]. Likewise, a CP loop antenna using a "branch wire" acting as a length of transmission line coupled to the loop was demonstrated [30].

The loop designed for MarCO (Figure 2.32) is a one wavelength planar square loop with two feed points fed in phase quadrature. The loop is placed above a
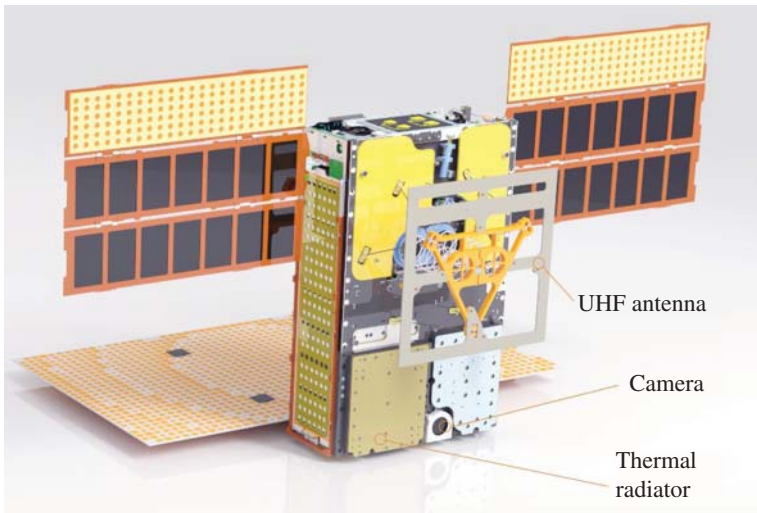

Figure 2.32 *MarCO 6U CubeSat fully deployed showing the proposed UHF loop antenna on top.*

Table 2.7   *UHF deployable antenna requirements.*

Property	Value
Frequency band (MHz)	401.6
Bandwidth (MHz)	>0.1
Gain within ±30°	>0 dBic
XPD within ±30°	>10 dB
Nominal beam pointing (Az. & El.)	0
Polarization	RHCP
Return loss	>14 dB

reflecting ground plane (GP) which is the spacecraft's body. The two feed points are separated by a quarter wavelength and produce radiation patterns with linear orthogonal polarizations. The quadrature phase between the two orthogonal (linear) polarizations thus produces the desired circular polarization. Finally, the finite GP (i.e. the CubeSat body) transforms the usual bidirectional loop radiation pattern into a more directive pattern. Before presenting this original deployable UHF antenna, a brief state-of-the-art is presented showing all antenna concepts available in the literature at the time MarCO development started. The UHF antenna requirements are summarized in Table 2.7.

2.4.1   State-of-the-Art of UHF Deployable CubeSat Antennas

2.4.1.1   Four Monopole Antenna

The most commonly used UHF and VHF antenna is the commercially available Innovative Solutions In Space (ISIS) deployable antenna [28]. It consists of four tape spring antennas of up to 55 cm length (Figure 2.33). It is compliant to CubeSat standard and is completely packaged. It includes the deployment mechanism, RF interfaces, and the option of accommodating a two solar cells on the top face of the antenna system. Various antenna configurations are available (monopole, dipole, or turnstile) allowing to obtain linear or circular polarizations with an omnidirectional pattern and a gain of about 0 dBi. Although this antenna presents excellent stowage efficiency, this antenna cannot meet MarCO's gain requirement.

2.4.1.2   Helical Antenna

Although helical antennas require deployment scheme to be stowed in a CubeSat, they offer a real alternative to monopole/dipole antennas in terms of gain and bandwidth due their non-resonant nature [31, 32]. A seven turns deployable helix was developed for CubeSats [33, 34]. This antenna provides more than 50% bandwidth and a gain of approximately 13 dBi at 360 MHz. As the gain of a helix is related to
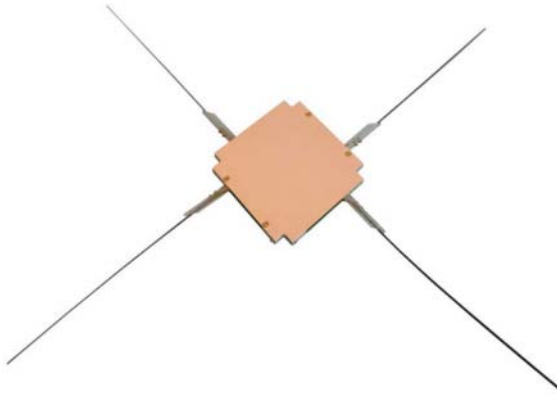
Figure 2.33   *ISIS deployable UHF and VHF antenna. Courtesy ISISpace.*

the number of turns [35], the antenna can be unreasonably long for a given gain. A long antenna can be challenging for spacecraft's attitude control; however, it is possible to reduce the length of the unifilar antenna by implementing bifilar or quadrafilar helices [36]. Bifilar and quadrafilar helices propose equivalent performance but requires the usage of baluns and/or hybrid/splitters components.

California Institute of Technology developed a new deployable antenna involving a helical or quadrifilar-helix antennas [32]. It uses helical composite supports winding in the opposite sense of conductors to form a helical pantograph, as shown in Figure 2.34. The structure is compacted axially much like a linear pantograph and can be compacted in the transverse direction by simply pulling four or eight points inward. In addition to helical and quadrifilar antennas, other interesting deployable antenna concepts are summarized in [32] involving log periodic antenna and conical log spiral antenna.

Figure 2.34   *Deployable wideband UHF antenna. Courtesy of California Institute of Technology, Pasadena, CA.*
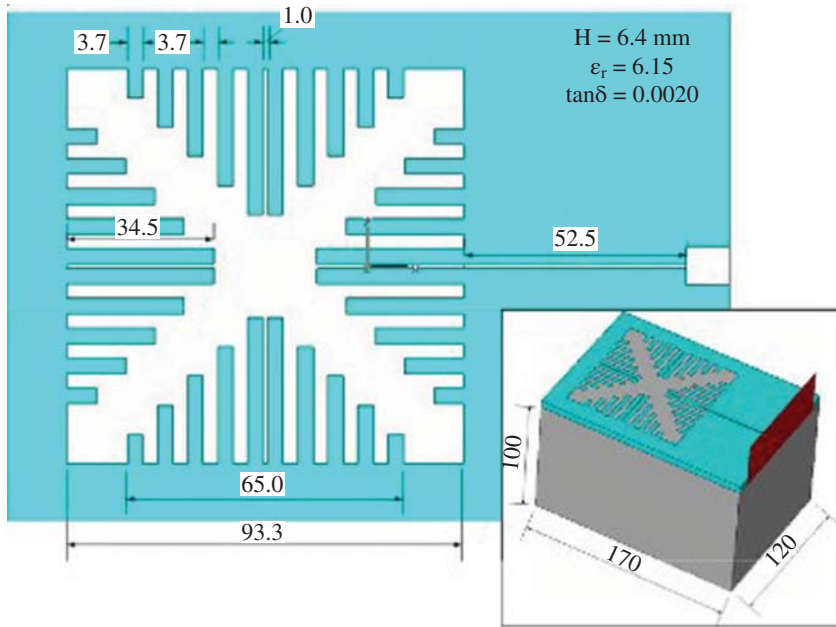
Figure 2.35   *Patch antenna for CubeSat. Source: From Kakoyiannis et al. [37]. ©2008 IEEE.*

2.4.1.3   Patch Antenna

Other types of UHF antenna for CubeSat are currently being investigated such as microstrip patch antennas. Again the real challenge is to fit the UHF antenna in a small volume allocation. For instance, the conceptual antenna designed at 436 MHz [37] consists of a microstrip patch antenna implemented on a thick dielectric substrate with high relative permittivity (i.e. $\varepsilon_r = 6.15$ and thickness $= 6.4$ mm). To increase the electrical length of the patch, tapered peripheral slits are used to further miniaturize the size of the antenna (Figure 2.35). Unfortunately, such electrically small antennas present low efficiency (i.e. $\eta \approx 30\%$) and low gain (i.e. ≈ 0 dBi) and may not be adequate for CubeSat configuration considering power handling, thermal view-factor, weight, and radiation in space.

2.4.2   Circularly Polarized Loop Antenna Concept

2.4.2.1   Loop Antenna Radiation and Polarization

While many loop antennas are constructed using tubing, single or multi-stranded wire supported by non-conducting posts [38], the loop described here is printed on a 1.524 mm-thick dielectric substrate that is stiff enough to hold its flatness. This
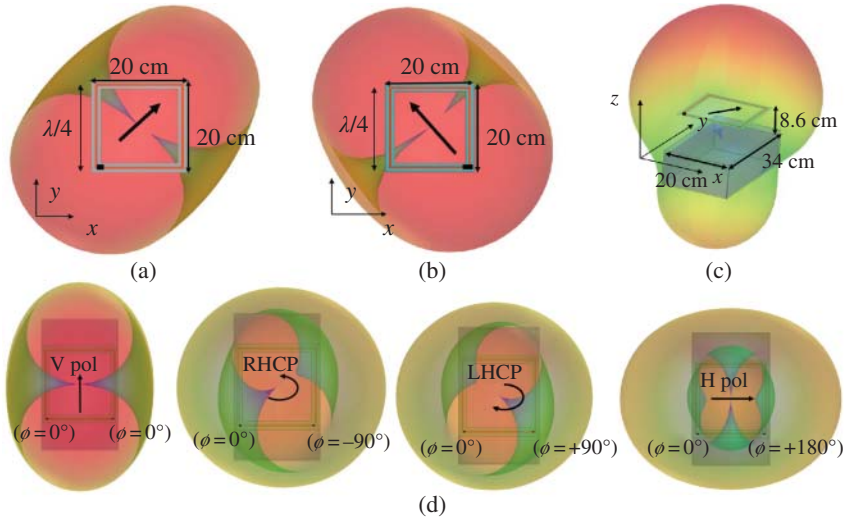
Figure 2.36 *(a) Printed one wavelength loop antenna showing the bidirectional pattern of the directivity and the orientation of the linear polarization (+45°); (b) Printed one wavelength loop antenna presenting the orientation of the linear polarization (−45°) based on the new position of the feed; (c) Loop antenna above the CubeSat bus, the antenna becomes more directive due to the reflection from the CubeSat; (d) Polarization of the loop antenna based on the different combinations of relative phase between the two feeds (V pol, RHCP, LHCP, H pol).*

trace-on-substrate approach greatly simplified the implementation of the required baluns and matching network because the later are implemented using microstrip lines. The one wavelength loop antenna is printed on a $200 \times 200 \, \text{mm}^2$ RT Duroid 4003 substrate ($\varepsilon_r = 3.38$ and $\tan\delta = 0.0027$).

When the loop is fed at the bottom left corner, it produces linear polarization oriented at $+45°$ as shown in Figure 2.36a. When it is fed at the bottom right corner, the linear polarization is oriented at $-45°$ as illustrated in Figure 2.36b. The input impedance simulated in this case is approximately $150 \, \Omega$ and is independent of the position of the feed on the loop. The addition of a finite ground plane (GP) lowers the input impedance and increases the directivity of the antenna [39]. In this case, the GP is the CubeSat itself (Figure 2.36c). It is placed at a distance of 86 mm (i.e. $0.11 \, \lambda_0$ at 401 MHz) to achieve a $\sim100 \, \Omega$ input impedance and a maximum directivity of 6.14 dBi. When the antenna is fed combining two sources, the polarization of the antenna loop is changing relative to the phase difference between the two feeds as depicted in Figure 2.36d. The impedance and directivity are nearly identical for all source locations.

The directivity as well as the resonant loop's input impedances are directly affected by the GP size and spacing between the loop and GP. Ideally, maximum

directivity for a one-wavelength loop occurs when the loop is a quarter-wavelength above an infinite GP. At 401 MHz, the ideal spacing would be 187 mm. For a 6U CubeSat, the available GP area is 340 mm × 200 mm. Reducing the spacing above the ground to 86 mm simplifies the deployment while achieving acceptable loop impedances and maintaining good pattern directivity.

The optimized loop shown in Figure 2.36c produces the impedances and directivity needed for the CubeSat mission. Although the axial ratio can be tuned simply based on the phase difference between the two baluns relative to the position of the feed, the aspect ratio of the 200 mm × 340 mm CubeSat-GP degrades the axial ratio of the antenna by approximately 3 dB. This is explained by the non-symmetric dimensions of the CubeSat which affect the amplitude of the two orthogonal linear polarization.

2.4.2.2   Infinite Baluns Design and Shielded Loop

In 1946, Libby explained the basic principles of the shielded loop antenna using coaxial cables [30] as shown in the schematic in Figure 2.37. The outer jacket of the coaxial cable is used to radiate. The inner conductor of the coax is soldered to the outer shell of a second coaxial line, thereby forming what is known as an infinite balun. The solid bold red arrows show the current flowing on the surface of the inner conductor of the coaxial cable. The dotted arrows represent the balanced current flowing in the internal surface of the outer conductor and the dashed arrows illustrate the current at the surface of the coaxial outer conductor.

The same basic principle is applied to the proposed loop antenna, except that coaxial transmission line are substituted by microstrip transmission lines. The microstrip lines facilitate the implementation of infinite baluns. In this
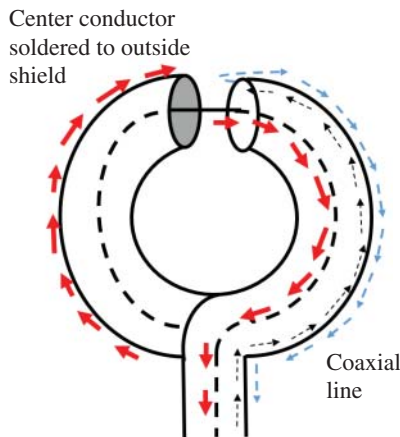

Figure 2.37   *Schematic illustrating the current flow of an electrically small shielded loop antenna using coaxial cable.*
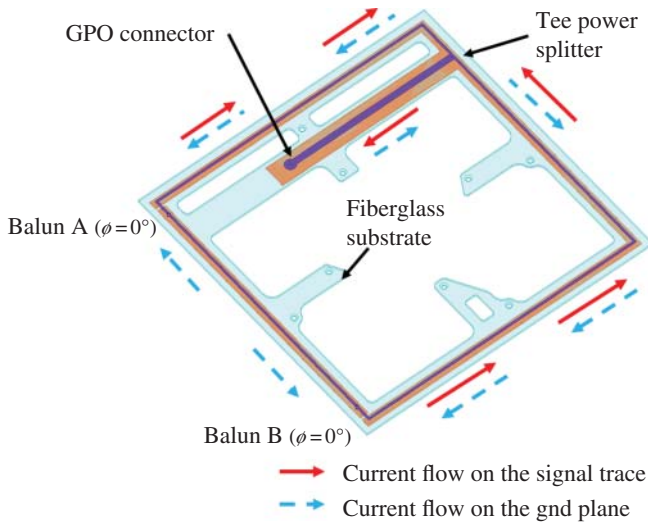
Figure 2.38 *Loop antenna design presenting the current flows on the signal trace and the ground plane in addition to the two baluns for the case of the V-pol configuration.*

configuration, the loop is created by a 5.6 mm-wide circuit trace. This trace is also used as GP for the microstrip lines. As illustrated in Figure 2.38, the infinite baluns are formed by the 100 Ω microstrip lines and the 1.38 mm gaps at two corners of the loop. It is worthwhile to underline that the gap for balun A is located at the standing wave current null for balun B (and vice-versa) so that the two infinite baluns do not interfere with one another.

The two baluns are separated by quarter-wavelength. The current radiating from the ground is represented in Figure 2.38 (in dashed arrows) as well as the current carried by the signal microstrip line (in solid arrows). The radiation of the antenna is due to the current flow on the microstrip line GP similar to the case of the shielded loop antenna.

2.4.2.3   Feeding Structure

The antenna input uses a GPO connector to transition from the input coax cable to a 50 Ω microstrip line (Figure 2.39a). The design of this component is illustrated in Figure 2.39a. In addition, a simple T-junction power splitter is also designed in microstrip line to feed two separate 100 Ω transmission lines as illustrated in Figure 2.39b. The position of the power splitter on the loop is used to adjust the lengths of the two 100 Ω microstrip lines in order to achieve the quadrature phase between the two infinite baluns that feed the loop. In other words, the electrical length difference between the antenna input connector and the two infinite baluns is designed to be one quarter wavelength.
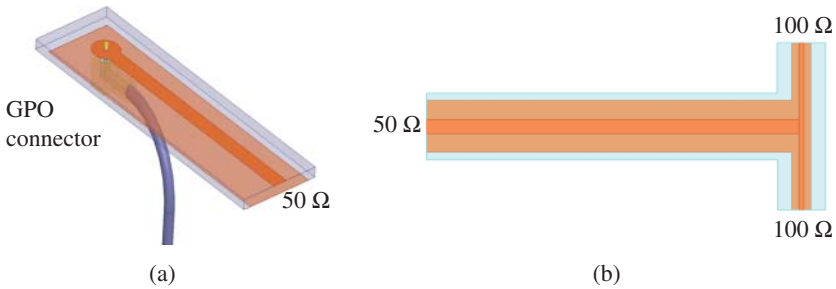
Figure 2.39   *(a) Transition from coaxial to 50 Ω microstrip line; (b) Power splitter showing the transition from 50 to 100 Ω microstrip line.*

The current with the usage of the two baluns is used to radiate, but a fraction of the current is carried back to the spacecraft through the external surface of the coaxial cable. One way to minimize its impact on the pattern and axial ratio is to use a flexible coaxial cable as vertical as possible and close to the center of the loop. Another way is to use ferrite beads along the cable to cancel the common mode (or unbalanced current) on the coaxial transmission line. However, ferrite beads increase mass, deployment risk and the volume of the antenna in stowed configuration. Consequently, we decided to account for the radiation from the coaxial cable as part of the design.

2.4.3   Mechanical Configuration and Deployment Scheme

The mechanical configuration of the UHF antenna is constrained by two main factors: stowed volume and tight schedule requirements due to the InSight launch date (approximately 8 months from design conception to delivery). In addition, the inherent tight integration of the RF design with the physical structure and deployment mechanism imposed design compromises.

Stowed volume is the other driving constraint on this antenna. To meet antenna performance and spacecraft thermal management requirements, the UHF loop circuit board needs to be positioned at least 80 mm off the spacecraft deck. However, in order to fit into the launch canister, the antenna is required to stow within a 6 mm height from the deck of the spacecraft. A deployment mechanism is thus required. To this end, the spring loaded cable tension structure shown in Figure 2.40 was developed. This mechanism allows for a very efficient stowed volume that meets the critical 6 mm stowage requirement. It also permits the circuit board loop to reach 90 mm deployed height and still maintain good structural stiffness.

Structural natural frequencies are the frequencies at which the deployed system will oscillate in the absence of any damping force. These frequencies do not depend on the applied mechanical excitation. If the fundamental natural frequency of the deployed mechanical structure is too low, there is a risk that its oscillations (in

Deployed   Stowed

Figure 2.40 *Stowed and deployed configurations of the UHF.*

the deployed state) will interfere with the Attitude Control System (ACS) of the spacecraft. This could result in an inability to point the spacecraft in the desired location relative to its inertial frame.

As a rule of thumb, large deployable structures attached to spacecraft bus structures strive for resonant frequencies on the order of 10–20 Hz or greater. The goal is for the structure's natural frequency to be above the control frequency of the spacecraft ACS system, so that the structure can be treated as a rigid body for spacecraft control purposes [40]. If the deployed structure is treated as a rigid body, the spacecraft can be reliably controlled by thrusters, reactions wheels, torque rods, etc. For the MarCO CubeSat, the ACS system required a deployed natural frequency greater than 5 Hz. It should also be noted that, it was demonstrated that precision driven structures are stiffness driven structures [41]. In other words, structural precision and stiffness go hand-in-hand, so, in order to get a more precise structure, its stiffness should be maximized.

Figure 2.41 shows the first four natural frequencies of the deployed UHF antenna calculated from the structural Finite Element Analysis (FEA) simulation [42]. The deformations in Figure 2.41 are highly exaggerated for visualization purposes only. The first natural frequency occurs above 90 Hz indicating that the deployed structure is extremely stiff and as a result there should be no issues with interference with the spacecraft attitude control system, and the antenna should have excellent deployed precision.

As presented in Figure 2.42, the main mechanical components of this deployable antenna are:

1. circuit board support (ULTEM material),
2. RF circuit board (RT Duroid 4003 material),
3. structural Hexapod tension cables (Vectran material),
4. compression deployment springs,
5. Tie-down/Tension mechanism,
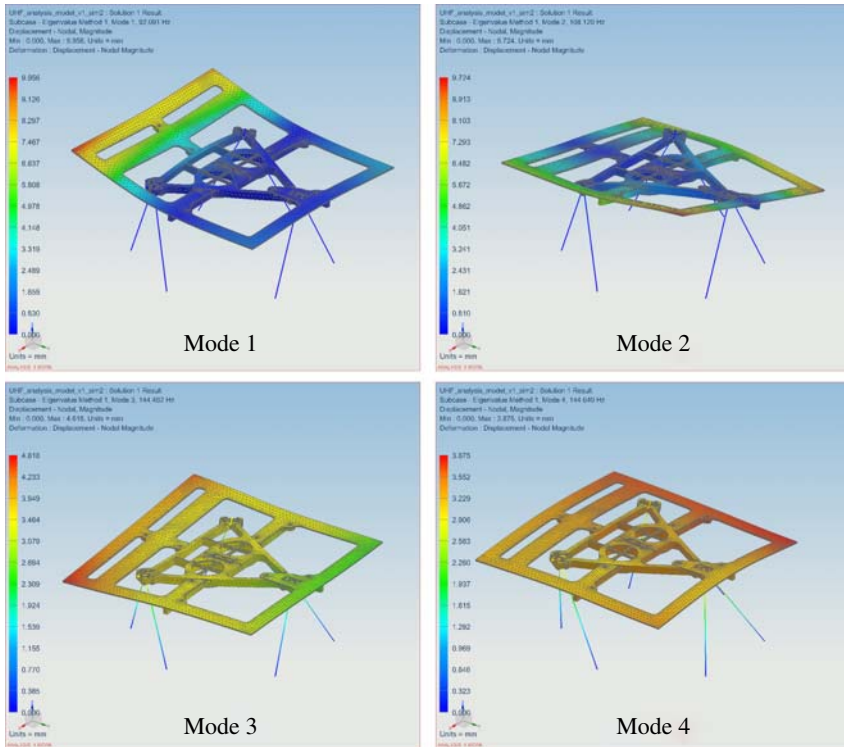6. burn wire release system.

Figure 2.41   *Selected mode shapes from Finite Element Analysis (FEA) Eigenvalue analysis of the 3D printed support structure with the printed loop antenna.*
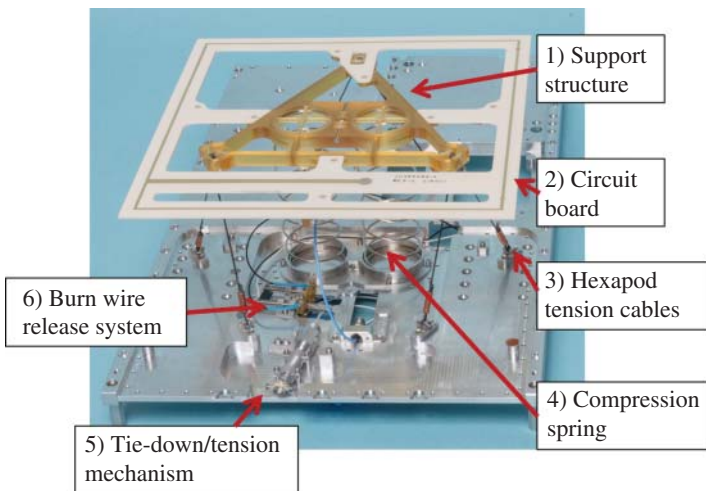

Figure 2.42   *Deployed UHF antenna mechanical components, nomenclature.*

The circuit board support structure is designed to meet stiffness requirements while minimizing RF interference and loss in the ULTEM material. To accomplish this, the material is concentrated at the center of the loop antenna while a minimum amount of material is added underneath the perimeter of the loop. It should be noted that the structural behavior of the overall antenna relies on the stiffness of the 1.524 mm Rogers 4003 circuit board. The main loads into this ULTEM support structure are from the Hexapod Tension Cables (item 3) and the compression springs positioned at the center of the loop (item 4) as highlighted in Figure 2.42. The two springs are placed at the center of the loop to minimize their impact on the antenna performance. The support structure is a triangle with two inscribed circles which mate with the deployment springs in order to efficiently handle the loads from the tension cables, which are arranged in a kinematic hexapod style configuration [43]. The overall thickness of the structure is sized to prevent bowing of the circuit board in the deployed state. In fact, the springs are pushing the structure away from the spacecraft while the tension cable tends to pull it back, and the combination of two opposite forces make the structure robust and stable.

In order to ensure accuracy and repeatability in length, the Vectran Hexapod tension cables, item 3, are fabricated on a custom tooling fixture. Vectran cables are bendable and similar to heavy duty fishing line, but have material properties suitable for the demanding environments of space [43–46]. The cables have open loops on each end with one loop formed from a single overhand knot [47] and at the other end of the cable a standard copper crimp is used. It should be noted that tensioned (flexible) cables make for efficient deployable structural elements because they can stow in a variety of compact geometries and carry loads in tension only, which is the most efficient use of a structural element [48]. The compression springs (made of nickel coated spring steel) which preload the tension cables supply a 7.6 N total preload, which is shared between the six hexapod cables. This preload (which results in a breakaway acceleration capability of about 7.5 m/s^2) was excessive for withstanding the minute loads encountered in space. In other words, there is no friction or counter forces in space to slow down the antenna during the deployment. The hexapod cables always remained tensioned despite different orientations with the gravity vector. So, when the spacecraft is in a vertical position, the antenna is not sagging due to the gravity.

For stowing and launch tie-down, the antenna uses another Vectran cable (140 lbf tension strength, which supports only the tie-downloads) combined with a novel miniature turnbuckle mechanism with integrated spring as shown in Figure 2.43.

The turnbuckle allows the Vectran tie-down cable to be easily tensioned without having to tie-off a knot under tension (which can be a difficult thing to do, especially in tight spaces). The integrated spring in the mechanism ensures that the assembly stays stowed and under tension, even if the Vectran tie-off cable changes length slightly due to thermal loads or launch vibrations. Lastly, the tie-off cable is released using two redundant burn wire mechanisms.
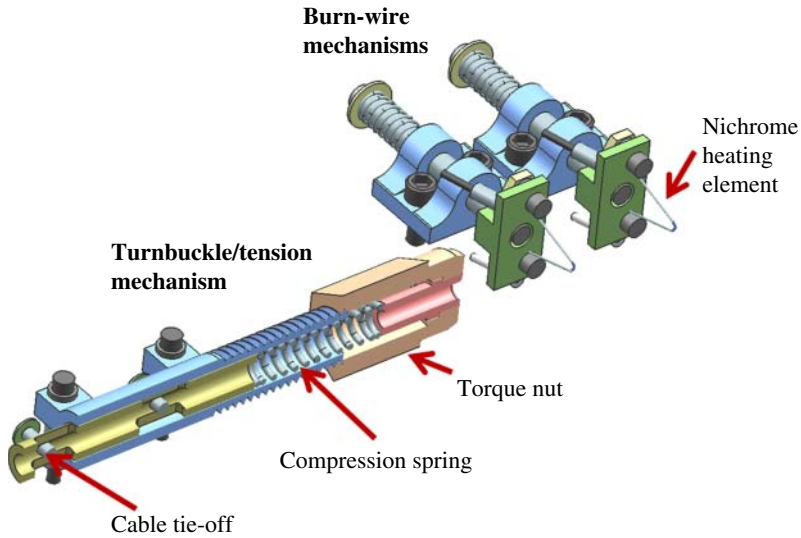
Figure 2.43   *Turnbuckle/Tension mechanism and Burn-Wire Mechanisms. (Note, no tie-off wire is shown in the figure).*

These mechanisms are based on an earlier design conceived at the Naval Research Laboratory (NRL) [49] and use a moving Nichrome hot-wire which thermally cuts through the Vectran tie-off cable. The burn wire mechanism typically cuts through the tie-down cable in less than 8 seconds after a current of 1.6 A current is applied to the device. Note that the burn wires are redundant and so either burn wire can cut through the tie-down wire and release the antenna for deployment.

Deployment repeatability, thermal cycle and random vibration tests were performed to verify that the antenna functions reliability in the extreme ±125 °C space environment of the MarCO mission. The deployment mechanism of the antenna as shown in Figure 2.43 has been tested at −60 °C (temperature to be expected during the deployment phase) in a thermal chamber to verify that the stiffness of the cold coaxial cable will not affect the loop release scheme.

2.4.4   Simulations and Measurements

The loop antenna simulation was performed using the 3-D finite-element electro-magnetic solver, ANSYS HFSS. The artwork of the manufactured loop antenna including detailed dimensions is shown in Figure 2.44. The antenna is designed to be sufficiently broadband to withstand frequency shifts due to the shrinkage and expansion of the material over the extreme ±125 °C temperature range [50].

Figure 2.44 *Drawing of the manufactured loop antenna (top and bottom sides) including dimensions in inches in the brackets and millimeters.*

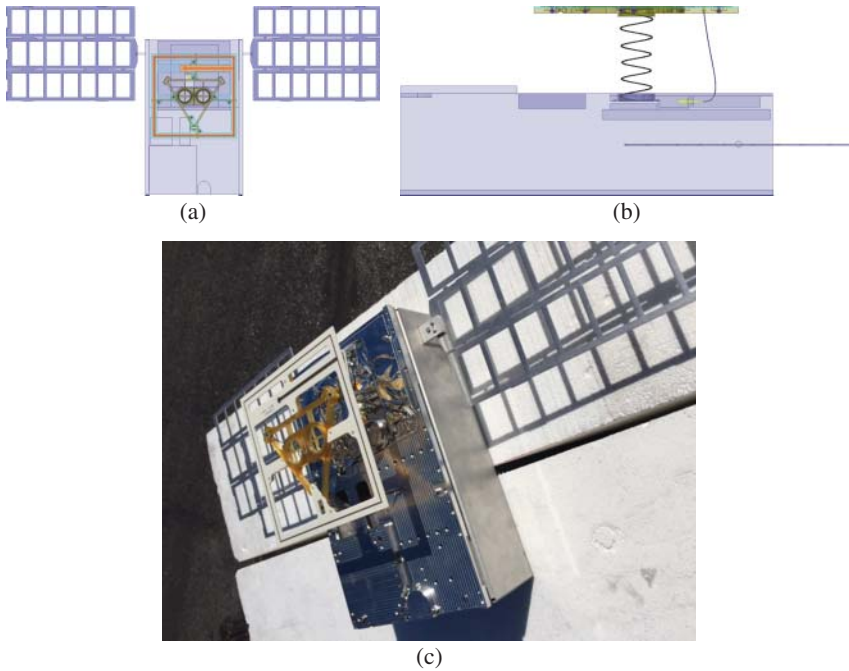(a)   (b)

(c)

Figure 2.45   *MarCO CubeSat UHF antenna as simulated in HFSS (a) top view); (b) side view; (c) photo of the fabricated CubeSat mockup model to verify the performance of the antenna.*

The HFSS model of the loop antenna mounted on MarCO spacecraft and a photo of the mockup are shown in Figure 2.45. The model does not include details that are small in terms of wavelengths, such as burn wire mechanism, hexapods and multi-layer thermal insulation. Note that the spacecraft includes two deployed solar panels, which are each represented by an aluminum "window pane" structure in the mockup.

Since the UHF antenna illuminates these $300 \times 220 \, \text{mm}^2$ solar panels, it is important to include them in the HFSS model. The overall effect of the solar panels is to increase the reflective surface in addition to the CubeSat body, resulting in a larger effective GP which provides an overall improvement in antenna directivity. The simulation only includes the grounded part of the solar panel as it was found that the addition of the solar cells to the panel only slightly improves the directivity of the antenna.

A total of four antennas are fabricated and evaluated using the CubeSat mockup. Figure 2.46 shows the simulated and measured reflection coefficients. The reflection coefficients of the four antennas are measured with an Agilent performance network analyzer (PNA) E8363B using a short-open-load (SOL) calibration. All measured
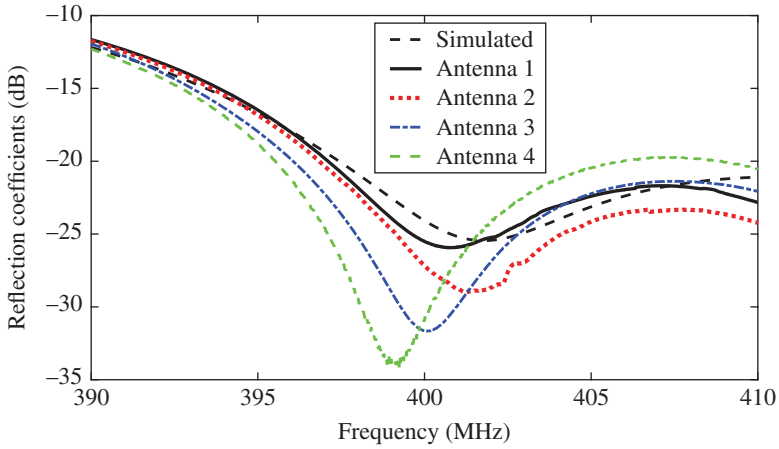
Figure 2.46   *Measured Reflection coefficients of the four fabricated antennas compared the HFSS simulated model.*

and simulated reflection coefficients are in reasonably good agreement, with differences attributed to the shape of the coaxial cable after deployments.

The radiation patterns are measured at the JPL on the 212 West Range [43] as depicted in Figure 2.47. The substitution method is used to extract the absolute gain of the loop antenna based on the measurements of two standard gain horn antennas.

Figure 2.48 shows a comparison between the simulated and measured RHCP and LHCP gain patterns at the center frequency (i.e. 401.6 MHz) in the azimuth and elevation planes. The error bars depict the discrepancies between the four measured antenna patterns. The maximum gain at boresight is 5 dBi (90% radiation efficiency). The gain at $\pm 30°$ in the elevation and azimuth direction is better than 2.5 dBi. The XPD is measured to be better than 10.5 dB in this range which corresponds to an axial ratio lower than 4 dB over the region of interest. The axial ratio value is largely caused by the finite GP defined as the CubeSat body with the solar panels. The aspect ratio $(870 \times 340 \text{ mm}^2)$ in the elevation compared to azimuth directions causes an estimated polarization loss of less than 0.3 dB at $\pm 30°$ in elevation and azimuth. It is clear from the plots in Figure 2.48 that the pattern is not symmetric due to asymmetry of the GP and the non-uniform distribution of the current along the loop.

In fact, the azimuthal asymmetry is primarily due to the presence of the microstrip feed and the non-uniform current distribution along the loop while the asymmetry in the elevation cut is due to the asymmetric placement of the antenna on the CubeSat and the asymmetric placement of the solar panels.

Return loss, Gain, XPD, return loss, and bandwidth requirement (as summarized in Table 2.7) are all met using this proposed deployable UHF loop antenna.

Figure 2.47 *West range antenna pattern measurement setup. The antenna under test is placed on top of the post and the ground is covered with absorber material to minimize multi-path interference.*
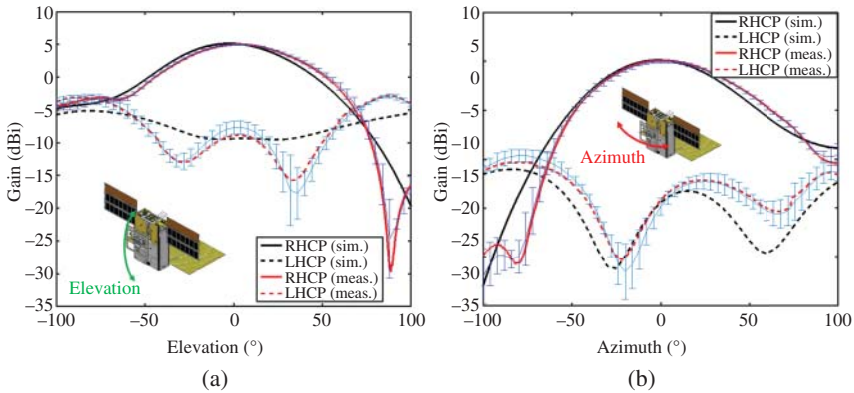

Figure 2.48 *Measured and HFSS simulated RHCP gain in the azimuthal and elevation planes. The difference between the RHCP and LHCP defines the cross discrimination polarization of the antenna. (a) Elevation. (b) Azimuth.*

2.4.5   In-Flight Performance

During InSight's EDL, the Iris radio was placed in bent-pipe relay mode where the UHF receiver was used to acquire the signal from InSight and the X-band transmitter was used to relay the information back to Earth in real-time. InSight's EDL sequence induces a highly dynamic scenario for the radio to maintain carrier
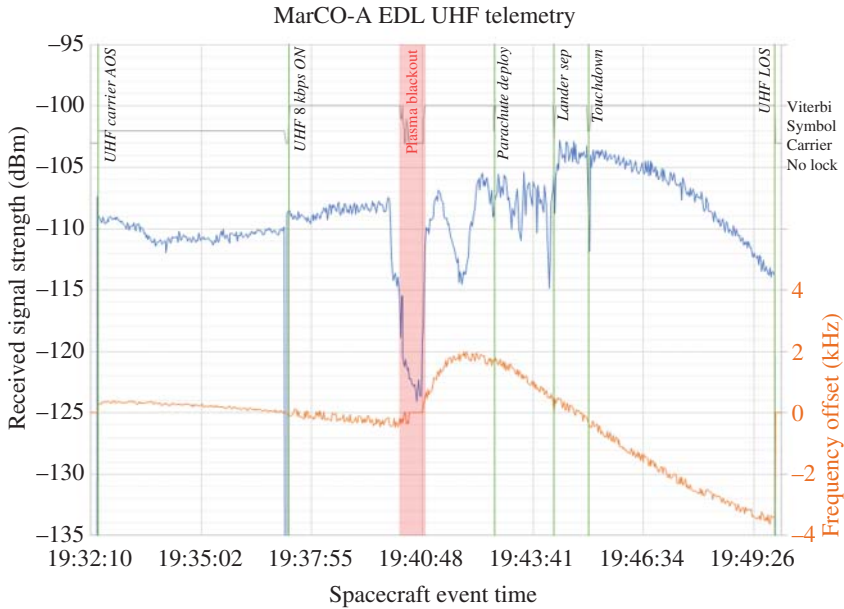
Figure 2.49   *Received signal strength and carrier frequency offset due to Doppler from InSight as seen by MarCO-A during EDL. AOS stands for Acquisition Of Signal and LOS for Loss of Signal.*

lock from events such as atmospheric entry, plasma blackouts, and parachute deployment. Figures 2.49 and 2.50 shows the received signal strength (interpolated from receiver gain control telemetry) and the carrier frequency offset as seen by each CubeSat.

The pre-EDL trajectory analysis between InSight and MarCOs predicted the received power to be approximately -110 dBm ± 3 dB. Both CubeSats saw strong signal strength within the expected range. During hypersonic entry to Mars atmosphere, communication blackouts and brownouts have been previously observed due to the higher plasma electron density compared to the X-band signal [51, 52]. MarCO-A observed a strong blackout period lasting 37 seconds, but MarCO-B observed a less severe plasma event with a pure blackout of only 9 seconds. It is hypothesized that the line-of-sight between MarCO-A and InSight had higher plasma density compared to that between MarCO-B and InSight. Further analysis of plasma formation in the wake regions of the entry probe are underway using orbit reconstruction and aero-thermodynamic modeling.

Through Monte-Carlo simulations, the expected nominal Doppler dynamics were estimated to have a frequency offset of ± 4 kHz with rates up to 50 Hz/s. Both CubeSats observed an overall frequency shift of 6 kHz during the EDL event, with MarCO-A observing a $+2/-4$ kHz shift and MarCO-B observing a $+4/-2$ kHz
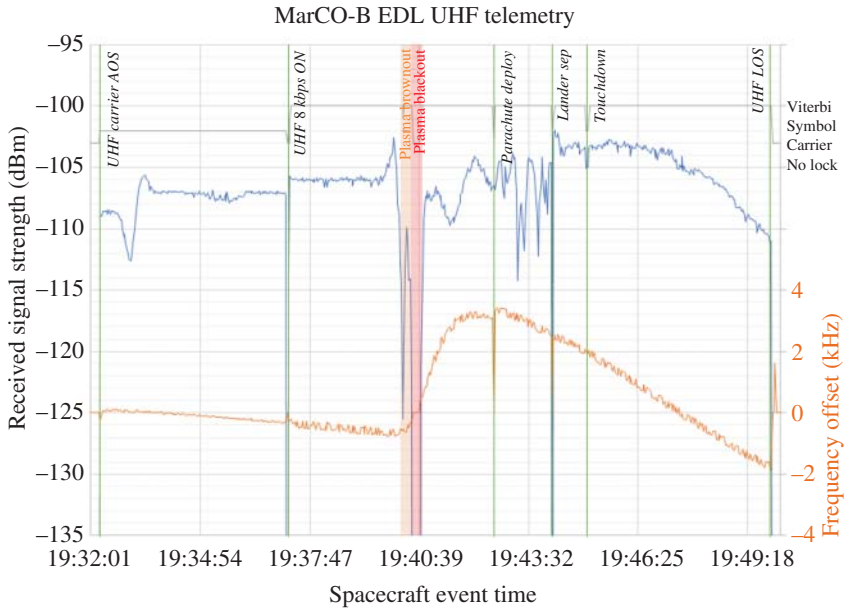
Figure 2.50 *Received signal strength and carrier frequency offset due to Doppler from InSight as seen by MarCO-B during EDL. AOS stands for Acquisition Of Signal and LOS for Loss of Signal.*

shift. The Doppler shift difference is mostly from the two fly-by trajectories of MarCOs (MarCO-A is placed south of the landing site whereas MarCO-B is placed north of the landing site in the fly-by B-plane), and the slight time difference. Rapid frequency change can be observed in the MarCO-B telemetry at parachute deployment on InSight.

2.5 Conclusions

The antenna development of MarCO was done in a very tight schedule of 9 months; this might have been one of the most challenging schedule of any NASA's JPL project. Despite the strenuous schedule, the four X-band low-gain antennas, the X-band deployable reflectarray antenna, and the deployable UHF loop antenna were delivered on schedule and all met the mission requirements. This work was performed by a very small team (Figure 2.51).

After thorough examination, NASA managers have decided to suspend the planned March 2016 launch of the Interior Exploration using Seismic Investigations Geodesy and Heat Transport (InSight) mission. The decision follows unsuccessful attempts to repair a leak in a section of the prime instrument in the science payload. MarCO mission was therefore delayed.
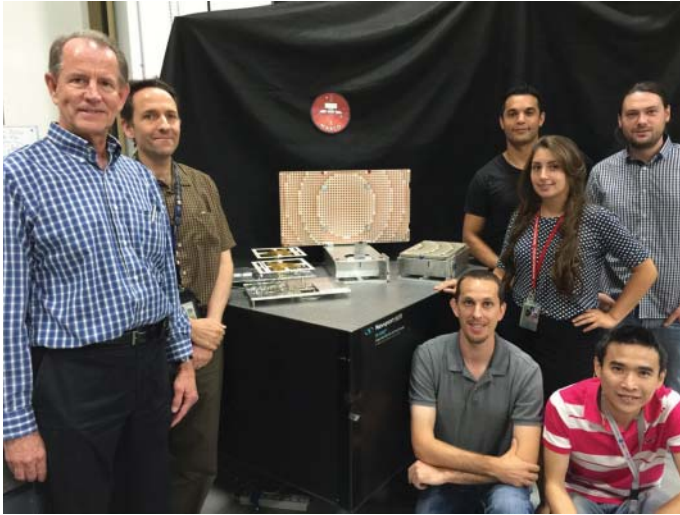
Figure 2.51 *MarCO antenna team with the high-gain deployable reflectarray antenna and the UHF deployable antenna. From the right to the left: Dr. Richard E. Hodges, Dr. Joseph Vacchione, Phillipe Walkameyer, Dr. Nacer Chahat, Brittany S. Velasco, Vinh Bach, and Dr. Emmanuel Decrossas.*

On May 5, 2018, NASA launched InSight to Mars. The MarCO satellites made the journey alongside NASA's InSight lander. The lander successfully touched down on Mars just before 3 p.m. ET on Monday, November 26, 2018. MarCO A and B transmitted flawlessly the EDL data from Insight to the 70 m DSN ground station. The X-band HGA gain was assessed to be well under 0.5 dB of the predicted value during the critical EDL event.

Beyond MarCO mission, the technologies developed within the project by the antenna engineers will be useful for a large amount of upcoming interplanetary CubeSat missions. For instance, numerous NASA's CubeSats such as Near-Earth Asteroid (NEA) Scout, Lunar Flashlight, LunaH-map, BioSentinel, Lunar Icecube, will use the X-band low-gain antennas. The deployable high-gain reflectarray antenna offers new capabilities for deep space communication, allowing to venture farther in space. These technologies will pave the way for future utilization of CubeSat antennas that will revolutionize future space and Earth observations and explorations. In 2016, the National Academies of Engineering, Science, and Medecine, have identified telecommunication as a stringent limitation for free-flying planetary Cubesats, implying the need for larger antennas. Since then, this limitation has been fully addressed with the successful development and demonstration of MarCO, along with many more antenna innovations to be covered in other Chapters of this book.

This demonstrates the tremendous national value of this work with a significant and lasting impact on NASA's space exploration program and the instruments it employs to explore the solar system.

Acknowledgments

References

1. N. Chahat, "A mighty antenna from a tiny CubeSat grows," *IEEE Spectrum*, vol. **55**, no. 2, pp. 32–37, Jan. 2018.
2. D. Bell, "Iris V2 CubeSat deep space transponder. X-, Ka-, S-band, and UHF deep space telecommunications and navigations," *National Aeronautics and Space Administration*, JPL 400-1604, 2016.
3. R. Hodges, D. Hoppe, M. Radway, and N. Chahat, "Novel deployable reflectarray antennas for CubeSat communications," *IEEE MTT-S International Microwave Symposium (IMS)*, Phoenix, AZ, May 2015.
4. R. E. Hodges, N. Chahat, D. J. Hoppe, and J. Vacchione, "A deployable high-gain antenna bound for Mars: developing a new folded-panel reflectarray for the first CubeSat mission to Mars," *IEEE Antennas and Propagation Magazine*, vol. **4**, Apr. 2016.
5. G. Hunyadi, D. M. Klumpar, S. Jepsen, B. Larsen, and M. Obland, "A commercial off the shelf (COTS) packet communications subsystem for the Montana EaRth-Orbiting Pico-Explorer (MEROPE) Cubesat," *Proceedings, IEEE Aerospace Conference*, Big Sky, MT, USA, 2002.
6. J. Praks, A. Kestila, M. Hallikainen, H. Saari, J. Antila, P. Janhunen, and R. Vainio, "AALTO-1 – an experimental nanosatellite for hyperspectral remote sensing," *2011 IEEE International Geoscience and Remote Sensing Symposium*, Vancouver, BC, 2011, pp. 4367–4370.

7. J. W. Cutler and H. Bahcivan, "Radio Aurora Explorer: a mission overview," *Journal of Spacecraft and Rockets*, vol. **51**, no. 1, pp. 39–47, Jan.–Feb. 2014.

8. J. H. Yuen, *Deep Space Telecommunications Systems Engineering*, Pasadena, CA: JPL Publication, Jul. 1982, pp. 82–76.

9. C. Chang, *DSN Telecommunications Link Design Handbook*, no. 810-005, Rev. E, Jet Propulsion Laboratory, California Institute of Technology, Nov. 2000.

10. S. C. Spangelo, M. W. Bennett, D. C. Meinzer, A. T. Klesh, J. A. Arlas, and J. W. Cutler, "Design and implementation of the GPS subsystem for the Radio Aurora eXplorer," *Acta Astronautica*, vol. **87**, pp. 127–138, Feb. 2013.

11. A. Williams, J. Puig-Suari, and M. Villa, "Low-cost, low mass avionics system for a dedicated nano-satellite launch vehicle," *2015 IEEE Aerospace Conference*, Big Sky, MT, 2015, pp. 1–8.

12. W. H. Swartz, L. P. Dyrud, S. R. Lorentz, D. L. Wu, W. J. Wiscombe, S. J. Papadakis, P. M. Huang, E. L. Reynolds, A. W. Smith, and D. M. Deglau, "The RAVAN Cube-Sat mission: advancing technologies for climate observation," *2015 IEEE International Geoscience and Remote Sensing Symposium (IGARSS)*, Milan, 2015, pp. 5300–5303.

13. C. L. Thornton and J. S. Border, *Radiometric Tracking Techniques for Deep-Space Navigation*, Jet Propulsion Laboratory, California Institute of Technology, Oct. 2000.

14. C. B. Duncan, A. Smith, and F. Aguirre, "Iris transponder – communications and navigation for deep space," *Small Satellite Conference*, Logan, UT, 2014.

15. A. T. Klesh, J. D. Baker, J. Bellardo, J. Castillo-Rogez, J. Cutler, L. Halatek, E. G. Lightsey, N. Murphy, and C. Raymond, "INSPIRE: Interplanetary NanoSpacecraft Pathfinder In Relevant Environment," *AIAA SPACE Conference and Exposition,* San Diego, CA, 2013, pp. 1–6.

16. A. Klesh and J. Krajewski, "MarCO: CubeSats to Mars in 2016," *Small Satellite Conference*, Logan, UT, 2015.

17. C. B. Duncan, "Iris V2 CubeSat deep space transponder. X-, Ka-, S-Band, and UHF deep space telecommunications and navigation," 2016. Available: online: https://deepspace .jpl.nasa.gov/files/dsn/Brochure_IrisV2_201507.pdf

18. F. A. Aguirre, "X-Band electronics for the INSPIRE Cubesat deep space radio," *Aerospace Conference*, Big Sky, MT, 2015.

19. *Proximity-1 Space Link Protocol – Data Link Layer*, Issue 5, Recommendations for Space Data System Standards (Blue Book), CCSDS 211.0-B-5, Washington, D.C.: CCSDS, Dec. 2013.

20. D. Antsos, "Mars Technology Program communications and tracking technologies for Mars exploration," *Aerospace Conference*, Big Sky, MT, 2006.

21. *AOS Space Data Link Protocol*, Issue 3, Recommendations for Space Data System Standards (Blue Book), CCSDS 732.0-B-1, Washington, D.C.: CCSDS, Sept. 2003.

22. M. M. Kobayashi, S. Holmes, A. Yarlagadda, F. Aguirre, M. Chase, K. Angkasa, B. Burgett, L. McNally, and T. Dobreva, "The Iris deep-space transponder for the SLS EM-1 secondary payloads," *Submitted to IEEE AES*, 2018.

23. R. Hodges, M. Radway, A. Toorian, D. Hoppe, B. Shah, and A. Kalman, "IS-ARA – Integrated Solar Array and Reflectarray CubeSat Deployable Ka-band Antenna," *IEEE APS Symposium,* Vancouver, July 2015.

24. D. M. Pozar and T. A. Metzler, "Analysis or a reflectarray antenna using microstrip patches of variable size," *Electronic Letters*, vol. **29**, pp. 657–658, Apr. 1993.

25. D. M. Pozar, S. D. Targonski, and H. D. Syrigos, "Design of millimeter wave microstrip reflectarrays," *IEEE Transactions on Antennas and Propagation*, vol. **45**, no. 2, pp. 287–296, Feb. 1997.

26. M. Zhou, S. B. Sørensen, R. Jørgensen, O. Borries, E. Jørgensen and G. Toso, "High-performance curved contoured beam reflectarrays with reusable surface for multiple coverages," *European Conference on Antennas and Propagation (EUCAP)*, Paris, 2017, pp. 71–75.

27. M. Milon, D. Cadoret, R. Gillard, and H. Legay, "'Surrounded-element' approach for the simulation of reflectarray radiating cells," *IET Microwaves, Antennas & Propagation*, vol. **1**, no. 2, pp. 289–293, Apr. 2007.

28. "Deployable UHF and VHF antennas," Available: online: http://www.isispace.nl/brochures/ISIS_AntS_Brochure_v.7.11.pdf

29. S. Okubo and S. Tokumaru, "Reactively loaded loop antennas with reflectors for circular polarization," *IECE Transactions (B)*, vol. **J65-B**, no. 8, pp. 1044–1051, Aug. 1982.

30. T. Nakamura and S. Yokokawa, "Loop antenna with a branch wire for circular polarization," *IECE Transactions (B)*, vol. **J70-B**, no. 11, pp. 110–117, 1987.

31. A. J. Ernest, Y. Tawk, J. Costantine, and C. G. Christodoulou, "A bottom fed deployable conical log spiral antenna design for CubeSat," *IEEE Transactions on Antennas and Propagation*, vol. **63**, no. 1, pp. 41–47, Jan. 2015.

32. G. Olson, S. Pellegrino, J. Costantine, and J. Banik, "Structural architectures for a deployable wideband UHF antenna," *53rd AIAA/ASME/ASCE/AHS/ASC Structures, Structural Dynamics and Materials Conference*, Honolulu, HI, Apr. 2012.

33. D. J. Ochoa, G. W. Marks, and D. J. Rohweller, "Deployable helical antenna for nano-satellites," US 8970447 B2, Mar 3, 2015.

34. D. J. Ochoa and K. Hummer, "Deployable helical antenna for nano-satellites," *28th Annual AIAA/USU Conference on Small Satellite*, Logan, Utah, 2014.

35. J. D. Kraus, *Antennas*, 2nd ed, New York: McGraw-Hill, 1988.

36. J. Costantine, D. Tran, M. Shiva, Y. Tawk, C. G. Christodoulou, and S. E. Barbin, "A deployable quadrifilar helix antenna for CubeSat," *Proceedings of the 2012 IEEE International Symposium on Antennas and Propagation*, Chicago, IL, 2012.

37. C. G. Kakoyiannis and P. Constantinou, "A compact microstrip antenna with tapered peripheral slits for CubeSat RF payloads at 436 MHz: miniaturization techniques, design & numerical results," *2008 IEEE International Workshop on Satellite and Space Communications,* 1–3 Oct. 2008, pp. 255–259.

38. W. L. Stutzman and G. A. Thiele, *Antenna Theory and Design*, New York: John Wiley & Sons, 1997.

39. A. A. Ayorinde, S.A. Adekola, and A. Ike Mowete, "Performance characteristics of loop antennas above a ground plane of finite extent," in *PIERS Proceedings*, Taipei, 2013, pp. 769–774.

40. J. R. Wertz and W. J. Larson, *Space Mission Analysis and Design (SMAD)*, 3rd ed, New York: Springer, 1999.

41. J. M. Hedgepeth, "Critical requirements for the design of large space structures," *Astro Research Corp*, Carpinteria, CA, NASA CR 3484, 1981.

42. N. X. Nastran, "Structural analysis," Version 9.1 Siemens, Plano, TX, 2014.

43. R. Chini, "The hexapod telescope – A never-ending story," *Reviews in Modern Astronomy 13: New Astrophysical Horizons*, vol. **13**, pp. 257–268, 2000.

44. "Vectran Technical Data Brochure," Kuraray America, Inc. Vectran Division, 2008.

45. "General Considerations for the Processing of Vectran Yarns," Kuraray America, Inc. Vectran Division, 2007.
46. R. B. Fette and M. F Sovinski, "Vectran fiber time-dependent behavior and additional static loading properties," NASA/TM-2001-212773, 2004.
47. C. W. Ashley, *The Ashley Book of Knots*, New York: Doubleday, 1944.
48. R. E. Skelton, J. W. Helton, R. Adhikari, J. P. Pinaud, and W. Chan, *An Introduction to the Mechanics of Tensegrity Structures*, Boca Raton: CRC Press LLC, 2002.
49. A. Thum, S. Huynh, S. Koss, P. Oppenheimer, S. Butcher, J. Schlater, and P. Hagan, "A nichrome burn wire release mechanism for cubeSats," *Proceedings of the 41st Aerospace Mechanisms Symposium*, Jet Propulsion Laboratory, Psadena, CA, May 16–18, 2012.
50. P. Kabacik and M. E. Bialkowski, "The temperature dependence of substrate parameters and their effect on microstrip antenna performance," *IEEE Transactions on Antennas and Propagation*, vol. **47**, no. 6, pp. 1042–1049, Jun. 1999.
51. D. Morabito, "The spacecraft communications blackout problem encountered during passage or entry of planetary atmospheres," *Jet Propulsion Laboratory, IPN Progress Report 42-150*, Pasadena, 2002.
52. D. Morabito, R. Kornfeld, K. Bruvold, L. Craig, and K. Edquist, "The Mars Phoenix Communications Brownout during entry into the Martian atmosphere," *Jet Propulsion Laboratory, IPN Progress Report 42-179*, Pasadena, 2009.

3

Radar in a CubeSat: RainCube

Nacer Chahat, Jonathan Sauder, Alessandra Babuscia and Mark Thomson

NASA Jet Propulsion Laboratory/California Institute of Technology, Pasadena, CA, USA

3.1   Mission Description

Launching multiple copies of a radar instrument is now possible with recent advances in miniaturized radar and CubeSat technologies. The radar in a CubeSat (RainCube) mission, developed at NASA's Jet Propulsion Laboratory (JPL) and launched in 2018, is a 6U ($\sim 12 \times 24 \times 36\,\text{cm}^3$) CubeSat precipitation radar [1] (Figure 3.1). It was put into orbit in May 2018 and was deployed from the International Space Station on June 25, 2018.

Thanks to the simplification and miniaturization of radar components, the Rain-Cube project at JPL has developed a novel architecture that is compatible with the 6U class. In comparison to existing spaceborne radars, the RainCube architecture reduces the number of components, power consumption, and mass by several order of magnitude. This opens up a new realm of options for low-cost spacecraft platforms saving not only on the instrument implementation but also on the launch and spacecraft costs.

We can now consider deploying a constellation of identical copies of the same instrument in various relative positions in low Earth orbit (LEO) to address specific observational gaps left open by current missions that require high-resolution vertical profiling capabilities.
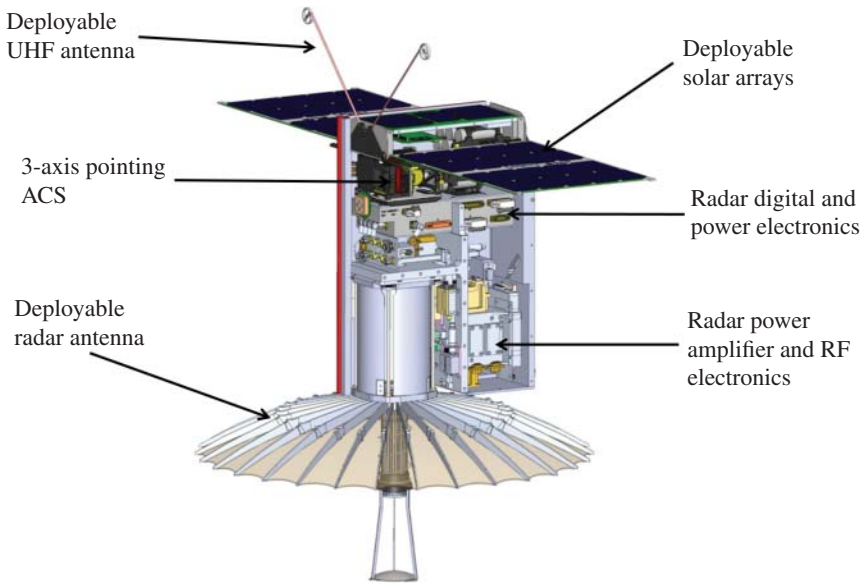
Figure 3.1   *RainCube 6U CubeSat description.*

RainCube is a proposed technology demonstration mission to enable Ka-band precipitation radar technologies on a low-cost, quick-turnaround platform. Rain-Cube developed, launched, and operated a 35.75 GHz radar payload on a 6U CubeSat. This mission validated a new architecture for Ka-band radars and an ultra-compact deployable Ka-band antenna in a space environment. It also demonstrated the feasibility of a radar payload on a CubeSat platform. The antenna and its radar payload are shown in Figure 3.2. The antenna can also be seen fully deployed when integrated to the spacecraft (Figure 3.3).

The RainCube instrument configuration is a fixed nadir-pointing profiler at Ka-band [1], with a minimum detectable reflectivity better than $+12 \, \text{dBZ}$[1] at 250 m range resolution and 10 km horizontal resolution at an altitude of 450–500 km. The key RainCube requirement relevant to the antenna is the 10 km diameter instantaneous radar footprint, which defines the antenna directivity and beamwidth ($<1.2°$). The gain is defined by the radar sensitivity. The sidelobe level needs to remain below $-17 \, \text{dB}$ in order to avoid radar ambiguities.

Despite its very limited volume, this small satellite carries a three-axis attitude determination and control system (ACS), two deployable solar arrays ($\sim 24 \times 36 \, \text{cm}^2$), multiple batteries, a deployable uplink and downlink UHF

---

[1] It is a logarithmic dimensionless technical unit used in radar, mostly in weather radar, to compare the equivalent reflectivity (Z) of a radar signal reflected off a remote object (in mm^6 per m^3) to the return of a droplet of rain with a diameter of 1 mm (1 mm^6 per m^3).
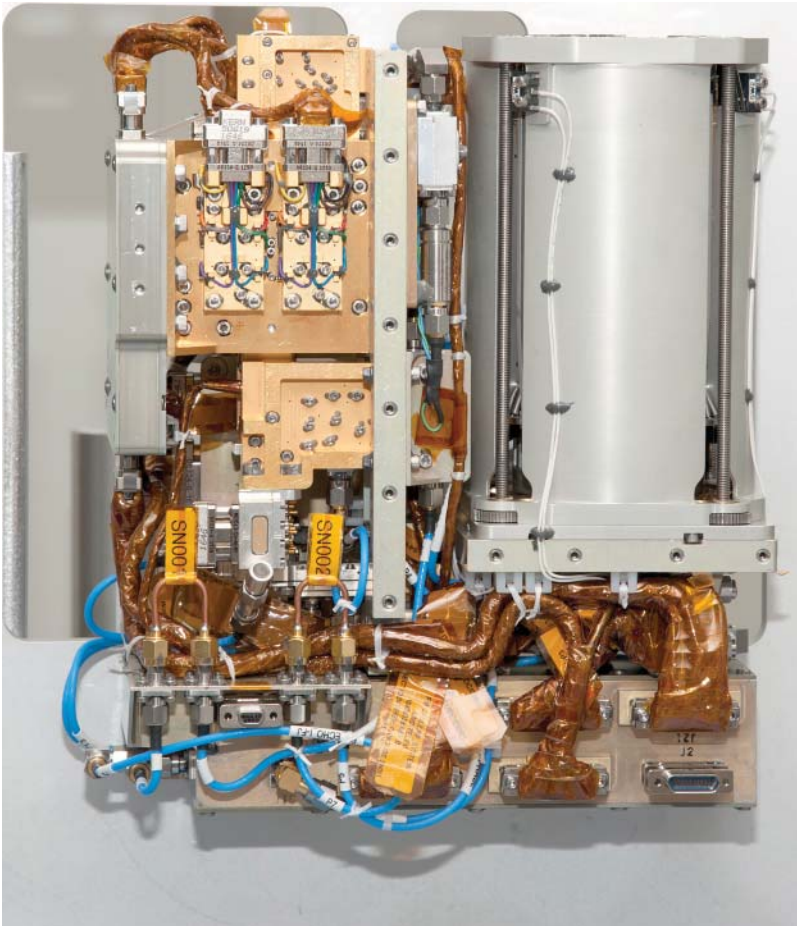
Figure 3.2   *The radar electronics and folded antenna integrated into the flight chassis.*

antenna for telecommunication, an S-band downlink patch antenna and a radio for telecommunication, the radar power amplifier and radio frequency (RF) electronics, the radar digital boards and power supply, and the radar deployable mesh reflector antenna.

One of the major challenges of this mission is to develop an antenna providing a gain of more than 42 dBi and fitting in a highly-constrained volume (<1.5U). The required antenna gain and limited stowage volume dictate utilization of a deployable antenna. This book chapter offers a detailed state of the art of deployable antennas for CubeSat with a focus on mesh deployable parabolic antennas. It also provides the basic knowledge required to design focal-fed reflectors and dual reflector antennas
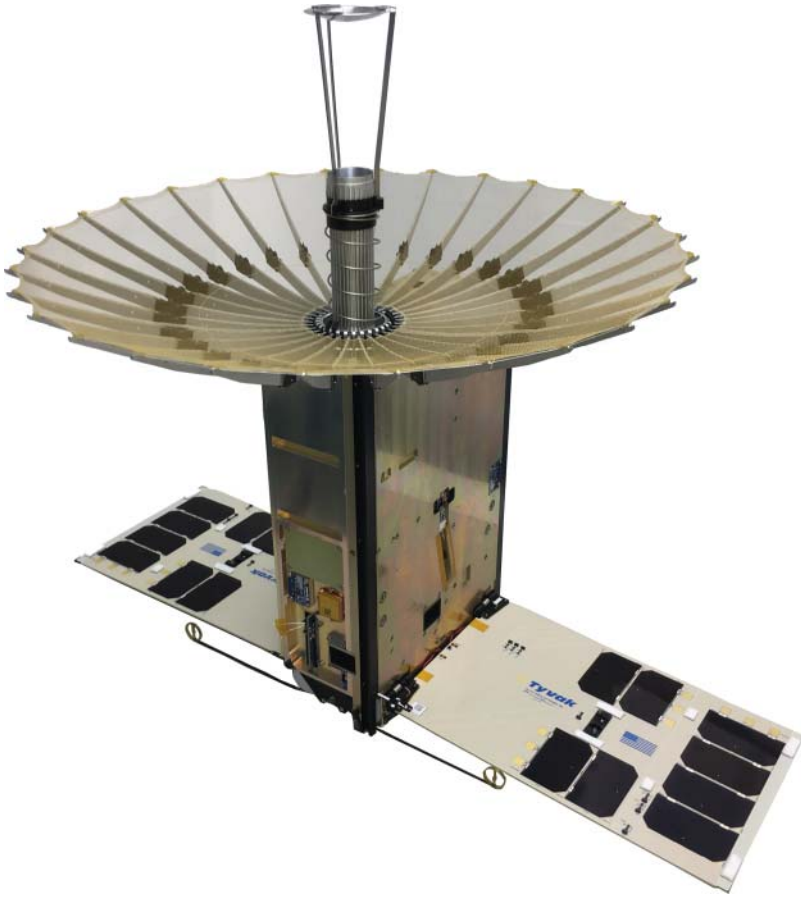
Figure 3.3   *Photography of RainCube spacecraft with its antenna fully deployed during integration and testing (I&T).*

(i.e. Cassegrain and Gregorian reflectors) as this is essential to understand how the RainCube antenna engineers converged into the final design. Analytical and experimental results are provided showing excellent agreement. A brief description of the S-band and UHF telecommunication capabilities are also provided.

3.2   Deployable High-Gain Antenna

3.2.1   State of the Art

Three deployable antenna technologies are currently under investigation for CubeSats: inflatable antennas (Chapter 7) [2], folded panel reflectarray antennas (Chapters 4 and 5) [3], and deployable mesh reflector antennas [4–6]. A brief state of the art is reported here and the pros and cons for each options is discussed.
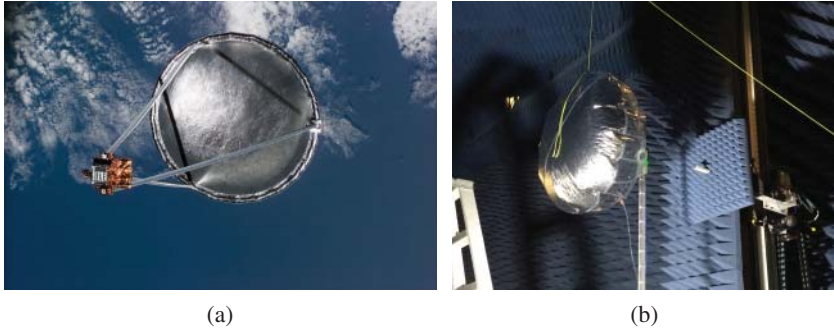
(a)   (b)

Figure 3.4   *(a) The inflatable antenna experiment; (b) S-band inflatable antenna for CubeSat. Courtesy of NASA's JPL/California Institute of Technology.*

3.2.1.1   *Inflatable Antennas*

While research on inflatable antennas dates back to the 1950s, the inflatable antenna experiment (IAE), a NASA experiment that began on May 19, 1996, is the only inflatable antenna deployment performed in space (Figure 3.4a). Launched from the space shuttle endeavor during the 1996 STS-77 mission, the 14 m parabolic reflector antenna successfully deployed, but the lenticular structure did not maintain the required shape due to a malfunction of the gas inflation system [7]. More recently, an inflatable antenna designed for CubeSats was introduced (Figure 3.4b), providing a gain of 21 dBi at S-band [2]. This inflatable antenna has a very high ratio of deployed to stowed volume [2]. However, the required surface accuracy for a Ka-band operation cannot be achieved using inflatable design due to wrinkling of the surface and pressurization that tends to deform the surface out of a parabola.

3.2.1.2   *Deployable Reflectarray Antennas*

While the topic of reflectarray antennas has been actively researched for many years, to date, only two reflectarray antennas have flown in space: ISARA and MarCO (see Chapter 2). Reflectarray antennas are lightweight, low-cost, and can be typically folded in panels to yield stowage efficiency. However, reflectarrays exhibit narrow bandwidth (<10% depending on element design and *F/D* [8]) and the maximum gain of current configurations is limited by the number of panels that can be practically folded into a CubeSat. Despite the inherent phase error and element dissipation losses, reflectarrays can achieve relatively high efficiency. For example, deployable flat panel reflectarrays have experimentally demonstrated 50% efficiency at Ka-band [9]. Moreover, a dual X/Ka-band reflectarray based on thin tensioned membrane suitable for inflatable systems also demonstrated 50% efficiency [10]. For space applications, reflectarray antenna materials must be evaluated for susceptibility to radiation effects and electrostatic discharge (ESD) [8]. Two reflectarray antennas for CubeSat applications have
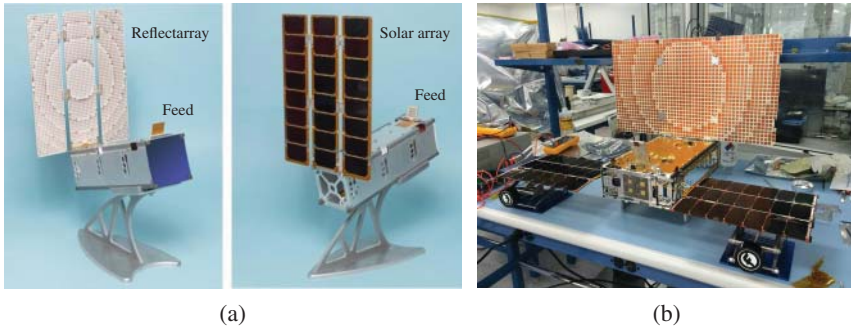
(a)   (b)

Figure 3.5   *(a) ISARA 3U CubeSat. Source: Based on Hodges et al. [3]. © 2015 John Wiley & Sons; (b) MarCO 6U CubeSat with its fully deployed reflectarray [11]. Courtesy of NASA's JPL/California Institute of Technology.*

been developed at NASA's JPL [3]. Under integrated solar array and reflectarray antenna (ISARA) project, a circularly-polarized reflectarray antenna operating at 26 GHz was developed at NASA's JPL (Figure 3.5a). Following the success of this approach, an X-band circularly-polarized reflectarray was developed for the Mars cube one (MarCO). MarCO's reflectarray employs in-house hinges allowing to reduce gaps between adjacent panels. These gaps are very critical as they result in a gain reduction (i.e. therefore efficiency reduction) and increase of side-lobe-levels. The two fully deployed reflectarrays are shown in Figure 3.5, along with their CubeSat. Reflectarrays are possible candidates for radar operating at Ka-band but they are highly sensitive to thermal variation and panel flatness. A larger Ka-band radar is under development at the NASA's JPL (Chapter 4 and Figure 3.6). This reflectarray consists of 15 deployable panels and one fixed panel and a deployable feed. It could be a good solution for future radar missions at Ka-band requiring higher gain for a smaller radar footprint on Earth.

3.2.1.3   *Deployable Mesh Reflector Antennas*

Reflector antennas are the most commonly used solutions for high-gain spacecraft antennas, as they provide high efficiency, and can support any polarization. The reflector's large bandwidth allows for multiple frequency operation using a multi-band feed system. General reflector antenna design guidelines are available in the literature [12, 13]. Although numerous reflector antenna deployment mechanisms have been developed and many have been flown in Earth orbit for defense and commercial applications, only a few deployable mesh reflectors have been used for scientific remote sensing missions. The most notable deep space antenna is the Galileo 5 m deployable high gain mesh reflector (Figure 3.7a), which failed to fully deploy after its first Earth flyby [14]. More recently, a 6-m deployable mesh reflector antenna (Figure 3.7b) was successfully deployed in LEO
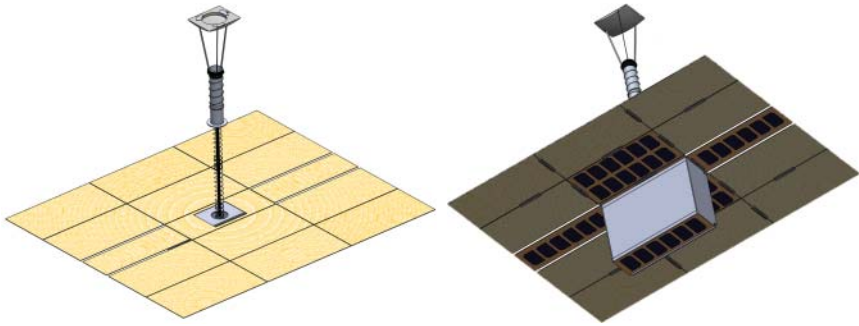
Figure 3.6   *One-meter Ka-band deployable reflectarray combined with solar arrays. Courtesy of NASA's JPL/California Institute of Technology.*

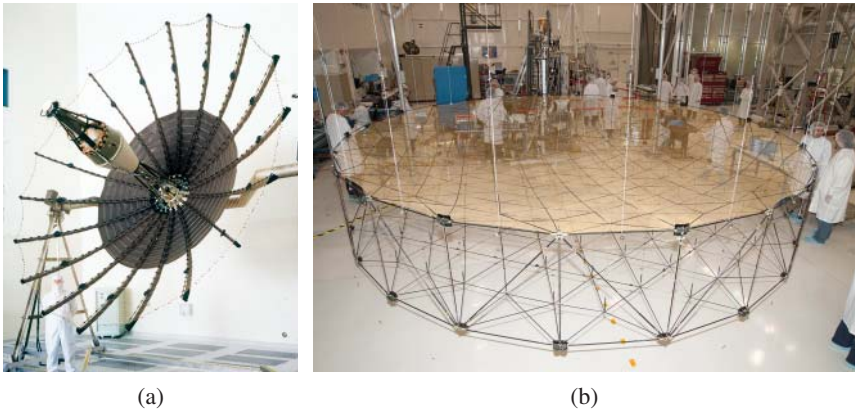(a)   (b)

Figure 3.7   *(a) Fully extended Galileo antenna; (b) unfurled SMAP mesh reflector antenna. Courtesy of NASA's JPL/California Institute of Technology.*

for the soil moisture active passive (SMAP) spacecraft that launched in January 2015 [15]. Before that, another deployable antenna had flown as part of the Highly Advanced Laboratory for Communications and Astronomy (HALCA) mission with an effective diameter of 8 m [16]. The NASA's JPL in collaboration with the India Space Research Organization (ISRO) is planning to fly a 12 m deployable mesh reflector operating at L- and S-band. for the NASA-ISRO Synthetic Aperture Radar (NiSAR) mission.

Apollo 11, 12, and 14 missions used a 3 m deployable mesh antenna operating at S-band for direct link to Earth. The Erectable S-Band Antenna was first flown on Apollo 11 and was intended to provide a stronger television signal. Because of the fact that the time during the brief Apollo 11 extravehicular activity (EVA) was so precious, the expected 19 minute deployment of the antenna would have a

major impact of productivity. Consequently, an assessment was made of the first few minutes of the bandwidth television (TV) signal coming through the Lunar Module's steerable antenna. The signal was deemed adequate, so the Erectable S-Band was not deployed. However, it was deployed on both Apollo 12 and 14. Deployment was intended to be easy enough that one person could do it. The deployment sequence assisted by an astronaut is illustrated in Figure 3.8a. The pointing of the antenna is performed by the astronaut itself as shown in Figure 3.8b showing astronaut Jim Lovell setting approximate elevation. More details about this antenna can be found in [17].

As part of the Apollo missions, several deployable mesh reflector antennas operating at S-band were flown. Apollo 15, 16, and 17, employed a lunar roving vehicle (LRV). LRV was an electric vehicle designed to operate in the low-gravity vacuum of the Moon and to be capable of traversing the lunar surface, allowing the Apollo astronauts to extend the range of their surface extravehicular activities. Three LRVs were driven on the Moon, one on Apollo 15 by astronauts David Scott and Jim Irwin, one on Apollo 16 by John Young and Charles Duke, and one on Apollo 17 by Gene Cernan and Harrison Schmitt. A large mesh reflector antenna was mounted on a mast on the front center of the rover. This high-gain mesh antenna operates at S-band and provides direct communication link with Earth (Figure 3.9).

All deployable reflectors flown to date have been developed for large spacecraft or Rover that can afford greater space within the launch shroud, which allows for spacecraft packaging to be adapted to accommodate antenna stowage [12–20]. Consequently, existing antenna designs do not address the requirement to fit within the rigid CubeSat packaging constraints. Furthermore, existing mesh reflector designs cannot be directly scaled to CubeSat dimensions because knitted mesh density and thickness are fixed by RF requirements and other deployment mechanism devices such as springs, hinges, and motors are not directly scalable. However, few deployable parabolic antennas for CubeSats have been studied but all were designed for S-band operation. One concept for a CubeSat antenna is a wrapped gore composite reflector, where slits are made in a composite parabolic shell, and then the entire reflector is wrapped around a center hub [21]. While this architecture may produce good surface accuracy, a 0.5 m antenna could not stow in a 1.5U volume. Another concept involves transforming the entire CubeSat body into a reflector with a parabolic-shaped center section [22], but this concept produces a rather small parabolic reflector. Finally, two S-band deployable mesh reflector antenna concepts have been developed. The first concept is a 50 cm diameter folded rib reflector (Figure 3.10), which was flown on the AENEAS spacecraft developed by University of Southern California, Information Sciences Institute [4]. The antenna deploys similarly to an umbrella, tensioning the mesh between each pair of ribs. The folding rib architecture allows the antenna to stow in a 1.5U volume and provides sufficient surface accuracy for S-band operation. However, this antenna design is not scalable to Ka-band, due to surface accuracy limitations and the prime focus feed configuration
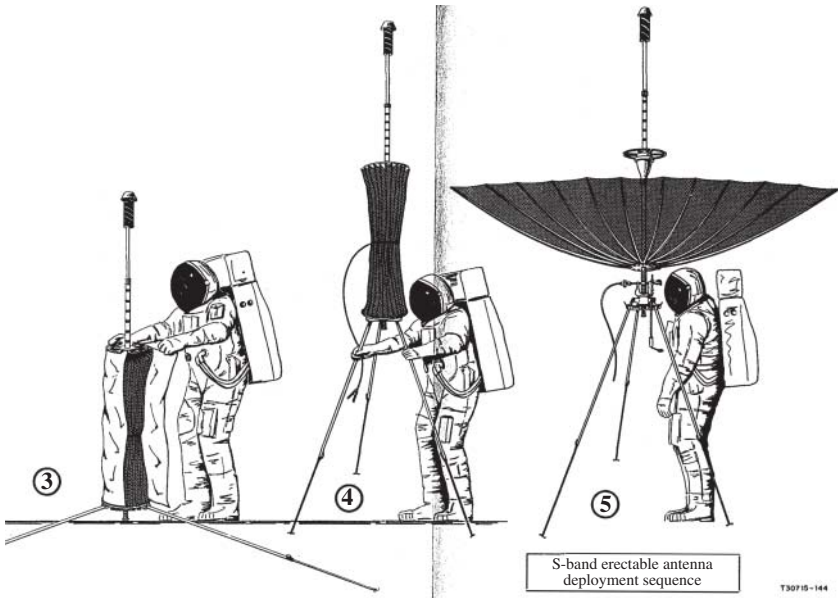
(a)
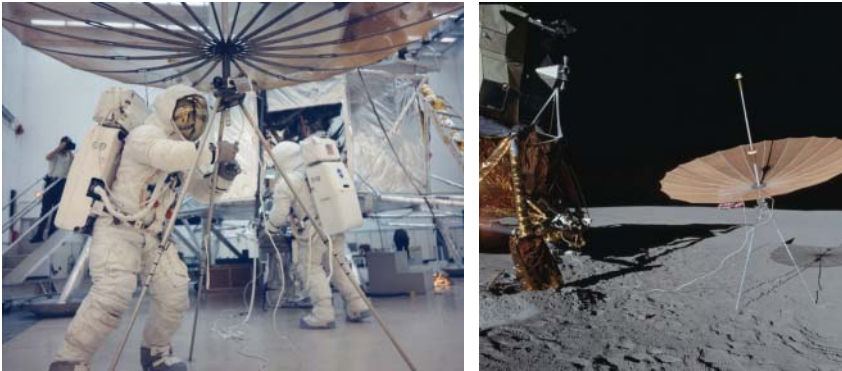
(b)

Figure 3.8 *Deployable mesh reflector antenna used during the Apollo 11, 12, and 13 missions used to provide television link between the Lunar Module and the Manned Spaceflight Network: (a) last and major three steps of the deployment of the antenna performed by one astronaut. Source: From Bryan and Strasburger [17]. © 1969 NASA ; (b) Apollo 13 training photo showing Jim Lovell using the crank to set approximate elevation; (c) Apollo 12 landing site showing the antenna fully deployed. Courtesy NASA.*
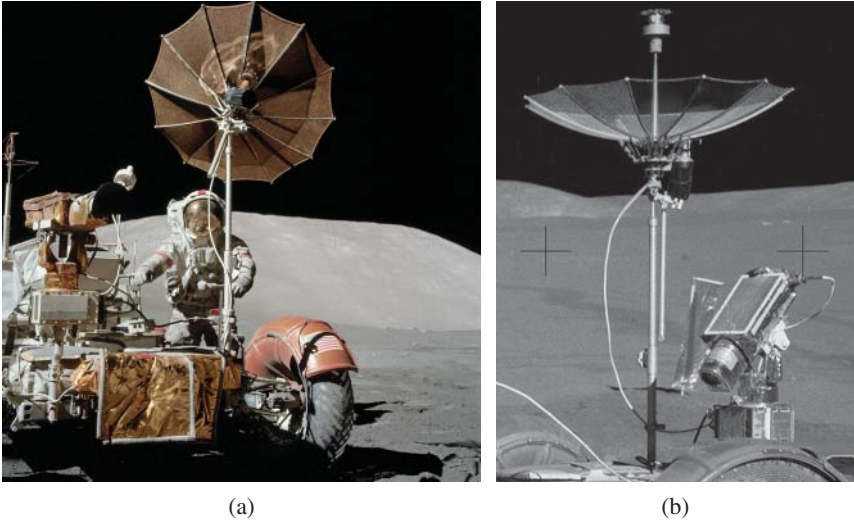
(a)   (b)

Figure 3.9 *(a) Apollo 17 LRV and astronaut Eugene Cernan on the moon. The high-gain mesh antenna is located in the front center of the rover; (b) the high-gain communications antenna with the TV camera in the stowed position on the Apollo 15 Lunar buggy chassis. Courtesy NASA.*
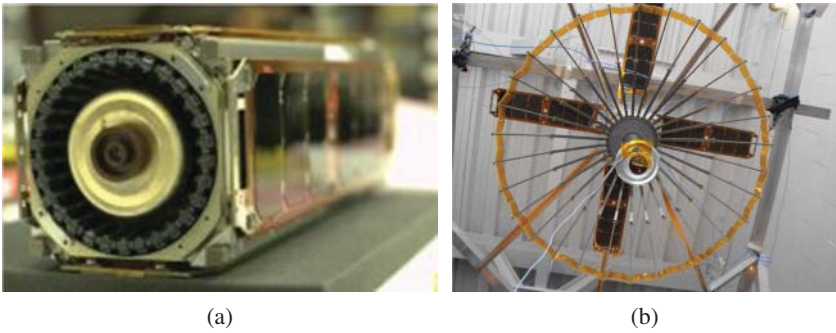

(a)   (b)

Figure 3.10 *(a) Integrated and stowed AENEAS antenna; (b) fully deployed AENEAS antenna. Courtesy of University of Southern California.*

(which leads to excessive blockage loss and feed loss). A wrap-rib style antenna with mesh attached to ribs wrapped around a center hub [6] has also been fabricated. Unfortunately, using thin, flexible ribs (required to enable the design to wrap around the small CubeSat hub) would not provide adequate rigidity to tension the mesh, as the ribs would be too flexible to hold the mesh in place when deployed.

3.2.2 Parabolic Reflector Antenna Design

Before discussing in details the design steps of the RainCube Cassegrain deployable mesh reflector, we will address the design procedure of typical dual-reflector antennas: Cassegrain and Gregorian reflector.

3.2.2.1 Paraboloidal Reflector

A paraboloidal reflector transforms a spherical wave radiated by a feed located at its focal point into a plane wave. A parabolic reflector is illustrated in Figure 3.11. The equations for the reflector surface are:

- In rectangular coordinates:

$$r^2 = 4F(F + z) \tag{3.1}$$

- In polar coordinates:

$$\rho = \frac{F}{\cos^2(\psi/2)} \tag{3.2}$$

where F is focal length, D the diameter, ρ the distance from the focus to the reflector, and ψ the feed angle from the negative z-axis. The reflector depth z_0 defined as the distance between the reflector rim to its center equals to:
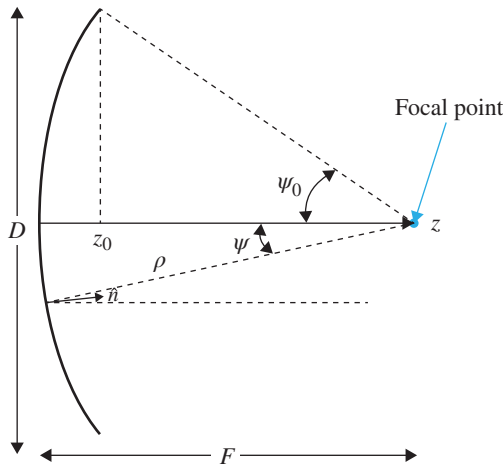
$$z_0 = \frac{D^2}{16F} \tag{3.3}$$

Figure 3.11   *Geometry of a parabolic reflector.*

The half-subtended angle ψ_0 relates to the ratio F/D by:

$$\psi_0 = 2 \tan^{-1} \frac{1}{4F/D} \qquad (3.4)$$

3.2.2.2   Dual-Reflector Antennas

Cassegrain and Gregorian reflectors are dual-reflector antennas using a sub-reflector to increase their effective focal length. Cassegrain dual-reflector antennas use a hyperbolic subreflector (Figure 3.12a) and Gregorian dual-reflector antennas use an elliptical sub-reflector (Figure 3.12b). One focus of the subreflector is located at the focus of the main paraboloidal reflector. The second focus of the subreflector is placed at the feed antenna phase center. The subreflector changes the curvature of waves coming from one focus into waves with their caustic at the second subreflector focus.

Clearly, as can been seen in Figure 3.12, the Gregorian design requires a larger subreflector because it extends farther from the main reflector vertex. The subtended angle of the main reflector is $2\psi_0$ but the effective subtended angle is $2\theta_0$. The subreflector eccentricity is given by:

$$\text{Cassegrain}: \quad e = \frac{\sin \frac{1}{2}(\psi_0 + \theta_0)}{\sin \frac{1}{2}(\psi_0 - \theta_0)} = \frac{c}{a} \qquad (3.5)$$

$$\text{Gregorian}: \quad e = \frac{\sin \frac{1}{2}(\psi_0 - \theta_0)}{\sin \frac{1}{2}(\psi_0 + \theta_0)} = \frac{c}{a} \qquad (3.6)$$

where $2a$ is the vertex distance and $2c$ is the foci distance of the subreflector, given by:

$$\text{Cassegrain}: \quad 2c = \frac{2Pe^2}{e^2 - 1} \qquad (3.7)$$

$$\text{Gregorian}: \quad 2c = \frac{2Pe^2}{1 - e^2} \qquad (3.8)$$

where P is given by:

$$\text{Cassegrain}: \quad P = \frac{2c(e^2 - 1)}{2e^2} \qquad (3.9)$$

$$\text{Gregorian}: \quad P = \frac{2c(1 - e^2)}{2e^2} \qquad (3.10)$$

The subreflector diameter D_{sub} can be found using:

$$D_{\text{sub}} = \frac{2e \cdot P \cdot \sin(\pi - \psi_0)}{1 - e \cdot \cos(\pi - \psi_0)} \qquad (3.11)$$
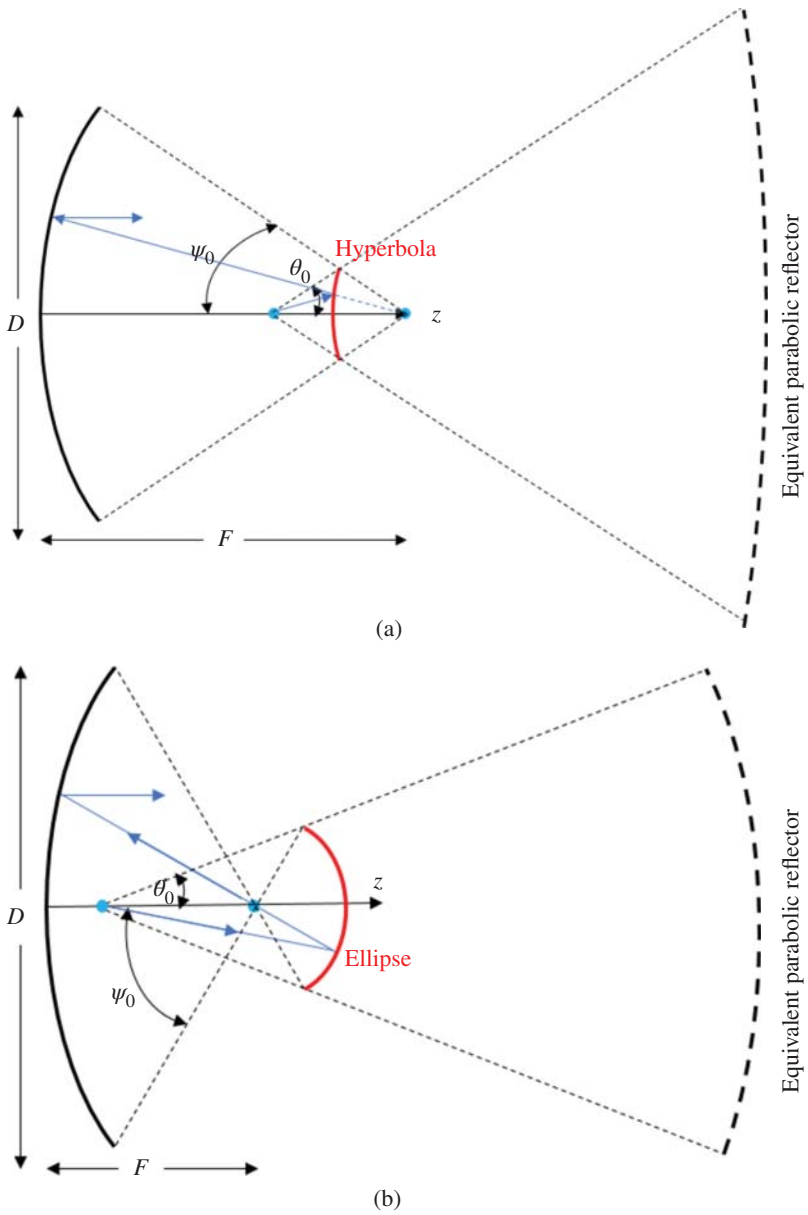
(a)

(b)

Figure 3.12   *(a) Cassegrain reflector antenna; (b) Gregorian reflector antenna.*

For the Cassegrain design, the hyperboloidal surface is defined by:

$$z = c - \frac{a}{b}\sqrt{b^2 + x^2 + y^2} \tag{3.12}$$

$$b = \sqrt{c^2 - a^2} \tag{3.13}$$

3.2.3   RainCube High-Gain Antenna

3.2.3.1   Antenna Choice: Cassegrain Reflector

While axially symmetrical reflector antennas such as Cassegrain reflectors, Gregorian reflectors, and splash plate configurations were identified as possible candidates for CubeSat deployable mesh reflector, the complexity of the mechanical deployment has led us to select a Casssegrain design. To understand, one need to consider the two main constraints set by the mechanical deployment:

1. The *F/D* ratio (where *F* is the focal length and *D* the reflector diameter) is determined by the need to minimize the rib curvature so that the ribs fit within the volume between the subreflector/horn deployment mechanism and the walls of the CubeSat. A minimum *F/D* ratio of 0.5 is determined for a 0.5 m reflector.
2. The height of the subreflector is directly influenced by the height of the stowed volume and the number of deployment mechanisms required to deploy the subreflector. To constrain the design to only one feed deployment mechanism, the subreflector needs to be at maximum 24 cm above the vertex (Figure 3.13).

Only a Cassegrainian design can accommodate the mechanical deployment mechanism constraints. For a 0.5 m reflector with a focal length of 0.25 m, a Gregorian and splash plate reflector cannot be used since the subreflector is forward of the focal point. This would place the subreflector at a distance greater than 24 cm above the vertex and would require two deployment mechanisms to deploy the subreflector. In contrast, Cassegrain reflector optics place the subreflector under the focal point, which places the subreflector within the required 24 cm space above the vertex (Figure 3.13).

3.2.3.2   Antenna Description

The Ka-band deployable mesh reflector antenna is a Cassegrain reflector which consists of four main elements: the feed, three struts, a hyperbolic subreflector, and a 0.5 m deployable parabolic mesh reflector. The focal length is set at the minimum required 0.5 *F/D* ratio (i.e. 0.25 m) to minimize the subreflector diameter to achieve the smallest blockage and lowest sidelobe performance [23]. The maximum possible directivity $D_{max} = 10 \cdot \log_{10}((\pi \cdot D/\lambda)^2)$ of the 0.5 m antenna is 45.45 dBi at 35.75 GHz.
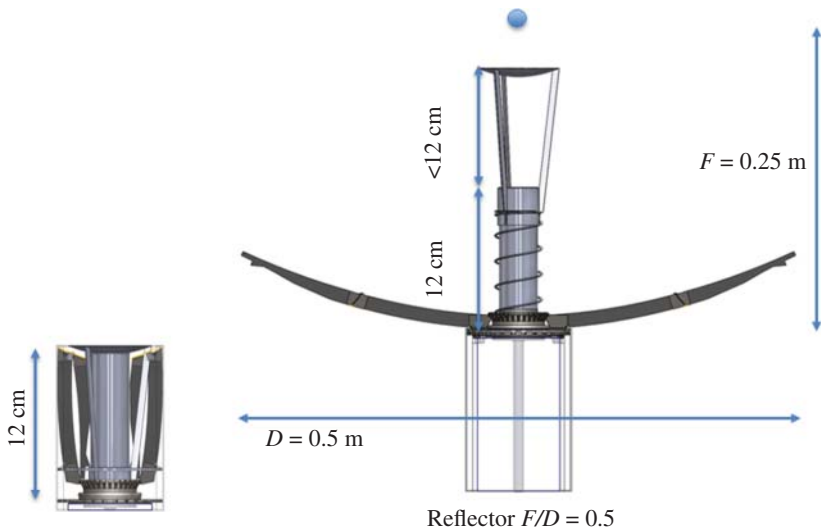
Figure 3.13   *Why a Cassegrain design? A Cassegrainian design limits the number of deployments by placing the subreflector closer to the vertex of the main reflector.*

3.2.3.3   *Perfect Paraboloid Antenna*

The antenna is first optimized with an ideal parabolic reflector surface with no ribs or surface distortion to assess and minimize taper and spillover losses, and subreflector blockage. The subreflector position and dimensions (Figure 3.14) were optimized to maximize the gain and minimize the sidelobe levels using a mode matching and body-of-revolution method of moment (BoR-MoM) based analysis. The simulation includes a model of the multiflare horn feed shown in Figure 3.15a and accounts for the subreflector blockage and multi-reflection between the subreflector, horn, and main reflector.

The multiflare horn provides good beam circularity, stable feed taper, and low cross-polarization [25]. It is also a convenient design for deployment as the horn is fed by a telescoping waveguide. When stowed, the telescoping waveguide fits inside the horn (Figure 3.15b). During deployment, the horn slides upward while the telescoping waveguide does not move (Figure 3.15b). A rectangular-to-circular waveguide transition, connected to the telescoping waveguide, is optimized to excite the feed with linear polarization. An illustration of the horn, telescoping waveguide, and transition is shown in Figure 3.15b. In order to minimize the taper and spillover losses, the feed horn is optimized to provide a minimum feed taper of -10 dB at $15.5°$ (Figure 3.16).

The rectangular-to-circular transition consists of a stepped matching section that is designed by numerical optimization. Its overall length is 3.65 mm. The horn performance is measured when connected to its telescoping waveguide and transition
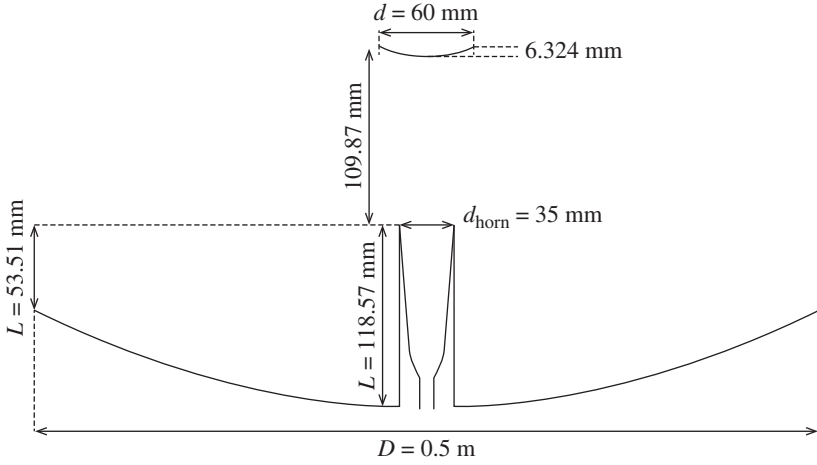
Figure 3.14 *Optimized Cassegrain reflector antenna design dimensions. Source: From Chahat et al. [24]. © 2016 IEEE.*
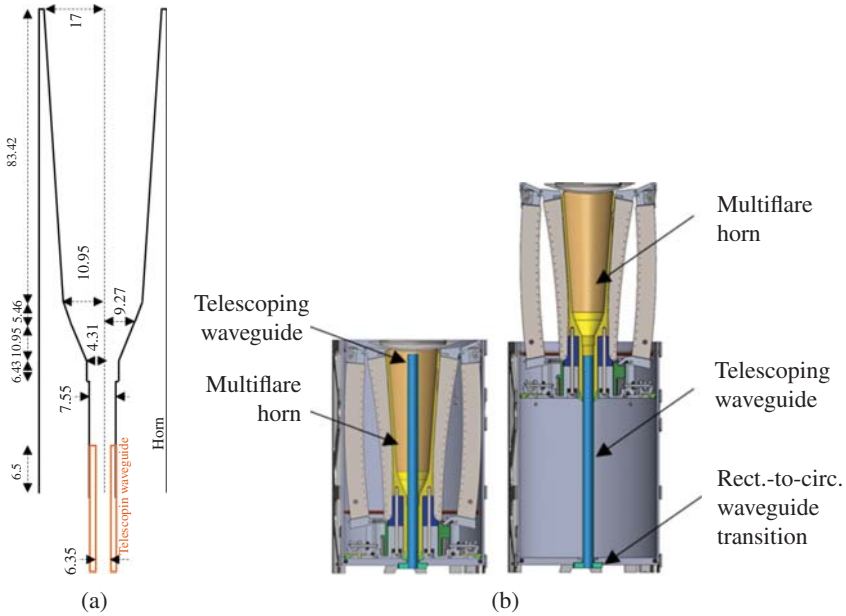

Figure 3.15 *(a) Multiflare horn antenna feed design (dimensions in mm); (b) multiflare horn, telescoping circular waveguide, and its rectangular-to-circular waveguide transition in stowed and deployed configuration.*
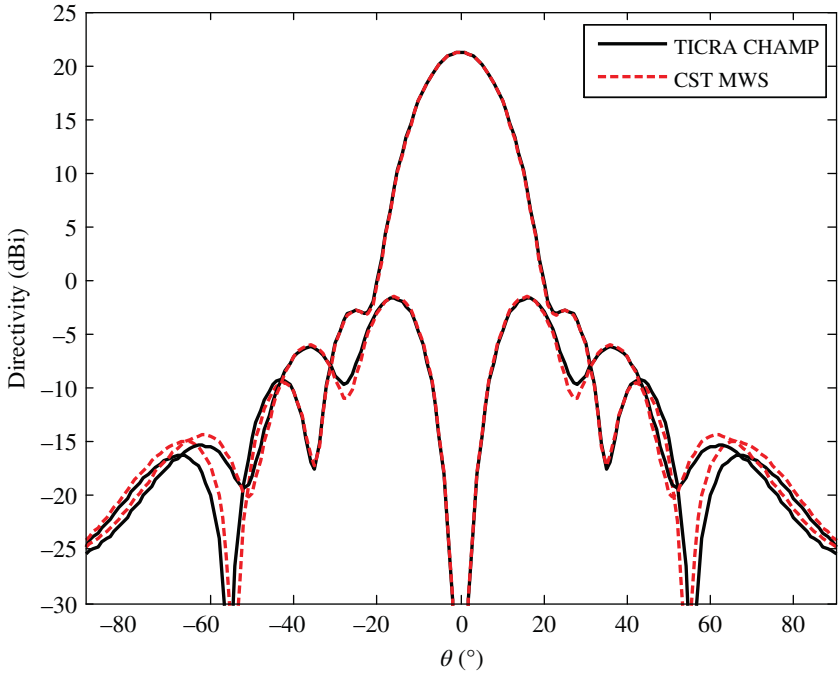
Figure 3.16 *Radiation pattern of the optimized multiflare horn feed providing a* $-11.5\,dB$ *taper at* $\psi_0 = 15.5°$ *at 35.75 GHz. The radiation pattern is provided for* $\varphi = 45°$.

as shown in Figure 3.17a. The measured and simulated reflection coefficients of the horn assembly are in excellent agreement as shown in Figure 3.17b and remains under $-30\,dB$ at 35.75 GHz.

For an ideal reflector, an overall efficiency $\eta = \eta_T \cdot \eta_S$ can ideally reach up to 81% (i.e. $-0.9\,dB$, where η_T and η_S are the taper efficiency and spillover efficiency, respectively) [23]. This efficiency number is driven by the antenna F/D and its feed edge taper. A Cassegrain design also suffers from subreflector blockage. The ratio d_{sub}/D should be minimized to increase the blockage efficiency. A study of the diffraction and blockage effects on the efficiency of a Cassegrain antenna was carried out in [26]. The optimum ratio d_{sub}/D is approximately given by Sudhakar Rao [26]:

$$\left(\frac{d_{sub}}{D}\right)_{opt} = \left[\frac{1}{16\pi^2}\frac{\lambda}{D}C^2\right]^{1/5} \tag{3.14}$$

where C is the mean amplitude taper at the subreflector edge. This equation allows to have a good starting point before thoroughly optimizing the subreflector size. The size of the subreflector d_{sub} was optimized to maximize the antenna gain and minimize the side lobe levels. The subreflector dimensions are as following:
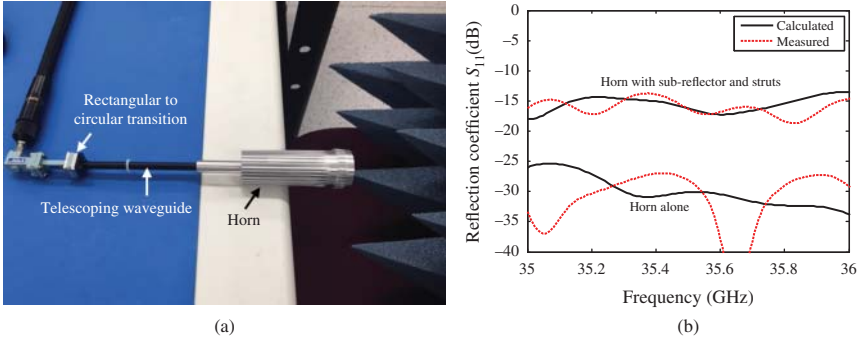
(a)   (b)

Figure 3.17 *(a) Reflection coefficient measurement set-up of the multiflare horn connected to its telescoping circular waveguide and its rectangular-to-circular waveguide transition (in deployed configuration); (b) reflection coefficient of the feed-horn alone (including the telescoping waveguide and transition) and with the struts and subreflector. Source: From Chahat et al. [24]. © 2016 IEEE.*

diameter d_{sub} of 60 mm, vertex distance of 80 mm, and foci distance of 130.2 mm. The subreflector to main reflector diameter ratio roughly equals to 0.12.

The spillover, taper, and blockage loss calculated at 35.75 GHz are summarized in Table 3.1. The taper and spillover losses are about 1.15 dB. The subreflector and spillover blockage equals to 0.33 dB. The blockage and diffraction loss ξ of the subreflector can be analytically calculated using [29]:

$$\xi = 20\log 10\left(1 - C_b\left(\frac{d_{sub}}{D}\right)^2 - C_d\sqrt{\frac{\lambda}{d_{sub}}}\sqrt{1 - \frac{d_{sub}}{D}}C\right) \qquad (3.15)$$

where:

$$C_b = \sqrt{\frac{G_f}{n_a}}\tan\left(\frac{\psi_0}{2}\right) \qquad (3.16)$$

and:

$$C_d = \frac{1}{2\pi}\frac{\sin(\psi_0)}{\sqrt{\sin(\theta_0)}}\sqrt{\frac{G_f}{n_a}} \qquad (3.17)$$

where G_f is the feed gain, n_a is the aperture efficiency of the Cassegrain when blockage and diffraction is neglected.

Using Equation (3.15), the blockage and diffraction loss is estimated to be 0.36 dB (Figure 3.18). This is in excellent agreement with the simulated result reported in Table 3.1 (i.e. 0.33 dB). Subtracting these losses from the 45.45 dBi area gain gives an optimized directivity of 43.97 dBi for the ideal Cassegrain reflector. The directivity calculated using TICRA GRASP (physical optics [PO]) is 43.97 dBi.
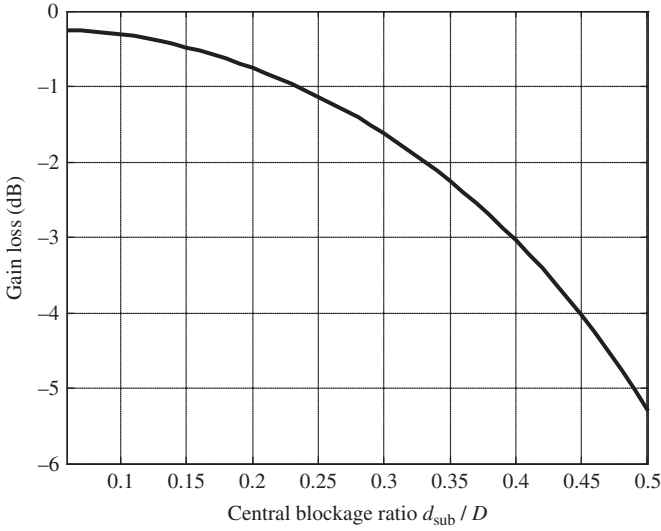
Figure 3.18 *Gain loss as a function of d_{sub}/D for an Edge Taper of -11.5 dB using Equation* (3.12). *Gain loss = 0.36 dB for $d_{sub}/D = 0.12$, $\psi_0 = 15.5°$, $\theta_0 = 59.6°$, and feed gain $G_f = 21.3$ dBi.*
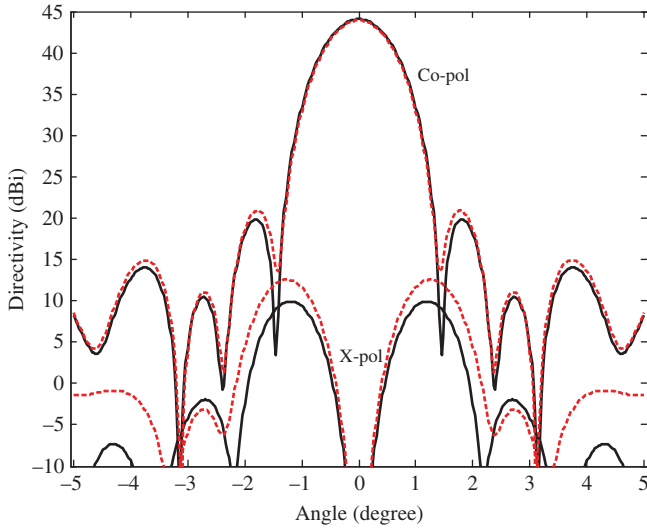

Figure 3.19 *Radiation pattern of the ideal parabolic reflector at 35.75 GHz using different simulations methods at $\varphi = 45°$. Solid line: TICRA GRASP. Dashed line: TICRA CHAMP. Source: From Chahat et al.* [24]. *© 2016 IEEE.*

Table 3.1   Gain table at 35.75 GHz after compensation (30 ribs).

	Gain (dBi)	Loss (dB)	Peak SLL (dB)
Ideal directivity	45.45	—	—
Spillover + Taper	44.3	1.15	23.1
Blockage	43.97	0.33	22.1
Surface ribs (30)	43.90	0.07	20.7
Struts	43.60	0.3	17.7
Surface mesh[a] (40-OPI)	43.35	0.25	17.4
Surface accuracy[b] (±0.22 mm)	42.88	0.47	16.8
Feed loss/telescoping waveguide/transition	42.76	0.12	—
Feed mismatch (RL = 15 dB)	42.62	0.14	—
Overall performance	42.62	2.83	16.8

[a]Based on calculated results using TICRA GRASP model of a 40-OPI mesh.
[b]Using Ruze's equation [27, 28]. The surface accuracy was adjusted with the measured number of ±0.22 mm.

The radiation patterns obtained using TICRA CHAMP (BoR-MoM) and TICRA GRASP (PO) are in excellent agreement (Figure 3.19). It is worthwhile to underline that the unfurlable model (i.e. including the mesh reflector) will be investigated essentially using TICRA GRASP since BoR-MoM method is applicable only with axially symmetric design.

3.2.3.4   Unfurlable Paraboloid with Ribs and Mesh Structures

The antenna gain and loss contributions are assessed thoroughly. They are summarized in Table 3.1 for the deployable antenna. The losses include taper, spillover, blockage from the subreflector, ribs, struts blockage and diffraction, surface mesh, surface accuracy, feed loss, and feed mismatch.

Ribs Effect   An unfurlable reflector surface consists of a discrete number of parabolic ribs that are connected by surfaces called gores as illustrated in Figure 3.20. Each gore is a section of a parabolic cylinder bounded between two adjacent parabolic ribs. The gore is formed by stretching a mesh between the two ribs. As a consequence, an unfurlable paraboloid deviates from a true paraboloid which results in ambiguity of optimal feed position. The number of ribs is a tradeoff between good RF performance, limited available stowage volume, and mitigation of the risk of deployment failure.

The optimal feed location for umbrella reflector surface was explored in [30, 31]. In [30], using physical optics (PO) with parallel ray approximation (POPRA) the best feed location can be found using:

$$\frac{F_{\text{ribs}}}{F} = \frac{N_{\text{g}}}{2\pi} \sin \frac{2\pi}{N_{\text{g}}} \tag{3.18}$$

where F_{ribs} is the optimum feed location for an unfurlable paraboloid with N_{g} gores.
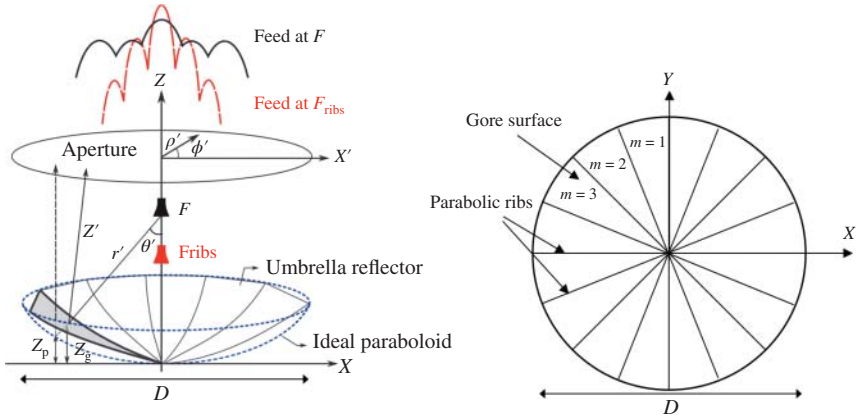
Figure 3.20   *Defocusing effect of gores. The focal point of the umbrella reflector and ideal paraboloid are different. Source: From author.*

We have implemented a method using PO to optimize the feed position of an unfurlable paraboloid reflector (Figure 3.21). The optimal position is obtained by optimizing four parameters: the gain loss, the beamwidth, and the side lobe levels for a focal fed unfurlable reflector for a given F/D and edge taper. We focused the study on our unfurlable reflector where $D = 0.5$ m, $F = 0.25$ m, and at frequency of 35.75 GHz. The radiation pattern for 30 and 25 gores is shown in Figure 3.23. It can be seen that Equation (3.18) is not optimal but it provides a good starting point. It is clear that our Ka-band reflector should use 30 ribs. Using 30 ribs, the gain loss is reduced to 0.24 dB as shown in Figure 3.22. The side lobe levels are also significantly improved as can be seen in Figure 3.23.

Although demonstrated on a focal-fed unfurlable reflector, this allows us to extract the optimal focal point of our reflector. On the dual reflector antenna, the subreflector should be redesigned to make sure one of its foci is placed at F_{ribs} and its second foci point should still be placed at the phase center of the feed horn. After re-optimization of the subreflector position and eccentricity, the loss caused by the 30 section rib-and-gore surfaces is only 0.07 dB. It is worthwhile to emphasize that without re-optimization, the loss is equal to 0.5 dB at 35.75 GHz (Figure 3.24). The equivalent gore surface root mean square (RMS) error calculated using Ruze's equation is about 0.23 mm [32]. The radiation pattern before and after re-optimizing the subreflector position is shown in Figure 3.24 where the improvement is clearly evident.

The reflection coefficient of the horn is shown in Figure 3.17b with the subreflector (after re-optimization of the subreflector position). Simulated and measured results are in good agreement. Although the effect of the struts is negligible (not shown here), the effect of the multiple reflections between the horn and the subreflector is rather significant. The ripples observed in the presence of the struts and subreflector is mainly due to the subreflector. Depending on the application, the reflection coefficient might need to be improved and different methodology could
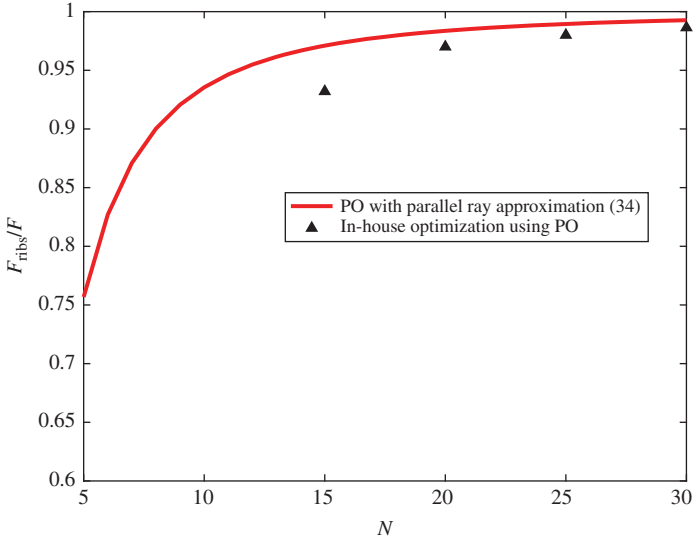
Figure 3.21   *Comparison of the optimal feed position for obtained using POPRA* [30] *and our in-house optimization method. Source: From author.*
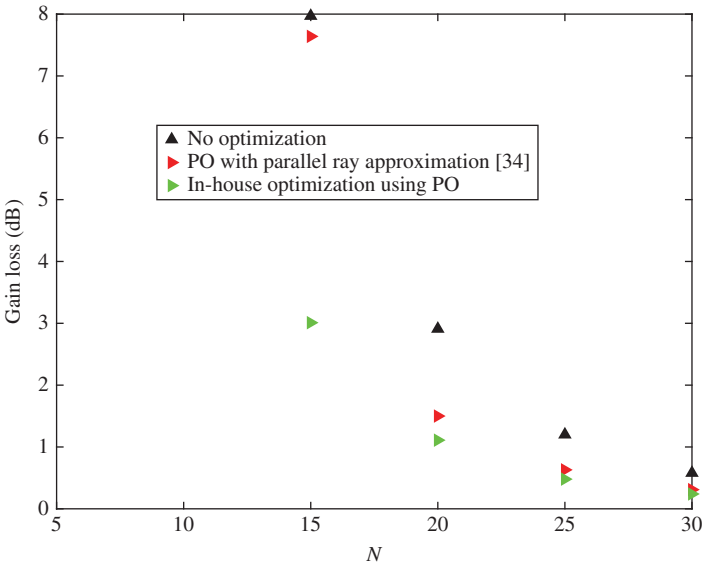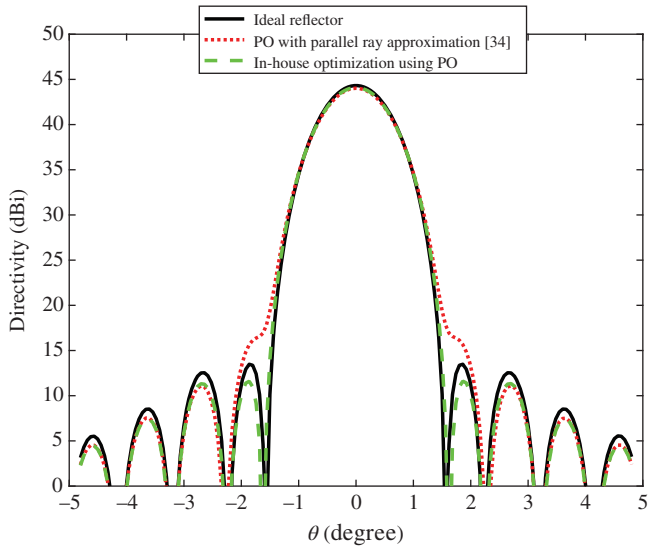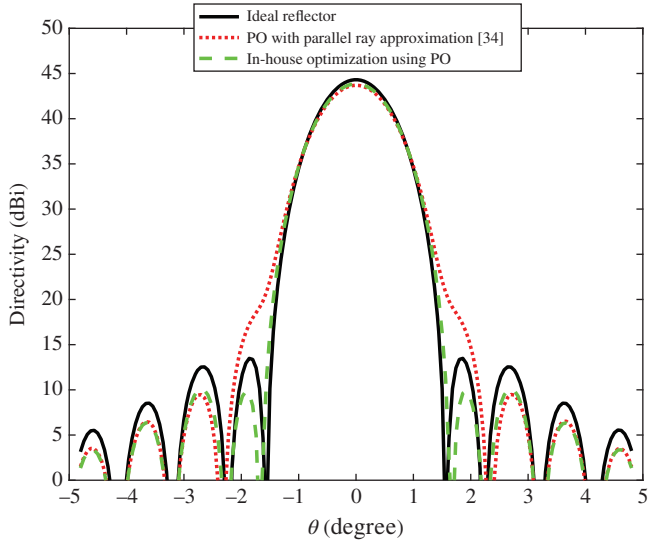

Figure 3.22   *Comparison of the gain loss improvement after optimizing the feed position. With 30 gores, the gain loss are respectively 0.58, 0.31, and 0.24 dB, without optimization, with POPRA* [30], *and with JPL's in-house optimization method. Source: From author.*

(a)

(b)

Figure 3.23   *Comparison of the radiation pattern after optimizing the feed position. Reflector parameters: D = 0.5 m, F/D = 0.5 m, and frequency = 35.75 GHz: (a) 30 gores; (b) 25 gores.*
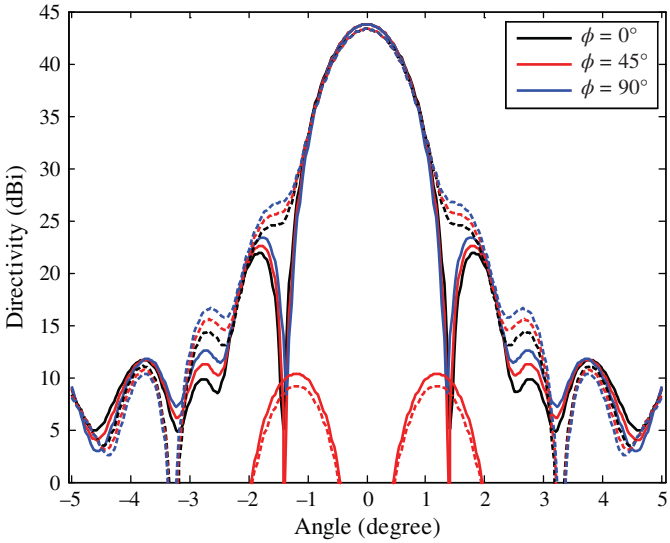
Figure 3.24 *De-focusing effect using 30 ribs. The subreflector is re-focused to compensate the ribs effect. Dash line: before correction. Solid line: after correction.* $Gain_{re-focused} = 43.9\,dBi$, $Gain_{de-focused} = 43.4\,dBi$.
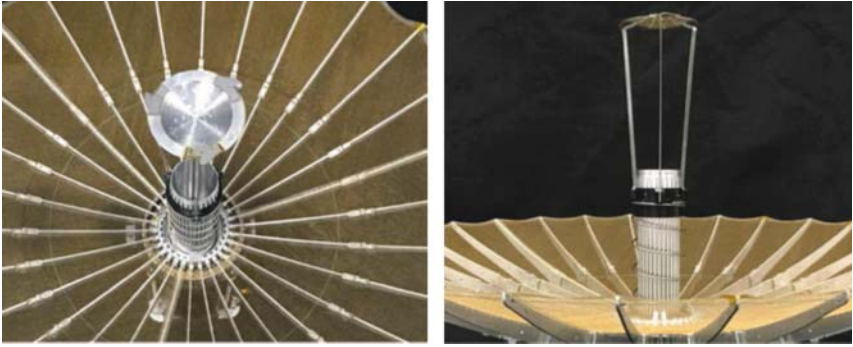

Figure 3.25 *Photograph of the feed horn with its three struts holding the subreflector.*

be employed (e.g. reshaping of the subreflector [33]). For RainCube, a return loss of 15 dB is acceptable.

Struts To maintain a good alignment of the subreflector, three stainless steel struts are employed (Figure 3.25). This affects the peak gain, the cross-polarization and the sidelobe levels. The three rectangular cross-section struts are 1.0 mm thick and 4.0 mm deep. The struts result in an overall increase in sidelobe level (∼3 dB),

reduce the peak gain (~0.3 dB at 35.75 GHz) and must be under 1.0 mm wide to avoid further losses. The three struts are aligned so that only one is very sensitive to the polarization, the two other struts are less sensitive. This is illustrated in Figure 3.26 where strut #1, collinear to the polarization, is contributing the most to the side lobe levels and cross polarization.

Mesh Opening Effects A common parameter to describe mesh surfaces is the number of openings per inch (OPI). To date, most large deployable antennas flown in space used 10-, 20-, and 30-OPI meshes. These meshes are available in densities suitable for use at frequencies up to Ka-band. Analytical and measured data on 10-, 20-, and 30-OPI meshes are reported in [32]. Reported results, shown in Figure 3.27, suggests that the 10-OPI mesh can be used up to C-band (4–8 GHz) as the reflectivity loss remains under 0.3 dB. In the other hand, the 20-OPI mesh can be used up to Ku-band (downlink: 11.7–12.7 GHz and uplink: 14–14.5 GHz). The reflectivity loss of 20-OPI mesh remains below 0.2 dB at Ku-band.

The proposed deployable antenna uses 40-OPI mesh knitted from 0.0008″ diameter gold plated Tungsten wire. The 40-OPI mesh provides excellent electrical performance but it is stiffer and more difficult to tension accurately with the deployment mechanism than a less dense mesh. The 40-OPI mesh is described in TICRA GRASP using a mesh grid which consists of two orthogonal sets of wires as illustrated in Figure 3.28. The spacing between the two wires is S_x and S_y in the x- and y-direction, respectively. The diameter of the wires is d_0. The wires are all in electrical contact. A mesh with unequal reflection coefficients for the x- and y-direction will be described with two different dimensions S_x and S_y. For simplification and also because our antenna is linearly polarized, we will assume $S_x = S_y$ for our analysis. For a circularly-polarized antenna, a mesh with unequal reflection coefficient in x- and y-direction will generate a cross-polar beam similar to the co-polar beam and with an amplitude given by $20 \cdot \log_{10}((R_y - R_x)/(R_y + R_x))$.

In practice, the tricot mesh is not rectangular as illustrated in Figure 3.29 which showcases a 10-OPI and 40-OPI mesh. The wire mesh is an adequate way of modeling the RF properties of the tricot mesh of unfurlable antennas. This can be done by defining an equivalent rectangular grid which, for any angle of incidence and polarization, gives the same reflected and transmitted field as the real mesh. To do so, we assessed the power reflection coefficient $R_{x,y}$, for the 40-OPI mesh in Figure 3.29b, for a normal incidence. The reflection coefficient $R_{x,y}$ was found to be $R_{x,y} = 0.9441$ at Ka-band.

The spacing $S_{x,y}$ of the equivalent rectangular grid can be found using [34]:

$$S_{x,y} = \frac{\lambda_0 \sqrt{\dfrac{1}{Rx} - 1}}{2 \ln \left(\dfrac{S_{x,y}}{\pi d_0} \right)} \tag{3.19}$$
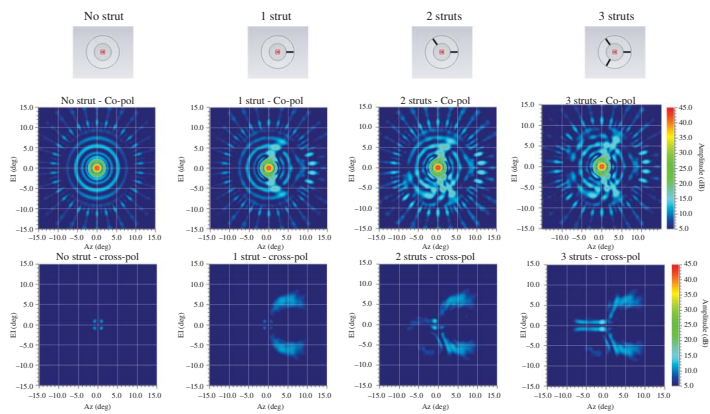
Figure 3.26 *Struts effect on the side lobe levels and cross-polarization.*
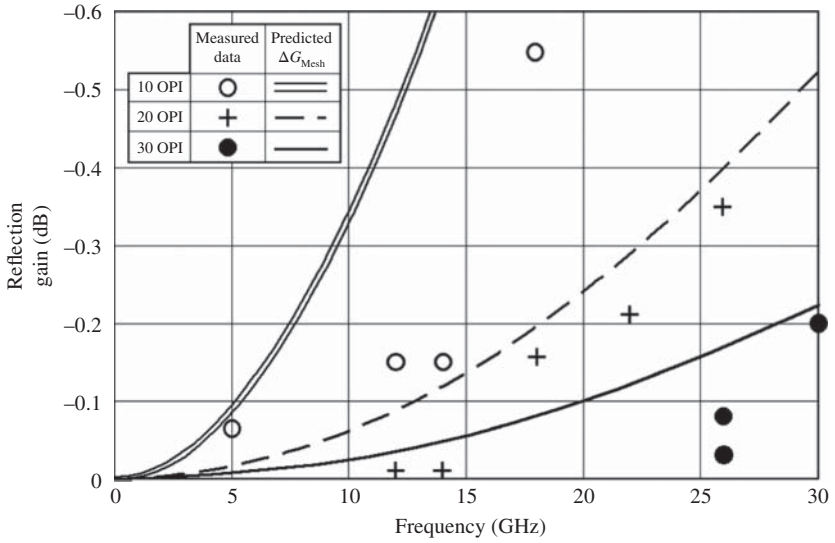
Figure 3.27   *Mesh reflectivity loss for different mesh type of meshes (10, 20, and 30 OPI) at frequencies up to 30 GHz. Source: From Thomson* [32]. *© 2002 AIAA.*
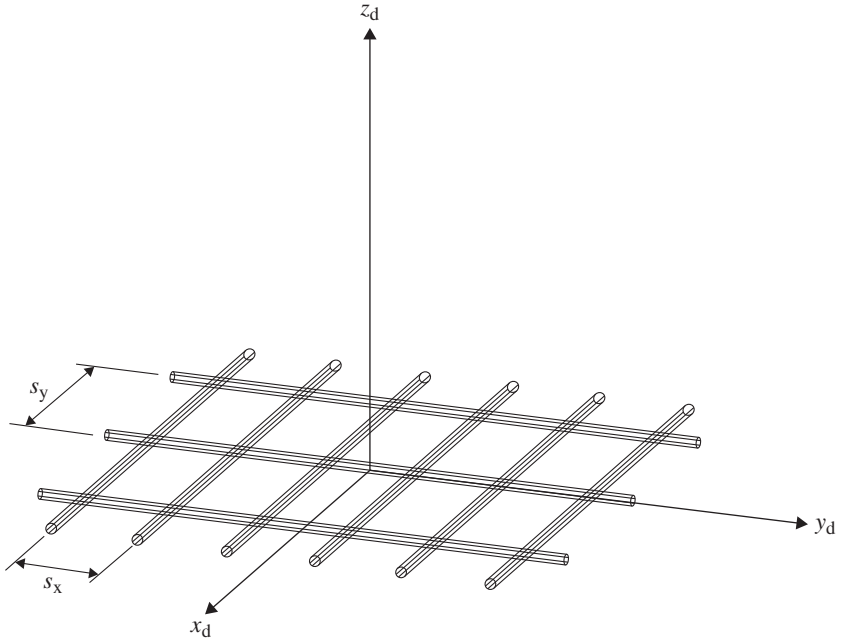

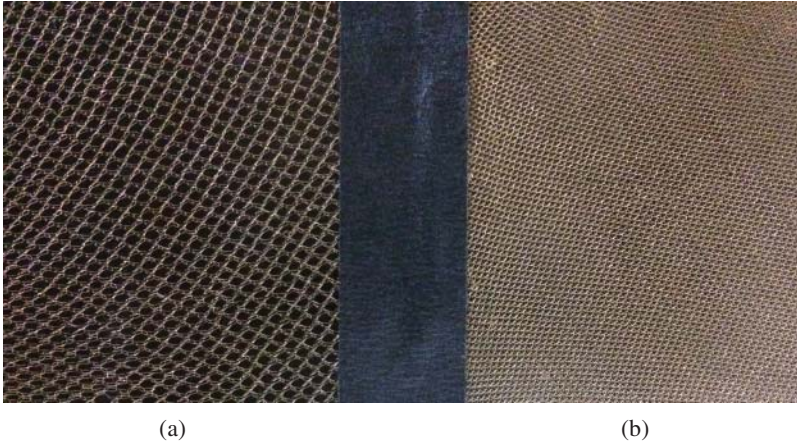**Figure 3.28**   *Mesh grid described using two orthogonal wires.*

(a)   (b)

Figure 3.29   *Photography of two mesh with different OPI: (a) 40-OPI mesh; (b) 10-OPI mesh.*

where $d_0 = 0.0008''$ and λ_0 is the free space wavelength. The separations S_x and S_y are $0.02'' = 0.508$ mm. The gain loss can be obtained using:

$$G_{\text{loss}} = 10 \log_{10}(1 - T^2) \tag{3.20}$$

with $R_x = 0.9441$, the expected gain loss is 0.25 dB. This is the output from TICRA GRASP which confirms the calculate spacing values. This sets the ideal parameters to describe the 40-OPI mesh. We will see later that the gain loss of 0.25 dB was confirmed experimentally.

Surface Accuracy   Ruze's equation predicts the gain loss of a reflector antenna as a function of its surface RMS error. It is given as [32]:

$$\text{Loss} = 10 \cdot \log_{10} e^{-\left(\frac{4\pi\varepsilon}{\lambda_0}\right)^2} \tag{3.21}$$

where ε is the surface RMS error of the reflector, λ_0 is the free space wavelength. As the frequency increases, the loss will also increase for a given surface RMS. Gain loss versus surface RMS is shown in Figure 3.30 for different frequency bands. It is clear that the surface accuracy achieved for this antenna could enable operation up to Ka-band (Table 3.2). For a surface RMS of 0.2 mm, Ruze's equation predicts 0.39 dB loss at 35.75 GHz [32]. At mm-wave, the surface RMS should be improved down to 0.1 mm. However, for a gain loss of 0.4 dB, a surface RMS of 0.9 and 3.2 mm are required at X- and S-band, respectively. While S- and X-bands are very forgivable, the challenge of designing a deployable mesh antenna is therefore very obvious at Ka-band and beyond.
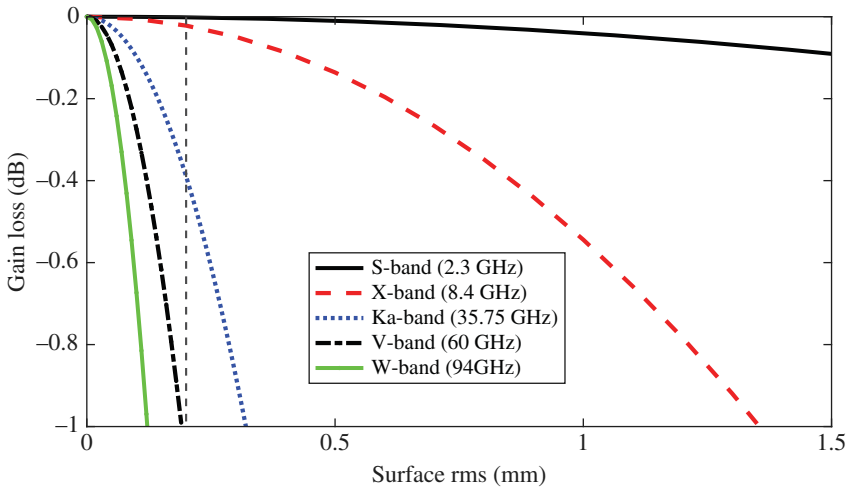
Figure 3.30 *Gain loss versus surface RMS for different frequency bands: S-band, X-band, Ka-band, V-band, and W-band.*

Table 3.2 *Gain loss for 0.2 mm surface RMS at S-, X-, Ka-, and W-bands.*

Frequency	S-band (2.3 GHz)	X-band (8.4 GHz)	Ka-band (35.75 GHz)	V-band (60 GHz)	W-band (94 GHz)
Gain loss (dB)	0	0.02	0.39	1.1	2.7

In order to maintain the required 0.2 mm RMS surface accuracy, the deployed rib positions are held in place by keeping all hinges pre-loaded against precision stops, ensuring the rib deploys consistently to the same position. Manufacturing errors during the machining process are eliminated by assembling the ribs on precision bonding fixtures, which greatly reduces inaccuracy caused by any component tolerance deviations.

3.2.3.5 Antenna Measurement Results

Two different prototypes were constructed, a solid non-deploying RF prototype, which was used to validate the RF design, and a mechanically deploying mesh prototype (Figure 3.31). The solid reflector, representing the gore-mesh reflector surface, and the deployable mesh reflector were tested in a planar near-field antenna measurement facility at NASA's JPL. A gain comparison between the mesh deployable antenna and the non-deploying RF prototype will allow us to precisely assess the losses due to the mesh opening and surface accuracy.

Figure 3.31 *Antenna prototypes in the near-field anechoic chamber of NASA's Jet Propulsion Laboratory: (a) solid non-deployable prototype; (b) mesh deployable prototype.*

Table 3.3 *Measurement results at 35.75 GHz.*

	Directivity (dBi)		Gain (dBi)		Loss (dB)[a]		Peak SLL (dB)	
	Calc.	Meas.	Calc.	Meas.	Calc.	Meas.	Calc.	Meas.
Solid	43.6	43.55	43.3	43.24	0.3	0.31	−17.45	−17.75
Mesh	–	43.28	42.61	42.48	–	0.8	−16.8	−18.33

[a]Loss = Directivity − Gain.

The radiation pattern was measured in elevation and azimuth planes at 35.75 GHz. The directivity, gain, loss, and peak side lobe level (SLL) are shown in Table 3.3 for the solid and mesh antenna prototype. The calculated and measured radiation patterns in *E*- and *H*-plane are shown in Figure 3.32a for the solid non-deploying reflector and they are all in good agreement. The beamwidth equals to 1.17° and 1.14° in *E*- and *H*-plane, respectively. The results for the deployable mesh reflector antenna are shown in Figure 3.32b. The measured and calculated results are in good agreement with prediction. The mesh does not have any significant impact on the cross-polarization level as it remains roughly identical.

After a successful deployment, the mesh was attached and measured to find an initial surface accuracy. The ribs were found to match the desired parabolic shape to within an error of 0.22 mm RMS resulting in 0.47 dB loss according Ruze's equation [32]. Hence, the numerical analysis has predicted loss of 0.7 dB for the surface RMS and the mesh opening. The loss resulting from the surface accuracy
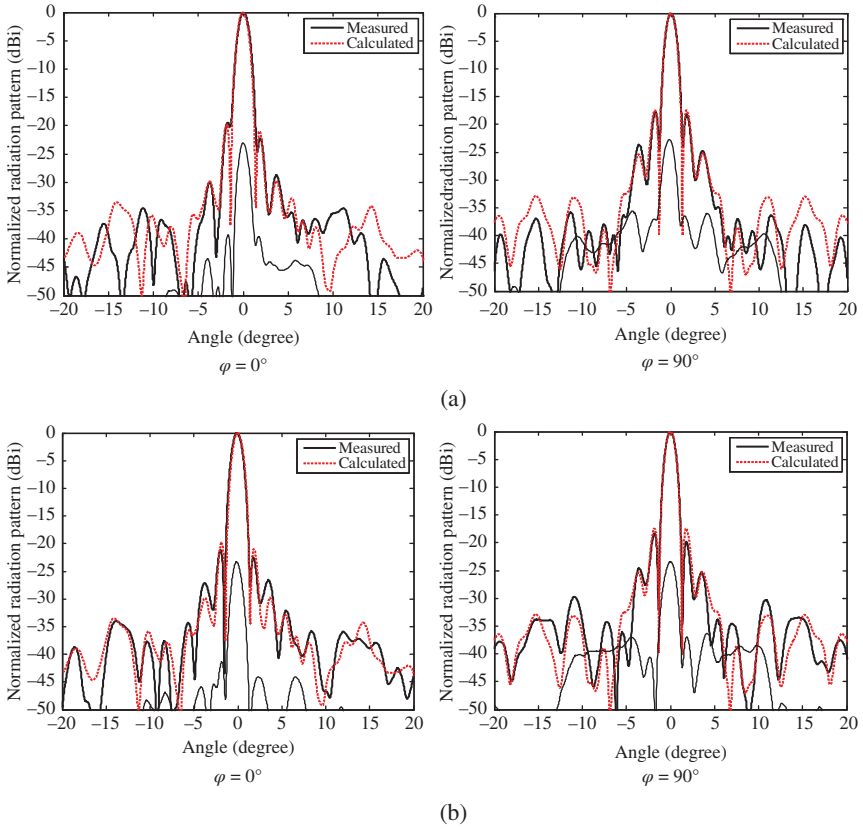
Figure 3.32 *Measured and calculated radiation pattern of (a) the gore-shaped solid non-deployable reflector antenna model and (b) the deployable mesh reflector antenna. Source: From Chahat et al. [24]. © 2016 IEEE.*

and mesh opening was assessed by comparing the solid reflector loss and the mesh reflector gain and equals to 0.76 dB.

The predicted and measured gain obtained for the mesh antenna equal to 42.59 and 42.48, respectively. The agreement is excellent and is within the measurement accuracy of the near-field range. The mesh loss δ_{mesh} can be easily retrieved by comparing the gain results of the solid reflector G_{solid} and the gain of mesh reflector G_{mesh} as the surface accuracy loss δ_{acc} was measured ($\delta_{mesh} = G_{solid} - G_{mesh} - \delta_{acc} = 43.24 - 42.48 - 0.47 = 0.29$ dB). This is in very good agreement with the calculated mesh loss using the equivalent rectangular grid model in TICRA GRASP.

Two deployments are performed and the antenna radiation pattern is measured after each deployment. Before each deployment, the antenna is carefully folded
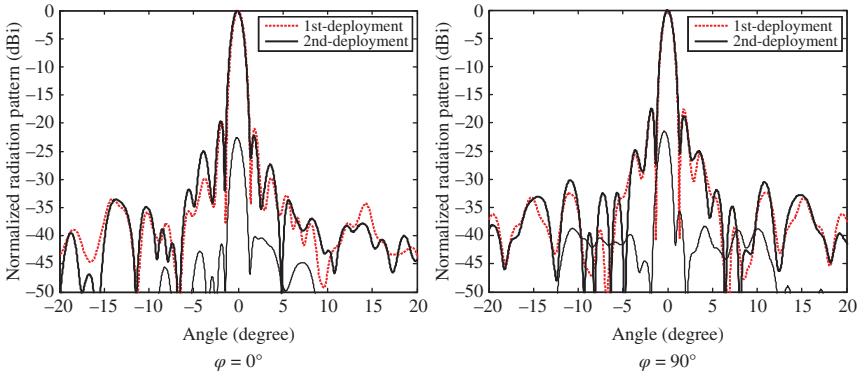
Figure 3.33   *Comparison of the radiation pattern after two deployments. Dashed line: 1st deployment. Solid line: 2nd deployment.*

back inside the canister. An experienced technician is manipulating the mesh and ribs during the folding process. This allows assessing the effect of the deployment on the RF performance as well as proving the repeatability of the mechanical design. The antenna gains measured before deployment and after the two deployments equal 42.5 and 42.7 dBi, respectively. The difference is within the near-field chamber measurement accuracy. This is in excellent agreement with the calculated/predicted gain of 42.6 dBi. The measured radiation patterns after each deployment is shown in Figure 3.33. The two results are in good agreement which demonstrates the repeatability of the deployment. The maximum side lobe level remains below −17.5 dB for each deployment. The mechanical deployment will be discussed in the next section.

3.2.4   Mechanical Deployment

The mechanical design of a deployable mesh antenna solves three key challenges. The first is a deployed antenna geometry, which balances RF performance and stowed size. The second is a method to deploy the antenna to a precise surface (with 0.20 mm RMS) which can still fold in a small volume. The third is applying significant deployment force to stretch the mesh, to remove any wrinkles from stowing, while avoiding impact loads during deployment.

Balancing RF performance and stowed size required many interactions between RF and mechanical design. Mechanical configurations that are easy to implement do not provide the required RF performance. On the other hand, optimal RF configurations did not stow in 1.5U volumetric goal. The main conflicting requirements occurred in determining the secondary reflector position and the number of ribs.

From a mechanical perspective, the height of the subreflector is influenced by the height of the stowed volume and the number of deployment steps required to deploy the subreflector. For instance, for a stowed height of 15 cm, if the subreflector is

less than 11 cm above the vertex of the parabola, no deployments are required (4 cm of height is consumed by the deployment mechanisms in the base of the antenna and curvature of the subreflector). If the subreflector is less than 22 cm above the vertex, only one deployment step is required. If less than 33 cm, two deployment steps are required. In order to reduce complexity and reduce risk, it was desired to have a maximum of one deployment step for the subreflector, which thereby limited its height above the vertex to 22 cm, as illustrated in Figure 3.8. In addition, the stowage-imposed constraint on rib curvature results in a minimum focal length requirement of 25 cm. If the radius of curvature becomes too small, the ribs will exceed the stowed volume when folded.

Another key limitation is the number of ribs that can be stowed in the volume. As the mesh is tensioned between the ribs, it becomes a flat surface between each of the ribs. Therefore, the greater the number of ribs, the closer the surface will be to a perfect parabola. For example, the extreme cases are only three ribs which creates a parabolic three-sided pyramid whereas an infinite number of ribs creates a perfectly parabolic surface. However, when stowed the antenna can only fit a finite number of ribs, and too many ribs increase mechanical complexity and cost. While up to 40 ribs could fit radially in the antenna stowed volume, there would be no clearance between each of the ribs increasing the probability of the ribs tangling with each other during deployment. In addition, RF losses due to a non-idealized parabolic shape were found to be minimal above 28 ribs, with only 0.6 dB in losses (before re-optimization). Therefore, the optimum number of ribs balancing clearance and RF performance was determined to be 30.

The next key challenge was to obtain the required surface accuracy from the deployed antenna with errors of less than 0.20 mm RMS from the designed surface profile. Achieving such a surface accuracy would keep RF losses due to mechanical imperfections to under 0.39 dB. The key to maintain a high surface accuracy, when deployed, is well-designed ribs and hinges. Tolerances on the ribs to ensure machined parabolic profile with an error of 0.13 mm or less. Hinges were designed with precision stops, which were located as far from the hinge pin as possible to improve accuracy of the deployed position. However, if stacking up the machining tolerances of both the ribs and hinges, the required 0.20 mm RMS tolerance could not be met. Therefore, an assembly process was developed to nearly eliminate error due to manufacturing tolerances. A precision bonding fixture was machined to have a high tolerance parabolic shape. Each of the five components that made up the ribs were bonded while in the fixture. This eliminated issues with tolerance stack up, and ensured all the ribs were uniform, as they were each bonded on the same fixture. After all the ribs were bonded, the next step was to attach the mesh. The mesh was stretched over a convex parabolic dish, and then the structural skeleton of the antenna, all 30 ribs, were placed on top of the mesh. The ribs were then stitched to the mesh, while the mesh was held in its tensioned state with over 2,000 stitches. This process allowed the mesh to assume the parabolic shape of the ribs.

The amount of force required to deploy the antenna is determined by the amount of force required to stretch the mesh such that it takes on the shape of the ribs. Inadequate deployment force would not pull out the wrinkles which occur when the mesh is stowed. The Ka-band 40 OPI mesh used in RainCube is much denser and requires greater force to tension it on deployment than the lighter mesh often used on S-band antennas. Each rib requires 12 N-cm of torque at its base to fully stretch the mesh. A standard approach to deploy such an antenna is to use strain energy stored in a spring. To provide adequate torque in each rib, a spring deploying the antenna requires 290 N of pre-load after the antenna is fully deployed. Of course, when stowed, the spring produces even greater force, resulting in the antenna being deployed with 860 N of force. This creates an undesirable impact when the antenna deployed. Therefore, an innovative deployment mechanism had to be invented.

The first solution concept designed was to use gas to deploy the antenna by pushing it upwards in the canister like a piston in an engine. The deployment sequence begins with a releasing launch lock (Figure 3.34a), which held the antenna in the stowed position against any residual pressure maintained in the system. Next, gas is metered into the canister slowly lifting the base of the antenna up and out of the CubeSat (Figure 3.34b). This was the key innovation enabling the antenna deployment. The gas is produced by a powder which sublimates when heated or a cool gas generator, like those developed by Cool Gas Generator Technologies [35]. As the base of the antenna nears the top of the canister, the root ribs interlock with a feature near the top of the canister, pulling them outwards (Figure 3.34c). Since the pressurized gas acts over a surface area, only 42.0 kPa of pressure is required to apply the 290 N force to fully deploy the ribs and tension the mesh. As the root ribs move outwards, a constant force spring located in the mid rib hinge deploys the tip ribs. Once the ribs fully deploy, the subreflector is released and a compression spring telescopes it along the horn (Figure 3.34d). By correctly defining machining tolerances, the sub-reflector deploys to within 0.2 mm on the z-axis and 0.1 mm on the x- and y-axis of its ideal position. As the subreflector is kept under pre-load by a spring, it repeatedly deploys to the same position. When the hub is elevated into its fully deployed location, latches lock the hub in place to ensure the antenna stays in the deployed position, even if the canister depressurizes (Figure 3.34d).

As can be observed in Figure 3.34, the gas-powered deployment system was built and tested. Gas was pumped into the canister using an air compressor. Unfortunately, near the end of deployment test, just before the tip ribs deploy, the antenna tilted by approximately 5° as the gas actuation mechanism does not provide any features to keep the antenna perpendicular to the canister. This tilt in the deployment prevented latching of the antenna. Therefore, when pressure was lost after deployment, the antenna did not keep its desired shape or precision. If this had occurred in orbit, it would have been a performance inhibiting failure. Further, detailed investigation into available cold gas generators and sublimating powders revealed, the gas would be released within 1/10th of a second, unlike the air compressor test where
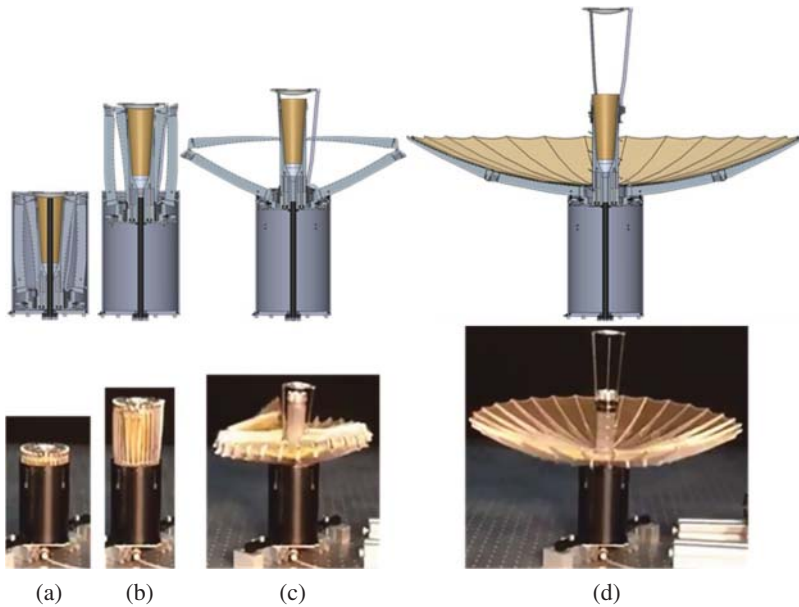
Figure 3.34 *Deployment sequence of the reflector antenna. The antenna is initially stowed in a 1.5U volume: (Top) computer-aided design (CAD) model of the antenna deployment; (Bottom) photos of the deployment sequence using a gas-powered deployment system.*

gas was pumped into the canister over the course of 1 minute. This would likely result in a large undesirable impact on the antenna, similar to a spring deployment. Therefore, a new deployment concept was needed.

While initial concepts for slowing the gas release with orifices and valves were considered, these were eliminated because of their complexity. Ultimately it was determined the best approach would be to use a motor and lead screw. As the motor would turn the lead screw, the base of the antenna would slowly be raise. While the lead screw option had come up in some of the initial mechanism brainstorming, the concept was eliminated as the best place to put a single lead screw was in the center of the antenna, but this volume was already consumed by the feed and waveguide.

The key innovation enabling the lead screw design was by placing four lead screws, one in each corner of the antenna cylinder (Figure 3.35). In order to keep the four lead screws in sync, a single motor was used with a unique planetary gear system, with a single sun gear keeping four planet gears (each attached to a lead screw) in sync with each other. The deployment as shown in Figure 3.34 occurs in the same fashion with the motorized lead screw deployment (Figure 3.36), except that the hub is now raised out of the canister with 290 N of force by the lead screws.
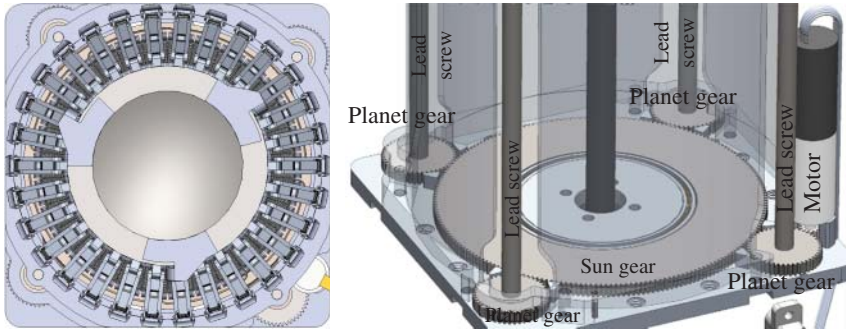
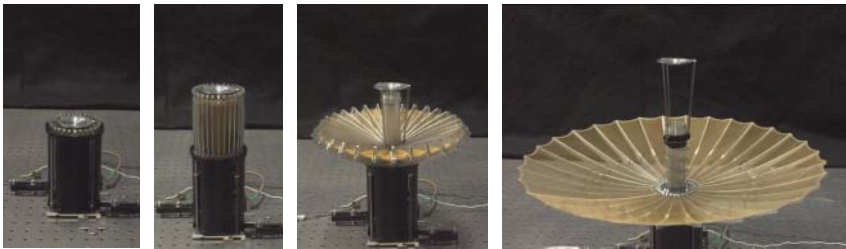**Figure 3.35** *A motorized lead screw deployment requires four synchronized lead screws.*

Figure 3.36 *Deployment sequence of the reflector antenna using a motor and lead screw. The antenna is initially stowed in a 1.6U volume. Photos of the deployment sequence of RainCube engineering model (EM). Reproduced with permission of IEEE.*

Lead screws offer a very high gear ratio, enabling a small motor to produce the large amount of required deployment force.

As this design was being implemented, one drawback was noticed. The stowed volume of the antenna increased from 1.5 to 1.6U, as the height increased to 16 cm. However, beyond a highly deterministic deployment, a number of additional advantages were observed on a motorized lead screw deployment over a gas deployment. First, the motorized deployment eliminated the need for a launch lock, as back driving the lead screws hold the antenna in place with hundreds of pounds of preload. Secondly, latches at the end of deployment were eliminated as once again, the lead screw holds the hub in place. Third, the motor now provides deployment feedback, as it can be determined how many rotations occurred to deploy the antenna. Fourth, there is no longer a canister of pressurized gas at the end of deployment, which if a leak were to occur it could negatively affect the attitude control of the spacecraft. Finally, deployment tests can now occur in air and at a much lower cost than a pressurized deployment, as each cold gas generator are fairly expensive, and three are required for each deployment test.
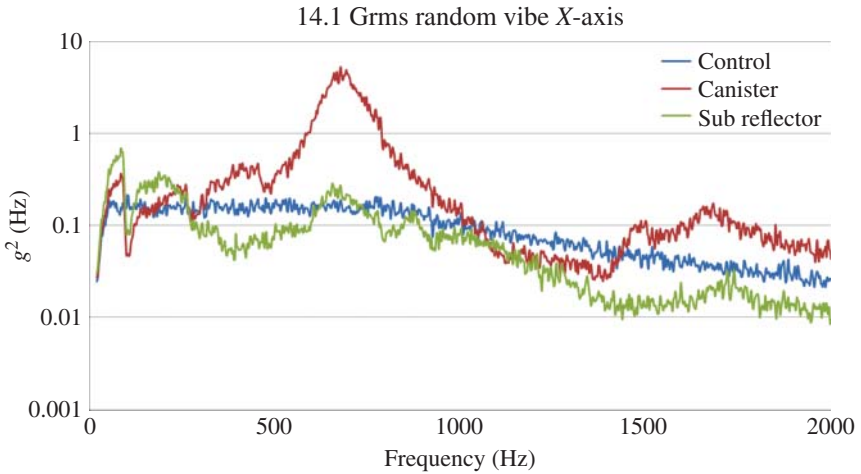
Figure 3.37   *Vibration testing of the antenna resulted in loads over 100 G's.*

3.2.5   Design and Testing for the Space Environment

After a final mechanical design was built and deployment test, the next step was to qualify the design by environmental testing. During launch, spacecraft hardware can be subjected to extreme G-loading and while on orbit, it is subject to large temperature variations as the spacecraft moves in and out of Earth's shadow in the vacuum of space. The spacecraft will be subjected to vibe and thermal swings prior to deployment, and thermal swing after deployment. To raise the technology readiness level (TRL) from 4 to 6, and provide confidence that the design will work on orbit, it is necessary to qualify the design through environmental testing. Environmental testing is generally done in the order that it will be experienced by the spacecraft, with vibration testing first, followed by thermal testing.

For the antenna, the most likely mechanism of failure would be due to failure of the structure in vibration, as extreme loads can occur. Therefore, prior to building the flight antenna, the prototype antenna went through vibrational testing. As it was initially unknown what launch RainCube would be occurring on, the vibration spectrum from the general environment validations spectrum (GEVS) was used, with a peak load of 14.1 G_{RMS}. This is a harsh spectrum meant to encompass the vibrational loads that could be seen in most launch vehicles. It is important to note while the value is given in RMS, which means peak vibrational loads at the shaker head can be as high as 42.3 G's. Further structural amplification, due to natural frequencies of the hardware can increase loading to over 100 G's. The antenna was mounted to a shaker, and the vibration response is as observed in Figure 3.37 as observed. As can be seen, peak accelerations of over 100 G's were experienced at the tip of the antenna (Figure 3.37).

After vibration, the engineering model antenna was deployed to ensure everything operated correctly. While the antenna did not exhibit any structural failures, the antenna did not fully deploy after vibration, as the tip ribs remain folded in place. This issue was that the constant force springs deploying the tip ribs provided too little torque margin. They did not have enough moment arm about the mid-hinge pin. The issue was not observed earlier. However during vibe the tip rib hinges settled into the lowest energy state possible, which resulted in to torque margin. To solve this issue, kick-off springs were added to several of the mid-rib hinges, to increase the moment arm of each constant force spring. The antenna then underwent additional vibration testing and then deployed. With the kick-off springs, adequate torque margin was achieve. To verify the deployed shape, radiation pattern were measured on the deployed antenna pre or post vibration. The results remains very constants (e.g. the antenna gain and directivity remained within 0.05 dB) and the radiation pattern almost overlaps. This demonstrates the repeatability of the mechanical deployment.

After successful vibration testing, the next step was to build the flight model of the RainCube antenna. The flight model was nearly exactly the same as the engineering model, with some very minor changes. One of the key changes was altering the geometry of the mid-rib hinge such that the constant force spring acted over a longer moment arm. This ensured the design achieved a greater torque margin.

The RainCube flight model was then first subjected to thermal testing prior to being integrated with the rest of the instrument. This was because the electromagnetic (EM) antenna had not undergone thermal testing, and thus it was desired to see if there were any issues with deployment in thermal vacuum. As two thermal test were to occur, one with the antenna alone, and one months later with the antenna integrated into the instrument, the RainCube had the advantage of performing a full deployment at both the hot and cold ends of the thermal spectrum. For the first test, a full deployment of the antenna occurred at hot temperature, and then a second motion of the antenna (where the antenna was driven in reverse for about $0.5''$ and then the antenna was commanded to deploy again) occurred at cold temperature (the reverse would be applied on the second test with the instrument). During the first test, it was discovered the circuit board on the motor controller would overheat a temperature of 65 °C. Therefore, the deployment temperature was dropped to 55 °C. While the circuit board had a maximum operating temperature of 85 °C, well under the tested environment temperature, operation of the circuit board without convective cooling caused it to overheat. As the spacecraft had plenty of margin on deployment temperature, it was determined the best approach was to reduce the range of deployment temperatures on the spacecraft, rather than redesign the motor controller chassis. After dropping the deployment temperature, the antenna deployed successfully. The thermal test profile is shown in Figure 3.38 for the antenna alone and the antenna integrated with the instrument. A photography of the antenna after thermal cycling is shown in.
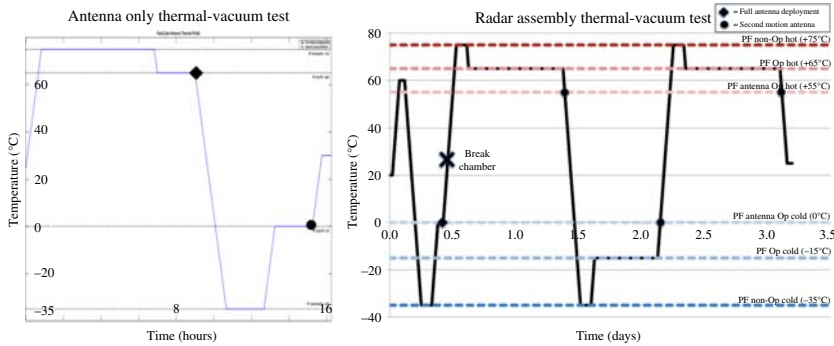
Figure 3.38 *Thermal test profile of the antenna alone (a) and then of the antenna integrated with the instrument (b) enabled testing of the antenna at both hot and cold.*

Figure 3.39 *Image of deployment in thermal vacuum at 0°C (cold finger and heat exchanger tube in foreground).*

After thermal testing, the antenna was then integrated with the rest of the instrument. The antenna would then be vibe-tested and deployed while attached to the instrument, as this simulates a more flight-like mounting condition. The vibration spectrum for the spacecraft was much lower than what the antenna was previously tested to, as RainCube was being launched as soft cargo to the International Space Station, which means the spacecraft is essentially launched in a cocoon of bubble wrap. This results in a 2 G_{RMS} vibrational load (with peak G's at the shaker head of 6 G's). As such a low level vibe would be insignificant, it was decided to perform and standard workmanship vibe at 6.8 G_{RMS}. This was still a low level vibration test which avoided damage to the hardware, but also provided greater qualification of the design.

After vibe testing, the antenna was immediately place in thermal vacuum, where it was deployed at cold (Figure 3.39). While a hot deployment is the condition where electrical systems are most likely to fail, a cold deployment tests the case where mechanisms are most likely to seize up or fail. This is due to both coefficient of thermal expansion changes in the antenna and that the grease used in the bearings and motor becomes thicker, and more resistant to motion. The antenna showed no anomalies during vibe. It then was successfully deployed in thermal vacuum at 0 °C. After deploying, a second motion of the antenna was performed at 55 °C, where the
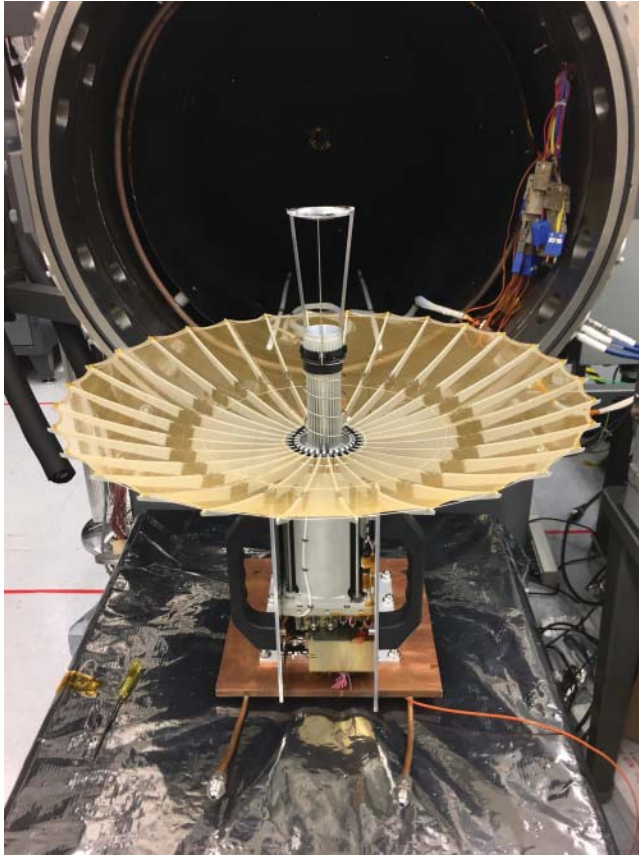
Figure 3.40   *Antenna after thermal vacuum testing at both hot and cold. The thermal vacuum chamber can be seen in the background.*

antenna was reversed and then driven through the highest torque portion of deployment, to ensure the antenna still operated at hot. The deployment in thermal vacuum after vibration fully flight qualifies this antenna (Figure 3.40).

In conclusion, the mechanical design has overcome its challenges. It has balanced RF performance with stowed size through careful collaboration between mechanical and RF engineers, which produced a Cassegrain secondary reflector and a 30 bi-folding rib design. Precise surface accuracy was achieved through accurate machining, precision hinge stops, and use of fixtures for assembly. Finally, adequate deployment force with a low impact was achieved by implementing a motorized lead screw design. Although the detailed descriptions of these mechanical developments have been discussed in [36], the key deployment processes were highlighted here for completeness.

3.2.6   In-Flight Performance

The Raincube CubeSat was released on July 13, 2018 from a NanoRacks deployer outside the International Space Station. The antenna was successfully deployed in LEO on July 28, 2018. The deployment of the antenna was witnessed by Tyvac's camera (star tracker). Screenshots of the video are shown in Figure 3.41. The image of the deployed antenna was overlapped with the image of the antenna deployed in our lab to verify the proper deployment of the ribs, subreflector, and horn. The antenna and the radar are operating nominally and collect critical science data. Unfortunately, unlike telecommunication antennas, it is extremely difficult to characterize accurately the antenna gain in orbit.

3.3   Telecommunication Challenge

The bus used for RainCube is developed by Tyvak and it features both a UHF and an S-Band telecommunication system to relay data to the ground (Figure 3.42).

The UHF telecommunication system was chosen for its high reliability and proven flight heritage. UHF telecommunication systems have now been used successfully on many CubeSat missions in LEO, and the Tyvak UHF radio has already been used for previous missions. The UHF antenna is composed by two rolled tape antennas folded on one of the 30×10 side. The end bobbins are used to facilitate the stowing of the tape and the deployment trigger is a burn wire which will be activated approximately 45 minutes after the release of the spacecraft from its canister. The UHF antenna provides an approximately omni-directional pattern with 0 dBi gain, which allows the spacecraft to be potentially always in contact with the ground station during any contact without the need for rotating or pointing the spacecraft. For this reason, the UHF telecommunication is to downlink health and safety telemetry data and to issue commands to the spacecraft. The data rate is 19.2 Kbps in both direction, which is achieved with plenty of margin even at worst case. The ground stations used to support the UHF links are located in Irvine (California) and in Tromso (Norway). Simulations show that the spacecraft will be in visibility only with the ground station in Irvine (Figure 3.43) for an average of seven contacts per day of approximately 6.5 minutes duration. Although the RainCube spacecraft will not need all these contacts at UHF every day, the availability of multiple passes ensures the possibility of promptly commanding the spacecraft if emergency arises. Despite its reliability and high flight heritage, one of the fundamental limitations of the UHF telecommunication system is the low data rate which is insufficient to relay the payload data.

The S-Band telecommunication system is used for high data rate downlink only to enable the highest possible data return for the RainCube radar. The system is composed of the S-Band Quasonic radio and of an S-Band patch antenna placed on the 10×30 side as shown in Figure 3.42. Both radio and antenna have extensive flight heritage on previous CubeSat missions. The ground stations that will
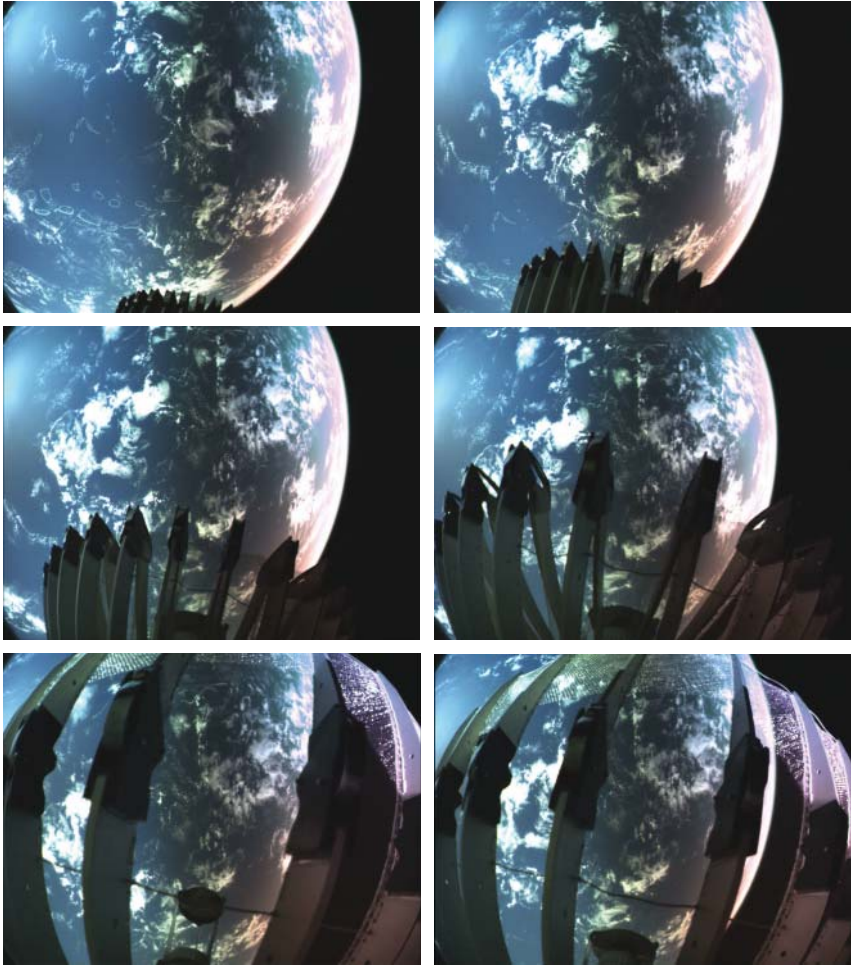
Figure 3.41   *RainCube antenna deployment in low Earth orbit.*

be used to receive the S-Band signal are part of the K-Sat network and they are located in different part of the world. Given the RainCube orbit, the K-Sat stations currently pre-selected for the missions are located in: Mauritius, Dubai, Hartebeesthoek, and Singapore. Given that the link analysis predictions show an expected data rate of approximately 4 Mbps, only two passes per day are needed to relay the currently predicted data volume. However, a third pass per day is planned for contingency purposes. The coverage analysis (Figure 3.44) shows an average of four possible contacts per day, which is sufficient to guarantee the three passes planned coverage.
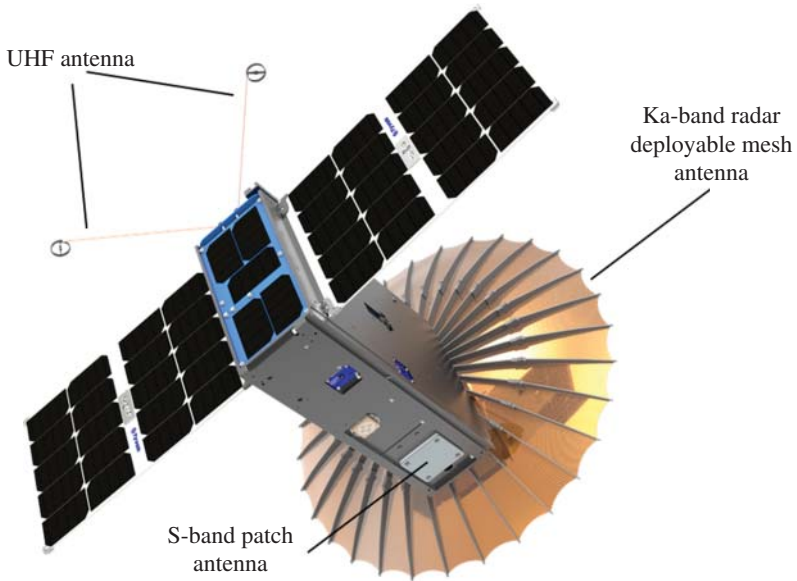
Figure 3.42   *CAD model of the RainCube spacecraft. All antennas are indicated. The UHF and S-band antennas are employed for telecommunication. The deployable mesh reflector is used for the radar.*
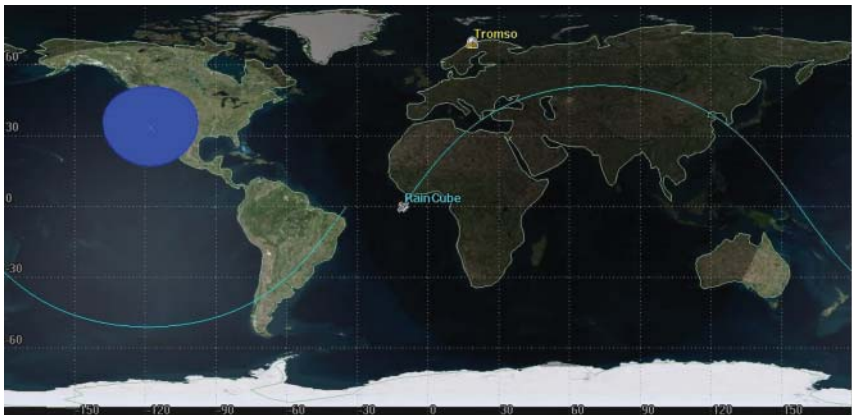
Figure 3.43   *UHF coverage map for RainCube. The two stations considered are located in Irvine (California), and Tromso (Norway). Given the inclination of the Rain-Cube orbit, the Irvine station will be the only one used for the UHF links. The circled area around the Irvine station shows all the possible tracks of the RainCube satellite across the 6 months of mission operation.*
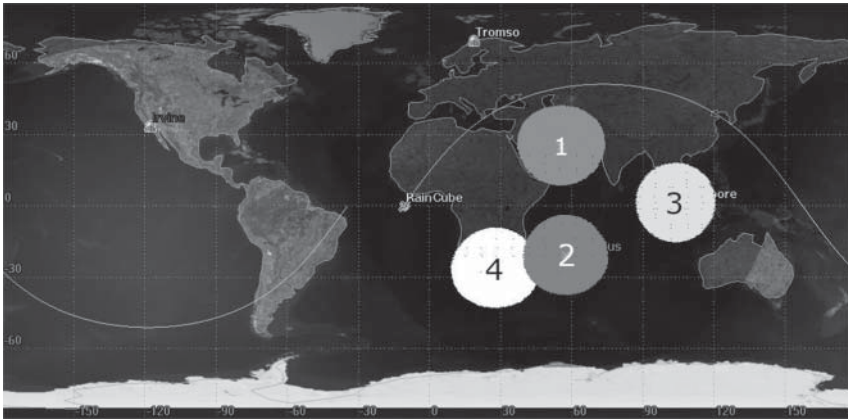
Figure 3.44   *S-Band coverage map for RainCube. The four K-Sat stations considered are located in Dubai, Mauritius, Singapore, and Hartebeesthoek. Given the inclination of the RainCube orbit, all the four stations will be able to track the satellite. The circular areas around each station (1 for Dubai, 2 for Mauritius, 3 for Singapore, and 4 for Hartebeesthoek) show all the possible tracks of the RainCube satellite across the 6 months of mission operation.*

The patch antenna on the CubeSat suffers inevitably from some shadowing due to the Ka-band parabolic antenna (placed on the bottom of the spacecraft) and to the solar panels (deployed from the top of the spacecraft). As a result, the only way to establish link with our ground stations is to rotate the spacecraft before the telecom pass, to allow visibility between the patch and the ground station.

The rotation angle required to point the CubeSat patch antenna is 70° from the zenith orientation. Attitude control system analysis shows that the actuators on the spacecraft will rotate the CubeSat back and forth from its zenith position in approximately 10 seconds. The duration of each pass is approximately 8 minutes. Hence, at the worst-case scenario of three passes per day, the spacecraft will be rotated and hence unable to perform radar measurements for approximately 25 minutes per day (1.7% of the time). This solution satisfies the key requirement on the duty cycle of the radar instrument, which must operate for at least 90% of the time. Hence, this solution was considered acceptable for the project.

3.4   Conclusion

CubeSats are strong candidates for Earth Science mission and the need for a high-gain antenna is crucial. This chapter provides a detailed description of a novel, highly constrained deployable mesh reflector antenna which is believed to pave the way for the future development of this technology. The proposed antenna provides a novel solution to the increasing need of Earth Science and Deep Space

missions aiming to launch small and low cost satellites. It also enables the mission RainCube, the first radar in a CubeSat.

The 0.5 m Ka-band high gain mesh reflector antenna employs Cassegrainian optics to accommodate a deployment mechanism that stows the reflector and feed assembly into a highly constrained 1.5U ($10 \times 10 \times 15$ cm^3) volume. It uses only one deployment step for the feed and subreflector.

The antenna demonstrates excellent performance at 35.75 GHz. A gain of 42.6 dBi and an efficiency of 52% were measured. All the critical aspects of the design (i.e. mesh effects, struts and blockage effects, feed mismatch and interactions, etc.) have been thoroughly addressed. Two RF prototype antennas, namely solid and mesh deployable have been developed and detailed measurements demonstrated excellent agreements with the simulation results. Two measurements were performed and the antenna radiation pattern was measured after each deployment. The antenna performance remains very stable which demonstrates that the surface accuracy is maintained.

Another 0.5 m Ka-band mesh reflector antenna was developed for Telecommunication operating at the deep space network (DSN) frequency bands [37]. This antenna version is right-handed circularly polarized and operates at both Tx and Rx DSN band.

Extensive research effort is on-going to achieve larger deployable antennas using mesh reflectors (Chapter 5) or reflectarrays (Chapter 4). The science community also expressed needs for higher frequency deployable concepts (e.g. 94 GHz and higher) which opens up a new challenge where the deployment accuracy is stringent and can hardly be fulfilled with mesh reflectors.

Acknowledgments

comments from Dr. Eva Peral (RainCube Principal Investigator) and Dr. Simone Tanelli (RainCube Project Scientist) in understanding RainCube's science goal and refining the antenna requirements. The authors would like to acknowledge the support of Dr. Diane Evans, former director for the Earth Science and Technology Directorate, at the Jet Propulsion Laboratory for her constant support in the early phase of the antenna development.

References

1. E. Peral, S. Tanelli, Z. S. Haddad, G. L. Stephens, and E. Im, "RaInCube: a proposed constellation of precipitation profiling Radars In Cubesat," *AGU Fall Meeting*, San Francisco, CA, Dec. 2014.

2. A. Babuscia, B. Corbin, M. Knapp, R. Jensen-Clem, M. Van de Loo, and S. Seager, "Inflatable antenna for cubesats: motivation for development and antenna design," *Acta Astronautica*, vol. **91**, pp. 322–332, Oct.–Nov. 2013, ISSN 0094-5765.

3. R. Hodges, D. Hoppe, M. Radway, and N. Chahat, "Novel deployable reflectarray antennas for CubeSat communications," *IEEE MTT-S International Microwave Symposium (IMS)*, Phoenix, AZ, May 2015.

4. M. R. Aherne, J. T. Barrett, L. Hoag, E. Teegarden, and R. Ramadas, "Aeneas – Colony I meets three-axis pointing," *5th Annual AIAA/USU Conference on Small Satellites*, Logan, Utah, Aug. 7–12, 2011.

5. N. Chahat, J. Sauder, R. Hodges, M. Thomson, and Y. Rahmat-Samii, "CubeSat deployable Ka-band reflector antenna for deep space missions," *APS/URSI 2015*, Vancouver, Canada, July 2015.

6. C. S. MacGillivray, "Miniature deployable high gain antenna for CubeSats," *2011 CubeSat Developers Workshop*, California Polytechnic State University, San Luis Obispo, CA, Apr. 22, 2011.

7. R. Freeland, S. Bard, G. Veal, G. Bilyeu, C. Cassapakis, T. Campbell, and M. C. Bailey, "Inflatable antenna technology with preliminary shuttle experiment results and potential applications," *18th Annual Meeting and Symposium*, Antenna Measurement Techniques Association, Seattle, WA, Sep. 30–Oct. 3, 1996.

8. J. Huang and J. A. Encinar, *Reflectarray Antennas*, Hoboken, NJ: *Wiley-IEEE Press*, Oct. 2007. ISBN: 978-0-470-08491-5.

9. R. Hodges and M. Zawadzki, "Ka-band reflectarray for interferometric SAR altimeter," *Joint IEEE/URSI International Symposium on Antennas and Propagation*, Chicago, IL, July 8–14, 2012.

10. C. Han, J. Huang, and K. Chang, "A high efficiency offset-fed X/Ka dual-band reflectarray using thin membranes," *IEEE Transactions on Antennas and Propagation*, vol. **53**, no. 9, pp. 2792–2798, Sep. 2005.

11. R. E. Hodges, N. Chahat, D. J. Hoppe, and J. D. Vacchione, "A deployable high-gain antenna bound for Mars: developing a new folded-panel reflectarray for the first CubeSat mission to Mars," *IEEE Antennas and Propagation Magazine*, vol. **59**, no. 2, pp. 39–49, Apr. 2016.

12. C. Granet, "Designing classical offset Cassegrain or Gregorian dual-reflector antennas from combinations of prescribed geometric parameters," *IEEE Antennas and Propagation Magazine*, vol. **44**, no. 3, pp. 114–123, June 2002.

13. S. F. Bassily and M. W. Thomson, "Chapter 8: Deployable reflectors," in *Handbook of Reflector Antennas and Feed Systems Volume III: Applications of Reflectors*, S. Rao, L. Shafai, and S. K. Sharma, Eds., Norwood, MA: *Artech House*, 2013. ISBN: 10: 160807515X.

14. M. Johnson, "The Galileo high gain antenna deployment anomaly," *JPL Technical Report*, May 1994.

15. P. Focardi, P. Brown, and Y. Rahmat-Samii, "A 6-m mesh reflector antenna for SMAP: modeling the RF performance of a challenging Earth-orbiting instrument," *IEEE International Symposium on Antennas Propagation (APSURSI)*, July 3–8, 2011, pp. 2987–2990.

16. E. Hanayama, S. Kuroda, T. Takano, H. Kobayashi, and N. Kawaguchi, "Characteristics of the large deployable antenna on HALCA Satellite in orbit," *IEEE Transactions on Antennas and Propagation*, vol. **52**, no. 7, pp. 1777–1782, July 2004.

17. C. Bryan and W. Strasburger, *Lunar Module Structures Handout IM-5*," *NASA Training Material in Support of IM-5 Structures Course*, Houston, TX: MSC, May 1969.

18. A. G. Roederer and Y. Rahmat-Samii, "Unfurlable satellite antennas: a review," *Annales Des Télécommunications*, vol. **44**, no. 9–10, pp. 475–488, Sep./Oct. 1989.

19. G. Tibert, "Deployable tensegrity structures for space applications," *TRI–MEK Technical Report* 2002:04, ISSN 0348–467X, *Royal Institute of Technology Department of Mechanics*, Doctoral Thesis, Stockholm, 2002.

20. W. D. Williams, M. Collins, R. Hodges, R. S. Orr, O. Sands, L. Schuchman, and H. Vyas, "High-capacity communications from martian distances - chapter 5," *NASA Tech Report*, NASA/TM-2007-214415, NASA Glenn Research Center, Cleveland, OH, Mar. 2007.

21. W. Reynolds, T. Murphey, and J. Banik, "Highly compact wrapped-gore deployable reflector," *52nd AIAA/ASME/ASCE/AHS/ASC Structures, Structural Dynamics and Materials Conference*, Denver, Colorado, 4–7 April 2011.

22. V. Shirvante, S. Johnson, K. Cason, K. Patankar, and N. Fitz-Coy, "Configuration of 3U CubeSat structures for gain improvement of S-band antennas," *AIAA/USU Conference on Small Satellites*, Logan, Utah, Aug. 2012.

23. Y. Rahmat-Samii, "Chapter 15: Reflector antennas," in *Antenna Handbook: Theory, Applications, and Design*, Y. T. Lo and S. W. Lee, Eds., Boston, MA: Springer, 1998. ISBN: 978-1-4615-6459-1.

24. N. Chahat, R. E. Hodges, J. Sauder, M. Thomson, E. Peral, and Y. Rahmat-Samii, "CubeSat deployable Ka-band mesh reflector antenna development for Earth Science missions," *IEEE Transactions on Antennas and Propagation*, vol. **64**, no. 6, pp. 2083–2093, June 2016.

25. N. Chahat, T. J. Reck, C. Jung-Kubiak, T. Nguyen, R. Sauleau, and G. Chattopadhyay, "1.9-THz multiflare angle horn optimization for space instruments," *IEEE Transactions on Terahertz Science and Technology*, vol. **5**, no. 6, pp. 914–921, Nov. 2015.

26. K. Sudhakar Rao and P. S. Kildal, "A study of the diffraction and blockage effects on the efficiency of the Cassegrain antenna," *Canadian Electrical Engineering Journal*, vol. **9**, no. 1, pp. 10–15, Jan. 1984.

27. Y. Rahmat-Samii, "An efficient computational method for characterizing the effects of random surface errors on the average power pattern of reflectors," *IEEE Transactions on Antennas and Propagation*, vol. **31**, pp. 92–98, Jan. 1983.

28. J. Ruze, "Antenna tolerance theory—a review," *Proceedings of the IEEE*, vol. **54**, no. 4, pp. 633–640, Apr. 1966.

29. P. S. Kildal, "Diffraction efficiencies of reflector antennas," *Antennas and Propagation Society International Symposium, 1982*, Albuquerque, NM, 1982, pp. 48–51.

30. P. Ingerson and W. C. Wong, "The analysis of deployable umbrella parabolic reflectors," *IEEE Transactions on Antennas and Propagation*, vol. **20**, no. 4, pp. 409–414, July 1972.

31. F. L. Hai, "The principle error and optimal feed point of umbrella-like parabolic reflector," *International Symposium Antennas, Propagtoin, & EM Theory*, Beijing, China, Aug. 2000, pp. 697–700.

32. M. W. Thomson, "AstroMesh deployable reflectors for Ku- and Ka-band commercial satellites," *29th AIAA International Communications Satellite Systems Conference and Exhibit*, AIAA, May 2002.

33. R. Corkish, "The use of conical tips to improve the impedance matching of cassegrain subreflectors," *Microwave and Optical Technology Letters*, vol. **3**, no. 9, pp. 310–313, Sep. 1990.

34. M. I. Astrakhan, "Reflection and screening properties of plane wire grids," *Radio Engineering (Moscow)*, vol. **23**, pp. 76–83, 1968.

35. "Cool gas generator technologies," Available: online: http://cgg-technologies.com/, [Accessed: Oct. 17, 2014].

36. J. Sauder, N. Chahat, M. Thomson, R. Hodges, E. Peral, and Y. Rahmat-Samii, "Ultra-compact Ka-band parabolic deployable antenna for RADAR and interplanetary CubeSats," *29th Annual AIAA/USU Conference on Small Satellites*, Logan, UT, Aug. 2015.

37. N. Chahat, R. E. Hodges, J. Sauder, M. Thomson, and Y. Rahmat-Samii, "The deep-space network telecommunication CubeSat antenna: using the deployable Ka-band mesh reflector antenna," *IEEE Antennas and Propagation Magazine*, vol. **59**, no. 2, pp. 31–38, Apr. 2017.

4

One Meter Reflectarray Antenna: OMERA

Nacer Chahat[1], Manan Arya[1], Jonathan Sauder[1], Ellen Thiel[1], Min Zhou[2] and Tom Cwik[1]

[1]*NASA Jet Propulsion Laboratory/California Institute of Technology, Pasadena, CA, USA*
[2]*TICRA, Copenhagen, Denmark*

4.1 Introduction

With the recent advances in miniaturized RADAR and CubeSat technologies, launching multiple copies of a RADAR instrument is now possible. The RainCube mission, developed at NASA's Jet Propulsion Laboratory (JPL), launched and demonstrated successfully the first active radar in a 6U CubeSat [1]. The enabling technology, the 0.5 m deployable mesh reflector antenna [2], deployed successfully on-orbit to collect precipitation measurement data from space.

A constellation of precipitation-profiling instruments in Low Earth Orbit (LEO) would provide spatial-temporal resolution necessary to observe the evolution of weather phenomena at the appropriate spatial and temporal scale, but the cost and timeframe of typical satellite platforms and instruments make this solution impossible. This can now be accomplished using 6U or 12U CubeSats. The potential RainCube follow-on mission will send a constellation of CubeSats to enable constellation mission and revolutionize climate science and weather forecast. The small volume and mass of CubeSats allows frequent and low-cost access to space through

ride-along launches with other larger manifested spacecraft, as well as single purpose launches where the cost is distributed among many small spacecraft.

An outstanding need associated with small spacecraft is a radio frequency (RF) aperture that is commensurate with the scale of the overall space system. For Earth-observing systems, solid optical apertures that fit into small satellites without deployment are in regular use meeting a range of requirements. Additional research continues for larger deployed optical apertures [2–5]. RF apertures that will produce high gain for telecommunication applications, or are needed to produce narrow beamwidths for Earth science needs, are currently under development. For apertures that will be larger than the bus dimensions and hence are deployed, both the deployed precision for the frequency of operation, as well as stowed volume during launch, are driving parameters. There is an additional system efficiency that must be considered, since growing the aperture too large results in pointing, thermal, and other issues that make the small spacecraft impractical from cost and spacecraft system accommodation standpoints.

One approach for an RF deployed aperture is a reflectarray antenna where the panels are held against the side of the spacecraft bus during launch and deployed in a hinged system on-orbit. The flat, two-dimensional reflectarray antenna geometry negates the additional volume needed for deployed parabolic or other conic three-dimensional surfaces of the traditional aperture antenna. The reflectarray panels can be fabricated to meet on-orbit thermal demands and launch dynamic requirements, providing the necessary deployed precision when coupled with appropriate hinges connecting the panels. A release mechanism allows the panels to deploy on orbit. A first application of this approach integrated solar panels with the reflectarray antenna (ISARA, Integrated Solar Array and Reflectarray Antenna) operating at Ka-band, combining the two functions and resulting in small additional mass and volume increase over the solar panels themselves [5]. This flight system has been built and tested on the ground and was launched and validated on orbit. This work was extended to an X-band telecommunication system using a reflectarray deployed from a 6U CubeSat jointly launched with the NASA InSIGHT Mars lander mission and provided auxiliary telecommunications during the entry descent and landing portion of that mission [4]. Mars Cube One (MarCO) X-band reflectarray provided real-time relay of telemetry from InSight during landing, avoiding hours of delay of the signal that confirmed that the spacecraft had landed successfully. The success of MarCO bodes well for future planetary small satellites of increasing sophistication and for future use of deployable reflectarray antennas in such missions.

The current work presented in this chapter extends the size of the reflectarray to what is considered practical for a 6U CubeSat space system, stacking panels on three faces of the spacecraft bus (i.e. $\pm x$ faces and $+z$ face) and employing a unique telescoping feed from the center of the bus [6]. This feed follows and extends work in the Raincube parabolic mesh antenna system to feed the reflectarray [2, 3]. The stowed feed and system of panels removes about 2U of volume within the spacecraft bus, allowing 4U of volume for bus systems and instruments. An accommodation study has shown that the Raincube instrument will fit in a 6U CubeSat with the proposed antenna. The antenna is shown in folded and deployed state in Figure 4.1.
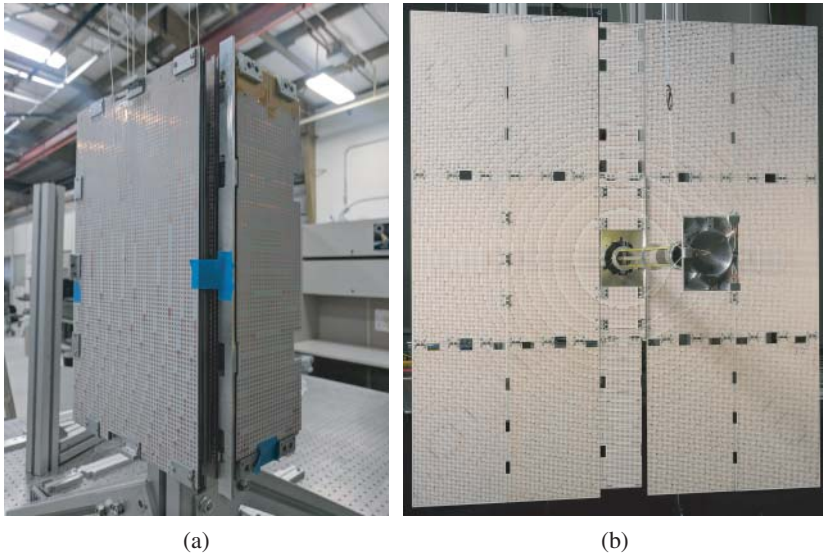
(a)   *(b)*

Figure 4.1 *One-meter deployable reflectarray antenna compatible with 6U-class CubeSats. (a) Folded. (b) Deployed.*

4.2 Reflectarray Antennas

4.2.1 Introductions to Reflectarray

A reflectarray is an antenna consisting of either a flat or curved reflecting surface and a feed ideally located at its focal point. The reflecting surface can use various radiating elements (e.g. square patches, rectangle patches, dipoles, open ended waveguides, etc.). This surface is illuminated by a feed – either directly or using a subreflector – with the reflectarray elements designed to reradiate and scatter the incident field with the desired electrical phases to form a planar phase front in the far-field. They are sometimes called "flat reflectors" because just like parabolic reflectors, it forms a planar phase front when the feed is placed at its focal point.

4.2.2 Advantages of Reflectarray

Reflectarrays can achieve good efficiency (i.e. >50%) for a very large aperture because as opposed to patch array, they do not require power divider. The efficiency of a reflectarray is driven by multiple factors: element design (type and dielectric properties), the focal-length-to-diameter (*f/D*) ratio, edge taper, feed loss, etc. Another advantage of reflectarray is that they can have its main beam designed to tilt at an angle from its broadside direction. In addition, when a spacecraft antenna requires a deployment mechanism, the flat structure of reflectarray enables to fold more efficiently, reliably, and simply. The ability of reflectarray to fold in a very constrained volume is very attractive for small satellite platforms.

Solar arrays can also be combined with solar arrays on the non-reflective side of the array [7]. Reflectarrays can cover multiple frequencies [8, 9] and they can potentially entirely be made of metal [10–12].

4.2.3   Drawbacks of Reflectarray

The key drawback of reflectarrays, generally, is the narrow bandwidth (i.e. <10%) that it is driven by its aperture size, focal length, element design, etc. The bandwidth of the reflectarray is limited by the bandwidth of the element itself and the differential spatial phase delay. Two well-known methods can be implemented to improve the bandwith: (1) increase the *f/D* and (2) use a concavely curved reflectarray with piecewise flat surfaces instead of a completely flat surface. While increasing the *f/D* is not always trivial in a deployable antenna, using a concavely curved reflectarray could easily be implemented in specific cases like ISARA or MarCO. The bandwidth can be also improved by creating elements with a broader bandwidth. Also, though the antenna operation is limited to the center frequency of the element, multi-frequency elements can be used to create multi-bandwidth antenna systems.

4.2.4   State of the Art

Extensive work on deployable reflectarray was initiated by Dr. John Huang at JPL in the 1990s. His book entitled "Reflectarray Antennas" [8] is still a reference and his work was avant-garde at the time. He proposed different concept of deployable membrane reflectarray antennas [8, 9] (Figure 4.2). He also introduced the concept of deployable reflectarray with integrated solar arrays in [7] which was then implemented on the ISARA.

To the best of our knowledge, the first reflectarray ever flown in space is the three-panel deployable reflectarray operating at 26 GHz and integrated in a 3U-class CubeSat: ISARA (see Figure 4.3). ISARA was launched in December 2017 and was successful deployed and tested in space as witnessed by the photography taken in LEO (Figure 4.3). ISARA is a 33 cm × 27 cm antenna demonstrating a gain of 33 dBic and an efficiency of roughly 26% at 26 GHz. While the efficiency of this antenna can appear to be very low, solutions exist to improve its efficiency. First, reducing the large gaps between the panels would improve the gain, efficiency, and side lobe levels. Another solution to improve its efficiency would be using a more efficient feed, such as a 2x2 linearly-polarized metal-only slot array, combined with the use of a reflectarray which converts an incident linearly-polarized wave into a reflective circularly-polarized wave.

The MarCO spacecraft (see Chapter 2) employs a 33.5 cm × 58.7 cm deployable reflectarray. Despite stowing in a stringent volume of 12.5 cm × 21 cm × 34.5 cm, this transmit-only antenna achieves a gain of 29 dBic at X-band. New hinges were specifically designed by JPL to reduce the gaps between panels. This improves the overall antenna performance. As a result, the aperture efficiency achieved by MarCO

(a)   (b)
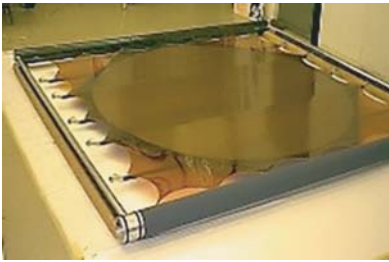
(c)   (d)

Figure 4.2   *(a) 1 m X-band pressure stabilized reflectarray* [9]. *(b) 3 m Ka-band pressure stabilized reflectarray* [9]. *(c) 3 m Ka-band inflatable reflectarray* [8]. *(d) 3 m dual-frequency membrane antenna* [8]. *Courtesy of NASA's JPL/California Institute of Technology.*

is about 42%. A picture of the antenna is shown in the lab during integration and testing at JPL and is also shown successfully deployed in space (Figure 4.4).

In addition, the Surface Water Ocean Topography (SWOT) mission is employing two deployable $5 \, \text{m} \times 0.5 \, \text{m}$ reflectarray antennas operating for his radar interferometer operating at 35.75 GHz. This spacecraft is currently under development and is scheduled for launch in 2021. The large deployable antenna is shown in Figure 4.5.

4.3   OMERA

4.3.1   Antenna Description

In order to achieve a wider bandwidth and higher efficiency, a large f/D ratio is generally needed for reflectarrays. A large f/D implies that the focal feed has to project

(a)   (b)
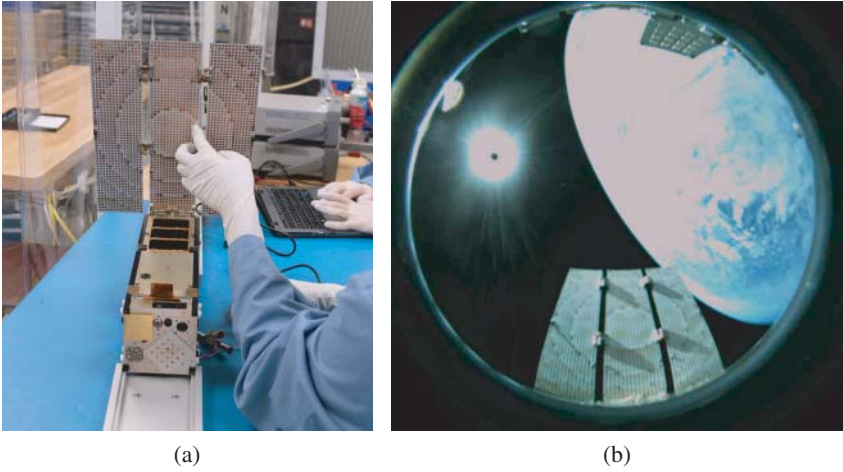
Figure 4.3   *(a) ISARA 3U CubeSat with its three-panel reflectarray antenna fully deployed during integration and testing. (b) Photography of the ISARA antenna taken in Low Earth Orbit becoming the first reflectarray ever flown in space. Courtesy of NASA's JPL/California Institute of Technology.*

(a)   (b)
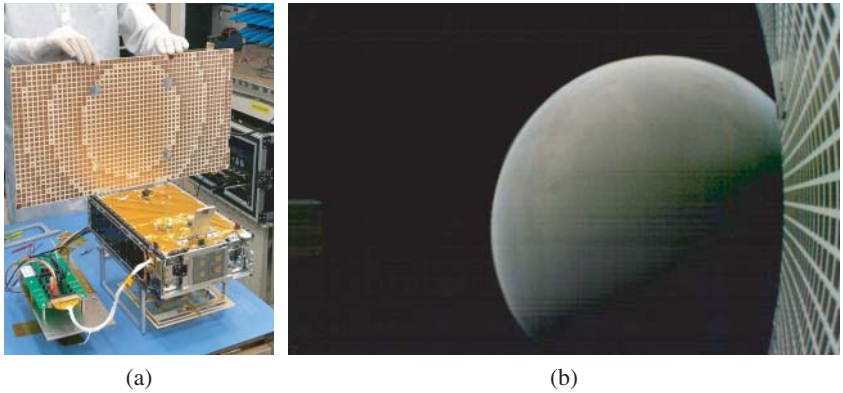
Figure 4.4   *(a) MarCO reflectarray antenna deployed during integration and testing. (b) MarCO reflectarray deployed in space on its way to Mars. Courtesy of NASA's JPL/California Institute of Technology.*

far from the array aperture, which results in a complex deployment and larger mass. The proposed Cassegrain configuration, shown in Figure 4.1, will reduce the feed and subreflector height while maintaining the same or a higher effective *f/D* ratio.

In addition, the transmission loss between the feed and the transceiver is significantly reduced, which is especially important at higher frequencies, such as

Figure 4.5 *Radiation pattern measurement of SWOT's engineering model reflectarray antenna. Courtesy of NASA's JPL/California Institute of Technology.*

Table 4.1 *Reflectarray requirements.*

Frequency	35.75 GHz
Number of elements	271×238
Unit cell	3.86×3.86 mm^2
Reflectarray dimensions	922.5×1049.2 mm^2
Substrate thickness	0.406 mm
Relative permittivity (ε_r)	3.55
Loss tangent ($\tan\delta$)	0.0027
Focal distance (F)	0.7 m
Subreflector vertex distance	0.095 m
Subreflector foci distance	0.22 m
Subreflector dimensions	95.0×124.0 mm^2

Ka-band. To mitigate these loss, coaxial cables are obviously not an efficient option. Hence, three telescoping waveguides are employed to maximize the antenna efficiency. The concept of telescoping waveguide was successfully introduced in [2]. This is however, the first time multiple telescoping waveguides are employed. In the proposed design, the circular waveguides are moving relative to each other, whereas in the previous design the horn moved relative to the fixed waveguide [2].

The reflectarray antenna operates at 35.75 GHz. The overall dimensions are 986×821 mm^2, which consists of 345×287 elements. The focal distance equals to 0.7 m. The geometrical parameters are summarized in Table 4.1. The subreflector vertex and foci distance equal 0.095 m and 0.22 m, respectively. The subreflector dimensions were selected to maximize the antenna efficiency while fitting inside the CubeSat stowage volume. The subreflector rim dimensions are 95×124 mm^2. It is important to highlight that the subreflector can easily be replaced by a reflectarray. Using a flat subreflector could reduce the overall mass of the antenna if needed.

The feed design is described in the next section. The maximum possible directivity $D_{max} = (\pi \cdot D/\lambda)^2$ of the reflectarray is 45.45 dBi at 35.75 GHz.

Table 4.2   *Telescoping waveguide dimensions.*

Waveguide no.	Inner dimension (mm)	Outer dimension (mm)
3	9.35	10.15
2	7.85	8.65
1	6.35	7.15

4.3.2   Deployable Feed

The telescoping feed consists of a multiflare-angle horn and three telescoping waveguides with increasing inner diameter. When stowed, the telescoping waveguides fit inside the horn. The bottom waveguide Wg1 (Figure 4.6), with the smallest diameter, remains fixed in the CubeSat. The two other waveguides, the feed horn, and the subreflector slide upwards using two lenticular tapes. The lenticular tapes are controlled by a set of encoders, which provide feedback to the driving motor. To further improve the feed deployment accuracy six quartz cables are employed. A cable hexapod is created using the six cables to precisely locate the secondary reflector.

Figure 4.7 illustrates how the ends of the tapes are bonded to the base of the collar. The upper portion of the collar is bonded to three subreflector struts. The top of the subreflector struts are bonded to the subreflector, providing a rigid connection between the upper collar (which also locates the horn) and the subreflector. The upper and lower collar are joined by a compression spring, which provides compliance in the joint. This allows the bottom half of the subreflector collar to just provide an upward force, and can be located less accurately, whereas the position of the upper half will be precisely controlled by the cables attached to the subreflector. This design also makes the architecture resistant to coefficient of thermal expansion (CTE) dimensional changes in the tapes.

The subreflector and feed deploy to within 0.2 mm on the z-axis and 0.2 mm on the x- and y-axis of its ideal position. The dimensions of each waveguide are summarized in Table 4.2. A compression spring is employed within the walls of the waveguide, to precisely locate the waveguides position. The feed deploys after the panel deployment is completed as shown in Figure 4.8.

The feed horn is shown when folded and fully deployed in Figure 4.6. The detailed dimensions of the feed horn are shown in Figure 4.9. The feed horn was optimized using our in-house code as described in [13]. The calculated and measured reflection coefficient of the feed horn with its three waveguides is shown in Figure 4.10. The calculated and measured results are in good agreement. The telescoping feed is measured in the cylindrical near-field anechoic chamber of NASA's JPL. The calculated and measured radiation patterns in E- and H-plane are shown in Figure 4.11 for the feed horn and its telescoping waveguides. The

(a)

(b)
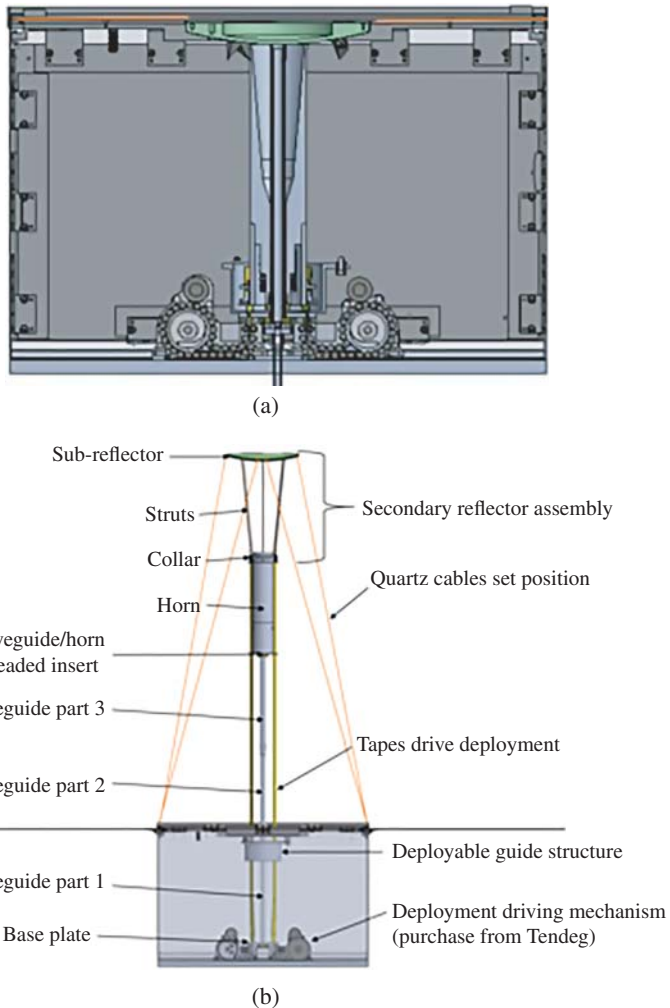
Figure 4.6 *Feed horn with its three telescoping waveguides in (a) folded configuration and (b) deployed configuration.*

calculated and measured gain and directivity are summarized in Table 4.3 and they are in excellent agreement.

4.3.3 Reflectarray Design

The proposed antenna uses as a unit cell a variable size square patch microstrip element. The required phase of each element is determined using the reflectarray
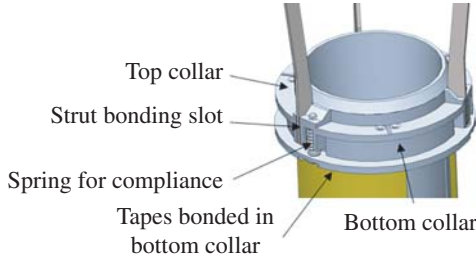
Figure 4.7   *Feed horn mechanical features for an accurate deployment in x-, y-, and z-axis.*
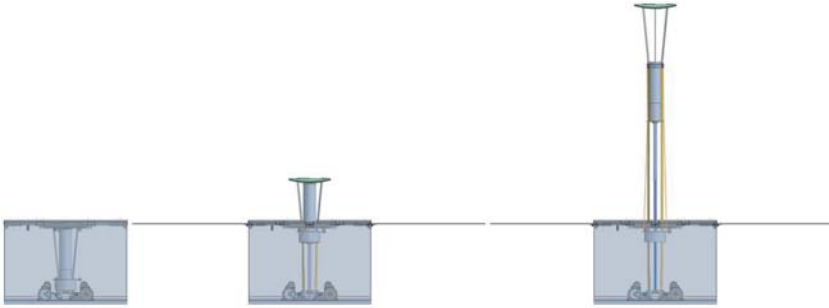
Figure 4.8   *Feed deployment occurring after the panel deployment.*
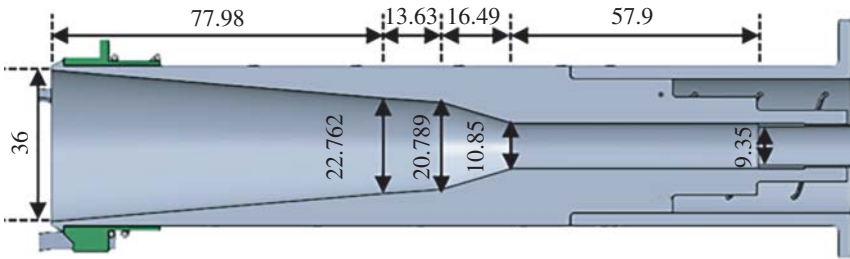
Figure 4.9   *Feed horn geometry and dimensions in mm.*

design equation:

$$\varphi_i - k_0(R_i + \bar{r}_i \cdot \hat{r}_o) = 2\pi N \tag{4.1}$$

where φ_i is the required transmission-line phase delay of the ith element, R_i is the distance from the focal point to the ith array element, $\bar{r}_i$ is a vector from the center of the array to the ith array element, $\hat{r}_o$ is a unit vector in the main beam direction,
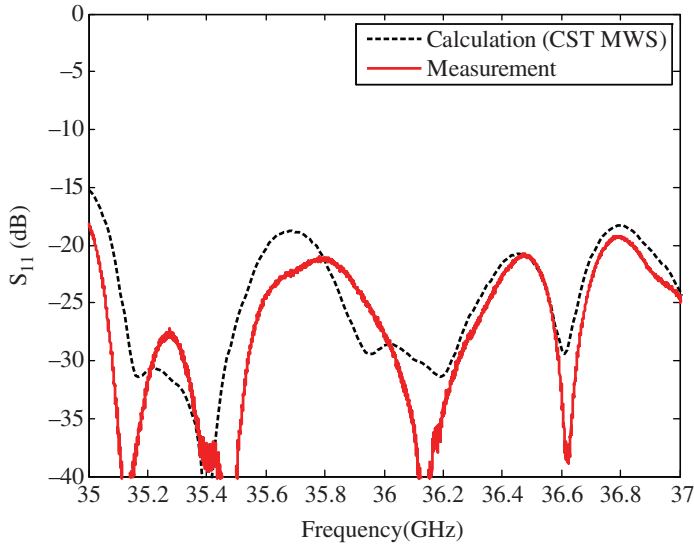
Figure 4.10   *Calculated and measured reflection coefficient of the feed-horn alone (including the telescoping waveguides and transition).*

Table 4.3   *Deployable feed horn calculated and measured directivity and gain.*

	Directivity (dBi)	Gain (dBi)
Calculated	20.82	20.52
Measured	20.95 ± 0.2	20.40 ± 0.2

and k_0 is the free space wavelength. The required phase delay distribution of the proposed reflectarray is shown in Figure 4.12.

Since the *f/D* ratio is small, the angle of incidence needs to be considered to maximize the antenna efficiency [14]. The central element directly below the feed has an incidence angle of 0°, whereas those elements at the edges of the reflectarray have larger angles of up to 45° (see Figure 4.12). The angles for the other elements have values between these extremes.

The theoretical reflectarray design assumes a planar surface of metal patches attached to a known substrate. In practice, gain reductions due to an imperfect reflectarray surface, are due to a lack of planarity in the individual panels making up the array, gaps between the panels and imperfections in the connecting hinges that do not allow the panels to be perfectly aligned over the deployed area.
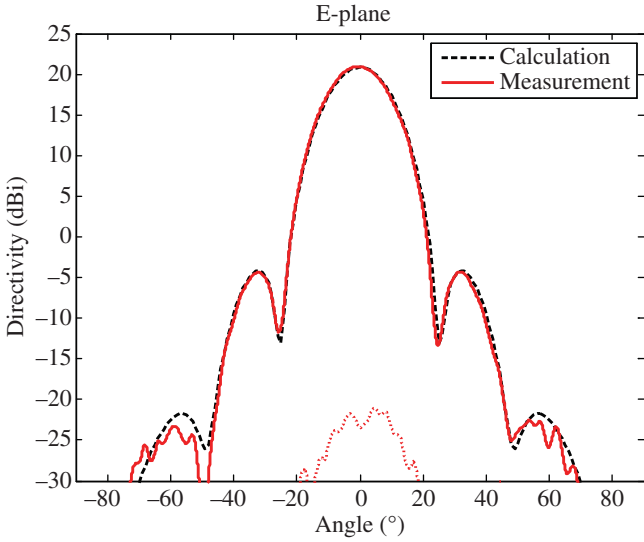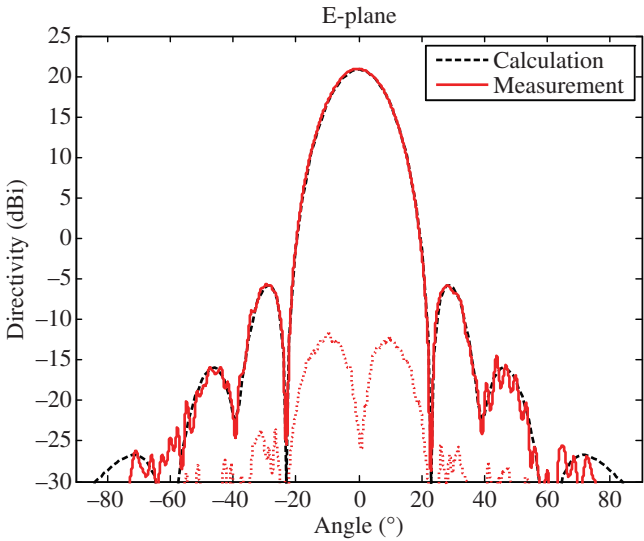
Figure 4.11   *Telescoping feed horn radiation pattern at 35.75 GHz at (a) ϕ = 0° and (b) ϕ = 90°.*
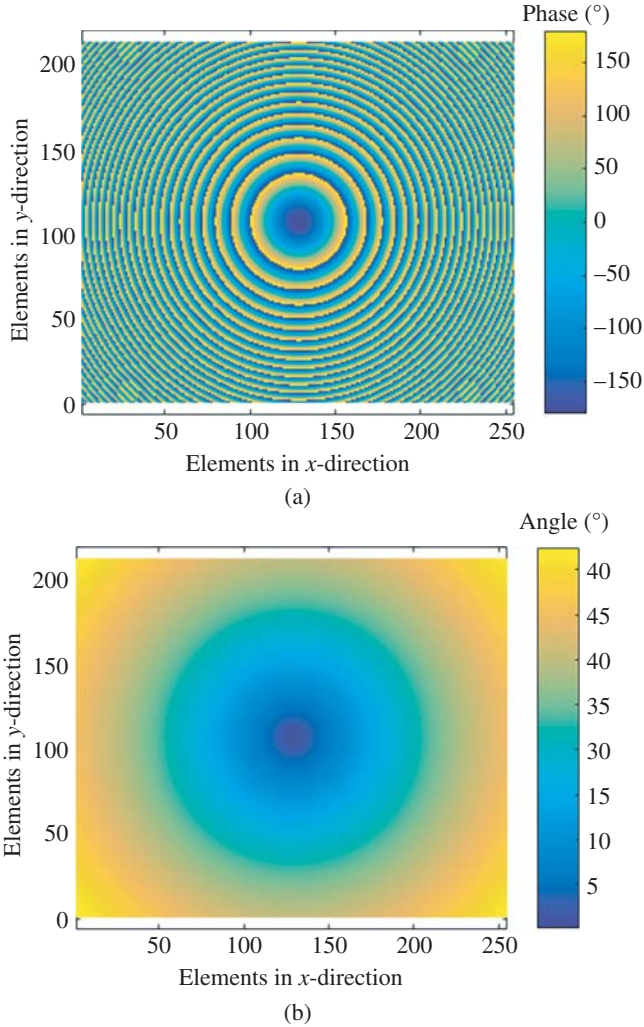
Figure 4.12   *(a) Required wrapped phase delay of all elements of the proposed reflectarray. (b) Angle of incidence of all elements of the proposed reflectarray.*

The reflectarray patch spacing is set to 3.86 mm, i.e. 0.46 wavelengths. The 16 reflectarray panels consists of two 0.813 mm-thick Rogers RO4003C ($\varepsilon_r = 3.55$ and $\tan\delta = 0.0027$), printed with the reflectarray patches on one side, co-cured with a central core of graphite composite. The central layer is a 0.589 mm-thick STABLCOR layer providing the required flatness over temperature. The cross section of the reflectarray panels is illustrated in Figure 4.13. The maximum

½ oz. (17 μm) electrodeposited copper foil

Rogers 4003–0.406 mm

STABLCOR composite structural board–1.22 mm

Rogers 4003–0.406 mm

2.08 mm
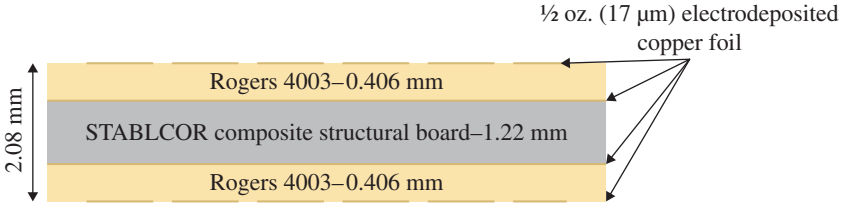
Figure 4.13   *Reflectarray panel layout.*
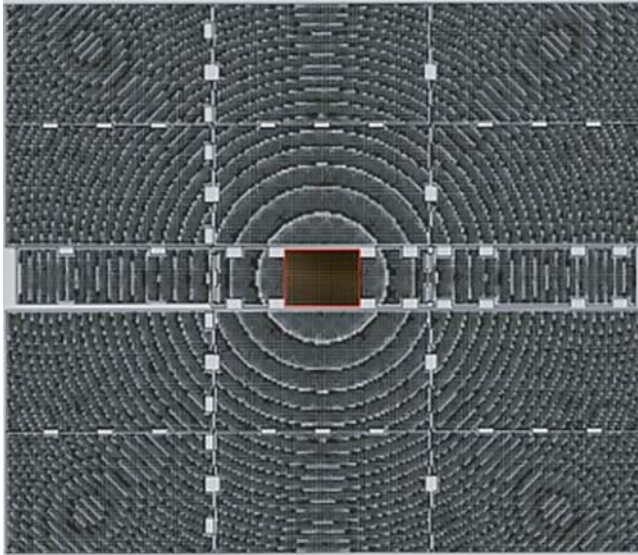
Figure 4.14   *Deployable reflectarray antenna panel layout. Cutouts and gaps in the reflectarray are included. The hinges are not included.*

out-of-plane deviation of an individual panel was measured to be within 0.4 mm. Most of the non-flatness was concentrated in 4 panels; the other 12 panels flatness within 0.25 mm. The symmetrical panel with a thickness of 2.08 mm results in a very high structural rigidity. The two Rogers RO4003C layers are printed with the reflectarray patches on the opposite side of each other to provide structural rigidity over larger temperature range (symmetry reduces large temperature gradients).

The reflectarray antenna and its 16 panels are shown in Figure 4.14. The deployable reflectarray consists of twelve 20.1 cm × 34.8 cm panels (top and bottom panels in Figure 4.14). Six of them are folded on each side of a 6U CubeSat large side ($\sim360 \times 220$ mm^2). They are all roughly separated by 0.254 mm gaps, which is negligible compared to the unit cell size. The two remaining panels fold on top of
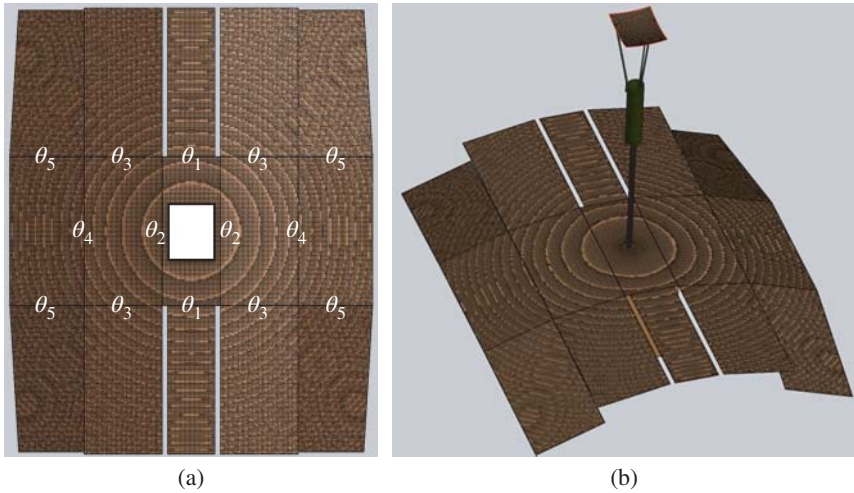
Figure 4.15   *(a) Deployment angle definition employed to perform a detailed misalignment analysis. (b) CAD model of exaggerated deployment errors.*

the fixed panel on the bus and deploys thanks to two spring loaded hinges. Custom hinges are specifically designed and developed for this mission to meet the deployment accuracy required at Ka-band and to minimize the gap between each panel.

There are gaps and cutouts in the reflectarray design as can be seen in Figure 4.14. The cutouts are there to accommodate the hinge volume, in stowed position, required to meet the deployment accuracy. The gaps are accommodating the CubeSat bus. These gaps and cutouts results in a gain loss of 0.15 dB. The reflectarray is modelled using TICRA's QUPES software [15] and all the gaps and cutouts are all included in our QUPES model (see Figure 4.14).

4.3.4   Deployment Accuracy

A very thorough analysis was performed to derive the deployment accuracy required to maintain satisfactory performance. To do so, five angles were defined as shown in Figure 4.15. The dependency between angles is also considered. For instance, if θ_2 is not null, which means it was not properly deployed, it will impact the 12 large panel deployment. The calculated deployment angle accuracy is summarized in Table 4.4. These numbers were used as the basis for designing our custom hinges. Assuming the deployment accuracy reported in Table 4.4 and perfectly flat panels, the predicted gain loss is about 0.33 dB.

Development of new hinges was required to meet the deployment accuracy of the reflectarray panels. The middle hinge of the three hinges that comprise a single hinge line has an adjustable end-stop that sets its deployed position. This end-stop comprises a fine-thread ball-end set screw that rests against a flat surface in the

Table 4.4   *Required and achieved deployment accuracy.*

Angle	Requirement (°)	Measured (°)
θ_1	±0.04	±0.03
θ_2	±0.04	±0.096
θ_3	±0.04	±0.009
θ_4	±0.04	±0.012
θ_5	±0.10	±0.006

deployed configuration. By adjusting the position of this set screw, the deployed angle of the hinge can be adjusted in fine increments. This adjustability relaxes the requirements on the accuracy of the assembly process; the deployed hinge angle can be measured after assembly, and adjusted to meet the deployed hinge angle requirement. This allows the deployed planarity of the array to be limited not by the assembly process (as it was with previous hinge design), but by our ability to measure and adjust the hinge angle. Additionally, if the ball-end set screw and the flat surface against which the set screw rests are made of similarly hard materials, this design also achieves better deployment repeatability than existing hinge designs.

The new one-sided hinges allow the panels to fold such that when folded, the gap between the panels can be arbitrarily small. This allows us to fold the panels with little wasted volume in the packaged configuration. In other words, the packaging efficiency is much higher than previously possible, by a factor of about 2. This is critical to fit in a 6U-class CubeSat.

Besides, the hinge attachment to the panel is innovative (Figure 4.16). Instead of using a double-sided hinge (which is what was used on MarCO) in which the panel is affixed using an epoxy adhesive (which not only increases the stowed volume but also allows for the panel position to shift within the hinge due to viscoelastic effects), we use a combination of alignment pins, metal bolts, low-profile threaded inserts, and an epoxy adhesive to attach the hinges to the panels. The alignment pins ensure good alignment between the hinge and the panel that does not drift over time, the bolts and inserts provide tensile stiffness and strength, and the epoxy adhesive distributes loads over the footprint of the hinge and avoids stress concentrations. The folding pattern avoids panel interference during deployment, and ensures that the panels do not jam against each other or against the spacecraft bus during deployment. Additionally, it facilitates the hinge and panel assembly process, since all of the hinges are attached to the same side of the panels.

Figure 4.16a shows two adjacent panels (1) and (4), fully unfolded. Figure 4.16b shows the panels in a partially unfolded state. Figure 4.16c shows the panels fully folded. One leaf (2) is fixed to one panel (1), and the other leaf (3) is fixed to the other panel (4). The two leafs are interconnected using a hinge pin (5); this interconnection allows the leafs to rotate about this hinge pin. One or more springs can provide stiffness and an unfolding force.

(a)

(b)

(c)
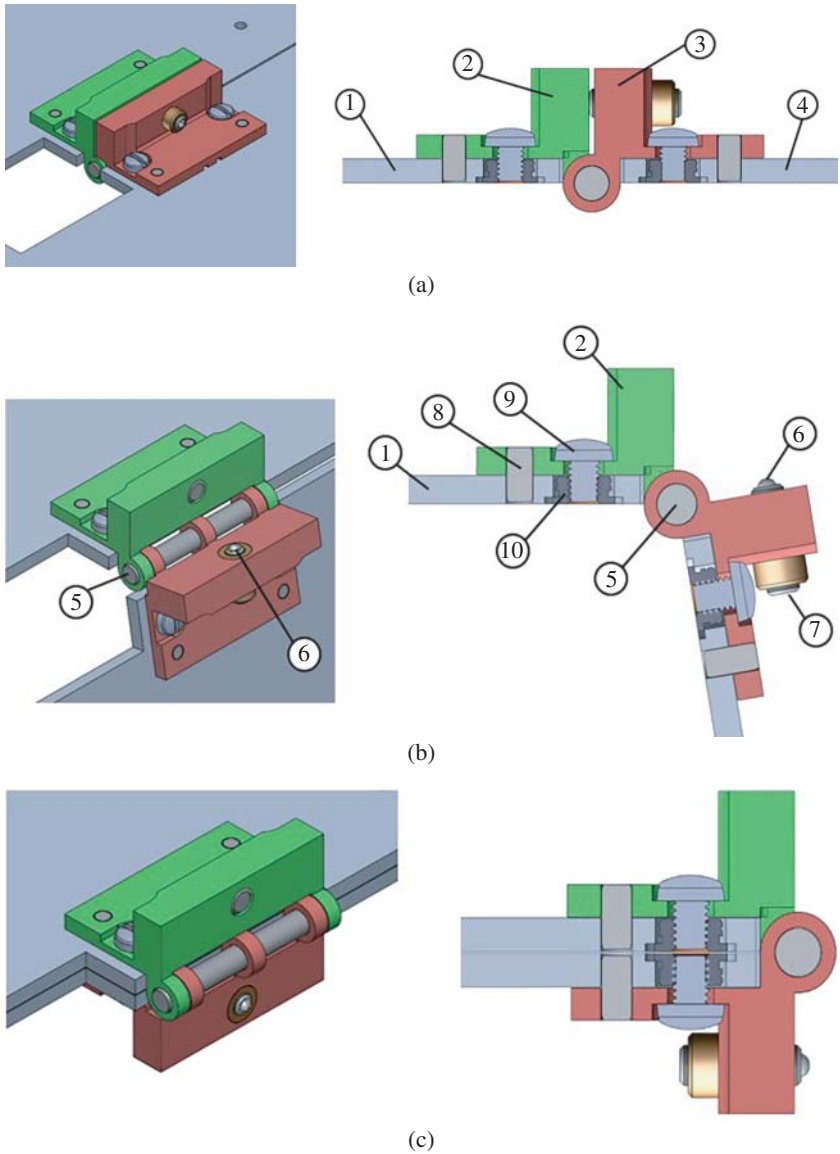
Figure 4.16 *Custom made hinges with adjustability features. The adjustable end-stop comprises a fine-thread ball-end set screw that rests against a flat surface in the deployed configuration allowing to adjust the deployment angle within few hundredths of a degree.*
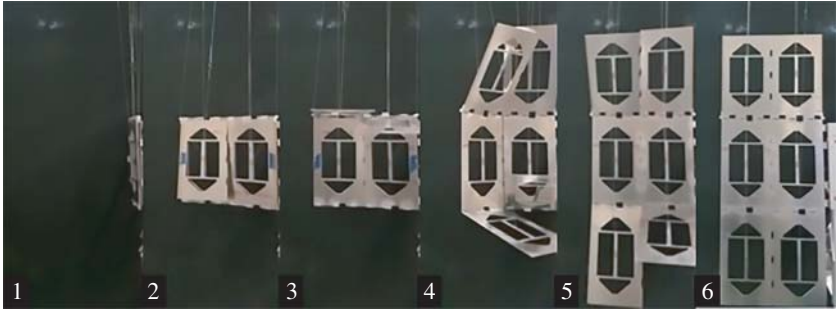
Figure 4.17   *Six-panel deployment with an offloading mechanism to simulate weightless condition.*

When fully unfolded, a ball (6) presses against a flat end stop (7), thereby dictating the final unfolded angle between the panels. The location of the ball with respect to the leaf (3) can be adjusted by turning a fine-thread set screw (7). The ball is attached to the end of the fine-thread set screw in a manner that allows the ball to freely roll, like a ball-point pen. Changing the location of the ball with respect to the leaf (3) allows for fine control of the final unfolded angle between the panels and allows for the correction of any manufacturing or assembly errors.

The leafs are attached to the panels using three parallel methods. For instance, the leaf (2) is attached to the panel (1) using an alignment pin (8), an externally threaded bolt (9) that threads into an insert (10), and an epoxy adhesive between the leaf and the panel. The insert has a flange that catches a counterbore on the panel, thus providing strength in tension and peel. The alignment pin precisely locates the leaf with respect to the panel.

A first set of tests was performed to demonstrate the adjustability and the deployment repeatability using two panels only. A faro arm with a laser scan head is used to measure the deployment angle. A deployment accuracy of $\pm 0.05°$ was observed with 158 deployments. In addition, deployment accuracy was tested on one side of the CubeSat (i.e. six panels). The deployment accuracy achieved using the custom-made hinges is well within the requirement as shown in Table 4.4.

The deployment of the antenna will be sequential. First, using a burn wire release mechanism, the two sets of six panels are deployed. Then, the two single panels are deployed using a second burn wire. Finally, the feed deployment occurs. The deployment of one set of the six-panels is shown in Figure 4.17. An offloading mechanism is employed to reproduce the zero gravity conditions.

4.3.5   Effect of Struts

Three stainless steel struts are employed to maintain a good alignment of the subreflector (i.e. ± 0.2 mm in z-axis and ± 0.1 mm in x- and y-axis). This affects

the peak gain, the cross-polarization and the sidelobe levels. The three rectangular cross-section struts are 1.0 mm thick and 4.0 mm deep. The struts result in an overall increase in sidelobe level (~3 dB), reduce the peak gain (~0.3 dB at 35.75 GHz). The struts were located and designed to ensure the panels can fit on either side of the S/C; this enables a compact 6U-class antenna design.

4.3.6   Predicted Gain and Efficiency

The feed horn, combined with the three struts, the subreflector, and three telescoping waveguides, is modeled as a method of moment (MoM)/multilevel fast multipole method (MLFMM) object using ESTEAM within the TICRA Tools framework [15]. A waveguide port is employed to excite the MoM/MLFMM object. The horn and telescoping waveguides are defined as one object using two piecewise linear body of revolution objects, one for the interior and one for the exterior. These two objects are combined in a scatterer cluster and define the horn geometry. A scatterer cluster including the feed horn and waveguides, the three struts and the subrefector, is created and used as a MoM/MLFMM object.

Scattering by the reflectarray elements are determined using the Spectral Domain Method of Moment in QUPES [15], in which the local periodicity approach is adopted. This means that each array element is analyzed assuming that the individual element is located in an infinite array of identical elements. The advantage of local periodicity approach is that the problem is restricted to a single periodic unit-cell, thus reducing the complexity of the problem and allowing the analysis of electrically large reflectarrays in a reduced amount of computation time and a reduced amount of memory as opposed to using MoM/MLFMM. Each array element is assumed to be illuminated by a locally plane wave and the direction of propagation of this incident field is assumed to be the direction of the Poyting's vector at the field point. Once the current is calculated on the reflectarray, the far field radiation pattern can be determined by integrating the currents.

The loss contributions are summarized in Table 4.5. The deployable reflectarray is expected to achieve a gain of 47.4 dBi, which translates into a 32% efficiency. Please note this surface accuracy can be improved by refining the bonding process of the hinges and by controlling the surface flatness of all panels. This would increase the gain by 0.6 dB and efficiency to 37%. The gain loss was calculated by including the measured surface of all panels.

It was shown in [16] that an increase of 0.5 dB can be achieved using a Jerusalem cross with an open loop element instead of square patches. Square patches are easy to implement, but are not known for providing the optimal performance due to a phase range that is usually is limited to <360°. However, this comes at the cost of increasing the thickness of the substrate (i.e. from 0.406 to 0.762 mm).

The spillover and taper loss are non-ideal for a cassegrain antenna and this is due to the packaging constraints: the subreflector dimensions are limited by the bus size. However, one could improve spillover and taper loss by shaping the subreflector. For

Table 4.5 *Gain table at 35.75 GHz.*

	Gain (dBi)	Loss (dB)
Ideal directivity	52.37	—
Spillover	51.46	0.91
Taper	49.95	1.51
Blockage	49.67	0.28
Struts	49.37	0.3
Gap loss	49.22	0.15
Patch dielectric/conductivity loss	48.97	0.25
Surface accuracy[a]	47.77	1.2
Feed loss/telescoping waveguide/transition	47.47	0.3
Feed mismatch (RL = 17 dB)	47.38	0.09
Overall performance	47.38	4.99

[a] The surface accuracy was adjusted with the measured surface dataset and indicates gain reduction due to the surface not being perfectly planar.

the flight unit, these improvements will be applied: (1) better surface flatness, (2) shaping of the subreflector, and (3) new reflectarray unit cell if it fits within the allocated volume.

4.3.7 Prototype and Measurements

A first fully deployable and operational prototype was fabricated (Figure 4.18). The antenna was folded and deployed a first time to align the panels. The hinges were adjusted to obtain the best surface accuracy. It was observed that the bowing of the panels was causing further deformation after bonding the hinges. Indeed, as can be
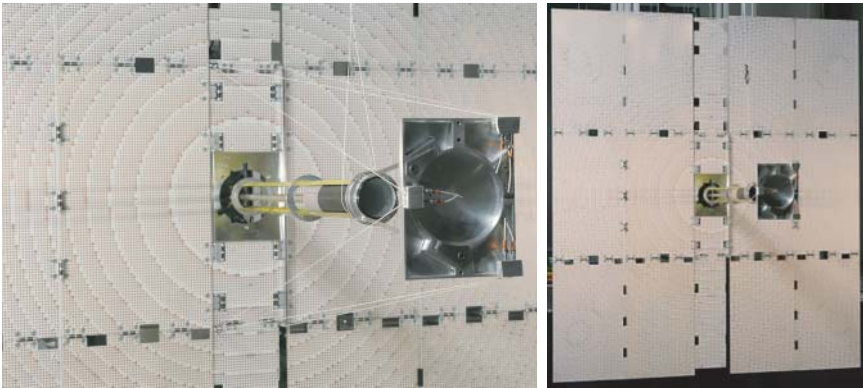
Figure 4.18 *Photography of the prototype tested in JPL's near field planar range.*
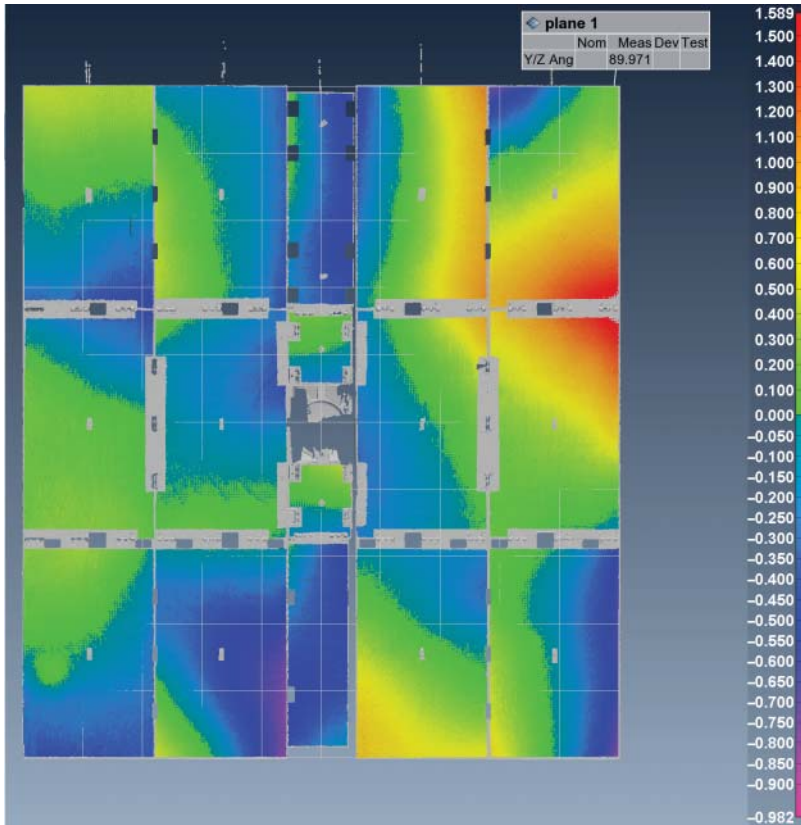
Figure 4.19 *The final adjusted reflectarray surface profile. The units on the color bar are in millimeters.*

seen in Figure 4.19, the out-of-plane deviation on the left side came out much better (0.98 mm) than the right side (1.59 mm). Note these are peak values that exist over small portions of the array as shown in Figure 4.19. As the panel flatness on the left side was originally better, the surface accuracy on the left side came up better than the right side. The surface flatness can be improved using a better bonding process of the hinges and by controlling the surface flatness of all panels. Improving the surface accuracy would limit the gain loss due to the panels not being perfectly planar and the hinges not being perfectly aligned.

The QUPES model is updated with the actual surface of each panels. The surface was measured with a faro arm and included in the model using tabulated surface for each reflectarray panels. The measured and calculated radiation pattern is shown in Figure 4.20. The measured gain equals to 47.1 dBic.
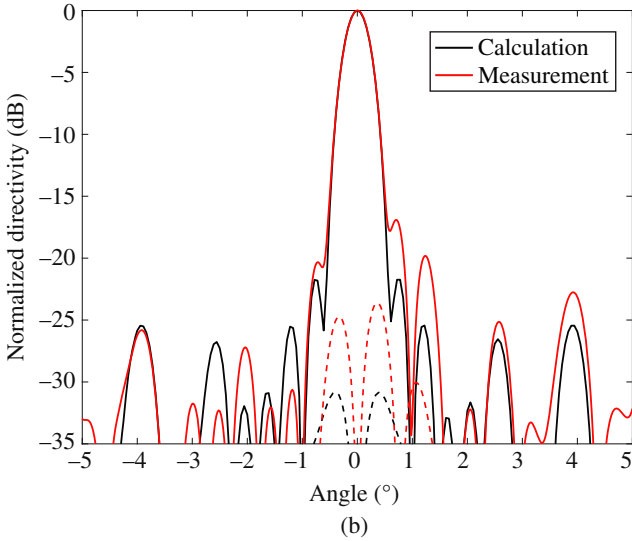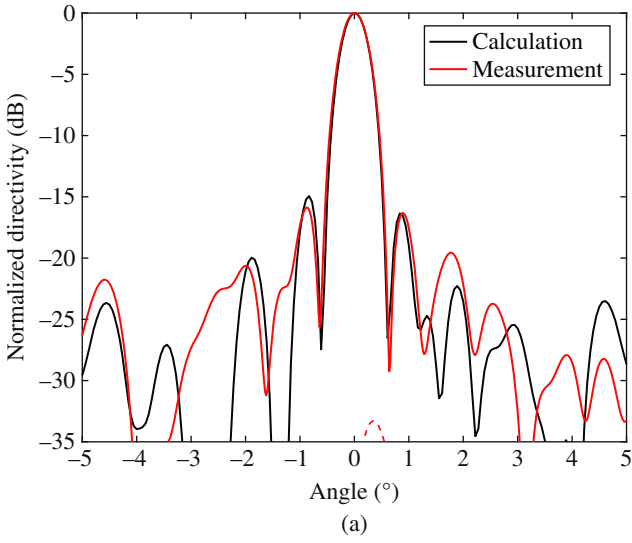
Figure 4.20   *Measured and calculated radiation pattern of the one-meter reflectarray deployable prototype. (a) φ = 0°. (b) φ = 90°.*

4.4   Conclusion

The need for a high gain antenna for CubeSats is of uppermost importance to push the limit of their capabilities for telecommunication and radar. This chapter provides a detailed description of a novel, deployable reflectarray antenna which is currently the largest Ka-band antenna for 6U-class CubeSats.

The Ka-band high gain reflectarray antenna employs Cassegrainian optics to accommodate a deployment mechanism that stows the reflectarray panels and feed assembly allowing accommodation into a very compact space. Despite these mechanical constraints, the antenna demonstrates acceptable performance at 35.75 GHz: a gain of 47.4 dBi and an efficiency of 32%. This is in line with previously reported Ka-band reflectarray such as ISARA (i.e. 26% at 26 GHz).

All the critical aspects of the design, namely, reflectarray panels, struts and blockage effects, feed mismatch and interactions, etc., have been thoroughly addressed. The RF prototype has been developed and detailed measurements demonstrated good agreements with the simulation results. "Solutions to improve the performance of the design have been introduced and will be implemented for the flight model."

Acknowledgments

References

1. E. Peral, S. Tanelli, Z. S. Haddad, G. L. Stephens, and E. Im, "RaInCube: a proposed constellation of precipitation profiling Radars In Cubesat," *AGU Fall Meeting*, San Francisco, CA, Dec. 2014.

2. N. Chahat, R. Hodges, J. Sauder, M. Thomson, E. Peral, and Y. Rahmat-Samii, "CubeSat deployable Ka-band mesh reflector antenna development for earth science missions," *IEEE Transactions on Antennas and Propagation*, vol. **64**, no. 6, pp. 2083–2093, 2016.

3. N. Chahat, R. E. Hodges, J. Sauder, M. Thomson, and Y. Rahmat-Samii, "The Deep-Space Network Telecommunication CubeSat Antenna: using the deployable Ka-band mesh reflector antenna," *IEEE Antennas and Propagation Magazine*, vol. **59**, no. 2, pp. 31–38, April 2017.

4. R. E. Hodges, N. E. Chahat, D. J. Hoppe, J. D. Vacchione, "The Mars Cube One deployable high gain CubeSat antenna," *2016 IEEE International Symposium on Antennas and Propagation (APSURSI)*, Fajardo, 2016, pp. 1533–1534.

5. R. Hodges, D. Hoppe, M. Radway, and N. Chahat, "Novel deployable reflectarray antennas for CubeSat communications," *IEEE MTT-S International Microwave Symposium (IMS)*, Phoenix, AZ, May 2015.

6. T. A. Cwik, N. E. Chahat, J. Sauder, M. Arya, and E. Thiel, "Deployable reflectarray antenna," US 15/850,861, Dec 2017.

7. M. Zawadzki and J. Huang, "Integrated RF antenna and solar array for spacecraft application," *Proceedings 2000 IEEE International Conference on Phased Array Systems and Technology*, Dana Point, CA, 2000, pp. 239–242.

8. J. Huang and J. Encinar, *Reflectarray Antennas*, Hoboken, NJ: Wiley, 2007.

9. J. Huang and A. Feria, "Inflatable microstrip reflectarray antennas at X and Ka-band frequencies," *IEEE Antennas and Propagation Society International Symposium*, Orlando, FL, vol. **3**, 1999, pp. 1670–1673.

10. H. Chou, Y. Chen, and H. Ho, "An all-metallic reflectarray and its element design: exploring the radiation characteristics of antennas for directional beam applications," *IEEE Antennas and Propagation Magazine*, vol. **60**, no. 5, pp. 41–51, Oct. 2018.

11. M. Yi, W. Lee, and J. So, "Design of cylindrically conformed metal reflectarray antennas for millimetre-wave applications," *Electronics Letters*, vol. **50**, no. 20, pp. 1409–1410, Sep. 2014.

12. H. Chou, C. Lin, and M. Wu, "A high efficient reflectarray antenna consisted of periodic all-metallic elements for the Ku-band DTV applications," *IEEE Antennas and Wireless Propagation Letters*, vol. **14**, pp. 1542–1545, 2015.

13. N. Chahat, T. J. Reck, C. Jung-Kubiak, T. Nguyen, R. Sauleau, and G. Chattopadhyay, "1.9 THz multi-flare angle horn optimization for space instruments," *IEEE Transactions on Terahertz Science and Technology*, vol. **5**, no. 6, pp. 914–921, Nov. 2015.

14. E. R. F. Almajali and D. A. McNamara, "Angle of incidence effects in reflectarray antenna design: making gain increases possible by including incidence angle effects," *IEEE Antennas and Propagation Magazine*, vol. **58**, no. 5, pp. 52–64, Oct. 2016.

15. TICRA, Denmark, www.ticra.com

16. M. Zhou, E. Jorgensen, S. B. Sorensen, A. Ericsson, M. F. Palvig, N. Vesterdal, E. Borries, T. Rubaek, and P. Meincke, "Design of advanced reflectarrays for future smallsat aplications," *40th ESA Antenna Workshop*, Noordwijk, The Netherlands, 8–10 Oct, 2019.

5

X/Ka-Band One Meter Mesh Reflector for 12U-Class CubeSat

Nacer Chahat[1], Jonathan Sauder[1] and Gregg Freebury[2]

[1]*NASA Jet Propulsion Laboratory/California Institute of Technology, Pasadena, CA, USA*
[2]*Tendeg LLC, Louisville, CO, USA*

5.1 Introduction

In the past few years, interest for CubeSats carrying science experiments in Low Earth Orbit (LEO) and Deep Space has exploded. The National Aeronautics and Space Administration (NASA), in particular, has launched multiple pioneering missions such as Mars Cube One (MarCO) [1] and Radar in a CubeSat (RainCube) [2, 3], which were enabled by innovative deployable antennas.

MarCO, had two twin 6U CubeSats on their way to Mars. They were the first CubeSats to travel into deep space and they carried a deployable X-band reflectarray designed to enable 8 kbps bent pipe relay communication from the Insight spacecraft at Mars (∼1 AU) during the critical Entry Descent and Landing of Insight. The success of this pair of cubesats achieved in relaying telemetry Insight demonstrates that such spacecraft can play key roles in future deep space missions.

The RainCube mission, deployed successfully in LEO, a 0.5-m mesh reflector from a 6U CubeSat to measure rain and snow precipitation [3]. A clear witness of CubeSat capabilities is the science data collected by Raincube and Tempest-D on September 28, 2018 while overflying Typhoon Trami less than 5 minutes apart
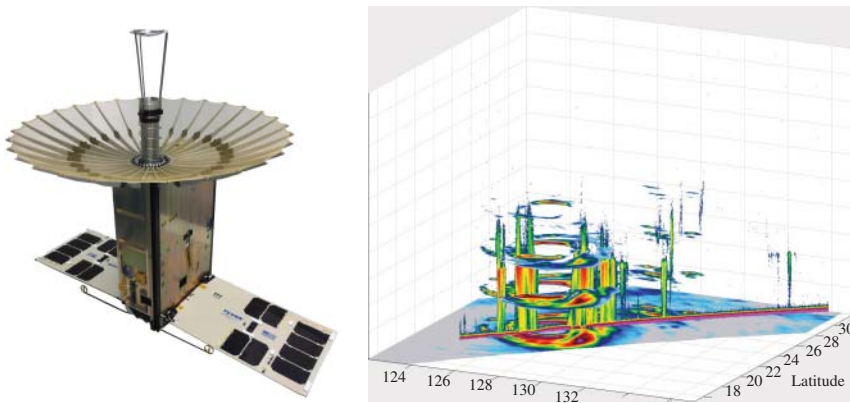
Figure 5.1   *RainCube nadir Ka-band reflectivity shown overlaid on TEMPEST-D 165 GHz brightness temperature illustrating complementary nature of these sensors in constellation for observing precipitation. Courtesy of Dr. Shannon Brown, JPL/Caltech.*

(see Figure 5.1). Raincube is an active radar measuring reflectivity and Tempest-D is a passive mm-wave radiometer. While this success was quietly advertised, it is worthy of higher accolades, paving the way for radar in CubeSats. In a constellation, these CubeSats will achieve unprecedented temporal resolution required to observe weather phenomena at short time-scale.

To further improve the capabilities of CubeSats for interplanetary missions, there is a critical need for larger radio frequency (RF) aperture. Research continues on larger deployed antenna apertures for CubeSat and SmallSat [3–5] that will produce high gain for telecommunications applications, or narrow beamwidths for Earth science needs. For deployable antennas, the deployed structure precision is critical for antenna mainbeam and sidelobe performance. The undeployed antenna stowed volume is critical for launch accommodations.

One approach for an RF deployed aperture is a reflectarray antenna where the panels are held against the side of the spacecraft bus during launch and deployed via a hinged system on-orbit. The flat, two-dimensional reflectarray antenna geometry minimizes the stowed volume especially when compared to parabolic or other conic three-dimensional surfaces of traditional aperture antennas. The reflectarray panels and hinge deployment mechanims can be fabricated to retain high physical integrity and fidelity in the presence of launch dynamics and on-orbit thermal variations. A first application of this approach integrated solar panels with the reflectarray antenna (ISARA, Integrated Solar Array & Reflectarray Antenna) operating at Ka-band, combining the two functions and resulting in small additional mass and volume increase over the solar panels themselves [5]. This design was extended to an X-band telecommunication system on MarCO using a reflectarray deployed from a 6U CubeSat launched with the NASA InSIGHT Mars lander mission to provide near-real-time bent-pipe relay during the entry descent and landing portion
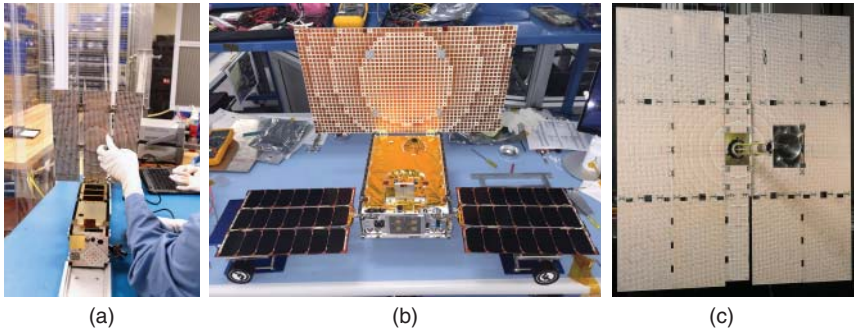
Figure 5.2 *Evolution of CubeSat reflectarray antennas. (a) ISARA [5]. (b) MarCO [1]. (c) OMERA [6].*

of that mission. Most recently, a larger one-meter Ka-band reflectarray antenna was developed and demonstrated on a 6U-class CubeSat employing 15 deployable panels [6]. The evolution of reflectarray deployable CubeSat antennas is illustrated in Figure 5.2. Although ISARA and MarCO are transmit-only antennas, reflectarray antennas can provide dual frequency operation using a dual frequency feed (e.g. slot array) combined with a broadband reflectarray unit cell. However, since the margin is much larger for uplink, there is no need for dual-band reflectarray for deep space communication. Commands are received through a low gain antenna. One drawback of reflectarrays is the difficulty of covering multiple frequency bands as opposed to mesh reflectors.

The European Space Agency is currently developing a 12U CubeSat, M-Argo, a standalone deep space CubeSat to rendezvous with a small <100 m diameter asteroid to characterize its physical properties [7]. M-Argo uses a deployable reflectarray which demonstrates that reflectarrays are establishing themselves as a standard for interplanetary CubeSat missions (Figure 5.3).
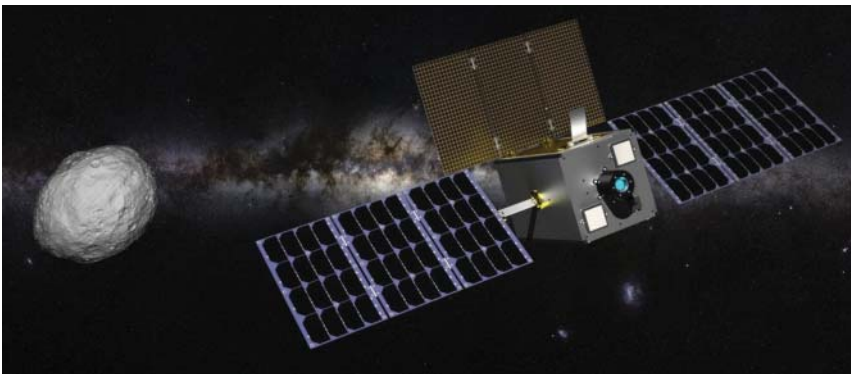
Figure 5.3 *ESA's 12U CubeSat M-Argo using a deployable reflectarray antenna [7]. Courtesy of European Space Agency.*

Another approach are deployable mesh reflectors flown in multiple NASA missions such as the Tracking and Data Relay Satellite System (TDRSS), Gallileo [8], Soil Moisture Active Passive (SMAP) [9], and Raincube [3]. On CubeSat platforms, a 0.5-m Cassegrain mesh reflector was demonstrated for the Raincube radar [3] and for telecommunication compatible with the Deep Space Network (DSN) frequency bands at Ka-band [4] (see Chapter 3).

The antenna presented in this chapter extends the telecommunication capabilities of CubeSats with a one-meter offset-fed mesh reflector compatible with 12U-class CubeSats. The antenna stows in a 3U volume. This antenna can either be used at X-band, Ka-band, or both. The deployable antenna is a commercially available mesh reflector invented and commercialized by Tendeg LLC [10]. This reflector was previously used for a Ka-band radar instrument [11] and is now considered for multiple potential applications by multiple agencies including commercial Synthetic Aperture Radar (SAR). This broad interest is explained by the ability to reuse this reflector at different frequency bands and to scale the reflector up to 3 meter. The antenna presented in this chapter is extending the telecommunication capabilities of CubeSats for interplanetary exploration where a large diameter deployable mesh reflector fits in very constrained stowage volume. Mission concepts such as Mars NanoOrbiter [12] (Figure 5.4), could directly benefit from this technology achieving 20 times higher data rate at X-band for the same RF output power.
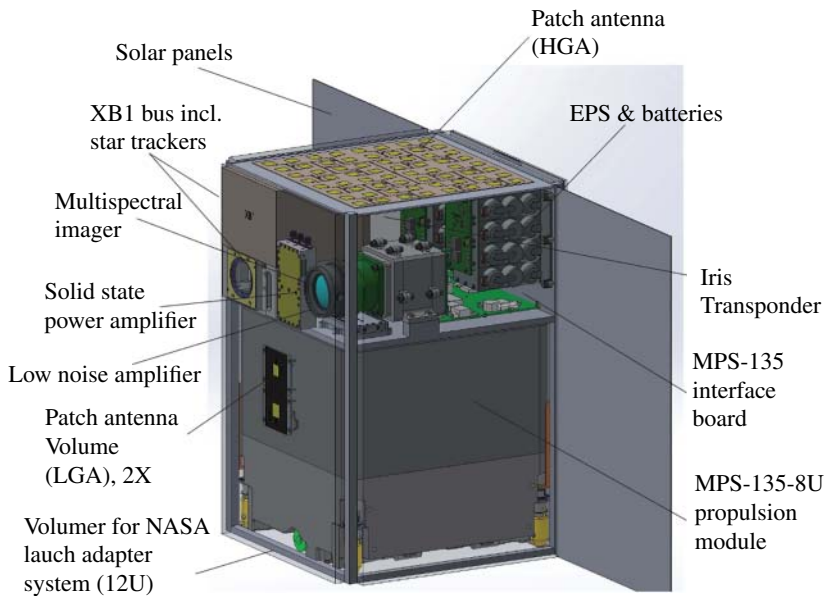
Figure 5.4 *Mars NanoOrbiter concept. Source: From Ehlmann et al.* [12]. *© 2018 Lunar and Planetary Institute.*

5.2   Mechanical Design

5.2.1   Trade Studies

5.2.1.1   Design Goals

The mesh reflector used in this chapter is a Tendeg patented technology [10] funded by NASA Earth Science Technology Office (ESTO) under an Advanced Component Technology (ACT) program. The mesh reflector was developed to meet the following requirements. The antenna should be able to operate at frequencies as high as Ka-band for radar or telecommunication. For telecommunication, the targeted aperture size is about 1 m, but there is a need for greater aperture size for radar. As a result, the reflector should be scalable to meet larger aperture size than 1 m (i.e. ideally 3 m).

As this antenna will be used on a 12U CubeSat ($20 \times 20 \times 30$ cm), the stowage volume is limited to approximately 3U ($10 \times 10 \times 30$ cm). This volume includes a statically mounted feed. An offset fed reflector is preferred with a target ratio between the focal length and the diameter (*f/D*) ranging between 0.65 and 0.75.

The surface accuracy of the reflector should be under 0.3 mm RMS. Surface reflective loss shall be less than 0.3 dB (exclusive of RMS) at Ka-band and this will drive the selection of the mesh opening per inch (OPI).

5.2.1.2   Rigid

Many architectures were considered and some were quickly ruled out. Rigid reflectors have the advantage of high precision surface manufacture either through forming or reinforced carbon fiber matrix layups. The challenge is that these rigid surfaces have to be segmented and folded or furled in some manner to fit within the 3U volume. At an *f/D* of 0.7 the major axis of the reflecting surface is about 108 cm and the circumference is over 300 cm. This would require dozens of segments that would then have to be linked or hinged in some manner that could be precisely deployed. This is not feasible and becomes even more challenging when scaled to larger apertures.

5.2.1.3   Elastic Composite

Elastic composites help simplify the challenge of folding rigid segments by allowing the surface and segments to flex, fold, or furl. Elastic composites are advancing rapidly and current state of the art laminates can withstand 2% strain limits. Even at cured thicknesses of 0.25 mm the bend radii must be greater than 6 mm. This does not allow full aperture folding like a coffee filter to fit within the 10×10 cm footprint. If the surface is segmented and furled then recovery of the free edges becomes critical to the surface accuracy. Creep from long term storage is another issue and

the surface segments end up thin which makes them susceptible to distortions from temperatures and gradients. Elastic composites show promise but at this time making a precision Ka-band surface with this level of packaging does not seem feasible.

5.2.1.4   Mesh

Reflecting surfaces made from knitted mesh have extensive space heritage dating back to the 1960s. The heritage material is gold plated molybdenum wire, approximately 25 micrometer diameter. By changing the needle density, guide bar settings and runner settings the density of the mesh can be modified in both the warp and weft directions. This allows mesh that is tuned for specific operating frequencies and the in-plane stiffness can be modified as well. The mesh needs to be tensioned to provide good loop to loop conductivity and to pull out any folding or creasing effects that may be a result of packaging. The mesh has advantages of being lightweight, highly transparent (low drag in LEO, doesn't shadow solar arrays), and packages very efficiently. The drawback is that it is expensive, fragile, must have proper in-plane stiffness properties, and must be properly tensioned. Despite these challenges, the gold wire mesh was down selected as the reflecting surface primarily because of its packaging capabilities and versatility to allow different operating frequencies, shapes and aperture diameters.

5.2.2   Structural Design of the Reflector

Numerous deployable architectures were considered that used a reflective mesh surface. The challenge was achieving Ka-band surface accuracy and getting the structural and actuator elements to package within the 3U volume (i.e. maximum volume that can be used in a 12U Cubesat). Any architecture with folding rigid radial ribs could not meet the surface accuracy due to large facet sizes at the outside perimeter. This required additional shaping elements between the ribs and to do an offset design required a boom that supported the center hub. A rigid but folded perimeter truss concept was considered but the volume needed for all the hinging elements excluded this concept.

As a result of this trade study, the down selected reflector incorporates a tensegrity design that utilizes dual tensioned nets and a tensioned perimeter truss. The compressive elements are radially aligned ribs that spiral wrap on a center spool and are deployed with an electrically redundant motor. This architecture is similar to Northrop Grumman's Astromesh [13] in that it incorporates the interconnected front and backside tensioned nets with triangular facets. This provides the accurate paraboloid surface and modifying the facet size allows optimization of gain and side lobes depending on operating frequency. Figure 5.5 shows the structural details of the reflector assembly.
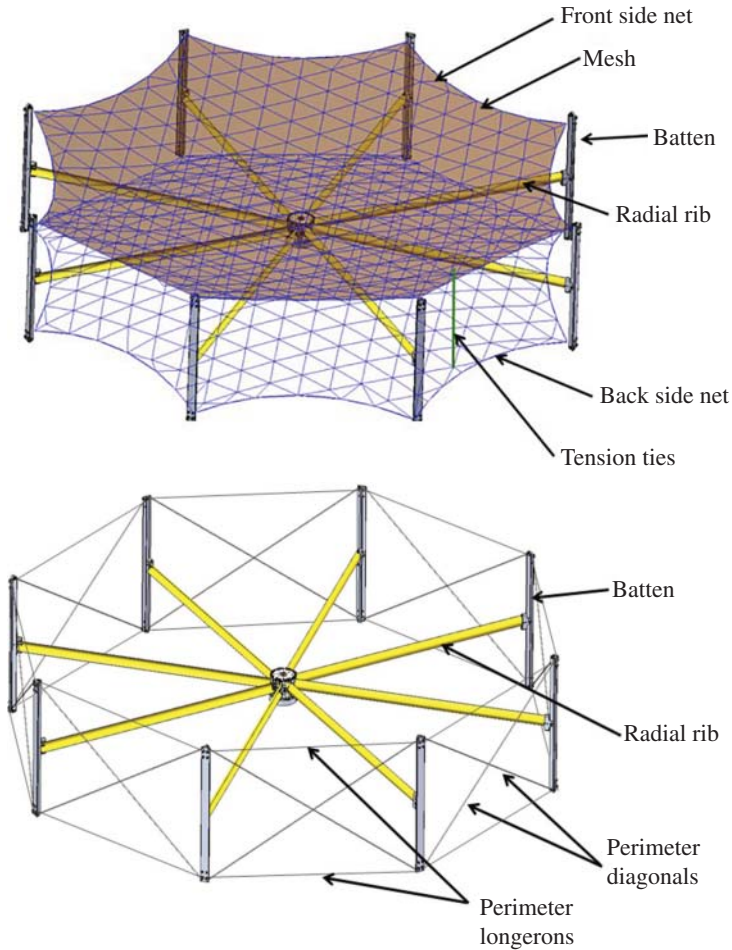
Figure 5.5   *Tendeg Ka-band mesh antenna for CubeSats (not all tension ties shown).*

    The reflector achieves the packaging goals by spiral wrapping the radial ribs onto a central spool. This pulls the battens radially toward the center hub. The ribs, hub and motor comprise the deployment actuator and the rigidizing structure. These elements package into a 3.5 cm diameter approximately 10 cm tall. This only consumes about $100\,cm^3$ of our total $3000\,cm^3$ volume. Figure 5.6 shows the deployment sequence of the prototype reflector. Another advantage of this architecture is that the mesh can be folded and pleated such that its peak tension only occurs at the final deployed state. Some hinging and folding architectures require the mesh to be over-tensioned to accommodate the articulating motions of its supports.
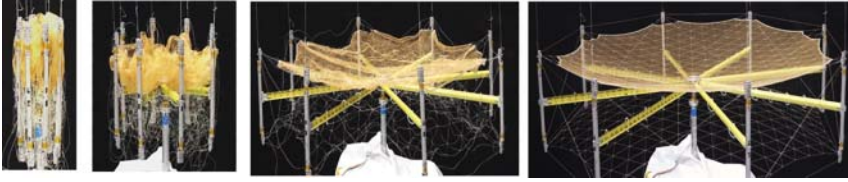
Figure 5.6   *Deployment sequence of the Tendeg Ka-band 1 m prototype reflector.*

| (a) | (b) | (c) |
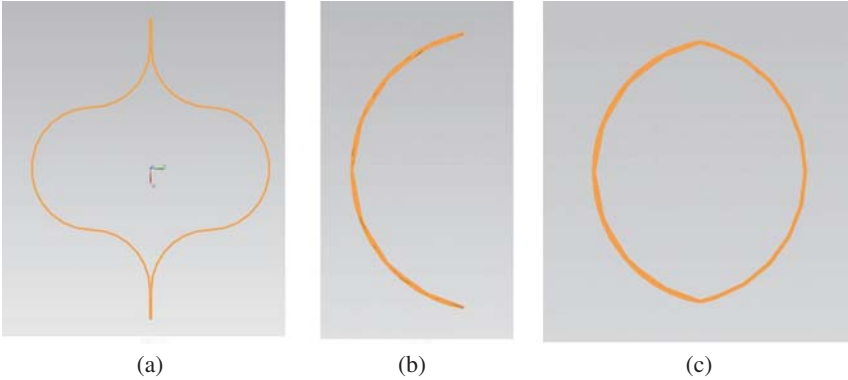
Figure 5.7   *Cross sections studied: (a) double omega; (b) carpenter tape; (c) lenticular.*

5.2.2.1   Ribs

The 1 m aperture reflector utilizes eight ribs. The number of ribs was a trade between compressive load per rib, span of the ribs and the required catenary size at the perimeter that still allows a 1 m effective aperture. The reflector can be modified to allow more or fewer ribs but at a 1 m aperture the eight ribs has worked well. Numerous rib architectures have been studied and shown in Figure 5.7.

The driving requirements for the rib include deployed properties (stiffness, buckling capacity), deployment authority (bending and torsional stiffness during deployment), and ability to transition from the deployed cross section to a flattened and spiral wrapped condition without damage or need of a complex mechanism. The required deployed properties and rib boundary conditions were derived from a finite element model (FEM). The desired tension for the mesh was known and with that strain state in the FEM the ribs needed to withstand about 18N of compressive force. At these load levels the open section carpenter tape design is adequate and provides a simple interface and packaging scheme. The carpenter tapes can utilize well understood metallic spring materials like stainless steel, carbon steel, beryllium copper and titanium alloys. They can also use elastic composites. For the prototype antenna the tried and proven Stanley carpenter tape was used and has proven to be extremely robust even when mishandled.

As the apertures grow in diameter the open section carpenter tapes, or slit tubes, break down and become more complex to package and the free edge tends to initiate buckling near the root transition. Closed cross sections are desirable and the double omega rib shows the most promise utilizing elastic composite materials. A scaling effort is underway and double omega ribs have been fabricated and tested for packaging robustness, stiffness and buckling. The ribs have been verified to allow 3 m apertures and scaling studies have shown capability up to 8 m apertures.

5.2.2.2 Hub

The hub is the central structure that packages and deploys the ribs. The hub includes the spool, hub frame, rib interfaces and the motor drive assembly. The primary challenge is creating a simple interface to the ribs that packages efficiently, doesn't overstrain the ribs as they transition from deployed to flattened and wrapped and allows the ribs to reach a final position that is radially aligned through the center of the hub. This alignment is critical because it minimizes the moment that would otherwise be reacted through the ribs and into the hub.

The motor assembly includes the motor and gearbox. The motor includes an encoder to give precise motor position feedback. The motor is directly tied into the spool assembly. The spool assembly includes the rotating rib interface features. The spool is supported on bearings within the hub frame assembly. The hub frame also includes the rib guide rollers which provide root support for the ribs during deployment. Figure 5.8 shows an exploded view of the hub assembly for the 1 m prototype reflector.

5.2.2.3 Battens

The battens set the height between the nets. Consequently they react a compressive force and a bending moment as the compressive force from the ribs is balanced by the tensile force from the nets. Structurally there isn't a difficult requirement imposed on the battens. They do need to be thermally stable so the construction will typically be a carbon fiber reinforced plastic (CFRP) with a near zero coefficient of thermal expansion (CTE). The batten assembly does include the interface to the rib and also houses a low rate spring. The low rate spring ensures that any thermal expansion in the rib or any tolerance stack-up in manufacturing or deployment precision does not dramatically change the compression force in the rib which in turn would change the net tension (Figure 5.9).

5.2.2.4 Nets

The most important requirement for the reflector is to provide an adequate surface and pointing accuracy. The surface accuracy is derived from a systematic error plus a multitude of errors that are from many sources including manufacturing and

DETAIL C
SCALE 2:3
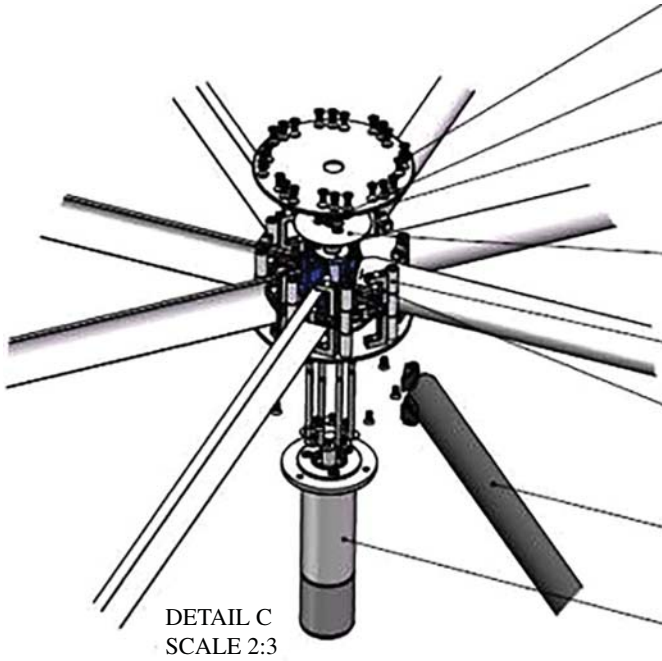
Figure 5.8   *1 m reflector hub and motor assembly.*
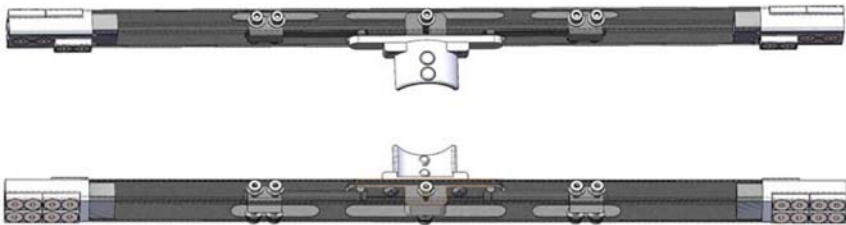
Figure 5.9   *Prototype reflector batten assembly.*

material effects. The systematic error for the Tendeg reflector is because the faceted net is not a perfect paraboloid. Obviously, the denser the net pattern, the more the net approaches a paraboloid. However, there are diminishing returns and a balance of performance versus complexity of the net must be achieved. Tendeg elected to use one-third of the surface accuracy budget on systematic error. This resulted in a desired facet size of approximately 65 mm (height of the facet projected into the aperture plane) assuming triangular facets. Tendeg considered different net patterns
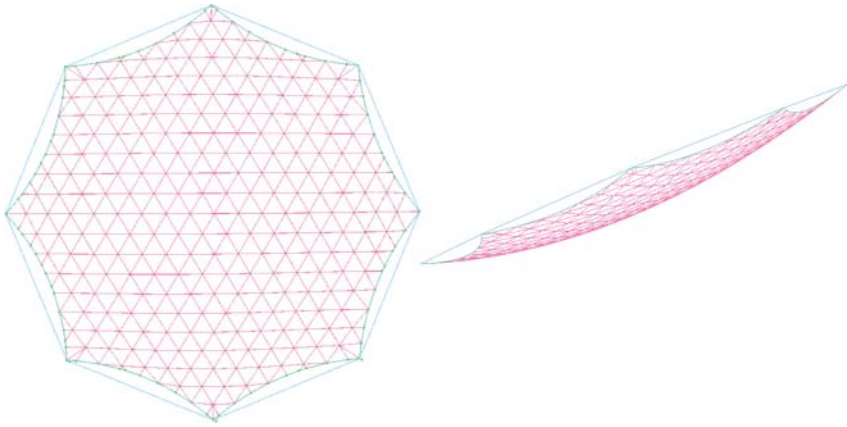
Figure 5.10   *Prototype reflector net design.*

and settled on a pseudo-geodesic pattern over eight ribs. Figure 5.10 shows the selected net pattern for the prototype reflector.

The net material selection was critical. Unidirectional aramid or carbon tapes would not work for this application because the tight packaging of the net would require the bend radii of the tapes to exceed their strain limits. A braided cord was selected and Tendeg reviewed numerous high-performance fibers. A fiber that demonstrated low stress relaxation was selected and a braided configuration study was done for each diameter. The variants included different yarn twist rates and different braiding twist rates. Each architecture was cycled to measure deflection vs. load. The repeatability, linearity and number of cycles to remove hysteresis were recorded. In addition, the samples were tested by Tendeg to determine general workability (termination and connections) and ability to package. From both the performance data and the workability testing, Tendeg selected a single architecture for each diameter (catenary, net, perimeter truss, tension ties). The cords were also coated. This provides an additional degree of workability by keeping the fibers and yarns from fraying and opening. The coating also provides proven atomic oxygen protection for low altitude LEO missions.

The prototype net was fabricated over a tool that allowed each node point of the facets to be placed on the correct offset paraboloid. The net cords were pre-tensioned to the predicted tensions from the detailed FEM that allowed the proper mesh tensioning with enough margin to eliminate or minimize pillowing effects. Pillowing can result when the mesh tension causes local buckling of the net cords. The net cords were then connected by hand at each node and the perimeter catenary was tensioned and the net cords were terminated to the catenary. The back-side net was made identically to the front-side net. During the fabrication of the nets the termination forces at the battens were controlled very tightly with digital load cells. This

is important because the ribs provide the same force at each batten and the front and backside nets have to balance each other.

5.2.2.5   *Perimeter Truss*

The perimeter truss comprises the longerons and the diagonals as shown in Figure 5.5. The diagonal is the more critical element because it provides shear stiffness for each batten bay which helps keep the battens vertical and coplanar to each other. The cords for the perimeter truss utilize the same material and braided properties described above. During final assembly the perimeter truss cords are tensioned to levels from the FEM and force balancing is maintained. The battens have cord adjustment and locking features that allow fine tuning.

5.2.3   Deployment

The offset design with an *f*/*D* of about 0.7 requires that the reflector must be positioned with a focal length of 0.7 m and an offset to the center of the aperture of 0.6 m. On a CubeSat bus that is only 30 cm deep and with a fixed feed this requires a deployable boom. The deployment sequence has three steps: (1) release the boom and reflector assembly, (2) deploy the 2-stage boom, and (3) deploy the reflector. The current baseline design has the booms deployed passively with spring energy and the reflector is deployed with a motor as described above.

5.2.3.1   *Boom Design and Deployment*

The boom assembly is shown in Figure 5.11. The boom assembly is three segments – tray, stage 1 and stage 2. The tray is the static structure that provides the mount for the fixed feed. The tray will be kinematically mounted to the cubesat bus. By including the tray it allows the boom, reflector and feed to be aligned as a payload. The tray will also minimize pointing misalignment that may be inherent in aluminum cubesat buses that are often dissipating heavy heat loads from embedded avionics.

The boom deployment sequence is shown in Figure 5.12. The boom segments clamshell around the reflector providing launch support and protecting the reflector and deployment mechanisms from contamination. After release, the first stage rotates away from the tray with passive spring energy. Before the first stage completes its full rotation the second stage is released by an internal mechanism. The second stage is also deployed with passive spring energy. The final position of the boom stages is determined by adjustable hard stops. The remaining spring force provides a final position preload and magnetic latches can also be included. The design does incorporate eddy current dampers to minimize the total deployment energy and impact loading at the end of rotations. If necessary, the eddy current dampers could be replaced with motors which would supplant the spring drives.
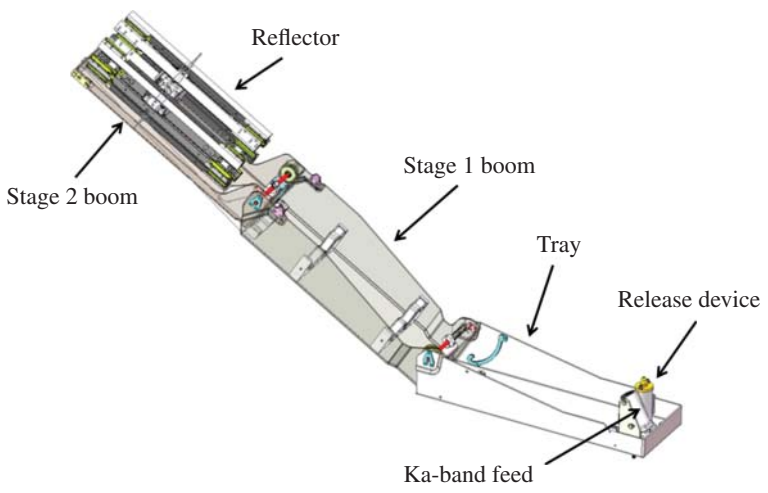
Figure 5.11   *Tendeg boom design.*
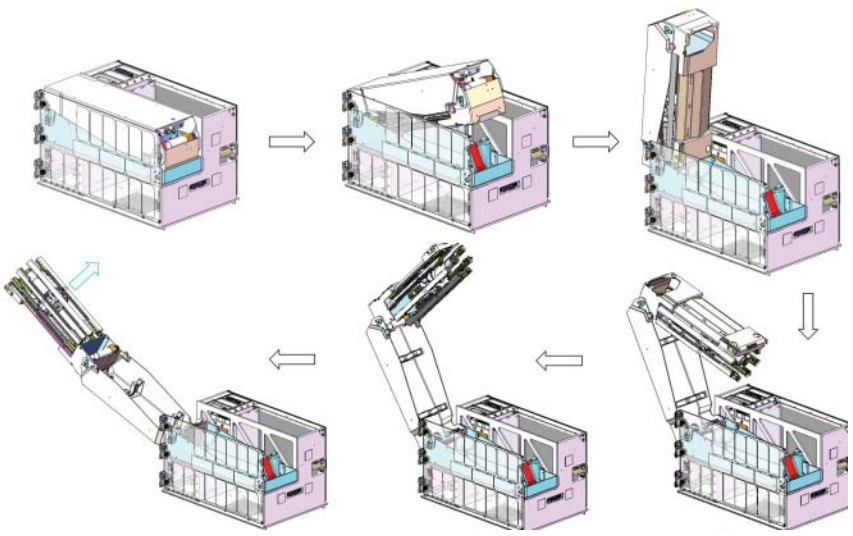
Figure 5.12   *Boom deployment sequence.*

Since the boom assembly is a critical structural element for the reflector positioning, it will be fabricated with low CTE carbon fiber reinforced polymer. At this time, the on-orbit thermal analysis does not show extreme temperatures that require specialized optical coatings.

5.2.3.2   Reflector Deployment

The spiral wrapped ribs contain a significant amount of stored strain energy. If the reflector was released from the stowed position the ribs would self-deploy. This type of deployment is not desired for several reasons. Primarily it introduces unwanted dynamics and would result in a rapid tensioning of the mesh and nets. And a dynamic deployment is difficult to properly offload in earth gravity. To make the deployment repeatable and low energy, the ribs are slowly unwrapped with a motor assembly. The motor provides negative torque through the full deployment until the final few degrees of rotation when the ribs go into compression.

During development, the transition to the final and fully tensioned geometry was a concern. If the compressive force builds up too soon it can cause the ribs to bloom on the spool or the combination of moment with axial force could cause the rib to buckle. However, this concern was not realized. Through careful design, the ribs are able to fully recover their cross section before they are axially compressed. And the compression only occurs when the ribs are nearly aligned radially. This means the ribs do not have to react a large moment at the end of deployment which could trigger a buckling mode. The end of the reflector deployment has been very robust and no failures have been detected. The antenna fully deployed is illustrated in Figure 5.13.
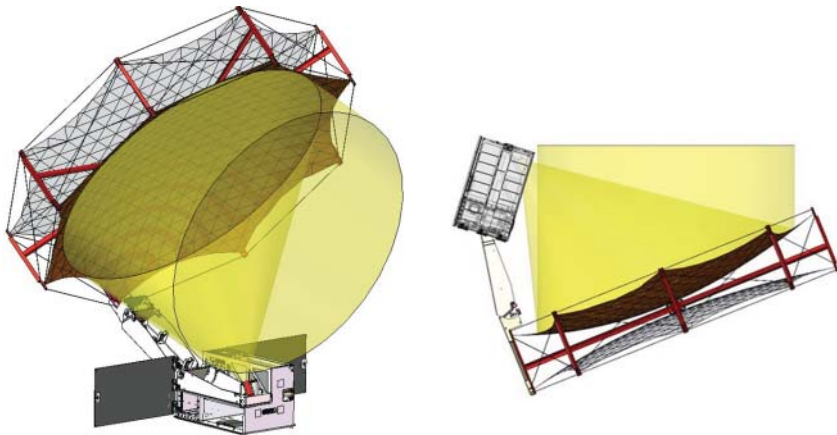
Figure 5.13   *Full deployment showing feed and bore illumination.*

5.2.3.3 *Deployment Issues*

Multiple deployments have been completed of a breadboard boom assembly and of both a breadboard and prototype reflector. The passively deployed booms did exhibit some large impact loads. This is often the case when sizing springs to carry 200% margin at the end of deployment against worst case temperature, friction and drag conditions. From these observations and simulations, eddy current dampers were added to the deployment mechanism.

The remaining reflector deployment issues are mainly due to cord management and snag potential. The perimeter longerons and diagonals have a long span and when the reflector is stowed they have the potential to loop over battens or snag on batten features. The prototype batten had some protruding headed fasteners that provided a snag feature. This has been corrected on the new batten design. However, fully managing the cords will require a shroud that is part of the battens. This will keep the cords from migrating during launch vibration and will prevent the cords from being able to loop over any battens.

The 1 m antenna assembly has been designed to generic mission requirements and the design is currently being fabricated to flight materials and tested in flight like environments (vibration, hot and cold TVAC (thermal vacuum chamber) deployments) to achieve technology readiness level (TRL) 6. Once a mission is defined additional analysis and testing is needed to verify that the antenna inertial loading during deployment does not destabilize the cubesat bus.

5.3   X/Ka RF Design

5.3.1   Antenna Configuration and Simulation Model

The mesh reflector is an offset reflector to accommodate the deployment of the reflector away from the feed to minimize the side lobe levels and minimize blockage from the feed or bus.

The reflector effective diameter is about 1 m and the focal length of the 1 m reflector is 0.75 m. For all efficiency calculation, an effective diamtere of 1 m will be assumed. The antenna optics is shown in Figure 5.14. For an edge taper of -10 dB, a feed directivity of 15.5 dBi is required. Theoretically, the taper and spillover efficiency of an offset reflector can be as low as 0.8 dB.

The antenna is simulated using TICRA GRASP using Physical Optics (PO) and method of moment (MoM) /multilevel fast multipole method (MLFMM) solver. The CubeSat and boom are described as a MoM object to assess the scattering from boom and CubeSat bus. The antenna configuration is illustrated in Figure 5.15. The feed is designed and analyzed using a full wave software (CST MWS). The field of the feed is imported as a tabulated feed where the pattern is described on a full sphere on a set of equidistantly spaced points in θ and φ. The phase center of the feed is located at the focal point of the reflector to maximize performance.
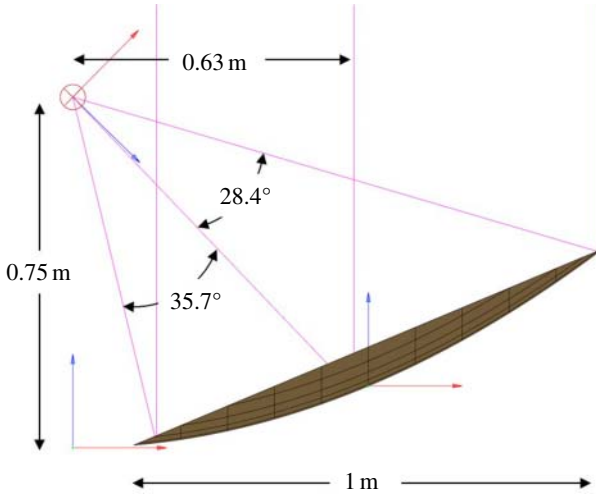
Figure 5.14   *One-meter deployable mesh reflector optics and dimensions.*
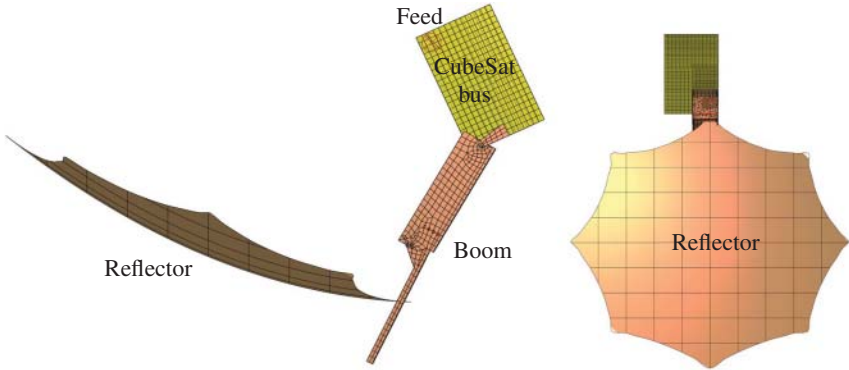
Figure 5.15   *Mesh reflector antenna model including the mesh reflector, deployable boom, and 12U CubeSat bus.*

The mesh reflector uses commercially available 30 OPI mesh which is suitable for X- and Ka-band. At X-band, a 30-OPI mesh reflects most of the incident power (i.e. <0.03 dB gain loss). At Ka-band, the 30-OPI mesh leads to a 0.25 dB loss. Please note that in [3, 4], a 40-OPI mesh that presents better performance at Ka-band was employed but 30-OPI mesh is more readily accessible.

The surface of the mesh reflector was measured using a FaroArm, a non-contact 3D laser scanning measurement technique before performing the RF test. The surface rms remains below 0.38 mm in the effective 1-m aperture (Figure 5.16). The
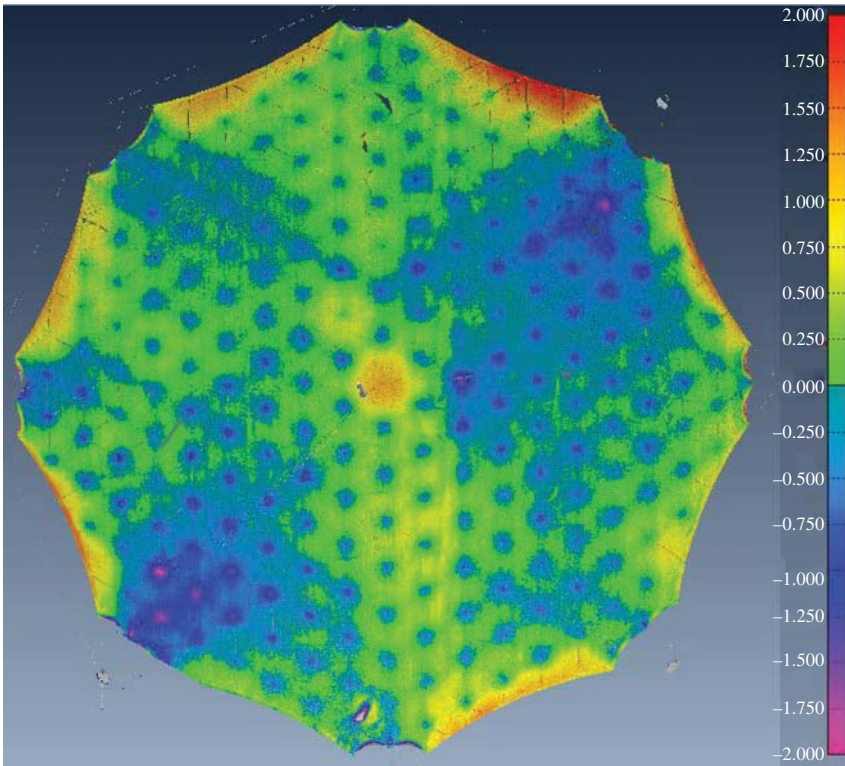
Figure 5.16   *Mesh reflector surface accuracy measurement demonstrating a surface rms of 0.38 mm.*

loss due to the surface deformation is calculated using Ruze's equation [14]. While this surface rms is negligible at X-band, it will lead to a 1.1 dB gain loss at Ka-band and will affect the side lobe levels. As a result, the mesh reflector is described using the actual measured surface in the TICRA GRASP's model. The reflector used in this test is a first article prototype and surface accuracy is expected to be improved with future builds. The antenna performance at X-band and Ka-band will now be discussed.

5.3.2   X-Band Feed and Mesh Reflector

The X-band feed needs to operate at X-band uplink (7.145–7.19 GHz) and downlink (8.4–8.45 GHz) frequency bands. The antenna needs to survive harsh temperature cycling and potentially high radiation levels. The X-band feed should be left handed circularly polarized (LHCP) at both uplink and downlink frequency bands. An innovative circularly polarized antenna, capable of operating in harsh environment was
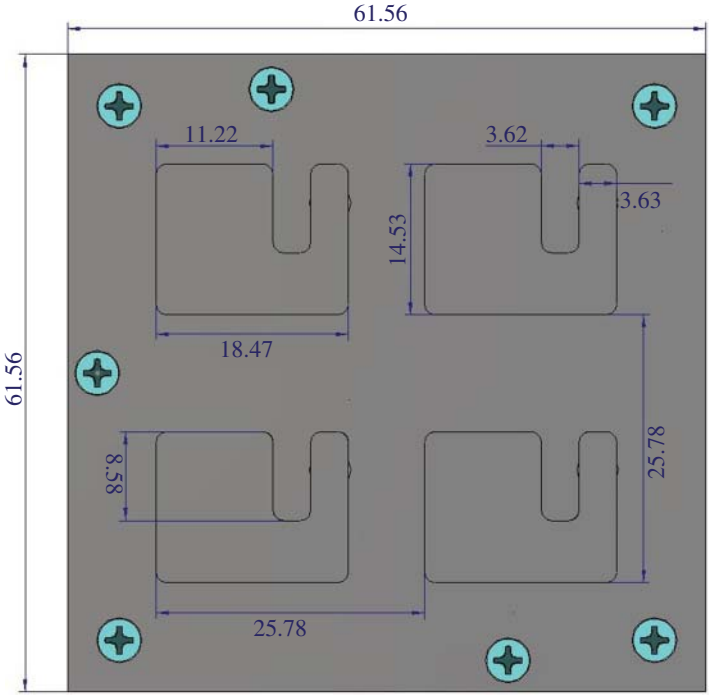
Figure 5.17   *Dual frequency X-band feed with LHCP polarization. Dimensions are in mm.*

proposed in [15] for the Europa Lander mission. As this antenna operates at both uplink and downlink frequency bands, it can be used to meet the mesh reflector requirements. As a result, a 2×2 patch array with LHCP was designed to illuminate the one meter mesh reflector. The feed antenna is shown in Figure 5.17. The unit cell is fed at a single point and is entirely made of metal. This element is single-fed thereby simplifying the feeding network and the antenna assembly. The unit cell was optimized in an array configuration to achieve an edge taper ranging between -10 and -12 dB.

The air stripline corporate feed network was designed to achieve less than -10 dB within the uplink and downlink frequency bands with sufficient thermal guard. The calculated and measured reflection coefficients of the antenna are in good agreement (Figure 5.18). The radiation pattern is measured in a planar near-field anechoic chamber at NASA's Jet Propulsion Laboratory, Pasadena, CA, USA. The radiation pattern is shown at the center frequency of uplink (i.e. 7.1675 GHz) and downlink (i.e. 8.425 GHz) frequency bands in Figures 5.19 and 5.20, respectively. The calculated and measured results are in good agreement. The calculated and measured directivity and gain of the X-band feed are summarized in Table 5.1.
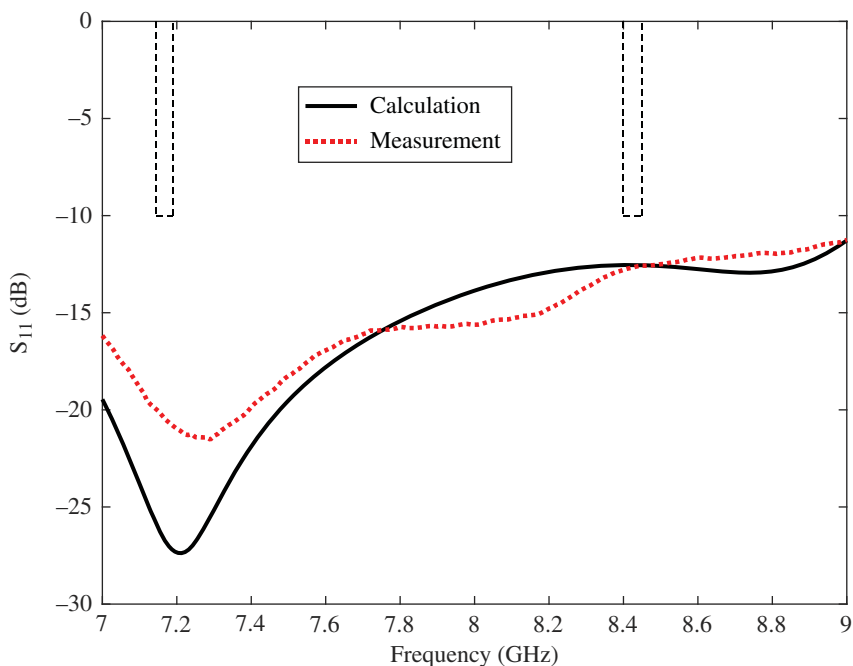
Figure 5.18 *Calculated and measured reflection coefficient of the X-band feed.*

One should note that the cross-polarization discrimination can be improved significantly by implementing sequential rotation. By doing that, the cross-polarization can be as good as 25 dB at both uplink and downlink frequency bands at the feed and reflector level. These results are not shown here.

Assuming an effective area of one meter, the standard directivity $D_{max} = (\pi \cdot D/\lambda)^2$ of the reflector is 37.5 and 38.9 dBic at 7.1675 and 8.425 GHz, respectively,. The loss contributions are summarized in Table 5.2. The taper and spillover loss are slightly higher than ideal as the edge taper is about -8 dB. At X-band frequency, the mesh OPI loss and surface accuracy loss are negligible (i.e. <0.05 dB). The gain loss at X-band as a function of surface rms is shown in Figure 5.21. It is worthwhile to note that a surface rms of 0.38 mm is good enough for X-band usage. The feed loss and mismatch loss are around 0.5 dB.

The calculated overall gain of the mesh reflector antenna is about 35.85 and 36.95 dBic at 7.1675 and 8.425 GHz, respectively. This translates into an efficiency of 68 and 64% at 7.1675 and 8.425 GHz, respectively. This is more than the Raincube antenna, as one would expect, since it is an offset reflector (i.e. no blockage from the struts and subreflector). In addition, the sidelobe levels are much smaller also due to the offset configuration (i.e. >20 dB as opposed to 15 dB for the Raincube antenna).
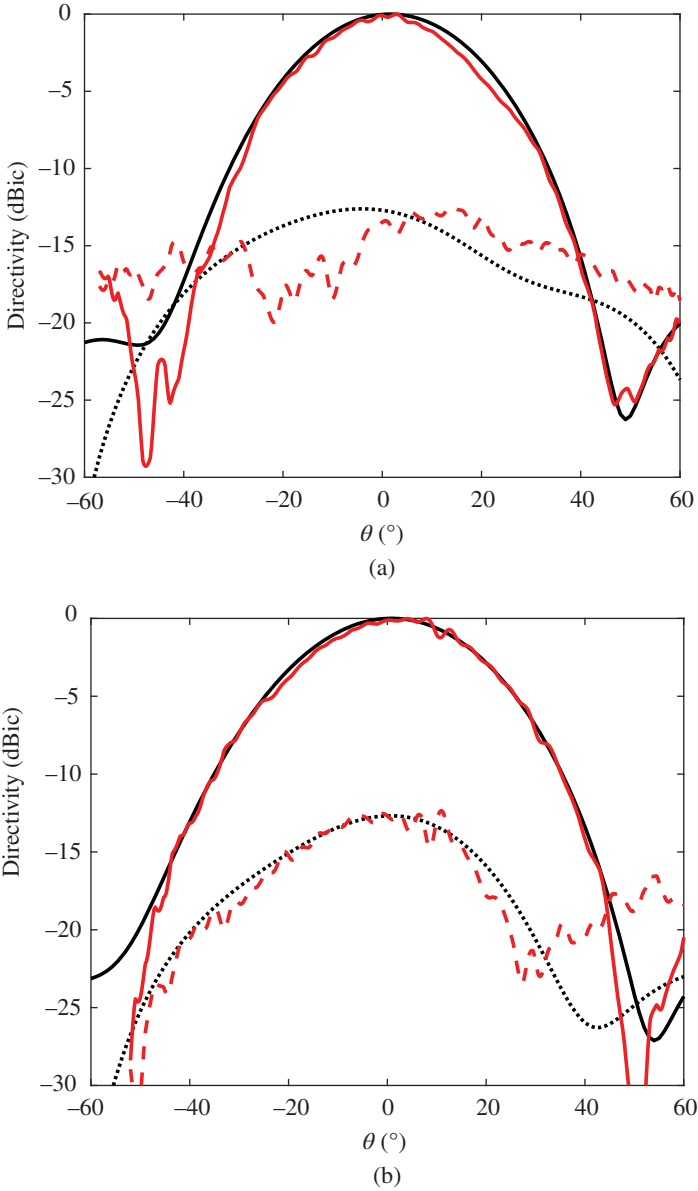
Figure 5.19 *Normalized X-band feed radiation pattern at 7.1675 GHz. — LHCP. ---*
RHCP. Calculation in black and measurement in gray. (a) φ = 0°; (b) φ = 90°.
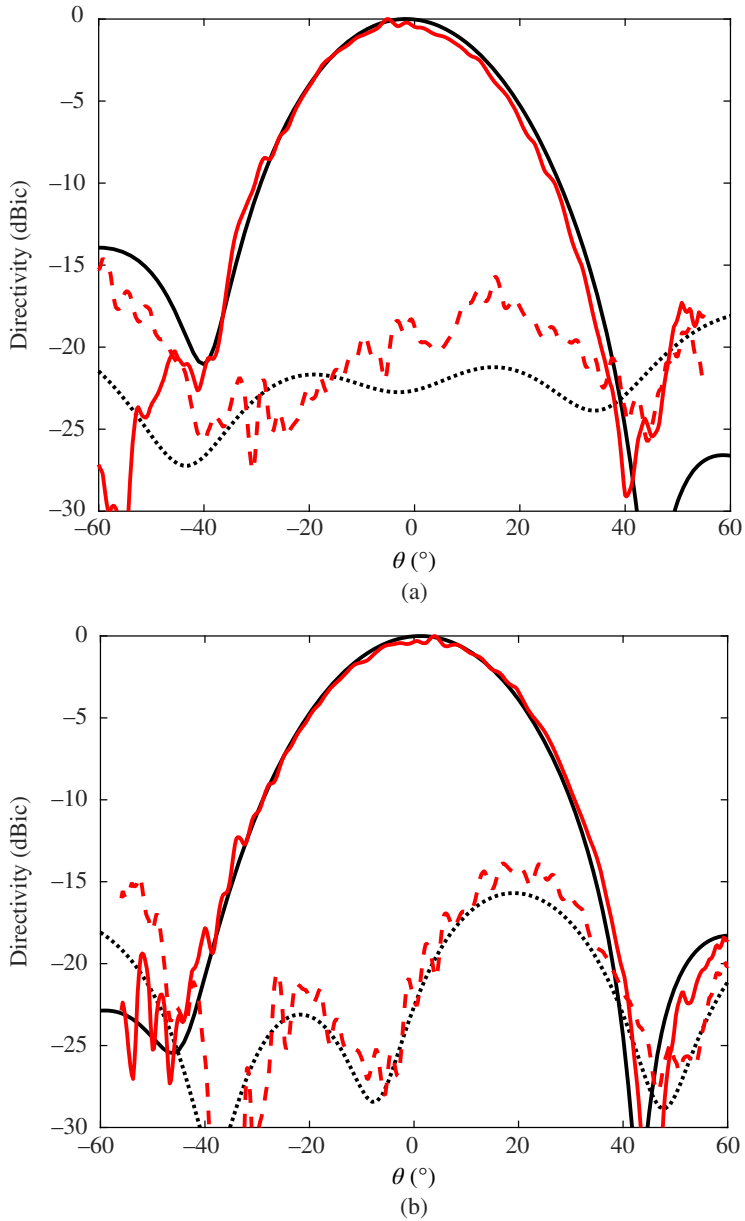
Figure 5.20   *Normalized X-band feed radiation pattern at 8.425 GHz. — LHCP. ---
RHCP. Calculation in black and measurement in gray. (a) $\varphi = 0°$; (b) $\varphi = 90°$.*

Table 5.1   Calculated and measured X-band feed performance.

Frequency (GHz)		Directivity (dBi)		Gain (dBic)	
		Calc.	Meas.	Calc.	Meas.
X-band	7.1675	13.5	13.8	13.4	13.1
	8.425	14.3	15.1	14.0	14.0

Table 5.2   X-Band mesh reflector gain table at X-band.

	Uplink		Downlink	
	Gain (dBic)	Loss (dB)	Gain (dBic)	Loss (dB)
Standard directivity	37.5	—	38.9	—
Taper	37.2	0.3	38.4	0.5
Spillover	36.3	0.9	37.4	1.0
Surface mesh[a] (30 OPI)	36.28	0.02	37.38	0.02
Surface accuracy[b] (±0.38 mm)	36.22	0.06	37.30	0.08
Feed loss	35.92	0.3	37.00	0.3
Feed mismatch (RL = 15 dB)	35.82	0.1	36.90	0.1
Overall performance	35.82	1.68	36.90	2.00

[a]Based on calculated results using GRASP model of a 30 OPI mesh.
[b]Using Ruze's equation [14]. The surface accuracy was adjusted with the measured surface accuracy.
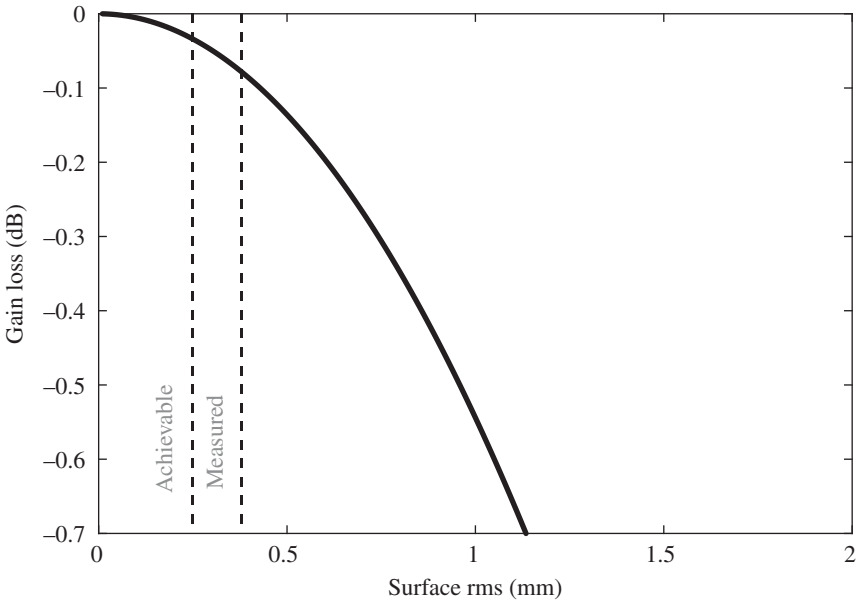
Figure 5.21   *Gain loss versus surface rms at X-band.*
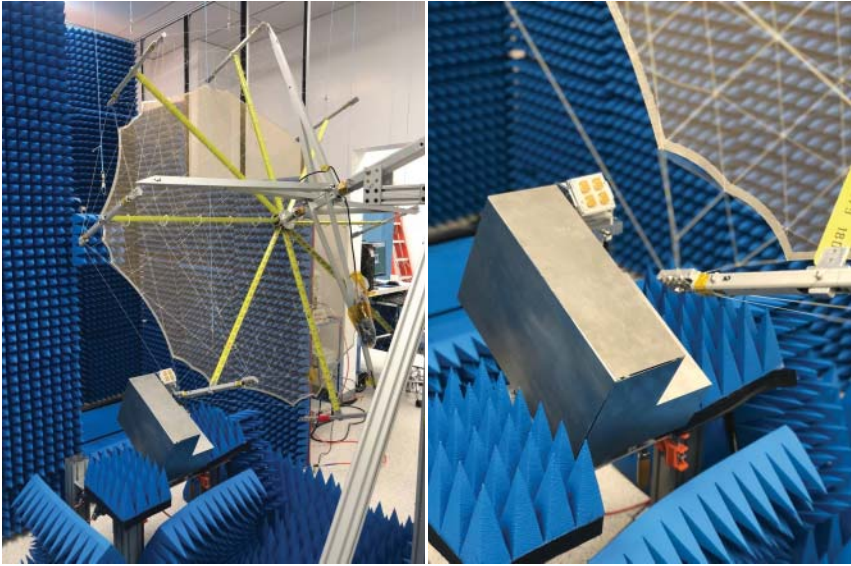
Figure 5.22   *X-band mesh reflector in the near field anechoic chamber with its off-load structure. Note that the boom is not included. The CubeSat bus is included.*

The radiation pattern is measured in a planar near-field anechoic chamber at NASA's Jet Propulsion Laboratory, Pasadena, CA, USA where the feed is mounted onto a bus simulator as can be seen in Figure 5.22. The radiation pattern of the reflector mesh antenna is shown in Figure 5.23. A good agreement is obtained. The axial ratio is lower than 3 dB within the downlink frequency band and lower than 4.5 dB within the uplink frequency band. The directivity and gain of the X-band mesh reflector are summarized in Table 5.3. A gain of 36.1- and 36.8-dBic is measured at uplink and downlink frequency bands, respectively. This translates into an efficiency of 72 and 62%, respectively.

It is important to discuss the impact of the achieved cross-polarization discrimination on the overall link budget with a DSN antenna. Most 34 and 70 m DSN antennas, have an XPD of 25 dB (i.e. axial ratio of 0.8 dB). At uplink, the antenna demonstrates an XPD of 12 dB (i.e. axial ratio of 4.4 dB) which would result in a polarization loss of 0.4 dB. At downlink, the XPD is around 17 dB (i.e. axial ratio of 2.5 dB) which would result in only 0.15 dB of polarization loss. Hence, the antenna is properly designed for deep space communications as the link will have excessive margin for uplink and 0.15dB of loss for downlink is acceptable.

However, as mentioned earlier, the cross-polarization discrimination can be improved significantly by using sequential rotation on the feed. More than 25 dB can be achieved at both uplink and downlink frequency bands by doing so.

This is a significant improvement compared to the state of the art. First, this antenna operates at both uplink and downlink at X-band and is fully compatible with
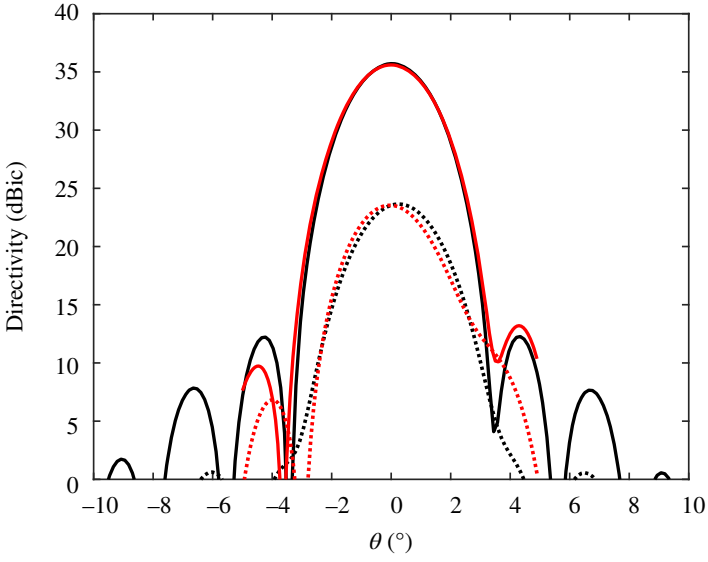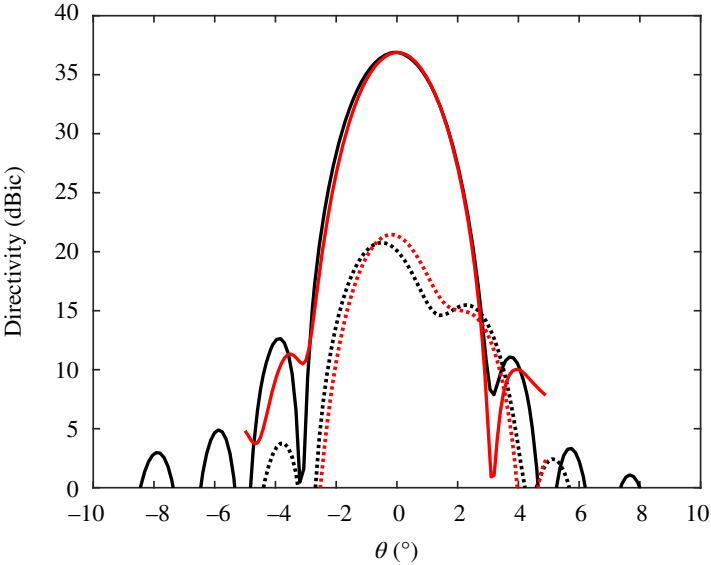
Figure 5.23 *X-band mesh reflector radiation pattern at (a) 7.1675 GHz and (b) 8.425 GHz. — RHCP. --- LHCP. Calculation in black and measurement in gray.*

Table 5.3 *X-Band mesh reflector directivity, gain, and loss at X-band.*

Freq. (GHz)	Directivity (dBi)		Gain (dBic)		Efficiency (%)	
	Calc.	Meas.	Calc.	Meas.	Calc.	Meas.
7.1675	36.3	36.9	35.8	36.1	68	72
8.425	37.4	38.2	36.9	36.8	64	62

the DSN. Compared to the MarCO high gain antenna, this represents an increase of 8 dB (∼6.3 times increase in data rate). However, the deployment complexity is higher and the stowage volume bigger. While MarCO's high gain antenna can only receive, this antenna can transmits telemetry and receive commands.

Using a 70 m DSN antenna, a telemetry data rate of 64 kbps can be achieved at a distance of 1 AU (i.e. 149 million km). Using a 34 m DSN antenna, the spacecraft could receive commands at 2 kbps at distances as large as 8 AU (i.e. 1.2 billion km).

5.3.3 Ka-Band Mesh Reflector

The design of a Ka-band is much simpler with a goal of achieving an edge taper illumination of −10 dB. The feed is designed using TICRA Champ, using mode-matching body of revolution (BoR) method, following the method described in [16]. The feed is a multiflare horn demonstrating low cross polarization, low side-lobe level, good return loss, and excellent beam circularity.

A genetic algorithm is used to optimize edge taper, directivity, cross-polarization, and beam circularity. It is also easy to fabricate. The antenna feed dimensions and photography are shown in Figure 5.24. As the feed antenna needs to provide LHCP, we designed a Ka-band polarizer operating at both uplink and downlink Ka-band.
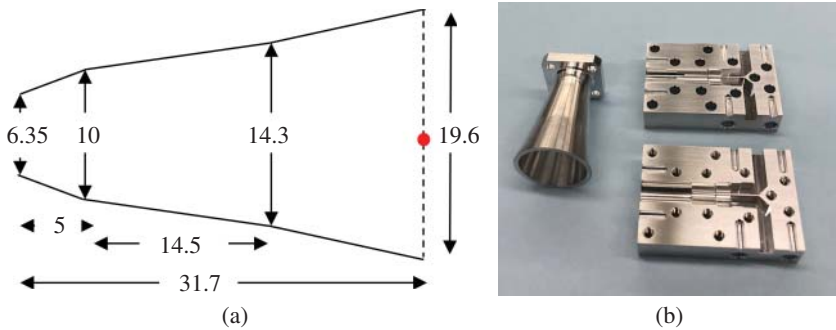
Figure 5.24 *(a) Ka-band feed horn dimensions in mm. The phase center of the antenna is shown in gray. (b) Photography of the fabricated Ka-band horn and polarizer.*
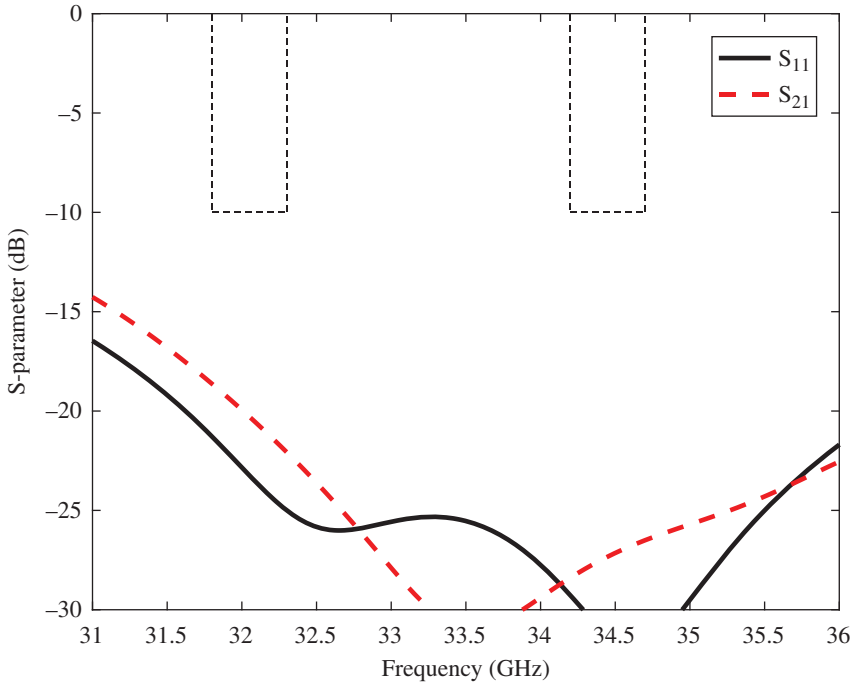
Figure 5.25 *The OMT polarizer reflection coefficient of LHCP port and isolation between the two input ports.*

The polarizer was specifically designed for this antenna to fit within the allocated volume. The refection coefficient of the antenna with its polarizer is shown in Figure 5.25.

The mesh reflector performance is calculated using TICRA GRASP. The feed horn phase center (shown in Figure 5.24) is located at the focal point of the reflector. The loss breakdown of the mesh reflector at Ka-band is summarized in Table 5.4. The taper and spillover loss are smaller than at X-band because it is easier to meet the edge taper requirement with a horn. The surface mesh and surface accuracy loss are obviously much larger than at X-band (0.25 and 1.1 dB, respectively). The total calculated loss due to the mesh is about 1.35 dB at 32 GHz. However, it is important to highlight that the reflector used in this test is a first article prototype and surface accuracy is expected to be improved with future builds. An improvement from 0.38 mm surface rms to 0.25 mm would improve the gain by 0.8 dB and this is illustrated in Figure 5.26 where the gain loss is shown for surface rms ranging from 0 to 0.4 mm. The surface accuracy is a critical parameter at Ka-band as it will impact the side lobe levels, directivity, and gain of the antenna. The mesh surface is measured accurately using a non-contact 3D laser scanning measurement technique

Table 5.4 *Ka-band gain table at 32 GHz.*

	Gain (dBic)	Loss (dB)
Standard directivity	50.5	—
Taper	49.9	0.6
Spillover	49.5	0.4
Surface mesh (30 OPI)	49.25	0.25
Surface accuracy (0.38 mm rms)	48.15	1.1
Feed loss	48.10	0.05
Feed mismatch (RL = 15 dB)	48.05	0.05
Overall performance	48.05	2.45
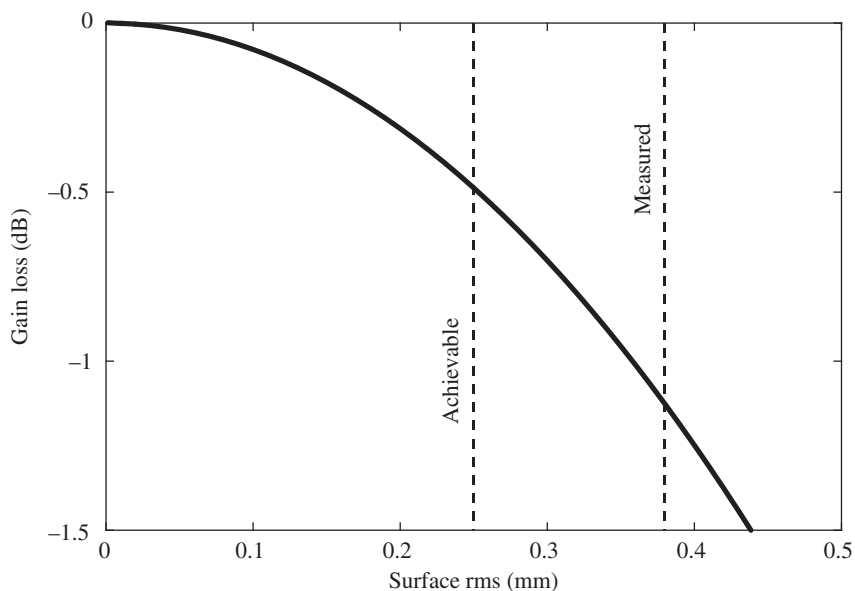
Figure 5.26 *Gain loss versus surface rms at Ka-band. Note that the mesh surface accuracy can be improved.*

and the data is incorporated into the calculation. The impact of the surface accuracy is illustrated in Figure 5.27, where the radiation pattern of an ideal reflector and the actual reflector are compared. The gain reduction and the side lobe level increase are obvious.

The radiation pattern is measured in a planar near-field anechoic chamber at NASA's Jet Propulsion Laboratory after replacing the X-band feed with the Ka-band feed. As shown in Figure 5.28, the calculated and measured radiation
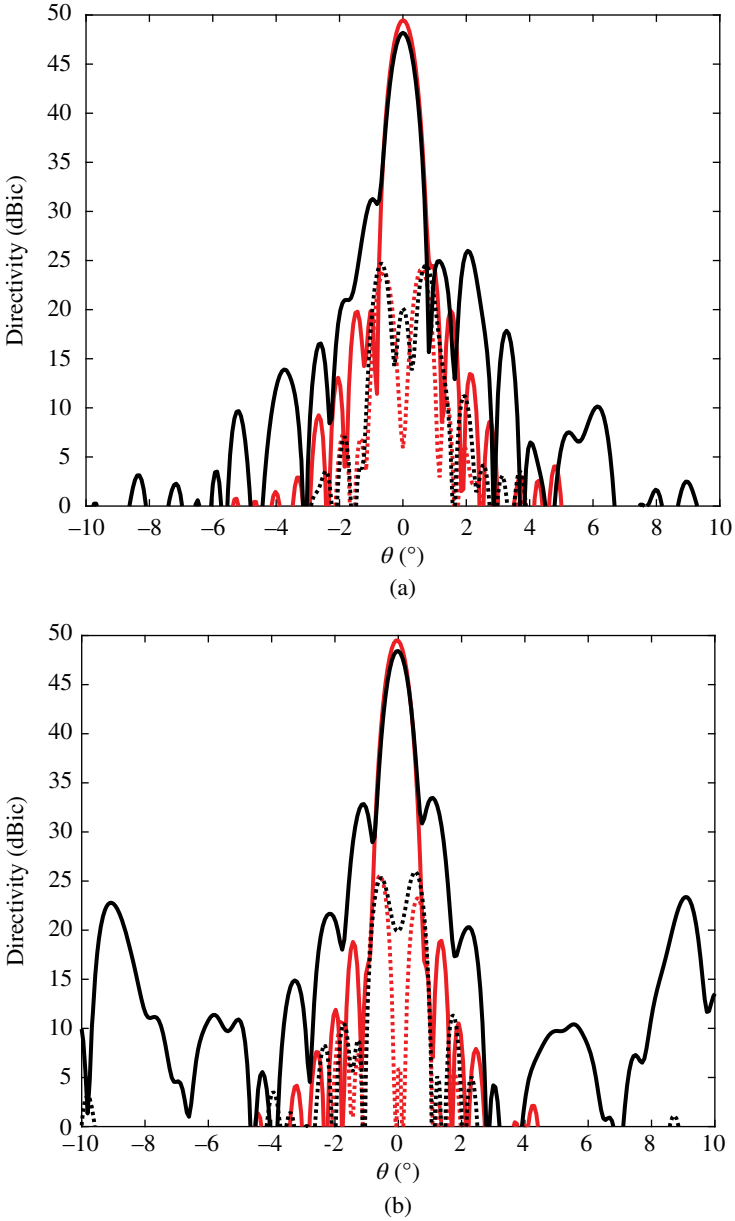
Figure 5.27   *Calculated radiation pattern of the Ka-band mesh reflector. — RHCP. ---LHCP. (a) $\varphi = 0°$. (b) $\varphi = 90°$. In gray: calculated with an ideal reflector. In black: calculated with the measured surface.*

(a)

(b)
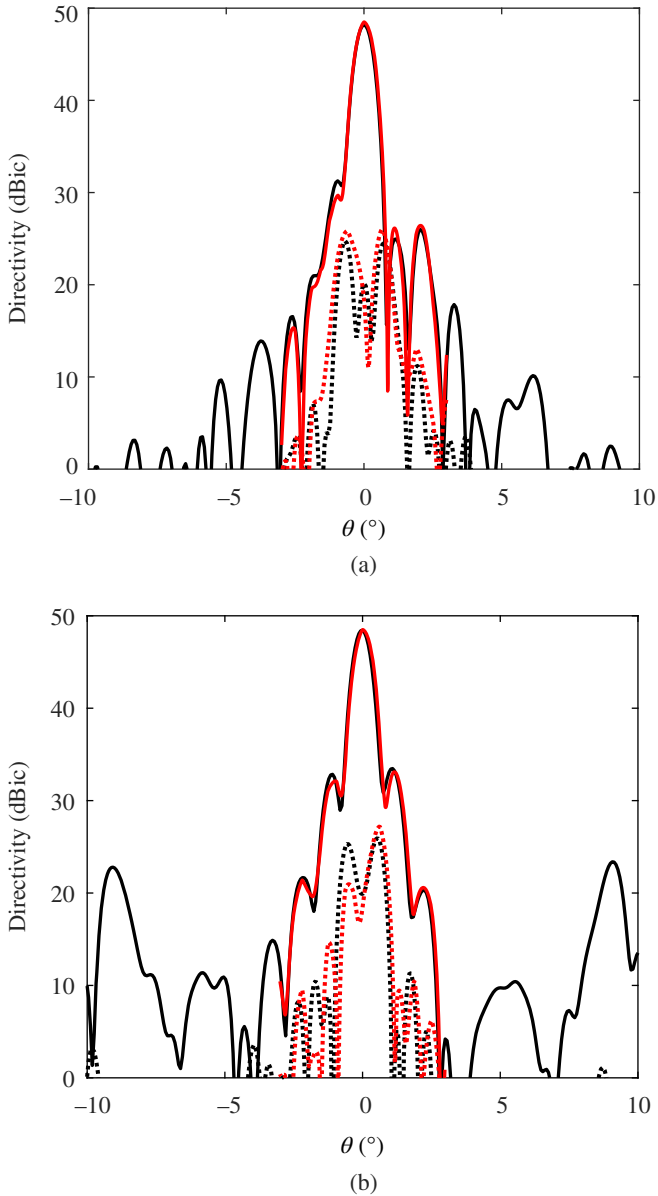
Figure 5.28 *Measured and calculated radiation pattern of the Ka-band mesh reflector.*
— RHCP. --- LHCP. (a) φ = 0°. (b) φ = 90°. In gray: measured. In black: calculated.

Table 5.5 Ka-band antenna directivity, gain, and efficiency at 32 and 34.45 GHz.

Frequency (GHz)	Directivity (dBi)		Gain (dBic)		Efficiency (%)	
	Calc.	Meas.	Calc.	Meas.	Calc.	Meas.
32	48.4	48.8	48.1	48.4	58	62
34.45	48.5	49.0	48.3	48.7	52	57

pattern are in good agreement. A gain of 48.4 dBic was measured at 32 GHz, which translates in a 62% efficiency, assuming an effective aperture of 1 m.

It is a 6 dB increase compared to the 0.5-m mesh reflector antenna presented in [4]. A 6 dB gain increase translates into a data-rate increase by a factor of 4. In theory, since this is an offset reflector, the side lobe levels can be much smaller (i.e. <25 dB) but they are affected by the surface accuracy of the reflector. At 34.45 GHz, a gain of 48.7 dBic was measured, which translates into a 57% efficiency (Table 5.5).

A closer look at Figure 5.27 is of great interest. The co-polar pattern in elevation ($\varphi = 0°$) is shown, with the pattern produced by the nominal paraboloid in gray and by a uniform mesh with the actual measured reflector in black (i.e. uniform mesh with hexagonal symmetry with equilateral triangle side length of 7.3 cm and 295 nodes). This mesh reflector exhibits the characteristic grating lobes around $|\theta g| = 9.0°$.

As a parabolic reflector with a feed at focus generates a constant aperture phase, it yields in the best possible performance. A nominal paraboloid can be conceptually be thought as a mesh reflector with triangular mesh side length m_1 tending to 0. When the paraboloid is generated by a mesh of planar triangular facets, the surface is no longer ideal leading to a reduction of peak directivity and the generation of grating lobes. The grating lobes will appear at an angle θg given by:

$$\sin \theta_g = \frac{2\lambda}{m_1} \tag{5.1}$$

in the $\varphi = 0° + p\,60°$ planes and by:

$$\sin \theta_g = \frac{2\lambda}{\sqrt{3}m_l} \tag{5.2}$$

in the $\varphi = 30° + p\,60°$ planes.

For $m_1 = 6.9$ cm, the grating lobes in $\varphi = 90°$ should be found at $|\theta g| = 9.1°$. The grating lobes can be reduced if necessary by using different mesh topologies. Making divisions in the radial direction at non-regular intervals (see Figure 5.29) allows to reduce the grating lobes by almost 10 dB without changing any fundamental components such as the number of divisions and the number of parts [17]. While the sidelobes are suppressed in the non-regular division case, the gain reduction is

(a)   (b)
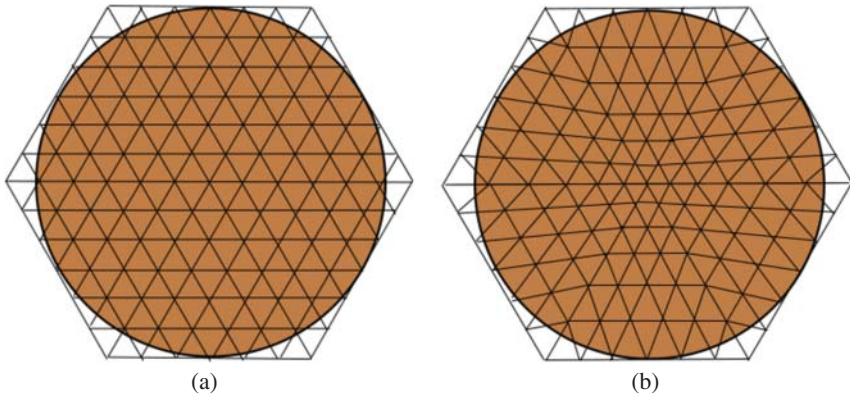
Figure 5.29   *Illustration of (a) uniform hexagonal mesh reflector and (b) non-uniform or arithmetic mesh for grating lobes suppression. Source: Modified from Orikasa et al. [17]. © 1993 John Wiley & Sons.*

slightly worse than with regular intervals and this is because the surface accuracy is slightly worse.

It was shown in [18] that the arithmetic pentagonal mesh can also decrease unwanted radiation pattern grating lobes by almost 10 dB compared to a uniform hexagonal mesh. This discussion is exclusively informative for the reader, as there is no need for deep space communication to control the grating lobes.

5.3.4   X/Ka-band Mesh Reflector

The two feeds can be used simultaneously with the one meter reflector while fitting in the stowage volume while meeting the telecommunication scenario. As the co-located feeds are not placed at the focal point of the reflector, the pointing, gain, and efficiency will be affected. The pointing is less of an issue. Typically, in a mission scenario where both X- and Ka-band are expected to be used simultaneously, commands will be received at X-band and telemetry transmitted to the DSN at Ka-band.

In this case, maximum gain should be targeted at Ka-band (i.e. >47.5 dBic) while a reduced gain at X-band (i.e. > 20 dBic) is needed to relax the pointing requirement. This is explained by two things:

1. the DSN RF output power (i.e. 20 kW) is significantly higher than the on-board solid state power amplified output power (i.e. typically around 5 W).
2. uplink data rate are usually around 1 or 2 kbps, much smaller than downlink data rates.

When both feeds are co-located, the X-band antenna demonstrates a gain of 35.2 and 36.8 dBic, at uplink and downlink frequency band, respectively. The Ka-band

Table 5.6　*Calculated directivity and gain of the X/Ka-band antenna.*

Frequency (GHz)	Directivity (dBi)	Gain (dBi)	Efficiency (%)	Pointing in Az (°)
7.1675	35.6	35.2	59	−2.1
8.435	36.8	36.3	55	−2.1
32	47.9	47.6	51	+0.6
34.45	48.0	47.8	46	+0.6

antenna has a gain of 47.8 and 47.6 dBic, at uplink and downlink frequency band, respectively. The directivity, gain, efficiency and pointing direction of the antenna is shown in Table 5.6.

The X-band antenna demonstrates a gain of 20.5 dBic at +0.6° in azimuth which is meeting the requirement to provide simultaneous X/Ka-band communication. An uplink data rate of 2 kbps can be achieved with 20.5 dBic of gain at a maximum distance of 2 AU (i.e. 299 million km) (Table 5.6).

5.4　Conclusion

The antenna presented in this chapter answers to a clear need for higher data rate for CubeSats or Small satellites. It also provides, for the first time, X- and Ka-band capabilities on a CubeSat. As this antenna folds in a 3U volume, it is compatible with 12U-class CubeSats.

At X-band, a gain of 36.1- and 36.8-dBic is achieved at uplink and downlink frequency bands, respectively. This translates into an efficiency of 72 and 62%, respectively. For the Ka-band only antenna, a gain of 48.4- and 48.7-dBic is obtained at downlink and uplink frequency bands which translates to a 62 and 72% efficiency.

The performance of the antenna is also given when both X-band and Ka-band feeds are collocated. The antenna efficiency at X-band is higher than 55% and higher than 50% at the Ka-band downlink frequency band.

This is a game changing technology for space exploration using Small Satellites enabling venturing farther into deep space while achieving higher data rate. As this mesh reflector is scalable to larger size (i.e. 3 to 4 m), this antenna has many other applications, such as remote sensing for NASA missions but also in the emerging new space for Synthetic Aperture Radar.

Acknowledgments

References

1. R. E. Hodges, N. Chahat, D. J. Hoppe, and J. D. Vacchione, "A Deployable High-Gain Antenna Bound for Mars: developing a new folded-panel reflectarray for the first CubeSat mission to Mars," *IEEE Antennas and Propagation Magazine*, vol. **59**, no. 2, pp. 39–49, Apr. 2017.

2. E. Peral, S. Tanelli, Z. S. Haddad, G. L. Stephens, and E. Im, "RaInCube: a proposed constellation of precipitation profiling Radars In Cubesat," *AGU Fall Meeting*, San Francisco, CA, Dec. 2014.

3. N. Chahat, R. Hodges, J. Sauder, M. Thomson, E. Peral, and Y. Rahmat-Samii, "CubeSat deployable Ka-band mesh reflector antenna development for earth science missions," *IEEE Transactions on Antennas and Propagation*, vol. **64**, no. 6, pp. 2083–2093, 2016.

4. N. Chahat, R. E. Hodges, J. Sauder, M. Thomson, and Y. Rahmat-Samii, "The Deep-Space Network Telecommunication CubeSat Antenna: using the deployable Ka-band mesh reflector antenna," *IEEE Antennas and Propagation Magazine*, vol. **59**, no. 2, pp. 31–38, Apr. 2017.

5. R. Hodges, D. Hoppe, M. Radway, and N. Chahat, "Novel deployable reflectarray antennas for CubeSat communications," *IEEE MTT-S International Microwave Symposium (IMS)*, Phoenix, AZ, May 2015.

6. N. Chahat, E. Thiel, J. Sauder, M. Arya, and T. Cwik, "Deployable One-Meter Reflectarray for 6U-Class CubeSats," *2019 13th European Conference on Antennas and Propagation (EuCAP)*, Krakow, Poland, 2019.

7. R. Walker, D. Koschny, C. Bramanti, and ESA CDF study team, "Miniaturised Asteroid Remote Geophysical Observer (M-ARGO): a stand-alone deep space CubeSat system for low-cost science and exploration missions," *Presentation at 6th Interplanetary CubeSat Workshop*, Cambridge, UK, 2017.

8. J. Taylor, K.-M. Cheung, and D. Seo, "Galileo telecommunications," in *JPL Deep Space Communication and Navigation Systems Center of Excellence*, Pasadena, CA: JPL, July 2002.

9. J. R. Piepmeier, P. Focardi, K. A. Horgan, J. Knuble, N. Ehsan, J. Lucey, C. Brambora, P. R. Brown, P. J. Hoffman, R. T. French, R. L. Mikhaylov, E.-Y. Kwack, E. M. Slimko, D. E. Dawson, D. Hudson, J. Peng, P. N. Mohammed, G. De Amici, A. P. Freedman, J. Medeiros, F. Sacks, R. Estep, M. W. Spencer, C. W. Chen, K. B. Wheeler, W. N. Edelstein, P. E. O'Neill, and E. G. Njoku, "SMAP L-band microwave radiometer: instrument design and first year on orbit," *IEEE Transactions on Geoscience and Remote Sensing*, vol. **55**, no. 4, pp. 1954–1966, Apr. 2017.

10. G. Freebury and N. Beidleman, "Deployable reflector," US patent 20170222308 A1, Jan 2016.

11. S. Gao, Y. Rahmat-Samii, R. E. Hodges, and X. Yang, "Advanced antennas for small satellites," *Proceedings of the IEEE*, vol. **106**, no. 3, pp. 391–403, Mar. 2018.

12. B.L. Ehlmann, A. Klesh, T. Alsedairy, R. Dekany, J. Dickson, C. Edwards, F. Forget, A. Fraeman, D. McCleese, S. Murchie, T. Usui, S. Sugita, K. Yoshioka, and J. Baker, "Mars nano orbiter: a Cubesat for mars system science," *49th Lunar and Planetary Science Conference*, The Woodlands, Texas, 19–23 March, 2018.

13. M. W. Thomson, "The AstroMesh deployable reflector," *AP-S*, Orlando, FL, July 1999, pp. 1515–1519.

14. J. Ruze, "Antenna tolerance theory—a review," *Proceedings of the IEEE*, vol. **54**, no. 4, pp. 633–640, Apr. 1966.

15. N. Chahat, B. Cook, H. Lim, and P. Estabrook, "All-metal dual frequency RHCP high gain antenna for a potential Europa lander," *IEEE Transaction on Antennas and Propagation*, vol. **66**, no. 12, pp. 6791–6798, Dec. 2018.

16. N. Chahat, T. J. Reck, C. Jung-Kubiak, T. Nguyen, R. Sauleau, and G. Chattopadhyay, "1.9-THz multiflare angle horn optimization for space instruments," *IEEE Transactions on Terahertz Science and Technology*, vol. **5**, no. 6, pp. 914–921, Nov. 2015.

17. T. Orikasa, T. Ebisui, and T. Okamoto, "Sidelobe suppression of mesh reflector antenna by non-regular intervals," *Proceedings of IEEE Antennas and Propagation Society International Symposium*, Ann Arbor, MI, 1993, pp. 800–803, vol. **2**.

18. J. R. de Lasson, C. Cappellin, R. Jorgensen, L. Datashvili, and J. Angevain, "Advanced techniques for grating lobe reduction for large deployable mesh reflector antennas," *2017 IEEE International Symposium on Antennas and Propagation & USNC/URSI National Radio Science Meeting*, San Diego, CA, 2017, pp. 993–994.

6

Inflatable Antenna for CubeSat

Alessandra Babuscia[1], Jonathan Sauder[2], Aman Chandra[2] and Jekan Thangavelautham[2]

[1]*NASA Jet Propulsion Laboratory/California Institute of Technology, Pasadena, CA, USA*
[2]*Arizona State University, Tempe, AZ, USA*

6.1 Introduction

The inflatable antenna for CubeSat concept has been in development at the Jet Propulsion Laboratory for more than 7 years. It is a new technology which aims at improving telecommunication for CubeSats and SmallSats by providing an inflatable antenna which can be stored in a very small space (less than 1 unit CubeSat, or $10 \times 10 \times 10 \, cm^3$ volume) and later deployed and inflated in space to provide high gain.

The basic concept is an inflatable balloon structure made of two different types of Mylar: a transparent Mylar and a reflective Mylar bonded together as shown in Figure 6.1. The antenna feed is designed using a simple patch antenna which can be placed inside or outside the inflatable structure depending on the shape and design of the reflector. In the final prototype discussed in this chapter, the patch antenna is placed inside the membrane.

One of the novelties of this antenna is the inflation mechanism which is realized using sublimating powder (mainly benzoic acid). The powder is stowed at the solid state inside the membrane of the antenna prior to launch. When the CubeSat reaches the desired orbit, a burn wire is used to open the canister which contains the antenna.
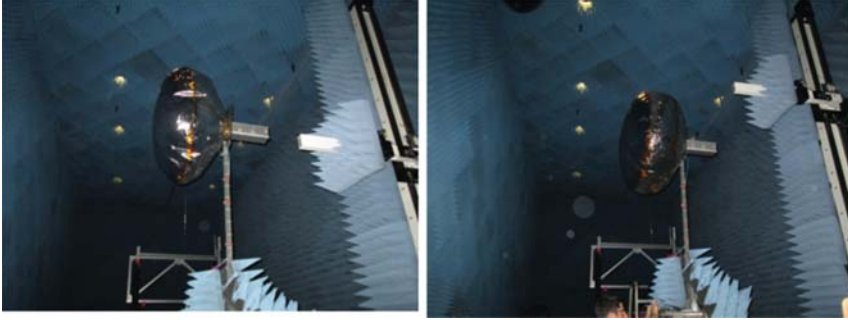
Figure 6.1   *Inflatable antenna prototype tested in anechoic chamber.*

The Mylar membrane is then left free to expand in volume and the difference of pressure with respect to the atmospheric pressure triggers the chemical reaction of benzoic acid allowing the antenna to inflate.

Another interesting feature of the benzoic acid is the possibility of being used as a make-up gas to compensate for eventual perforations in the membrane caused by micro meteoroids. In fact, not all the benzoic acid will instantaneously inflate when the antenna is deployed, but only the amount necessary to fill the volume. The remaining powder will remain in its solid state and sublimates only when the equilibrium changes in pressure or volume as it could happen in the case of micro meteoroids impacts.

Finally, another unique feature of the inflatable antenna design is the ultra violet (UV) rigidization that takes place in space. The rigidization is a feature that was introduced later in the design in an attempt to counteract the inevitable variations in the membrane shape that could happen as a result of the space environment, in particular the temperature fluctuations. The UV paste is applied to the inflatable antenna prior to launch. Once in space, the UV paste is exposed to the UV radiation by pointing the antenna to the Sun for a little less than half an hour. During this time, the UV radiation acts on the UV paste and rigidize it, which allows the inflatable antenna to maintain its shape regardless of temperature changes and even micrometeoroid punctures whenever the sublimating powder is fully exhausted.

The inflatable antenna was designed initially for S-Band and more recently for X-Band. The prototype described in this chapter refers mainly to the X-Band design, although some details on the S-Band experiment are described in Section 6.2. The dimension of the antenna is 1 m in diameter. This size was chosen mostly for ease of manufacturing, handling and testing, although the authors are considering expanding this design to larger structure.

In terms of applications, this antenna has been designed primarily with CubeSats in mind. However, it can be applied to all kind of SmallSats and constellations as described in [1]. Additionally, the inflatable antenna concept could be of interest for

Figure 6.2   *Rendering of the concept of a back-up inflatable antenna on board of a large spacecraft.*

larger spacecraft as a potential back up antenna to keep stored and deployed only as needed as shown in Figure 6.2.

6.2   Inflatable High Gain Antenna

6.2.1   State of the Art

The concept of inflatable antennas has been actively researched for many years and only few prototypes have ever been flown in space. This section provides an overview of the history of inflatable antennas research with a focus on the history of the development of the CubeSat prototype.

6.2.1.1   *History of Inflatable Antennas Research and Experiments*

Research in the area of inflatable structures and inflatable space antennas started in the 1950s. The first experiment in the field can be traced back to the National Aeronautics and Space Administration (NASA) Echo Balloons Project, developed in the late 1950s. Echo-I [2] was an inflatable spherical balloon made from a 12 μm Mylar with vapor-deposited aluminum. Echo-I was 30.5 m in diameter and at launch weighted approximately 72 kg including 15.12 kg of sublimating powder. The balloon was designed to function as a reflector and not a transceiver and it was used to reflect intercontinental telephone, radio and television signals. Launched in 1960, it was designed to survive approximately 4 years, but lasted until May 24, 1968 [3].

Echo-II [4] was a 41.1 m diameter balloon (Figure 6.3) and it was the last experiment of NASA Echo Balloons Project. Similarly to Echo-I, also Echo-II

Static Inflation Test of 135 Ft Satellite In Weeksville, NC
NASA Langley Research Center   6/28/1961   Image # EL–1996–00052

Figure 6.3   *NASA Echo-I balloon project tested on the ground. Credits: NASA.*

was developed to perform passive communication experiments. However, Echo-II was also designed to investigate the dynamics of large spacecraft and global geometric geodesy. Another interesting aspect of the Echo-II [5] design was that its membrane was rigidizable. Hence, the balloon was capable of maintaining its shape and survive the effect of micrometeoroids. Echo-II was launched in 1964 and reentered in the atmosphere in 1969.

After the Echo Balloons Project, research in the areas of inflatable structures and antennas seemed to slow down due to the fact that active satellites became a preferred choice for telecommunication rather than passive communication reflectors. However, research in inflatable antennas revived in the 1990s when an inflatable antenna was designed and tested in space on board the STS-77 mission [6–8]. The antenna was a 14 m diameter off-set parabolic reflector, which was connected to the spacecraft by an inflatable torus and a set of 28 m struts. The experiment was managed by the Jet Propulsion Laboratory and the antenna concept flown was based on the L'Garde structural concept. The experiment was flown in 1996 (Figure 6.4): the basic antenna support structure was deployed successfully, although in an uncontrolled way. An issue in the gas inflation system caused the reflector surface to not completely inflate and unexpected spacecraft dynamic effects were observed during deployment as a result of residual air in the inflatable components.

Figure 6.4 *Inflatable antenna experiment on board the STS-77. Credits: NASA* [9].

Other recent work in the field of inflatable antennas includes the development and testing of the Microstrip Reflectarrays for X-Band and Ka-Band by ILC Dover [10]. The X-Band reflectarray structure includes a 1 m diameter inflatable torus to support the membrane. This antenna was designed mostly for radar applications.

Finally, another recent study [11] presents the structural design of a 3.2 m inflatable structure which has been developed and the radiation pattern experimentally measured.

It is important to mention that those previous studies and experiments have provided a great foundation for the development of the inflatable antenna for CubeSats. For example, the Echo Balloons provided the concept of using the sublimating powder as the inflation mechanism and the idea of rigidizing the antenna in flight. However, no one of the previous concepts for inflatable antennas was exactly compatible with the CubeSat form factor and for this reason a new design was developed. The next section describes the history of the project from the initial conception up to the current design.

6.2.1.2 History of the Inflatable Antenna for CubeSat Concept

Research on the inflatable antenna for CubeSat concept started in 2012. That time is particularly significant as it coincided with the rise of the concept of "interplanetary CubeSats." Around that year, the Jet Propulsion Laboratory started the development of the interplanetary nanospacecraft pathfinder in relevant environment

(INSPIRE) [12] mission, the first interplanetary CubeSat. At about the same time, many new conferences focusing on interplanetary CubeSats started to appear in the aerospace community and a new scientific and engineering community started to develop around the idea of using the CubeSat platform to perform exploration of the solar system. As this new scientific community started to form, it became clear that there were some obvious challenges that needed to be overcome in order to allow CubeSats to become really interplanetary. Together with propulsion, telecommunication emerged immediately as one of the area that needed more development. In fact, the telecommunication systems that were carried at that time on most of the low Earth orbit (LEO) CubeSat were very simple systems at UHF and S-Band with limited power (1–2 W) and mostly omni-directional or low gain antennas. Hence, new radios and antenna concepts were needed. As a result of this shift in the CubeSat community, many antenna developments began, some of which are also described in other chapters of this book.

The first study on the inflatable antenna for CubeSat [13] focused on developing an initial design concept to be further investigated. A trade space among two different designs was performed. The first concept was to use a design similar to what proposed by Cadogan [10] and to scale it down to fit into a 3U CubeSat. The result (Figure 6.5) of that analysis showed that a similar design would have unfortunately occupied the entire 3U volume. Hence, this design was not selected. The second design instead consisted of two parabolic membranes joined together: one
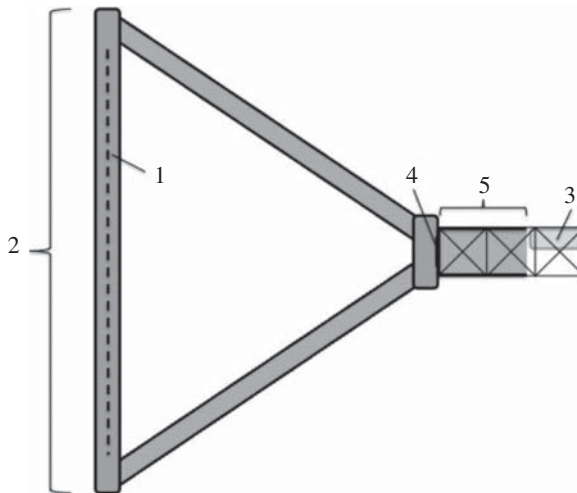
Figure 6.5   *Schematic of the concept based on Cadogan* [10]. *The numbers indicates: (1) membrane, (2) tubolar inflatable structure, (3) gas tank, (4) feed, (5) storage canister. Source: Modified from Cadogan et al.* [10]. © *1999 John Wiley & Sons.*
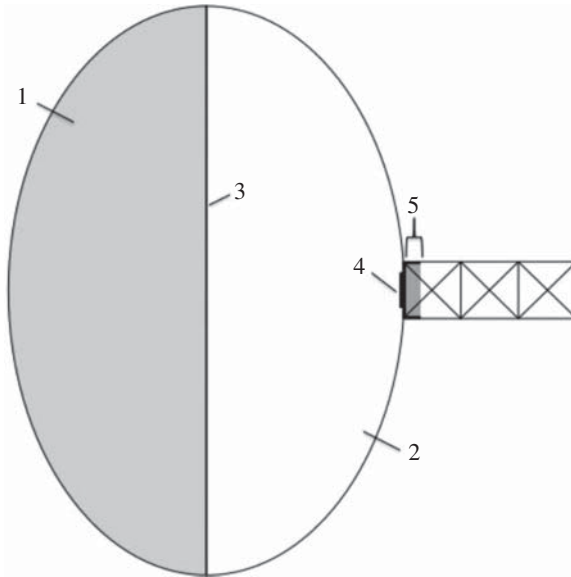
Figure 6.6 *Schematic of the second design. The numbers indicates: (1) reflective membrane, (2) transparent membrane, (3) bonding, (4) patch antenna feed, (5) required storage on board. Source: From Babuscia et al.* [14]. © *2013 Elsevier.*

of the membrane is coated with conductive material and acts as a dish reflector, while the other is radio frequency (RF) transparent and it is attached to the CubeSat bus as shown in Figure 6.6. The estimated mass (0.69 kg) and volume (0.4 L) for this design were much more compatible with the CubeSat form factor and for this reason the concept was selected for further study.

The second study on the inflatable antenna for CubeSat [14] focused on refining the design for the S-Band version. The initial concept shown in Figure 6.6 was furtherly developed and two shapes were compared in terms of RF performance as well as structural resistance. The two shapes were a conical shape and a cylindrical shape as shown in Figure 6.7. Both shapes were simulated using FEKO (a German software tool for radiation analysis "feeldberechnung für körper mit beliebiger oberfläche") and the cylindrical design was found to have more gain than the conical: 23 vs. 21 dB. It is worth noticing that the differences in gain are significant only at S-Band and they become negligible at the X-Band. For this reason, when designing at X-Band the initial shape that was selected for further development was the conical as it occupies less volume in the CubeSat.

Both the S-Band designs were manufactured using 50.8 µm thick metalized Mylar on the reflective part and 25.4 µm thick transparent Mylar for the rest of the membrane. The manufacturing of the first reflector was performed initially by researchers
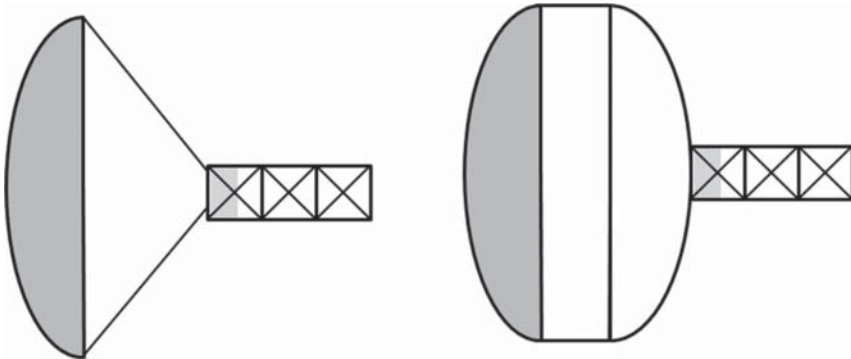
Figure 6.7   *Two shapes (conical and cylindrical) were compared in designing the S-Band prototype for the inflatable antenna. Source: From Babuscia et al.*[15]. *© 2014 IEEE Aerospace Conference.*

Figure 6.8   *Inflatable antenna manufacturing and petals bonding on the reflective side* [16]. *Reproduced with permission of IEEE.*

themselves by cutting petal-shaped pieces out of the Metalized Mylar and combining them to form the required surface. Kapton tape and epoxy were used to bond the plastics (Figure 6.8). It is worth mentioning that this initial manufacturing technique caused many issues of leakage and for this reason it was modified when moving to the X-Band prototypes which is now manufactured by a professional company with expertise in bonding Mylar surfaces.

The S-Band antenna was tested in the vacuum chamber [16] at the Massachusetts Institute of Technology in December 2012. The inflatable antennas with cylindrical

Figure 6.9 *Vacuum chamber test performed on the S-Band prototype. The inflatable antenna is vacuumed and inserted in the chamber (a). The cylindrical shape is obtained (b). The conical shape is also obtained (c)* [16]. *Reproduced with permission from IEEE.*

shape and conical shapes were vacuumed and then inserted into the chamber. Pressure was dropped and both the antennas inflated reaching a cylindrical and a conical shape as shown in Figure 6.9. However, the issue of residual air in the membranes caused both the antennas to prematurely inflate before the correct pressure was reached. To solve this issue a new setup for this test was developed at Arizona State University were the X-Band prototype has been tested (more on this is on the following sections of this chapter).

As part of the tests and experiments performed on the S-Band prototypes [15], both the cylindrical and conical antennas were folded with different techniques to quantify the total volume occupancy of the antenna. The result was that the cylindrical antenna occupies a volume of approximately $500 \, cm^3$, while the conical occupies $320 \, cm^3$. This measurements do not include the patch antenna, the canister and the added volume caused by the UV curing paste.

Another test that performed on the S-Band was the deployment [15]. The deployment mechanism was made of two plates: an ejector plate and a base plate. The inflatable antenna was connected to the ejector plate which was mounted on top of four rods each placed on the corners of the plate. The base plate was fixed to the CubeSat structure and the four rods were fastened to the plate. A compression

Figure 6.10 *Inflatable antenna deployment test* [15]. *Reproduced with permission from IEEE.*

spring was used on each of the rods. The CubeSat door was manufactured in aluminum and held closed when the antenna was not inflated. When the antenna was ready to be deployed, a burn wire was used to swing the door open. At that point the compression spring pushed the ejector plate up deploying the antenna. The deployment system was successfully tested at ambient at the Massachusetts Institute of Technology in August 2013 (Figure 6.10).

Lastly, the S-Band prototype was tested in the anechoic chamber at the Jet Propulsion Laboratory in May 2013 [15]. The objectives of the test were to measure the gain of the antenna in the two configurations (cylindrical and conical). The test setup in the chamber required the development of a specific stand in which the antenna was mounted. Inflation was achieved by compressing air through a polycarbonate adapter plate. The polycarbonate plate strongly affected the radiation, especially for the cylindrical configuration. Apart from that, the measurement showed a general agreement with the simulation results.

After this set of tests on the S-Band prototype more work needed to be done for the antenna to be developed into a real flight prototype. However, the focus of the research moved from S-Band to X-Band. The main reason for this shift in frequency was due to the fact that the development in the field of CubeSat radio

[17] was mostly in X-Band especially at the Jet Propulsion Laboratory with the IRIS radio. Consequently, the authors wanted to design an inflatable antenna that could be compatible with IRIS and with the ground capabilities offered by the Deep Space Network. The next section of this chapter focuses on the development of the X-Band prototype.

6.2.2   Inflatable Antenna Design at X-Band

The inflatable antenna for CubeSat at X-Band went through multiple design cycles before reaching the current design maturity. Section 6.2.2.1 describes the initial design at X-Band and the lessons learned which allowed development of the final design described in Section 6.2.2.2.

6.2.2.1   *Inflatable Antenna at X-Band: Initial Design and Lessons Learned*

Initially, the design for the inflatable antenna at X-Band followed the original S-Band concept of using a conical transparent Mylar structure with a parabolic reflector bonded at the end (Figure 6.11).

This kind of antenna works as a single reflector (see this chapter) with a feed (patch antenna) placed at the end of the conical structure as shown in Figure 6.11. This concept was initially tested at the anechoic chamber (Figure 6.12) but it failed to achieve the desired gain [18]. The measured gain was approximately only 25 dBi, 7 dB lower than the simulation.
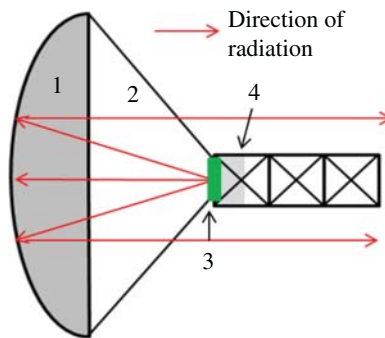
Figure 6.11   *Inflatable antenna concept. The antenna is composed of a transparent Mylar section (2), bonded with a metalized Mylar section (1) designed as a parabolic shape. The patch antenna feed (3) is glued to the end of the membrane and it is mounted at the end of the 3 unit CubeSat. Number 4 indicates the stowage capacity needed to contain the antenna. Source: From Babuscia et al. [18]. © 2016 IEEE Aerospace Conference*

Figure 6.12 *Inflatable antenna at X-Band tested at the anechoic chamber of the Jet Propulsion Laboratory. The structure with off-loading mechanism allows the antenna to be pointed correctly.*

This issue was investigated through additional tests and simulations and the root cause was found in the inflation process and in the shape of the membrane. Specifically, the antenna was tested at the photogrammetry laboratory at the Jet Propulsion Laboratory. The antenna was inflated (Figure 6.13) at different values of pressure ranging from 0.13 to 0.21 psi.

During the photogrammetry experiment, it was discovered that when air is pushed through the Mylar membrane, the membrane tends to deform into a surface which resembles more a sphere than a parabola. The surface measurements taken in photogrammetry were also used to simulate the radiation pattern which confirmed the experimental results showing that the curvature induced by the air was compromising the reflector shape and hence the quality of the overall antenna gain. This initial design of the inflatable antenna provided valuable lessons learned that were applied into the final design.

6.2.2.2 *Inflatable Antenna at X-Band Final Design: Reflector and Feed Placement*

The major lessons learned when developing and testing the first prototype of the inflatable antenna at the X-Band was that no matter how precise is the parabolic surface design and manufacture, the inflation process will tend to change that shape into a sphere. As a result, a new design approach (Figure 6.14) was followed which consisted in designing the inflatable antenna as a sphere instead of a parabola and into changing the placement of the feed inside the antenna.

Figure 6.13 *Inflatable antenna photogrammetry test. Black and silver targets are placed on the surface of the antenna in a given pattern and cameras are used to take a set of images of the antenna for different values of pressure. Following the test, the images are post-processed to provide the characterization of the surface shape.*

This new configuration [19] as several advantages. First, it eliminates the problem of trying to inflate the membrane into a parabolic shape: the sublimating powder now inflates the membrane into a sphere which is what the gas tends to do whenever the reaction occurs. Second, the new design allows for improved gain as it is better illuminated. Third, since in this new design the patch antenna is mounted inside the membrane and the inflatable is completely spherical, there is no particular reason for attaching the CubeSat to the transparent side. Hence, as it is shown in Figure 6.14, the CubeSat is now mounted on the reflector side. This new configuration avoids additional losses of gain due to the presence of the CubeSat body which was a significant problem in the previous design. Challenges of this new design are undoubtedly the support of the feed and the manufacturing of the membrane, now a more complex design. The structural and manufacturing challenges are discussed in Section 6.2.3.
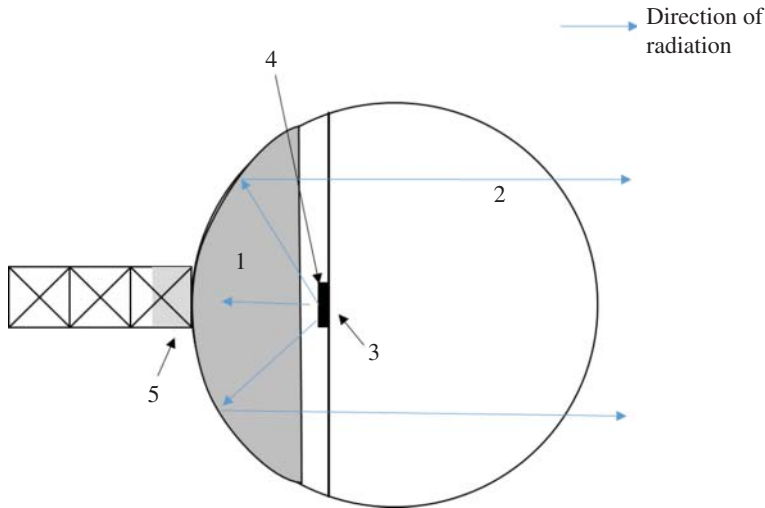
Figure 6.14 *New inflatable antenna configuration. The antenna is designed as a sphere in which a portion (1) is fabricated using metalized Mylar, while the rest (2) is transparent. The patch antenna feed (4) is now placed inside the membrane on a support (3) and connected to the main CubeSat body through a low loss cable (not pictured in this graphic). The volume occupied by the membrane is shown in 5.*

Although the feed is still an X-Band patch antenna, one of the main changes is feed placement. Moving from the previous configuration to the spherical one, the feed was moved inside the membrane to improve the illumination. Simulations were performed to optimize feed placement.

Two reflector-feed configurations were considered and evaluated with TICRA GRASP. The first design prioritized gain maximization. Figure 6.15 demonstrates how gain changes when the reflector diameter is held constant and the feed placement is varied. Gain is maximum when reflector diameter is 71.3 cm and feed placement is 22 cm from the reflector. The second design constrained the feed placement such that the seam of the feed support was co-located with the reflector seam, as this design would have been easier to manufacture. In this case, gain was only a function of reflector diameter and was maximum with a reflector of 81.9 cm. Figure 6.16 compares the radiation patterns of the two reflector-feed configurations. The first design with a reflector diameter of 71.3 cm was selected because it yields a higher gain with lower sidelobes and the increased manufacturing complexity is non-consequential.

The antenna was manufactured according to specifications (Figure 6.17), and a testing campaign was conducted at Morehead State University to measure the radiation pattern of the antenna.

Max gain vs. feed placement
71.3 cm reflector
Optimal placement = 22 cm, Gain = 32.79 dB
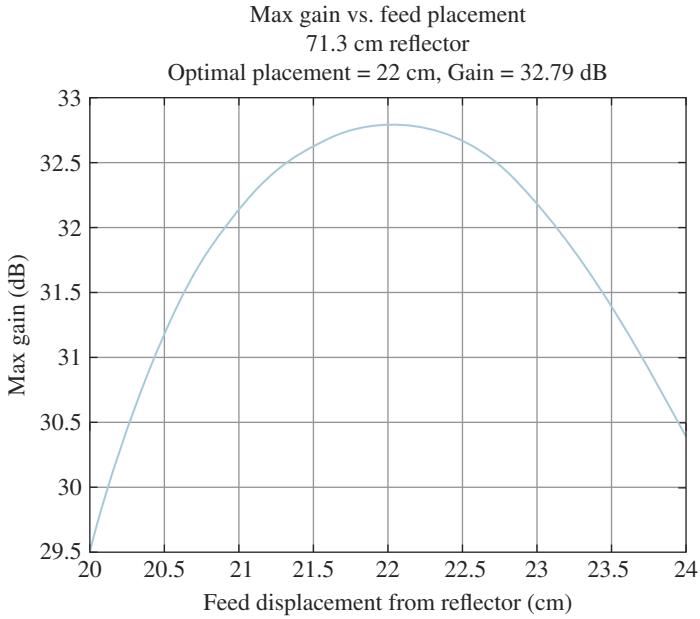
Figure 6.15 *Gain and feed displacement for a 71.3 cm reflector. Source: From Babuscia et al. [19]. © 2017 IEEE Aerospace Conference.*
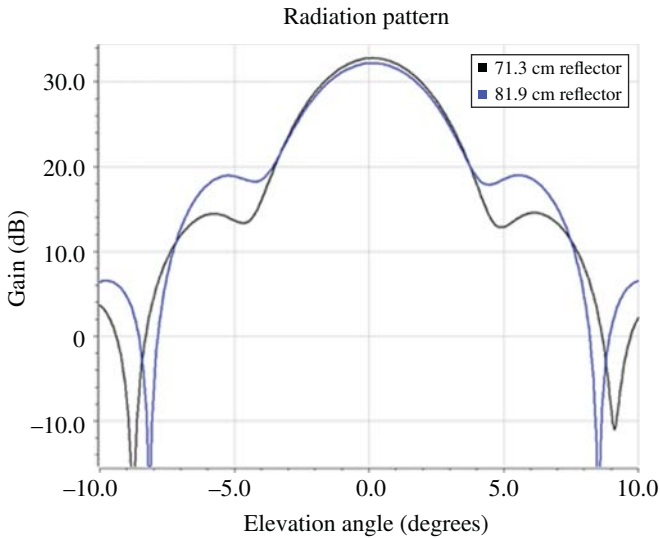
Radiation pattern

Figure 6.16 *Radiation pattern of the inflatable antenna for two different values of the reflector size (71.3 cm reflector demonstrates higher gain and lower sidelobe levels than the 81.9 cm reflector). Source: From Babuscia et al. [19]. © 2017 IEEE Aerospace Conference.*

Figure 6.17   *Inflatable antenna prototype inflated at Morehead State University prior to anechoic chamber tests.*

6.2.2.3   Antenna Measurements

A measurement campaign for the inflatable antenna at X-Band was carried out in January 2017. The measurements were performed at the anechoic chambers of the Morehead State University in Kenutcky. To properly test the antenna, a pressure control system (Figure 6.18) was developed to inflate the antenna with compressed air and to ensure that the antenna was maintained at a constant pressure during the test. Pressure control is particularly important for this kind of test as even minimal pressure variations can change the shape and hence affects the measurement of the radiation pattern. The optimal pressure needed to test the inflatable antenna has been characterized through different sets of photogrammetry tests and was found to be 0.2 psi.

The setup of the experiment at Morehead is shown in Figure 6.19. The antenna was placed on a stand to allow to maintain the appropriate pointing. Two cables were routing outside the balloon: one for the inflation air and the other one for the electrical connection.

The antenna pattern was measured using a HP 8563E spectrum analyzer and the COMSAT antenna verification program (CAVP) system in the anechoic antenna test chamber. The inflatable antenna was inflated on a platform of one inch thickness with a 20 in. diameter hole cut into it to support the round structure. The antenna was then placed on top of an antenna positioner. For the receive band, (8.4–8.5 GHz), and the transmit band, (7.19–7.235 GHz) a carrier signal was generated by a synthesized sweeper and fed to a standard gain horn. The spectrum analyzer was set to external 10 MHz, 0 Hz frequency span, 100 Hz resolution bandwidth, and 1 Hz

Figure 6.18   *Pressure control system developed to maintain the antenna at the desired pressure during the test.*
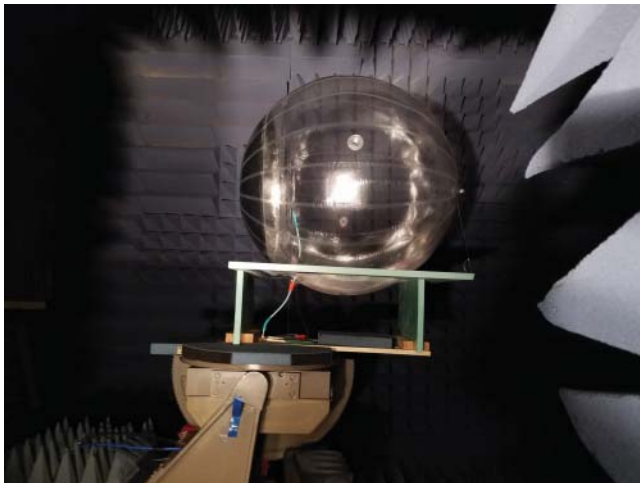
Figure 6.19   *Setup of the inflatable antenna in the anechoic chamber at Morehead State University. A nylon string was used to gently anchor it to the foam support. Red duct tape was used to seal the sphere where the coaxial cable and the filler tube were inserted.*
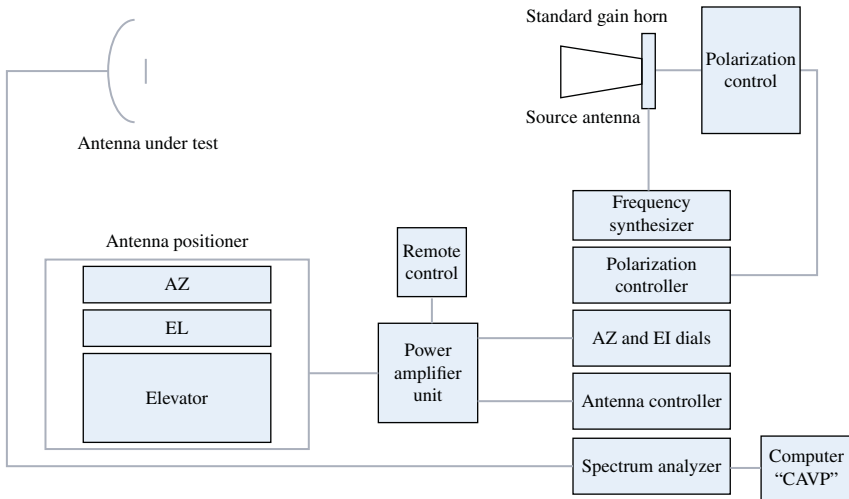
Figure 6.20   *Block diagram of the anechoic chamber test chamber equipment used for the testing of the antenna.*

video filter bandwidth. The sweep time was set to match the time required to slew the antenna over the various pattern angles and the reference level was adjusted for peak signal near the top of the screen on the 10 dB per division setting. With this setup (Figure 6.20), 70 dB dynamic range was achieved. The gain for the antenna was determined by two methods. CAVP was created by COMSAT Laboratories to more accurately calculate the gain by pattern integration. The measured patterns have three correction factors. These corrections are (0.30) dB for less than 360° of pattern cut, feed and VSWR (voltage standing wave ratio) losses (0.20 dB), and cross-polarization energy (0.10 dB). The alternate measurement for measured antenna gain uses the 3 and 10 dB beamwidths and calculating estimated directive gain by using the 3/10° beamwidth formula.

The inflatable antenna was initially measured at 8.4 GHz and at 0.10, 0.15, 0.19, 0.20 psi values of pressure. The measured gain values are listed in Table 6.1 and pattern is shown in Figure 6.21. Measurements were also performed at 0.2 psi at different values of frequency as shown in Table 6.2. The pattern angles for gain measurements for directive gain were set to ±35°. These angles used to calculate directive gain by pattern integration as recommended by the CAVP program.

It can be observed that the peak gain of the measured antenna is slightly below the peak gain computed through simulation. The difference is approximately 1–2 dB depending on the values of pressure and on the type of method used to compute the gain (integrated vs. 3/10). However, it is important to notice that the simulated gain (discussed in Section 6.2.2.2) does not account for cable losses (estimated at 0.7 dB). Besides cable losses, additional factors that may have affected the gain are

Table 6.1   *Inflatable antenna measurements at different values of pressure at 8.4 GHz.*

Freq. (GHz)	N2 pressure (psi)	Integrated gain (dBi)	3 dB beamwidth (°)	10 dB beamwidth (°)	Estimated 3/10 gain (dBi)
8.4	0.10	29.86	4.055	10.93	31.33
8.4	0.15	29.80	4.124	11.01	31.09
8.4	0.19	29.70	4.166	11.12	31.01
8.4	0.20	29.71	4.124	11.14	31.07
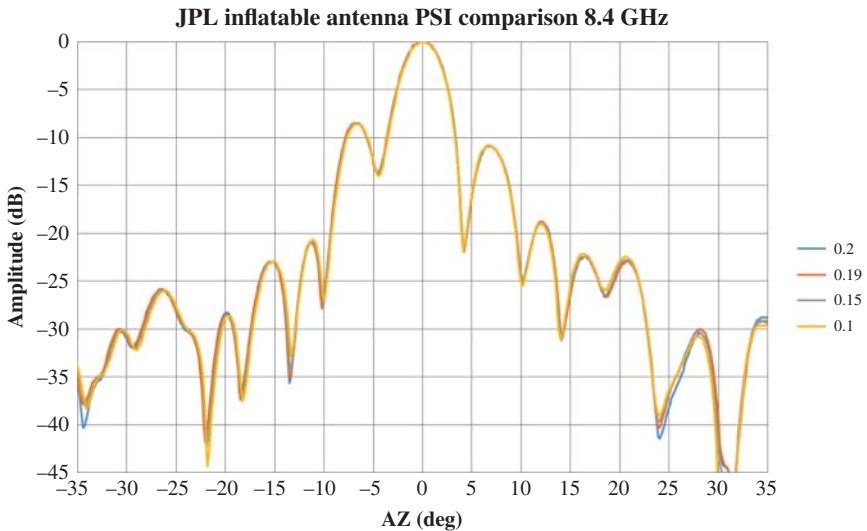
Figure 6.21   *Inflatable antenna pattern comparison for different pressure values (0.1, 0.15, 0.19, 0.2 psi).*

potential wrinkles and seams at the bounding of the Mylar membranes. Despite cable losses and wrinkles, these measurements show for the first time the feasibility of developing an antenna concept based on inflatable membranes which has the potential to be game changing for future CubeSat missions.

6.2.3   Structural Design

The mechanical design of the antenna had to solve two primary issues. The first is ensuring the antenna could withstand the pressure required to inflate it, and the

Table 6.2   *Inflatable antenna measurements at 0.2 psi for different values of frequency.*

Freq. (GHz)	N2 pressure (psi)	Integrated gain (dBi)	3 dB beamwidth (°)	10 dB beamwidth (°)	Estimated 3/10 gain (dBi)
7.145	0.20	28.67	4.922	12.74	29.64
7.19	0.20	28.70	4.926	12.66	29.65
7.235	0.20	28.74	4.789	12.54	29.85
8.4	0.20	29.68	4.212	11.17	30.93
8.45	0.20	29.28	4.081	11.06	31.15
8.5	0.20	28.82	4.214	11.12	30.94

second was to ensure the antenna took on the right shape when inflated. While the first issue was relatively easy to solve, the second issue was much more challenging.

To build the antenna, it was required to use multiple sheets of Mylar, which created the three dimensional shape (as a flat sheet of Mylar could not form the required geometry). Each of these sheets were bonded together, which was created the weak link in the system. If over pressurized, these bonded joints would begin to split due to shear forces, allowing air to leak between the sheets. It was empirically determined by the balloon manufacturer that leaks began to occur at 0.29 psi, with complete seal failure at 0.36 psi. Therefore a pressure relief valve was installed in the system, set to activate at 0.22 psi. The pressure relief valve consisted of a simple plate, held in place by a compression spring. The activation pressure could be adjusted by preload in the spring. Once the pressurized area of the plate exceeded the force on the spring, the valve would activate by compressing the spring, removing the plate from covering the hole behind the pressure relief valve, allowing air to follow around it. This would prevent the balloon from over pressurizing, as it would start to relieve pressure if the antenna ever over inflated.

Achieving the desired geometry of the antenna was a much more challenging problem. As the antenna inflates, the pressure pushes the membranes into a different, more spherical shape. This means the shape the balloon is constructed to will not match the shape that the balloon inflates to. To most easily illustrate this, imagine the two flat sheets of a standard Mylar balloon. While originally these two sheets are parallel with each other, when inflated they become rounded lobes. Figure 6.22 shows some initial simulations of the original (in black) and deformed (in gray) shape of an inflated object.

Perhaps the biggest challenge is that the deformed shape is extremely pressure dependent. To try and understand the pressure dependence of the shape two different antennas were built and then tested, using both photogrammetry. One antenna was constructed to the desired parabola (Figure 6.22a), while the other was constructed to form a cone (Figure 6.22b). Both were found to deform significantly with

(a)   (b)
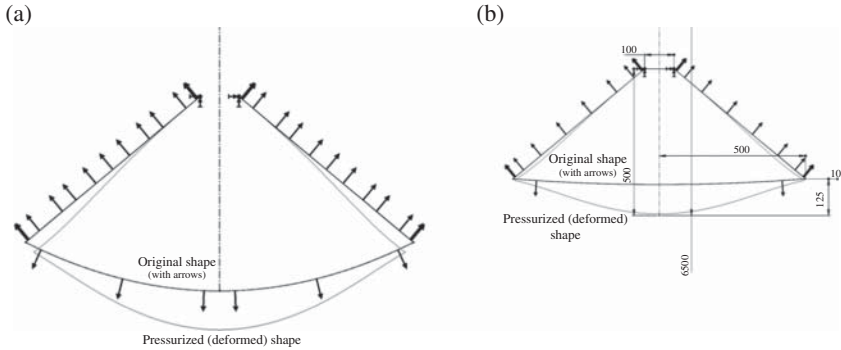
Figure 6.22   *Original and deformed shapes makes geometry challenging.*

pressure, as illustrated in the graphs below which shows how the best fit parabolic focal point changes with pressure (Figure 6.23).

Interestingly, the most impactful portion on antenna surface design was the number of seams occurring in the reflective surface of the balloon. A reflective surface with many seams, required to build an "as built" parabolic shape ended up with a surface distorted by many creases. However, a surface constructed as a flat surface had a much smoother shape when inflated (Figure 6.24). Therefore, it was determined that a desirable approach was to construct the surface as a flat shape, and then allow inflation to deform the flat shape to the required curved surface. This would result in the as built shape appearing like a cone.

The next step was to explore if simulations could accurately predict the deformed shape of the balloon. Initially, models were run in solidworks simulation and NAS-TRAN (National Aeronautics and Space Administration Structure Analysis), but were found to converge only for extremely low pressures. If pressures exceeded 0.01 psi, the solution would not converge. Solutions nearing these pressures showed radical deformation. After consulting with the individuals familiar with simulation software, it was determined the correct approach to use was a software called Sierra. This produced much more realistic results, as illustrated below (Figure 6.25). It can be seen that Sierra not only predicts the shapes bulk deformation, but also simulates wrinkles occurring the balloon.

The next steps in the design process would be to first verify the simulations by comparing the photogrammetry data to the simulation results. After the accuracy of the software was verified, the software would then be used to determine what as built shape would deform into the correct parabola. However, this would have been a complex and time consuming series of simulations to perform, and would require compromise to achieve an exact parabolic shape. Further, accuracy of such a design would be extremely sensitive to pressure fluctuations, as illustrated in Figure 6.23.
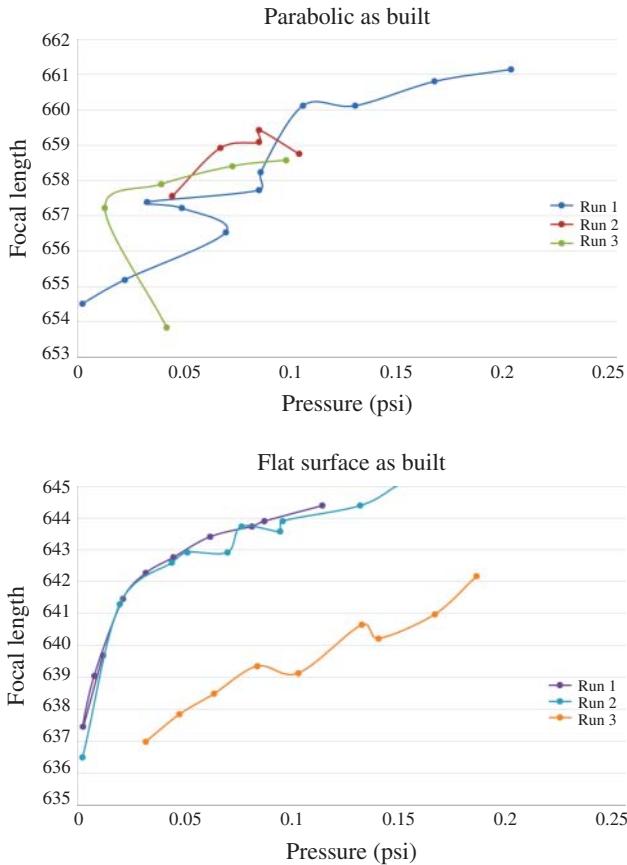
Figure 6.23   *Antenna deformation vs. antenna pressure was highly variable.*

At this time it was also found that correct design of the antenna feed would allow a spherical surface to be used. A spherical surface is the shape and inflated object naturally wants to deform to, therefore it was determined it would be much more prudent to design the antenna to be a spherical surface, instead of try to manufacture an antenna to one shape, and then inflate it to another shape. Using a spherical surface is also very robust against pressure changes. Therefore, adapting the antenna feed to operate on a spherical reflector was much more practical than trying to achieve a parabolic surface.

It should be noted that the STS antenna experiment was able to achieve a parabolic surface, created by deformation due to inflation, but this required three different inflatable structures, each inflated to a different pressure to achieve the desired shape. One of the key structures included a ring, which applied a specified tension

Figure 6.24 *A flat surface on the antenna achieved a better surface than a curved surface.*
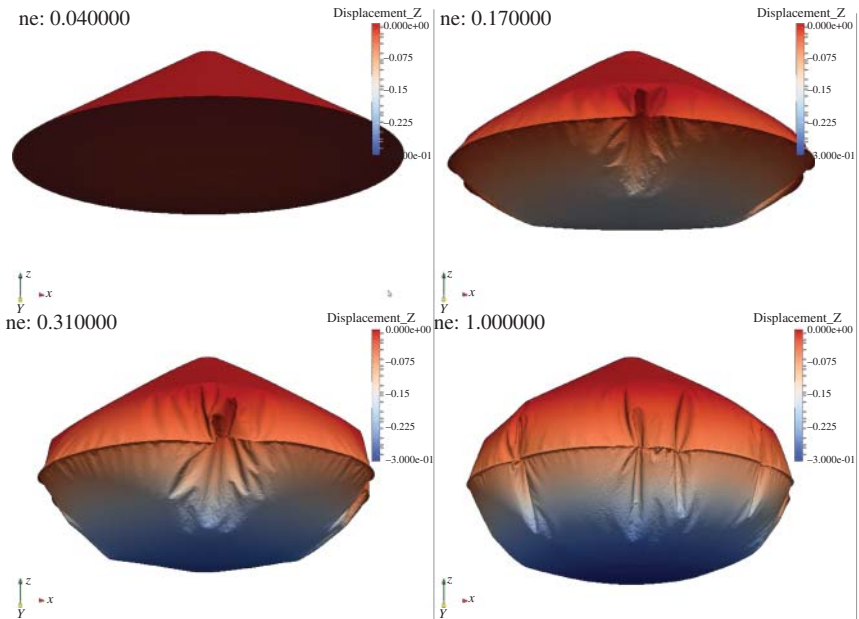
Figure 6.25 *Simulations of the deformed antenna could be created, but were hard to achieve.*

to the perimeter of the reflector surface to develop a precise shape. However, for a CubeSat antenna, it is not desirable to have a design with demands such complexity.

6.2.4   Inflation and On-Orbit Rigidization

Inflation and rigidization represent key aspects of the inflatable antenna design as they are the mechanism through which the antenna is maintained in the desired shape. Inflation can be performed in many different ways with a wide range of possible inflation gases. In the case of the inflatable antenna, the choice for inflation mechanism is the sublimating powder. This mechanism is completely passive and does not necessitate a tank for gas storage allowing for great volume reduction. The sublimating powder is kept at the solid state inside the antenna until deployment. When the antenna is deployed, the powder turns into a gas and inflates the antenna to an approximate pressure of 10^{-3} Torr.

The process of sublimation is a function of the powder's state pressure and temperature. In order for solids to convert into gas, energy equivalent to bond in the solid must be provided. This energy is characterized by sublimation enthalpy (ΔH_{sub}). Sublimation enthalpy of a given material in a given state is determined experimentally. However, the equipartition law [20] provides a reasonable approximation of the sublimation enthalpy:

$$\Delta H_{\mathrm{sub}}(P, T) = -U_{\mathrm{Lattice\_energy}}(P, T) - 2RT \tag{6.1}$$

Here $U_{\mathrm{Lattice\_Energy}}$ is the energy required for molecules to break their crystal lattice and convert to gas, and R is the universal gas constant. In high vacuum environments, ΔH_{sub} decreases dramatically and sublimation can be achieved over a very small temperature range. In effect, sublimation can thus be achieved isothermally. Our present work takes advantage of this property to achieve inflation in high vacuum. The mass flow rate of conversion from solid to gas is:

$$\frac{\mathrm{d}m}{\mathrm{d}t} = \alpha \sqrt{\frac{M}{2\pi RT}}(p_{\mathrm{eq}} - p) \tag{6.2}$$

Here α represents a proportionality constant that is material specific, M is the molecular mass, R is the gas constant, T is temperature, p is the ambient pressure, and p_{eq} represents equilibrium vapor pressure. The equilibrium pressure depends on temperature: Equation (6.3) shows that the process tends to stop once ambient pressures approaches the sublimates natural vapor pressure at that temperature. This is very significant for the inflatable antenna as it excludes the need for an external pressure controller making the inflation process simple and reliable.

$$p_{\mathrm{eq}} = \beta \sqrt{\frac{2\pi R}{M}} T \mathrm{e}^{-\frac{\lambda}{RT}} \tag{6.3}$$
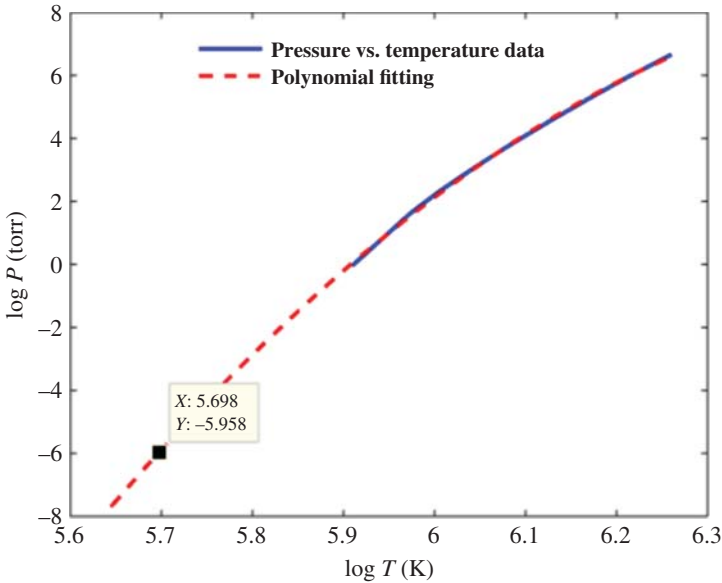
Figure 6.26 *Equilibrium pressure for benzoic acid. Source: From Babuscia et al.* [18]. *© 2016 IEEE Aerospace Conference.*

β and λ are specific material constants. The equilibrium pressure for benzoic acid is shown in Figure 6.26:

   If the sublimating powder carried onboard the antenna is greater than the amount needed for the primary inflation, the residual powder will remain at the solid state and will sublimate whenever leaks in the antenna cause the volume to change. This condition is shown in Figure 6.27:

   $\dot{Q}_{in}$ represents the volume flow rate into the membrane due to sublimation and $\dot{Q}_{out}$ is the volume flow rate out of the inflatable due to punctured area. Condition
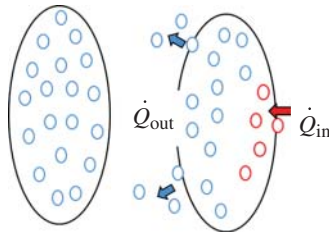
Figure 6.27 *Sublimation process in case of punctured membrane.*

for sublimation is:

$$\dot{Q}_{in} \geq \dot{Q}_{out} \tag{6.4}$$

The volume flow rate generated by a sublimate of mass flow rate $\dot{M}$, molecular weight m, having equilibrium vapor pressure of P_{eq} at temperature T is computed as:

$$\dot{Q}_{in} = \frac{\dot{M}RT}{mP_{eq}} \tag{6.5}$$

Leakage rate out of the inflatable is a function of the area of damage and of the molecular diffusivity of the sublimate as seen below [14]:

$$\dot{Q}_{out} = \left(\frac{\sum A_i p_i M_{tot}}{\text{time}} \right) \sqrt{\frac{kT}{2\pi m}} \tag{6.6}$$

The first term in the parenthesis indicates the total expected damage area, while the term under the square root is the sublimate mobility. Whenever the condition for sublimation occurs, sublimation will act to compensate for the puncturing until powder is exhausted. Approximately 1 g of sublimating powder like benzoic acid allows the antenna to operate for over a year as shown in [16].

Given the novelty of this inflation mechanism, research and tests were conducted [18] to select the most appropriate powder and to characterize the overall inflation process. In particular, a study that we performed and documented in [18], compared at least 30 different possible sublimating powder compounds to identify the more promising ones for the antenna. The study was based on the principle that chemical sublimates exert vapor pressure, the magnitude of which depends on ambient pressure and temperature [20]. The powders were reviewed using criteria considered critical for usage in space such as: stability in high vacuum conditions, high molecular diffusivity and large gas vapor volume for mass ratio. Results (Figure 6.28) showed that benzoic acid, salicylic acid and o-methoxy benzoic acid were the more feasible sublimating powder compounds to use for the project. Among these three substances, benzoic acid was chosen to be used in the vacuum chamber experiments due to ease of availability and low cost.

In addition to the survey of the different sublimating powder, tests vacuum chamber were performed to characterize the process of inflation. The test campaign was conducted at Arizona State University in 2014 and 2015 using a vacuum chamber built specifically for this purpose. The chamber is design for complete evacuation of the antenna before dropping pressure. This feature is extremely important as it allows for elimination of the residual air and guarantees that inflation is effectively caused by the powder and not by residual air issue that might have remained during some of the experiments performed in 2013. The inflation process is shown in Figure 6.29, while the pressure measurement over time is shown in Figure 6.30.
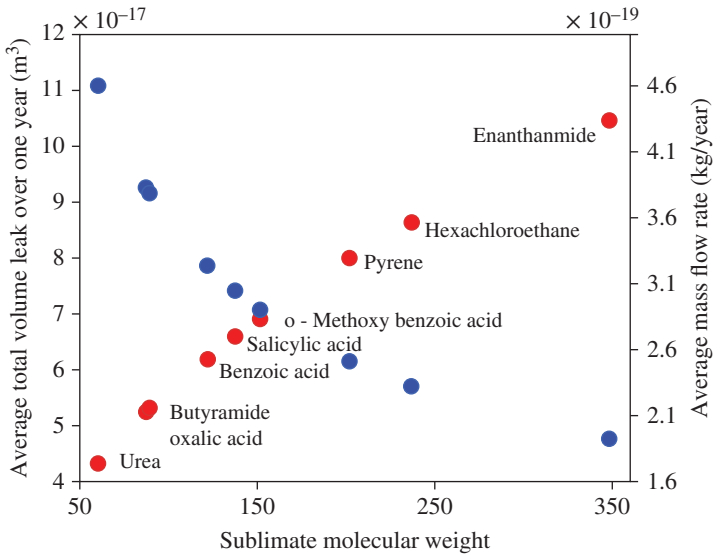
Figure 6.28 *Results of the sublimating powder study. Source: From Babuscia et al.* [18]. *© 2016 IEEE Aerospace Conference.*
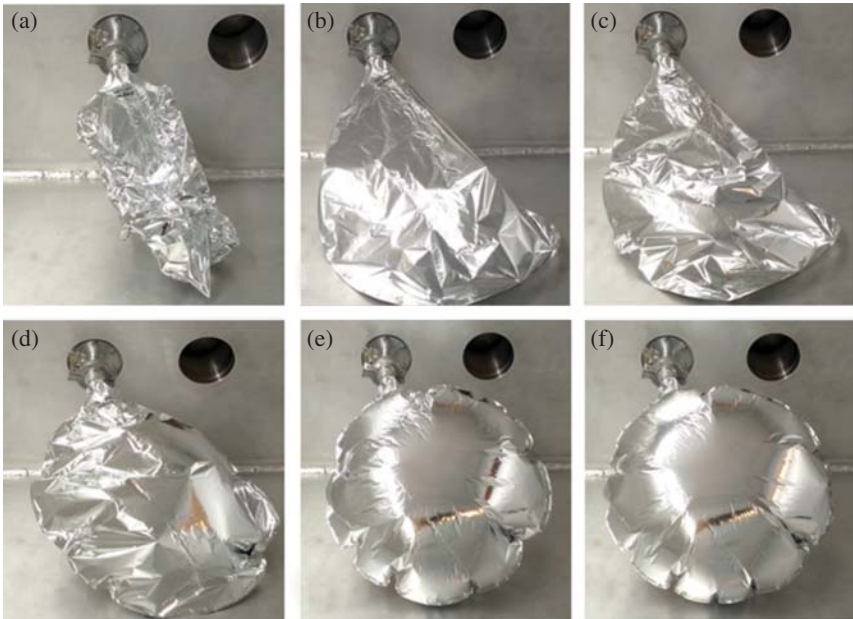
Figure 6.29 *Inflatable antenna inflation process* [18]. *Reproduced with permission from IEEE.*
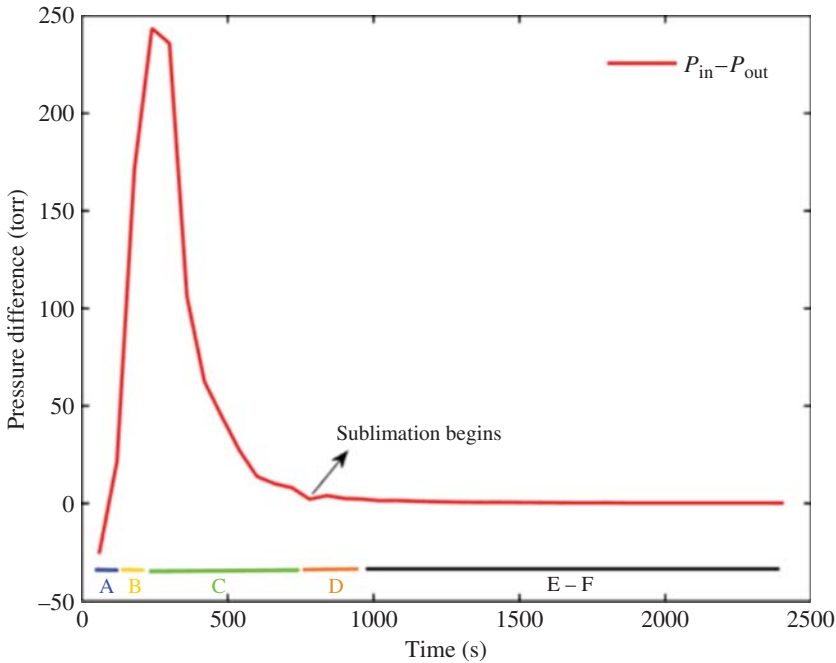
Figure 6.30   *Pressure profile over time for the different inflation stages. Source: From Babuscia et al. [18]. © 2016 IEEE Aerospace Conference.*

Phase A represents the inflatable evacuation stage. At this phase, the pressure difference between external pressure and internal is negative as shown in Figure 6.30. Phase B corresponds to a rise in internal pressure due to redistribution of air pockets formed during the evacuation (Phase A). Phase C corresponds to the progressively lowering of the temperature. Phase D constitutes the point where internal pressure is low enough for the sublimation process to begin, as it can be noticed by the sharp fall in internal pressure at the end of this phase. Phases E and F represent equilibrium conditions with constant internal pressures of 0.0026 Torr.

Differently from inflation, rigidization allows maintenance of the shape of the antenna even in case of puncturing and loss of pressure caused by thermal variations. UV curable resins can be used as rigidization technique as they harden to form "glassy" structures upon exposure to ultraviolet radiation. This process is due to radiation induced polymerization called UV curing. A dynamical equation describing UV polymerization in terms of reacted concentration as a function of thickness x from surface and exposure time t is:

$$\frac{\partial C(x,t)}{\partial t} = kI_0 e^{-\varepsilon A x} C(x,t) \tag{6.7}$$

I_0 is the incident Intensity at polymer surface, ε is the attenuation constant of the material, and A is the fraction of reactive molecules [21]. Reference [21] shows curing efficiency to rapidly slow down beyond depths of 20 µm. UV induced polymerization reaction duration is of the order of hours given incident radiation flux of 100–10000 µW/cm^2. This is advantageous as the process of inflation is of the order of minutes. This can be leveraged to attain complete inflation prior to rigidization. Non-uniform polymerization can be caused due to factors such as atomic oxygen in the LEO, high energy electron and ion fluxes, X-ray and Y-irradiations. The most significant challenge posed to fluid epoxies is their evaporation in high vacuum. The rate of evaporation is:

$$W = \frac{P}{17.14} \sqrt{\frac{M}{T}} \tag{6.8}$$

P is the material's equilibrium vapor pressure, M is the molecular mass of monomer, and T is the temperature [22].

An initial survey of rigidization methods was performed and an initial experiment using a small piece of Mylar was described in [18]. Recently, an experiment to rigidize the entire antenna surface was carried out at the Arizona State University vacuum chamber facility. The antenna was covered with UV resins as shown in Figure 6.31.

UV resin filled envelopes were used to provide the amount of UV paste needed for the rigidization while minimizing the risk for outgassing in the vacuum chamber.

UV resin filled
envelopes

Sublimate powder
holder
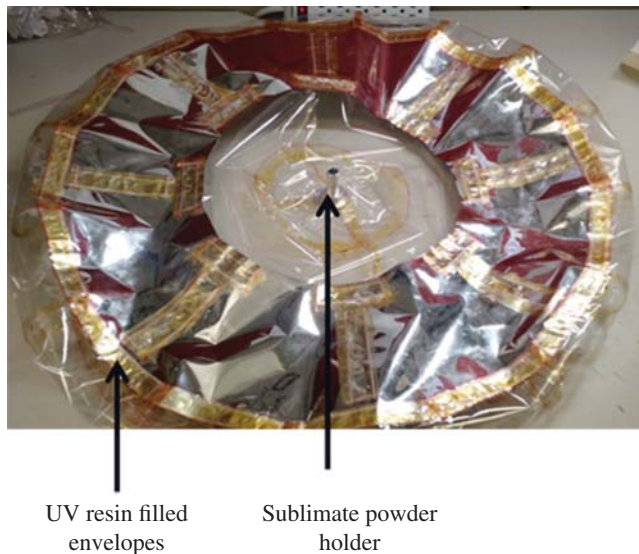
Figure 6.31   *UV resins applied to the inflatable antenna membrane* [19]. *Reproduced with permission from IEEE.*
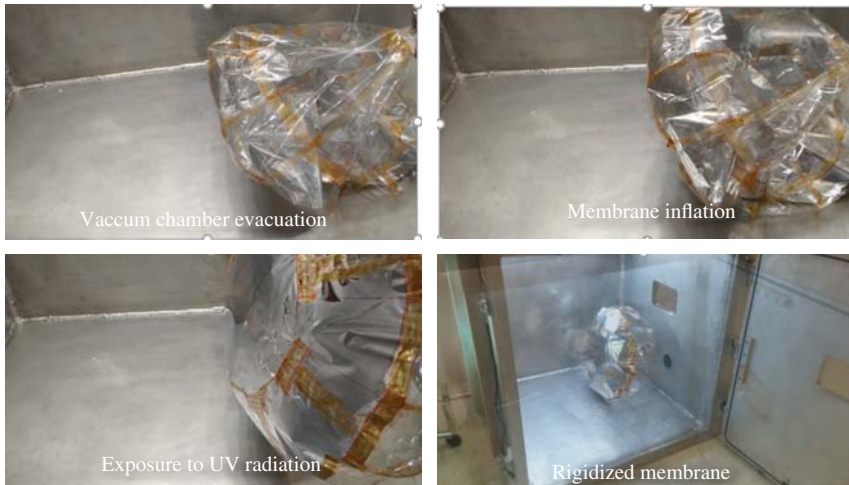
Figure 6.32   *Rigidization sequence. The antenna is vacuumed, membrane is inflated, and exposure to UV radiation is used to rigidize the antenna* [19]. *Reproduced with permission from IEEE.*

The rigidization sequence is shown in Figure 6.32. After the antenna is vacuumed, the pressure is reduced up to the point when it triggers the inflation with the powder. The time required to reach the point of sublimation is approximately 15 minutes. After that, inflation happens in a couple of minutes. When inflation is completed, an UV source is turned on inside the chamber for a couple of hours to allow the resin to cure for the required time. Approximately 2 hours are sufficient for the rigidization to take place. At the end of the experiment, the pressure is raised back to ambient and the vacuum chamber is opened to verify the status of the membrane. As observed in Figure 6.32, the UV curing process allows to partially maintain the inflated shape: without UV curing the antenna would have all been deflated as the sublimating powder goes back to powder state when pressure is raised. However, the shape is very far from the full inflated antenna, because the UV curing is not applied uniformly on all the reflector surface as this would excessively increase mass and volume. Current research is focused on improving the rigidization process as a way to increase the life of the inflatable antenna in space, while respecting the current mass and volume constraints.

6.3   Spacecraft Design Challenges

The inflatable antenna for CubeSat can significantly improve their telecommunication capabilities. However, it is a complex design that needs particular

accommodation on the spacecraft. This section is focused on the main design challenges associated with the inflatable antenna: Earth atmospheric drag and dynamics.

For Earth atmospheric drag, a study conducted in 2013 [14] showed that at very low altitudes, drag torque is dominant. This problem does not affect interplanetary applications as in those cases the antenna will be deployed very far from Earth. However, this problem affects a technology demonstration mission that could be launched in LEO to test this prototype. The study demonstrated that very low orbits (500 km or lower) are not acceptable for the inflatable antenna. A technology demonstration mission would needed to be flown at a minimum altitude of 600–700 km. It is worth noticing that this kind of altitude is very well within the reach of the current CubeSat launch vehicles and hence should not constitute an insurmountable problem. However, this aspect needs to be considered when the spacecraft is designed.

Another important challenge is the dynamic control of the spacecraft. The antenna dimensions, coupled with the flexibility of its material and with the presence of the sublimating powder add complexity to the design of the attitude control system. A test campaign has been carried out in the small satellite dynamic testbed facility at the Jet Propulsion Laboratory [19] with the goal of characterizing the dynamical behavior of the inflated antenna, and in particular its response to rotation commands along a direction perpendicular to the boresight. The antenna was mounted on a three degree of freedom (DOF) spherical air bearing system. Vicon Motion Capture was selected as the main measurement system and, as a redundancy, a set of coded targets was placed on the antenna to provide a second data source for additional post processing. The setup (Figure 6.33) was equipped with the XACT suite from Blue Canyon Technologies which includes a set of reaction wheels and gyroscopes, controlled wirelessly from a console. A controller was used to feed the actuators with real-time commands and to handle the sensors readings. The inflated antenna was mounted with the boresight direction parallel to the gravity vector. The test consisted of observing the behavior whenever a command is applied to the frictionless plate. The reaction wheel controller was programmed to stabilize the system.

Tests were stopped either because of wheel saturation occurred or because the system diverged. The cause for this result was the gravity torque, which was characterizing the system as an inverted pendulum. It is worth mentioning that during this test several contributions were different with respect to the conditions found in orbit: gravity torque, air in the environment instead of vacuum, air inside of the antenna instead of sublimating gas, antenna position on the plate, and inertia of additional components. Regardless, test results showed that the inflated antenna is controllable with state of the art reaction wheel systems for CubeSats and hence compatible with foreseen mission profiles and selected hardware configurations. Stable and unstable behavior are shown in Figures 6.34 and 6.35.

Figure 6.33 *Test setup* [19]. *Reproduced with permission from IEEE.*
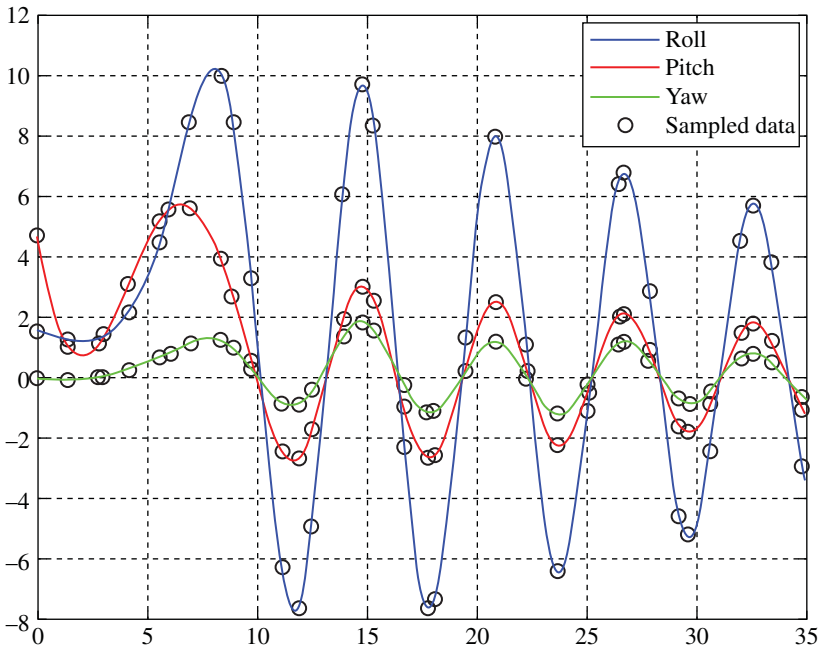
Figure 6.34 *Stable behavior. Source: From Babuscia et al.* [19]. *© 2017 IEEE Aerospace Conference.*
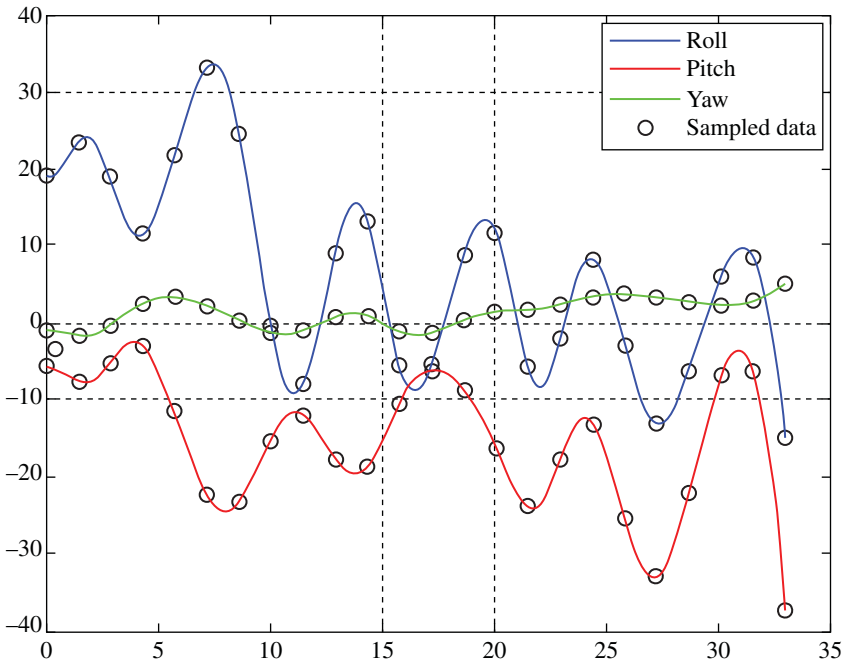
Figure 6.35   *Unstable behavior. Source: From Babuscia et al. [19]. © 2017 IEEE Aerospace Conference.*

6.4   Conclusion

The inflatable antenna for CubeSat project has been developed at the Jet Propulsion Laboratory over 7 years with the support of multiple partner institutions. During this period of time, two different prototype concepts were developed and tested which are the S-Band and the X-Band prototypes described in this chapter. Simulations and tests have shown how the inflatable antenna can be a promising technology to achieve high antenna gain while maximizing stowing efficiency onboard the spacecraft. However, the development of such antenna presents inevitably several challenges especially in relation to surface accuracy, proper inflation, shape maintenance, thermal control, micrometeoroid puncturing, and rigidization. Different studies and experiments have been carried out to solve some of these issues as described in this chapter. More research and test are expected to happen in the next few years as the project proceeds into transitioning from technology development to flight prototype. The final goal is to develop a technology demonstration mission in LEO to deploy the antenna and to characterize its performance in relevant environment. If this test is successful, missions could start carrying an inflatable

antenna as their primary or secondary antenna to support long range and high data rate interplanetary links.

Acknowledgments

References

1. A. Babuscia, T. Choi, and K. -M. Cheung, "Arrays of inflatable antennas for collaborative communication in deep space," *IEEE Aerospace Conference*, Big Sky, MT, 2015.
2. R. E. Freeland, G. D. Bilyeu, G. R. Veal, and M. M. Mikulas, "Inflatable deployable space structures technology summary," *49th International Astronautical Congress*, Melbourne, Australia, 1998.
3. J. M. Harrison, I. I. Shapiro, P. E. Zadunaisky, H. C. Van De Hulst, C. De Jager, and A. F. Moore, "Solar radiation pressure effects, gas leakage rates, and air densities inferred from the orbit of Echo I," *Space Research II, Proceedings of the Second International Space Science Symposium*, Florence, 1961.
4. NASA, "Echo II," Available: online: http://nssdc.gsfc.nasa.gov/nmc/spacecraftDisplay .do?id=1964-004A. [Accessed Jan. 9, 2017], Dec. 8, 2016.
5. C. Staugaitis and L. Kroben, "Mechanical and physical properties of the Echo II metal-polymer laminate," NASA TN D-3409, 1966.
6. R. E. Freeland and G. D. Bilyeu, "In-step inflatable antenna experiment," *Acta Astronautica*, vol. **30**, pp. 29–40, 1993.
7. R. E. Freeland, G. D. Bilyeu, and G. R. Veal, "Development of flight hardware for a large, inflatable-deployable antenna experiment," *Acta Astronautica*, vol. **38**, pp. 251–260, 1996.
8. R. E. Freeland, G. D. Bilyeu, G. R. Veal, M. D. Steiner, and D. E. Carson, "Large inflatable deployable antenna flight experiment results," *Acta Astronautica*, vol. **41**, pp. 267–277, 1997.
9. NASA, "Image inflatable antenna," NASA, Available: online: http://www.nasaimages .org/luna/servlet/detail/nasaNAS~7~7~35424~139291:Following-its-deployment-from-the-S [Accessed Jan. 9, 2017].
10. D. P. Cadogan, J. K. Lin, and M. S. Grahne, "The development of inflatable space radar reflectarrays," *40th Structures, Structural Dynamics, and Materials Conference and Exhibit*, St. Louis, MO, Apr 1999, 12–15.

11. Y. Xu and F. -L. Guan, "Structure design and mechanical measurement of inflatable antenna," *Acta Astronautica*, vol. **76**, pp. 13–25, 2012.
12. A. Klesh, J. Baker, J. Castillo-Rogez, L. Halatek, N. Murphy, C. Raymond, and B. Sherwood, "INSPIRE: interplanetary nanospacecraft pathfinder in relevant environment," *27th Annual AIAA/USU Conference on Small Satellites*, Logan, UT, 2013.
13. A. Babuscia, M. Van de Loo, M. Knapp, R. Jensen-Celm, and S. Seager, "Inflatable antenna for CubeSat: motivation for development and initial trade study," *iCubeSat*, MIT, Cambridge, 2012.
14. A. Babuscia, B. Corbin, M. Knapp, R. Jensen-Clem, M. Van de Loo, and S. Seager, "Inflatable antenna for CubeSats: motivation for development and antenna design," *Acta Astronautica*, vol. **91**, pp. 322–332, 2013.
15. A. Babuscia, M. Van de Loo, Q. J. Wei, S. Pan, S. Mohan, and S. Seager, "Inflatable antenna for CubeSat: fabrication, deployment and results of experimental tests," *IEEE Aerospace Conference*, Big Sky, MT, 2014.
16. A. Babuscia, B. Corbin, R. Jensen-Clem, M. Knapp, I. Sergeev, M. Van de Loo, and S. Seager, "CommCube 1 and 2: a CubeSat series of missions to enhance communication capabilities for CubeSat," *Proceedings of IEEE Aerospace Conference*, Big Sky, MT, 2013.
17. C. Duncan, "IRIS for INSPIRE CubeSat compatible, DSN compatible transponder," *27th Annual AIAA/USU Small Satellite Conference*, Logan, UT, 2013.
18. A. Babuscia, C. Thomas, S. Jonathan, C. Aman, and J. Thangavelautham, "Inflatable antenna for CubeSat: development of the X-Band prototype," *IEEE Aerospace Conference*, Big Sky, MT, 2016.
19. A. Babuscia, J. Sauder, A. Chandra, J. Thangavelautham, L. Feruglio, and N. Bienert, "Inflatable antenna for CubeSat: a new spherical design for increased X-band gain," *Proceedings of IEEE Aerospace Conference*, Big Sky, MT, 2017.
20. S. Miyamoto, "A theory of the rate of sublimation," *Transactions of the Faraday Society*, vol. **140**, pp. 794–797, 1933.
21. A. Kondyurin, B. Lauke, and R. Vogel, "Photopolymerisation of composite material in simulate free space environment at low Earth orbital flight," *European Polymer Journal*, vol. **42**, no. 10, pp. 2703–2714, 2006.
22. A. Kondyurin, "Direct curing of polymer construction material in simulated Earth's Moon surface environment," *Journal of Spacecraft and Rockets*, vol. **48**, no. 2, pp. 378–384, 2011.

7

High Aperture Efficiency All-Metal Patch Array

Nacer Chahat

NASA Jet Propulsion Laboratory/California Institute of Technology, Pasadena, CA, USA

7.1   Introduction

The all-metal patch array discussed in this chapter was originally developed for the potential Europa Lander mission [1, 2] to enable for the first time, direct link to earth from a Lander on Jupiter's icy moon Europa [3]. However, a smaller version of the antenna would be an ideal candidate for CubeSat missions.

The antenna is primarily composed of metal to ensure survivability in the harsh environment of Jupiter's icy moon (i.e. very low temperature and high radiation). The Europa Lander antenna for direct to earth (DTE) communication is shown in Figure 7.1 on the Europa Lander. A small portion of this antenna can easily be integrated into 6U- or 12U-class CubeSat exposed to high radiation levels or simply in need for high aperture efficiency. Indeed, this antenna not only operates at the uplink (7.145–7.190 GHz) and downlink (8.40–8.45 GHz) Deep Space Network (DSN) frequency bands, it also demonstrates unprecedented aperture efficiencies (>80%) [3]. To back up this statement a comparison with the state of the art will be provided.

NASA's Jet Propulsion Laboratory developed a new type of all-metal right-handed circularly-polarized (RHCP) patch array with the goal of achieving more than 80% efficiency at both uplink and downlink frequencies. It leverages construction methods developed for the Juno MicroWave Radiometer

Figure 7.1 *An artist's concept of a potential Europa Lander with the all-metal dual-frequency RHCP HGA for Direct to Earth (DTE) communication* [3]. *This antenna was highlighted as the enabling technology for this mission* [3].

single-frequency linearly polarized patch array antennas [4]. To design such an array, the heart of the challenge lies with the proper design of the array elements. The proposed array employs an all-metal single-fed element that supports circular polarization over the two DSN frequency bands. The element is self-supported, easy to machine, and structurally strong enough to handle vibrations and loads during launch.

Going forward, it is likely we will witness more CubeSats fly alongside interplanetary missions, hitching rides to try inventive, new, and game changing technologies. Deep Space CubeSat missions will come with extreme challenges due to high radiation levels and extreme temperatures. High energy electron environment is harmful for many materials, it can alter their dielectric properties or damage the material; the material will be vaporized and/or carbonized. Due to the very low conductivity of the dielectrics, electrons can be accumulated in dielectrics over the time. Once enough charge has been accumulated within a dielectric, electrostatic discharge (ESD) events such as arcing or discharge can occur if the resultant electric field strength exceeds the material's breakdown limit, dielectric strength. Extremes temperatures in Deep Space are another major design challenge and knowledge of dielectric properties over such temperature is sometimes unknown. For these reasons, the use of dielectrics in an antenna located outside of the CubeSat is challenging. Another challenge associated with the use of dielectric, is the development of
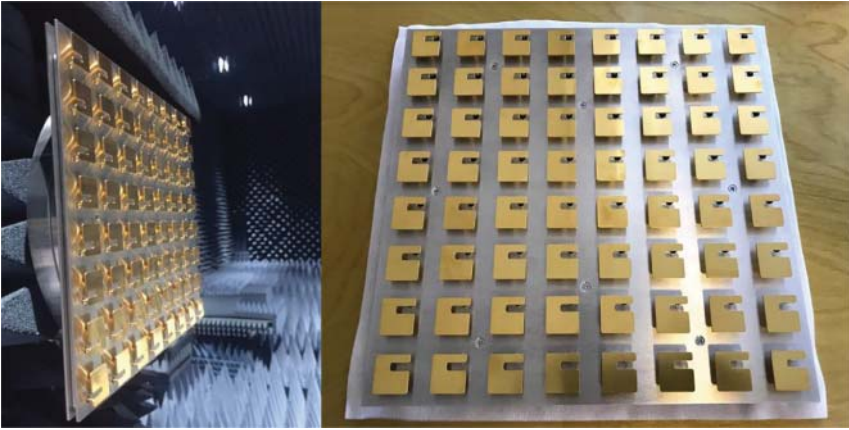
Figure 7.2 *The prototype 8 × 8 patch array designed to survive harsh environment and to achieve high aperture efficiency at both uplink and downlink DSN frequency bands.*

a reliable bonding process between materials with large CTE mismatch. As the antenna aperture increases, the bonding process becomes more challenging and drives the temperature limits. Besides, as the available volume on a CubeSat is very limited, an antenna with high aperture efficiency would maximize the data-rate and communication range capabilities. Hence, to withstand the harsh temperature conditions and radiation levels, the antenna should be made primarily of metal.

Once again, while this antenna is a good candidate for CubeSat platform, it was originally designed for the potential Europa Lander mission and is currently the baseline antenna enabling DTE from Europa. More information can be found in [3]. A photography of the prototype antenna is shown in Figure 7.2. For the potential Europa Lander mission, a 32 × 32 patch array will be used as shown in Figure 7.1. This antenna was successfully fabricated, tested, and qualified. It reached technology readiness level 6 after completing RF testing in a relevant environment, thermal cycling, and vibration testing.

7.2 State of the Art

Finding a single-layer, single fed element that supports circular polarization over the two targeted frequency bands is far from being straightforward. Traditional circularly polarized patch antennas are narrow band. The bandwidth defined as a reflection coefficient below −10 dB and an axial ratio under 3 dB is usually around 2% [5]. Adding to that the dual-frequency criteria compounds the problem. Over the years, researchers have investigated different approaches to obtain dual-band or wideband performance in circularly polarized patch antennas, including stacked patch antennas [6], slotted patch shapes, slotted ground planes [7], E-shaped [8, 9], U-slot [10], L-shaped [11], and so on. None of the aforementioned solutions are compatible with all-metal solutions that can be scaled to large arrays.

Figure 7.3   *The prototype 8×8 patch array designed to survive harsh environment and to achieve high aperture efficiency at both uplink and downlink DSN frequency bands. Courtesy of NASA/JPL Caltech.*
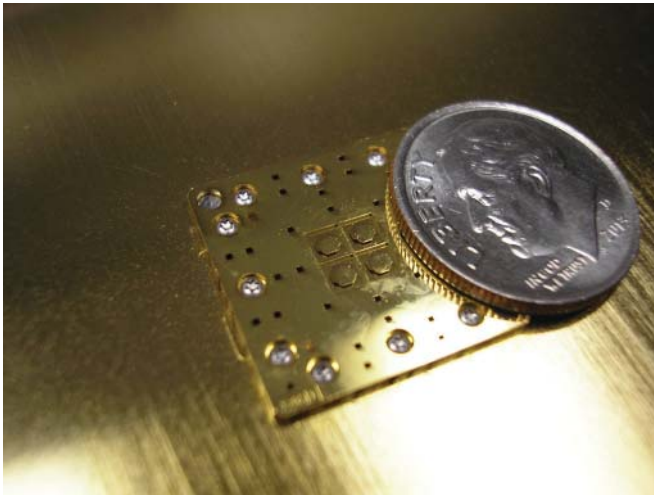
Figure 7.4   *A dual-polarized W-band metal patch antenna element for phased array applications. Courtesy of NASA/JPL Caltech.*

The Juno MicroWave Radiometer single-frequency linearly polarized patch array antennas, shown in Figure 7.3, was the first all-metal patch array developed for a NASA mission. Multiple versions of this antenna are flying and operating successfully on JUNO on Jupiter Orbit [4].

A 2×2 patch array of dual-polarized metal patch elements intended for electronically scanned array applications was designed at W-band [12] (Figure 7.4). This antenna was implemented in Polystrata® technology.

RUAG Space has also developed patch antennas entirely made of metal for space mobile communication satellites at L- and S-band with high aperture efficiency [13] (Figure 7.5).

Figure 7.5 *RUAG Space has developed array elements at L- and S-band for Mobile communication satellite systems. The Patch Excited Cup (PEC) element is designed for high aperture efficiency, excellent PIM properties, low losses and low mass. Source: From RUAG Space* [13]. *© 2016 RUAG Space.*

The Mars Science Laboratory high gain antenna (HGA) [14], currently operating on Mars on the Curiosity Rover, operates at both uplink and downlink frequency band with roughly 49 and 45% (not accounting for the loss in the rotary joint). This antenna was designed to survive Mars environment. A picture of the antenna on Mars is shown in Figure 7.6.

A radial line slot array (Figure 7.7) was proposed [15] to cover both uplink and downlink frequency bands. These antennas are intrinsically narrow band but a trade-off was made to get reasonable efficiency at both frequency bands (roughly 40 and 20%, respectively). One advantage of this design is the absence of dielectrics. It can be entirely made of metal.

A first attempt to provide dual-frequency with circular polarization was done through a collaboration between NASA's Jet Propulsion Laboratory and University of California Los Angeles (UCLA). The antenna is shown in Figure 7.8. The use of a thick dielectric combined with an half E-shaped patch element enables the bandwidth improvement. The axial ratio performance over the two frequency bands was successfully achieved but the reflection coefficient needs to be improved [9]. In general, the use of dielectric is challenging in deep space because of the aging properties of the material, coefficient of thermal expansion (CTE) mismatch resulting in delamination issues, varying dielectric properties over temperature, lower aperture efficiency, etc. For instance, on MarCO, the LGAs were bonded to an aluminum plate and extensive tests were performed to make sure the bonding will survive the thermal cycles. On previous NASA missions, we have witnessed failures during their qualification campaigns, due to improper bonding or radio frequency (RF) cables pulling into the SMA connector causing the patch to detach.

Another design entirely made of metal is worth mentioning. A Ka-band modulated metasurface antennas fabricated by metal additive manufacturing was recently proposed [16] (Figure 7.9). This antenna operates at a single frequency band but
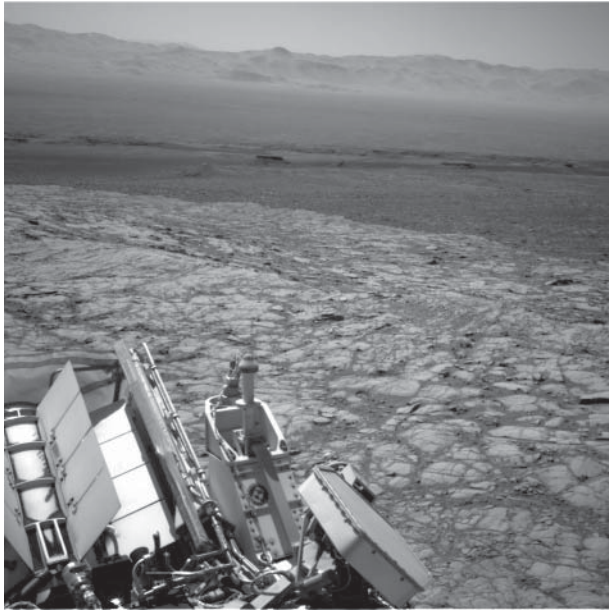
Figure 7.6   *Photography of the high gain antenna on the Curiosity Rover on Mars. Courtesy of NASA/JPL Caltech.*

Figure 7.7   *Photography of the radial line slot array. Reproduced with permission of IEEE.*
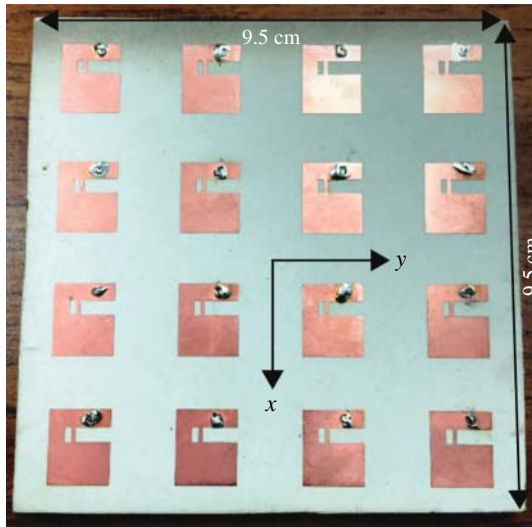
Figure 7.8 *Circularly polarized patch array antenna using thick dielectric* [5]. *Courtesy of NASA/JPL Caltech.*

Figure 7.9 *Ka-band modulated metasurface antennas fabricated by metal additive manufacturing* [16]. *Courtesy of NASA/JPL Caltech.*

could be potentially designed to cover two frequency bands as described in [17]. The aperture efficiency is around 40%.

7.3   Dual-Band Circularly Polarized 8×8 Patch Array

7.3.1   Requirements

The antenna should fit in one size of the CubeSat to avoid any unnecessary deployment. The CubeSat platform for this antenna is a 6U- ($12 \times 24 \times 36 \, \text{cm}^3$) or 12U-class ($24 \times 24 \times 36 \, \text{cm}^3$) Cubesat. As a result, the antenna should fit within $1 \times 24 \times 36 \, \text{cm}^3$.

To satisfy the dual-band communication link with NASA's DSN at the X-band, the antenna needs to meet stringent requirements across both uplink and downlink frequency bands with a sufficient thermal guard band. The antenna should be right-handed circularly polarized. Its efficiency should be higher than 80% at both frequency bands to provide at least a gain of 23.9 dBic and 25.0 dBic at 7.1675 and 8.425 GHz, respectively. The antenna axial ratio should be better than 3 dB and antenna return loss should remain higher than 14 dB at both frequency bands.

The antenna must survive and perform within $\pm 130 \, °\text{C}$. It should also be immune to high radiation levels and ESD. In addition, it should handle an input power of 25 W in vacuum.

7.3.2   Unit Cell Optimization

The key innovation to support the needed requirements is the all-metal unit cell providing RHCP at both uplink and downlink frequency bands. The all-metal patch element is shown in Figure 7.10. This element is single-fed thereby simplifying the feeding network and the antenna assembly. This patch element is entirely made of aluminum and is grounded to the antenna ground through a structural post. This structural post does not affect antenna performance as it is located where the current is null. The unit cell is optimized in an infinite array to obtain the required radiation pattern, axial ratio and impedance. Once the performance of the unit cell is achieved, its performance in an array is verified. If necessary, the dimensions are refined in the array configuration. Once the optimization is completed, a tolerance analysis is performed to make sure that the optimized shape is not sensitive to small dimensional or form variations.

The unit cell was optimized to achieve a good reflection coefficient and circular polarization within both Rx and Tx frequency bands using CST MWS (Finite integration technique) with a genetic algorithm. The parameter vector being optimized is defined as:

$$\underline{p} = [W_1, W_2, W_f, L_1, L_2, L_3, h] \tag{7.1}$$

(a)
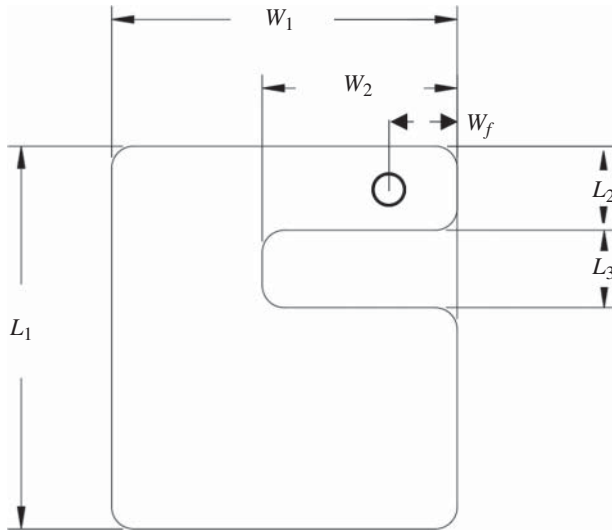
(b)

Figure 7.10 *All-metal unit cell providing RHCP at Tx and Rx frequency bands with a single feed point. (a) CAD model of the patch element including the feeding pin and the structural post. (b) Patch element geometry including the parameters being optimized to achieve RHCP within the two frequency bands.*

where the parameters being optimized are illustrated in Figure 7.10. The height of the patch h, not shown in the figure, is also being optimized.

The cost function is being minimized during the optimization process as:

$$C(\underline{p}) = \gamma_1 \cdot |\Delta_{\mathrm{Re}}(\underline{p})| + \gamma_2 \cdot |\Delta_{\mathrm{Im}}(\underline{p})| + \gamma_3 \cdot |\mathrm{AR}(\underline{p})| \qquad (7.2)$$

where:

$$\Delta_{\mathrm{Re}}(\underline{p}) = \frac{|\mathrm{Re}(Z_{\mathrm{ant}}(f_0, \underline{p})) - Z_0| + |\mathrm{Re}(Z_{\mathrm{ant}}(f_3, \underline{p})) - Z_0|}{2} - 20 \qquad (7.3)$$

Table 7.1   *Dimensions of the optimized patch element.*

Parameters	Optimized dimensions (mm)
W_1	15.6
W_2	8.8
W_f	3.7
L_1	17.3
L_2	1.9
L_3	3.5
h	4.1

$$\Delta_{\mathrm{Im}} (\underline{p}) = |\mathrm{Im}\,(Z_{\mathrm{ant}}\,(f_0,\underline{p})) - \mathrm{Im}\,(Z_{\mathrm{ant}}\,(f_3,\underline{p}))| - 15 \tag{7.4}$$

$$\overline{\mathrm{AR}}(\underline{p}) = \frac{1}{4} \sum_{n=0}^{3} \mathrm{AR}(f_n,\underline{p}) - \sqrt{2} \tag{7.5}$$

where $\mathrm{Re}(\cdot)$ and $\mathrm{Im}(\cdot)$ are real and imaginary operator, respectively. Z_0 is the input impedance of the patch element (i.e. $100\,\Omega$), $Z_{\mathrm{ant}}(f,p)$ is the antenna impedance function and $\mathrm{AR}(f,p)$ is the axial ratio function in magnitude evaluated with parameter p at frequency f, $f_0 = 7.145\,\mathrm{GHz}$, $f_1 = 7.190\,\mathrm{GHz}$, $f_2 = 8.4\,\mathrm{GHz}$, and $f_3 = 8.45\,\mathrm{GHz}$. The cost function is pre-coded to include the weighting control γ_1, γ_2, γ_3 for stressing on the importance of each optimized performance parameters (impedance and axial ratio). $\gamma_1 = 1/10$, $\gamma_2 = 2/15$, $\gamma_3 = \sqrt{2}$, are chosen such that the real and imaginary parts of the impedance and axial ratio are equally weighted. The optimized dimensions are summarized in Table 7.1.

The spacing element is set to roughly $0.62\,\lambda_0$. The reflection coefficient of the optimized unit cell is shown in Figure 7.11. It is below -15 dB within the two bands. The axial ratio is below 3 dB within the two frequency bands. The calculated gain of a unit cell is 6.8 and 8.7 dBic at uplink and downlink frequency bands, respectively. The impedance and axial ratio requirements were also successfully achieved in the 8×8 patch array.

To understand the behavior of the unit cell and how the circular polarization is generated, the currents are shown in Figure 7.12 for two points in time $\omega t = \Omega_0$ and $\omega t = \Omega_0 + \pi/2$, where Ω_0 is the reference phase which can be chosen arbitrarily. For the first time instance, x-directed mode dominates the currents, while in the second time instance, the y-directed mode dominates. Equal magnitudes between the x and y components is also an important feature for circular polarization radiation, and the figure indicates that both x and y directed current modes have similar magnitudes.
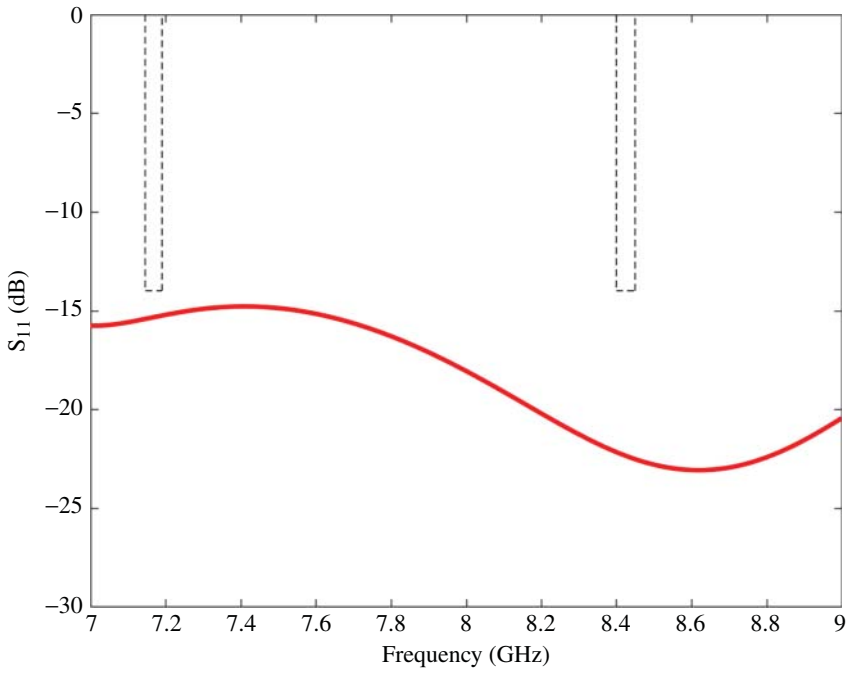
Figure 7.11 *Calculated reflection coefficient of the optimized single patch element with infinite boundaries.*
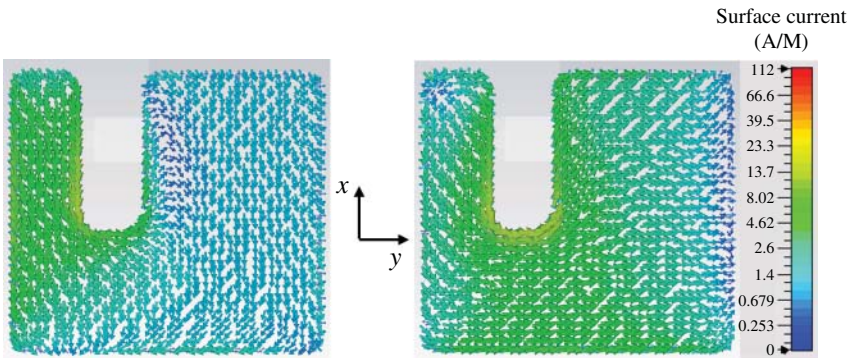
Figure 7.12 *Simulated electric surface current vectors on the unit cell for two time instances to demonstrate circular polarization at 7.145 GHz.*
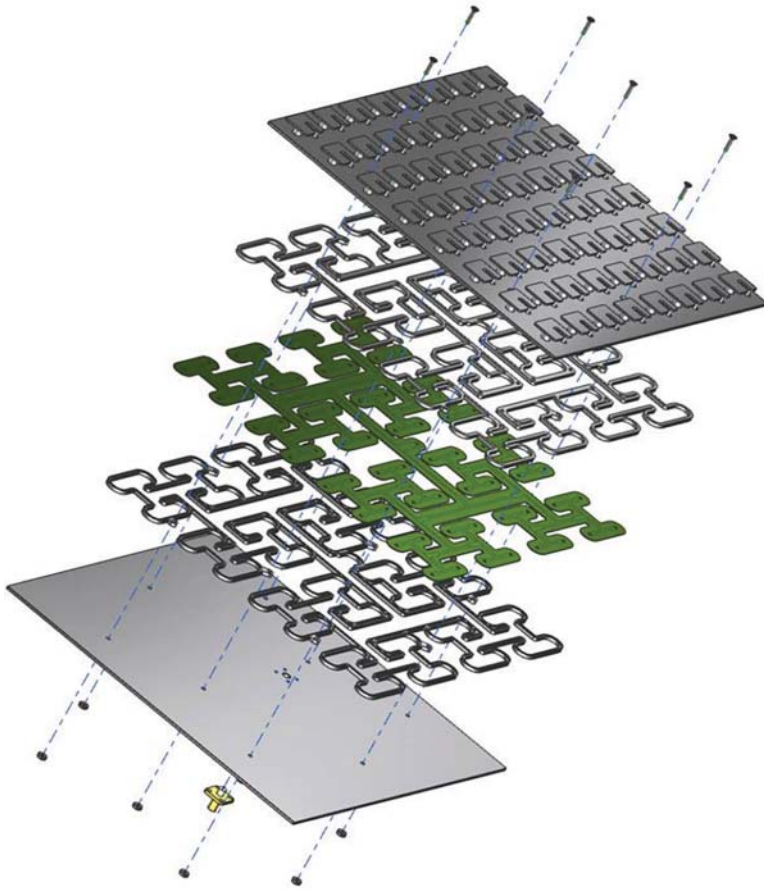
Figure 7.13   *Exploded view of the 8 × 8 patch array.*

7.3.3   8 × 8 Patch Array

The fabrication and assembly of the array is innovative but yet, very elegant and simple. The exploded view of the array is shown in Figure 7.13. The assembly of the array was carefully designed to minimize its complexity, thus facilitating low cost assembly of the final structure. It consists of: 64 patch elements, the top ground plane, the top and bottom walls in which the suspended substrate board is sandwiched and maintained in place, the bottom ground plane, the connector, and six fasteners/washers/bolts.
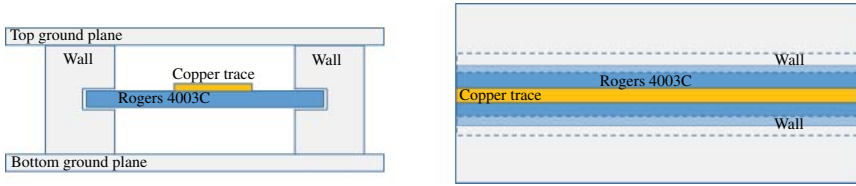
Figure 7.14 *Air stripline illustration.*
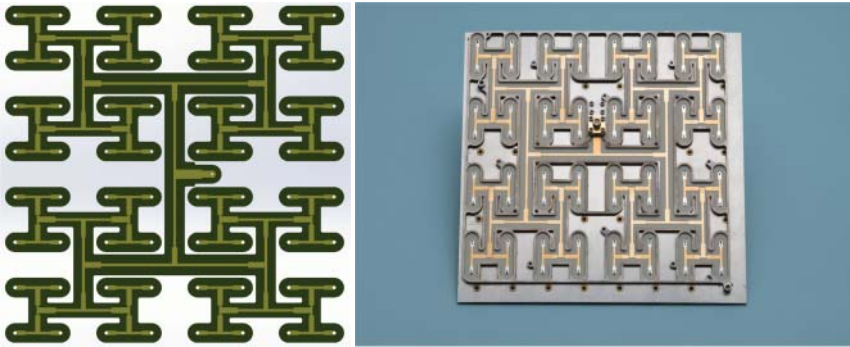
Figure 7.15 *Bottom view of the 8 × 8 patch array feed network.*

The patches are fed using an air stripline feed network. The air stripline consists of a 0.305 mm-thick Rogers 4003C substrate ($\varepsilon_r = 3.55$, $\tan \delta = 0.0027$) suspended between two ground planes separated by 1.75 mm (Figure 7.14).

The air stripline corporate feed network is shown in Figure 7.15. It was designed to provide equimagnitude and equiphase excitations to each of the elements. One can significantly simplify the matching network and design time by using the same power divider as illustrated in Figure 7.16. In this case, each power divider impedance input and outputs are $100\,\Omega$.

The air stripline is very low loss (i.e. less than 0.2 dB). The distance between the two ground planes was chosen to have sufficient margin against multipaction (i.e. more than 20 dB).

A prototype was fabricated and measured. A picture of the array prototype in an anechoic chamber is shown in Figure 7.2. The calculated and measured reflection coefficient of the array is shown in Figure 7.17. From 7 to 9 GHz, the reflection coefficient is below −10 dB and below −15 dB within the two frequency bands for relative permittivity variation of +/−10%. They are in excellent agreement.
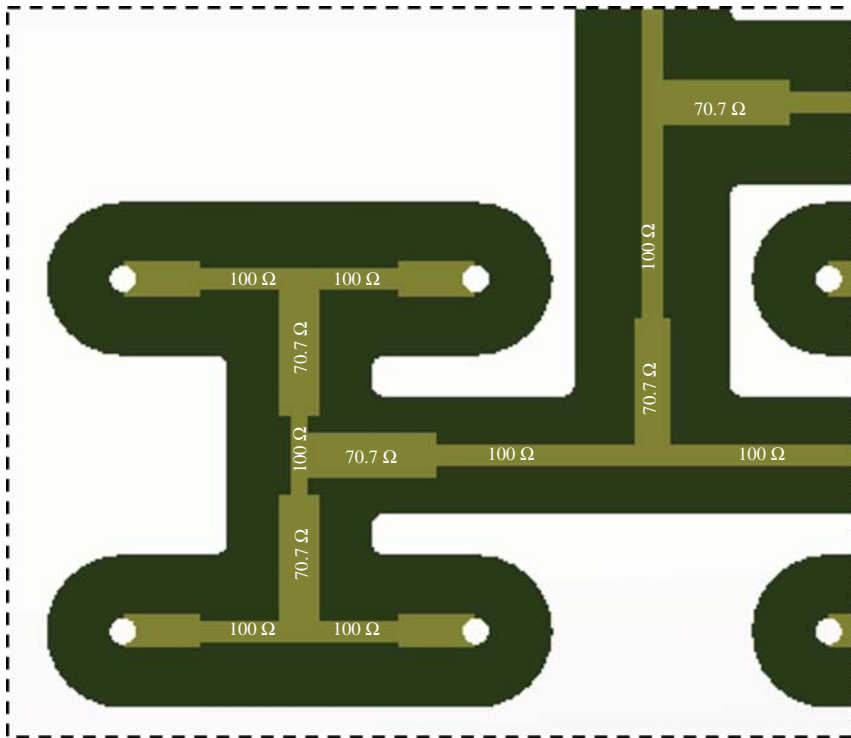
Figure 7.16   *Stripline feed network with impedance of each striplines.*

The radiation pattern is measured in a planar near field antenna measurement facility at NASA's Jet Propulsion Laboratory, Pasadena, CA. The gain is measured by substitution method using a standard horn. The calculated and measured radiation pattern is shown in 7.18. Excellent agreement is found between calculation and measurement for the radiation pattern. The antenna directivity, gain, and axial ratio are summarized in Table 7.2. The axial ratio is under 2.2 dB across the uplink and downlink frequency bands.

We investigated the effect of the changes of the dielectric permittivity that could be caused by thermal variation or radiation levels. For instance, the thermal coefficient of the relative permittivity (ε_r) of Rogers 4003C is 40 ppm/°C. Hence, a variation of 10% is extremely conservative and could not possibly be caused by a temperature change. The reflection coefficient is shown in Figure 7.19 and it remains below −10 dB within the uplink and downlink frequency bands. The boresight gain of the antenna remains within 0.1 and 0.03 dB at uplink and downlink, respectively.

The performance of the array is shown over a wider frequency band of 7–9 GHz in terms of gain (Figure 7.20) and axial ratio (Figure 7.21). The performance of the
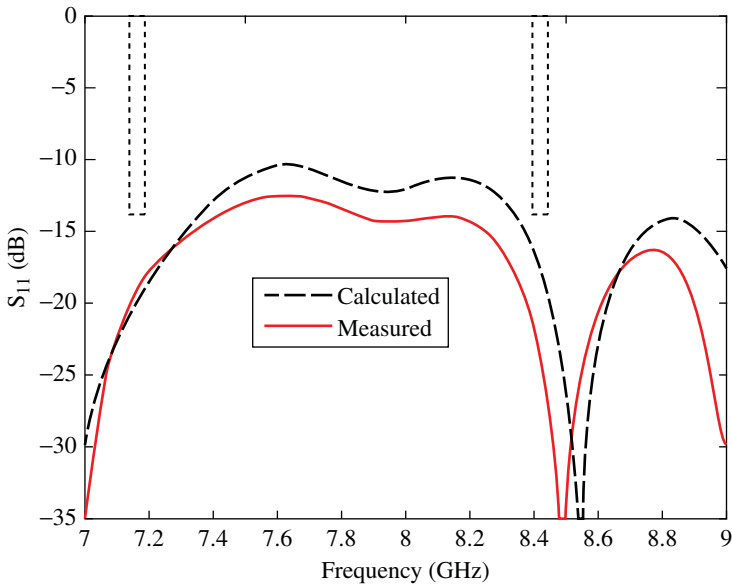
Figure 7.17   *Calculated and measured reflection coefficient of the 8 × 8 patch array.*

antenna are excellent even between the uplink and downlink frequency bands. The axial ratio could further be improved if required.

7.3.4   Comparison With State-of-the-Art

In this chapter, we define the aperture efficiency as the ratio of the realized gain of the antenna to its standard directivity. The standard directivity is $4\pi A/\lambda_0^2$, where A is the area of the antenna aperture and λ_0 is the free space wavelength. This defines how efficiently the area of an antenna is used. The antenna aperture efficiency is significantly higher than any dual-frequency low-profile antennas published in the literature. The aperture efficiency is a critical figure of merit as the antenna volume is limited on a CubeSat.

The performance of the proposed antenna is compared to the HGA antenna operating on Mars on the Mars Exploration Rover [18] and the Curiosity rover [14] and a dual frequency spiral radial line slot array antenna [15] in Table 7.3. The metal patch array presented here shows a significantly higher aperture efficiency than either of the listed antennas. The radial slot array antenna (RLSA) [15] exhibits low efficiency (i.e. roughly 40 and 20%) and as a result, to achieve the same gain, the antenna would need to be significantly larger, unfit with a CubeSat form factor.
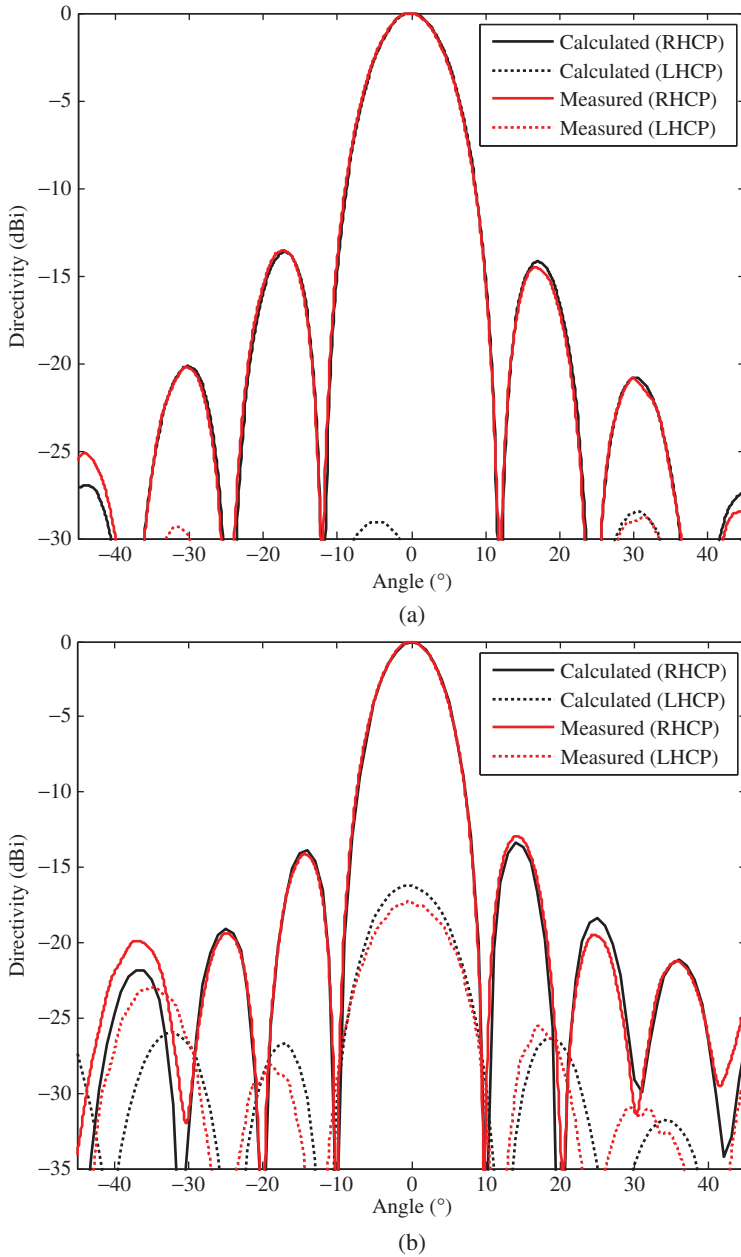
Figure 7.18 *Calculated and measured radiation pattern of the 8 × 8 patch array. (a) 7.1675 GHz. (b) 8.425 GHz.*

Table 7.2   *Measured and calculated directivity, gain, and axial ratio.*

Frequency (GHz)	Directivity (dBi)		Gain (dBic)		Axial ratio (dB)	
	Calc.	Meas.	Calc.	Meas.	Calc.	Meas.
7.1675	24.9	24.9	24.5	24.1 ± 0.4	0.3	0.3
8.425	26.0	26.0	25.6	25.3 ± 0.4	2.7	2.2
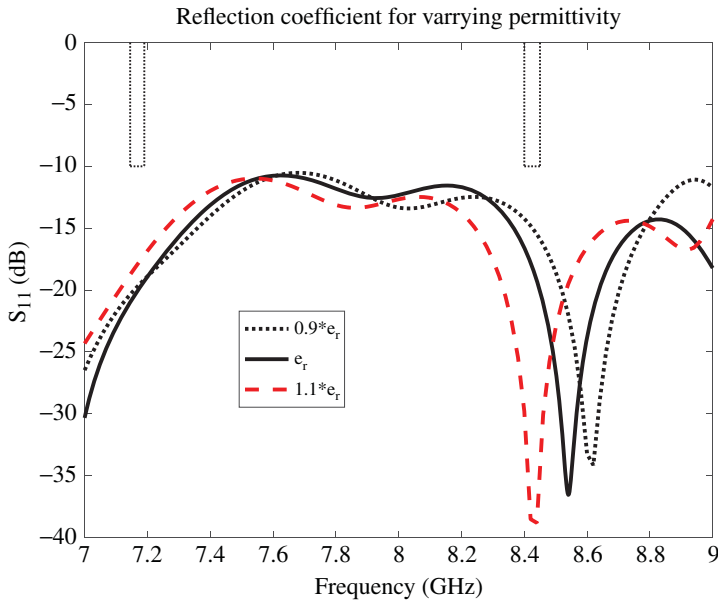
Figure 7.19   *Calculated reflection coefficient of the 8 × 8 patch array for varying permittivity (±10%).*

Due to its gain, size, mass, and power handling capabilities, this array is a strong candidate for future Mars Rover missions enabling higher data rate when combined with a high power amplifier (i.e. 100 W traveling wave tube as opposed to the currently used 15 W solid state power amplifier [14]).

7.3.5   Other Array Configurations

The advantage of patch arrays is that they can easily come in different configuration. Table 7.4 summarizes the performance of a wide range of array size all compatible with 3U- to 12U-CubeSats. The antenna gain and half power beamwidth (HPBW) is provided to facilitate mission formulation.
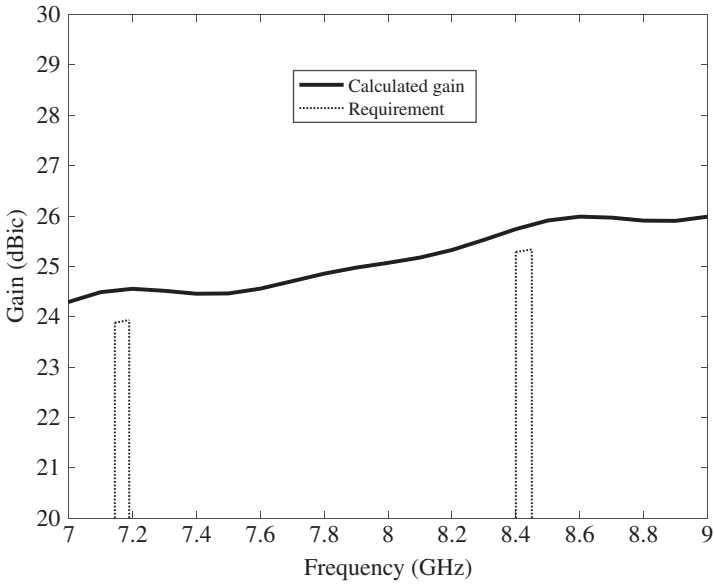
Figure 7.20   *Calculated realized gain over frequency of the 8 × 8 array.*
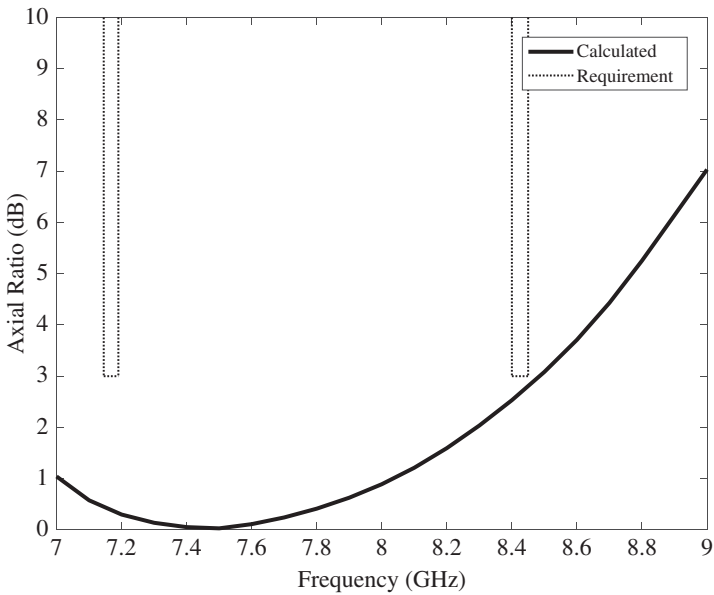
Figure 7.21   *Calculated axial ratio over frequency of the 8 × 8 array.*

Table 7.3   *Antenna performance comparison with state-of-the-art.*

	Aperture efficiency (%)	Gain (dBic)	Area (cm²)	HPBW (degree)	Mass (kg)
This work	84/80	24.1/25.3	428.5	10.4/8.7	0.5
RLSA [15]	37/18	25.3/23.5	1,256.6	6.0/5.1	1.24
MER [18]	25/49	20.5/24.8	615.8	10.0/8.4	1.1
MSL [14]	49/44	22.9/23.8	551.2	10.0/8.4	1.4

Table 7.4   *Metal patch arrays for different form factor.*

Array	Size (cm × cm)	Gain (dBi)		HPBW (°)	
		UL	DL	UL	DL
2 × 2	5.2 × 5.2	12.5	14	37.2	33.4
2 × 4	5.2 × 10.4	15.4	16.9	20.0	17.2
4 × 4	10.4 × 10.4	18.2	19.8	20.0	17.2
8 × 4	20.8 × 10.4	21.0	22.2	10.4	8.7
8 × 8	20.8 × 20.8	24.1	25.3	10.1	8.7

7.4   Conclusion

The HGA described in this chapter is primarily made of metal to survive the harsh environment of deep space with high radiation levels and extreme temperatures. The single-fed and single-bloc radiating element is entirely made of metal which also simplifies the fabrication and assembly of the array. This antenna could be mounted on one side of the bus using fasteners removing any CTE mismatch. It could even be fabricated on the bus itself.

The 8 × 8 patch array was fabricated and measured. Calculated and measured results are in excellent agreement. A gain of 24.1 and 25.4 dBic was demonstrated at both frequency bands. This translates into an aperture efficiency of 84 and 80% at uplink and downlink bands respectively. This antenna was fully qualified and reached TRL 6 after completing RF measurements, thermal cycling, vibration testing, and pyroshock testing.

Acknowledgments

References

1. C. B. Phillips and R. T. Pappalardo, "Europa clipper mission concept: exploring Jupiter's ocean moon," *Eos, Transactions American Geophysical Union*, vol. **95**, no. 20, pp. 165–167, May 2014.

2. NASA/JPL, "Europa Lander study 2016 report, Europa Lander Mission," *JPL D-97667*, Feb. 2017.

3. N. Chahat, "All-metal dual frequency RHCP high gain antenna for a potential Europa Lander," *IEEE Transaction on Antennas and Propagation*, vol. **66**, no. 12, pp. 6791–6798, Dec. 2018.

4. N. Chamberlain, J. Chen, P. Focardi, R. Hodges, R. Hughes, J. Jakoboski, J. Venkatesan, and M. Zawadzki, "Juno microwave radiometer patch array antennas," *2009 IEEE Antennas and Propagation Society International Symposium*, APSURSI'09, Charleston, SC, 2009.

5. J. M. Kovitz and Y. Rahmat-Samii, "Using thick substrates and capacitive probe compensation to enhance the bandwidth of traditional CP patch antennas," *IEEE Transactions on Antennas and Propagation*, vol. **62**, no. 10, pp. 4970–4979, Oct. 2014.

6. P. Nayeri, K.-F. Lee, A. Z. Elsherbeni, and F. Yang, "Dual-band circularly polarized antennas using stacked patches with asymmetric U-slots," *IEEE Antennas and Wireless Propagation Letters*, vol. **10**, pp. 492–495, May 2011.

7. X. Q. Nasimuddin and Z. N. Chen, "A wideband circularly polarized stacked slotted microstrip patch antenna," *IEEE Antennas and Propagation Magazine*, vol. **55**, no. 6, pp. 84–99, Dec. 2013.

8. F. Yang, X. Zhang, X. Ye, and Y. Rahmat-Samii, "Wide-band E-shaped patch antennas for wireless communications," *IEEE Transactions on Antennas and Propagation*, vol. **49**, no. 7, pp. 1094–1100, July 2001.

9. J. M. Kovitz, J. P. Santos, Y. Rahmat-Samii, N. F. Chamberlain, and R. E. Hodges, "Enhancing communications for future mars rovers: using high-performance circularly polarized patch subarrays for a dual-band direct-to-Earth link," *IEEE Antennas and Propagation Magazine*, vol. **59**, no. 4, pp. 50–61, Aug. 2017.

10. K.-F. Tong and T.-P. Wong, "Circularly polarized U-slot antenna," *IEEE Transactions on Antennas and Propagation*, vol. **55**, pp. 2382–2385, Aug. 2007.

11. S. S. Yang, K. Lee, A. A. Kishk, and K. Luk, "Design and study of wideband single feed circularly polarized microstrip antennas," *Progress in Electromagnetics Research*, vol. **80**, pp. 45–61, 2008.

12. N. Chamberlain, M. S. Barbetty, G. Sadowy, E. Long, and K. Vanhille, "A dual-polarized W-band metal patch antenna element for phased array applications," *IEEE Antennas and Propagation Society International Symposium*, Memphis, TN, 2014, pp. 1640–1641.

13. RUAG Space, "Mobile communication antennas," Available: online: https://www.ruag .com/sites/default/files/2016-12/Mobile_communication_Antennas.pdf

14. A. Olea, A. Montesano, C. Montesano, and S. Arenas, "X-band high gain antenna qualified for mars atmosphere," *Proceedings of the Fourth European Conference on Antennas and Propagation*, Barcelona, 2010.

15. M. Bray, "A radial line slot array antenna for deep space missions," *2017 IEEE Aerospace Conference*, Big Sky, MT, 2017.

16. D. Gonzalez-Ovejero, N. Chahat, R. Sauleau, G. Chattopadhyay, S. Maci, and M. Etorre, "Additive manufactured only-metal metasurface antennas," *IEEE Transactions on Antennas and Propagation*, vol. **66**, no. 11, pp. 6106–6114, Nov. 2018.

17. D. Gonzalez-Ovejero, G. Chattopadhyay, and S. Maci, "Multiple beam shared aperture modulated metasurface antennas," *2016 IEEE International Symposium on Antennas and Propagation (APSURSI)*, Fajardo, 2016, pp. 101–102.

18. J. Taylor, A. Makovsky, A. Barbieri, R. Tung, P. Estabrook, and A. G. Thomas, "Mars exploration rover telecommunications," *JPL Deep Space Communications and Navigation Systems Center of Excellence: Design and Performance Summary Series*, Oct. 2005.

8

Metasurface Antennas: Flat Antennas for Small Satellites

David González-Ovejero[1], Okan Yurduseven[2], Goutam Chattopadhyay[3] and Nacer Chahat[3]

[1]*Centre National de la Recherche Scientifique – CNRS, IETR UMR 6164, Rennes, France*
[2]*Queen's University Belfast, Belfast, UK*
[3]*NASA Jet Propulsion Laboratory/California Institute of Technology, CA, Pasadena, USA*

8.1   Introduction

Metasurfaces (MTSs) have recently sprung up as a very versatile technology. They have indeed enabled the design of a myriad of devices in a large fraction of the electromagnetic spectrum, from microwave to optical frequencies, including the terahertz gap [1–3]. Among the most popular applications, one finds the control of beam transmission/reflection and MTS lenses [4, 5], circuits for the manipulation of surface-waves (SWs) [6–10], and antennas [11–16]. Although there are several topologies of MTS antennas [11–13], here, we will focus on modulated MTS [14–15, 17] and holographic antennas [16, 18]. In modulated MTS antennas, an inductive impedance boundary condition (IBC) supports the propagation of a dominantly transverse magnetic (TM) SW. This SW is gradually radiated owing to the IBC modulation, tailored in such a way that the -1 Floquet mode in the field expansion becomes a leaky-wave (LW). Similarly, in holographic antennas, a holographic

pattern consisting of a set of meta-atoms allows one to radiate the power carried by a reference wave.

To date, most of the implementations of modulated MTS antennas consist of planar circular apertures made of sub-wavelength patches (or slots) printed (or etched) on a grounded dielectric slab and fed at their center by a monopolar source. However, as we will discuss here, there are alternatives consisting of metal-only structures. Besides, we will also present the use of quasi-optical systems to excite holographic MTS antennas at the end of this chapter. Regardless of the implementation, this class of antenna is inherently flat and low mass, which renders it of great interest for space, in general, and particularly for CubeSats and SmallSats platforms.

8.2   Modulated Metasurface Antennas

8.2.1   State of the Art: Pros and Cons

One of the most attractive features of MTS antennas is their capability of providing high- to very-high gains with low-profile structures. Traditional high-gain antennas, such as parabolic reflectors, require large volumes because of the nature of their antenna structure. Even for the recently popular 2-D flat antennas, like reflectarrays and transmitarrays, the overall volume is substantial, as it needs a feed deployed out in the third dimension. On the contrary, MTS antennas are truly low profile as they are fed with a probe or waveguide at the center of the antenna aperture without any protruding parts. This low-profile characteristic makes MTS antennas appealing to a host of applications, including for space based systems [17], and in particular for CubeSats or Smallsats. Among their other advantages, it is important to note their capability of conforming to curved surfaces [18], and providing a simple on-surface control of the aperture fields for beam shaping, pointing and scanning.

Modulated MTS antennas also come with their own drawbacks. Essentially, the first realizations suffered from a low aperture efficiency. For instance, the 10 cm radius spiral LW antenna operating at 17 GHz and tested in [17] yielded a 25% aperture efficiency. Other two early prototypes of circular antennas at X-band [19] also provided a measured aperture efficiency relatively low, around 36%. To better illustrate this limitation, let us consider circular apertures, ignore the effect of losses and assume that the feed transforms 100% of the delivered power into SW power. Under these assumptions, we can calculate the antenna efficiency as the product of conversion and taper efficiency. The conversion efficiency represents the fraction of radiated LW power with respect to the SW power, whereas the taper efficiency is related to the directivity loss of a given aperture illumination with respect to a uniform distribution. It is possible to prove [20] that for a uniform modulation index, the maximum theoretical efficiency is 58% when $\alpha R = 0.9$, where α is the leakage factor and R is the antenna radius. Nonetheless, one may overcome this fundamental limitation by using a non-uniform modulation index $M(\rho)$ [21]. Indeed, an optimum choice of $M(\rho)$ yields theoretical values for the efficiency as

high as $(R/\lambda_0)/(R/\lambda_0 + 2)$, with λ_0 being the free-space wavelength at the center frequency f_0 [20]. In [22], one may find two examples of modulated MTS antennas with measured aperture efficiency as high as 70% for a 37 dBi broadside pencil beam antenna with right-handed circular polarization (RHCP), and 58% for a 33 dBi squinted beam RHCP antenna.

Nonetheless, designs with high aperture efficiency impose a toll on the antenna bandwidth. This limitation can be quantified by computing the fractional bandwidth of antennas with radius R larger than $3\lambda_0$ and an optimal choice of $M(\rho)$ [23]. An approximate expression for the fractional bandwidth is then given by $\Delta f/f_0 = 1.2(R/\lambda_0)(v_g/c)$, where c is the speed of light in free space, and v_g is the group velocity of the SW at f_0 when it propagates along a uniform average impedance. Practical values of $\Delta f/f_0$ may vary between 3 and 9% when the antenna gain goes from 40 to 28.5 dBi (see figure 5 in [23]). However, recent studies have proven that it is also possible to obtain a dual-band behavior by combining on the antenna aperture the modulations needed at each individual frequency [22, 24]. Broadband MTS antennas [22] are also feasible, given that one is willing to accept a compromise between gain and bandwidth. To increase the bandwidth, we can exponentially chirp the period of the modulation along the radius of circular apertures. The obtained relative bandwidths (above 20%) are considerably wider than the ones obtained by MTS antennas with constant period, while these antennas can still can provide high gain pencil beams. Typical low profile and wideband antennas with one feeding point consist of logarithmic spirals backed with high-impedance surfaces. However, the gains obtained with this solution are usually moderate. The broadband MTS structure proposed in [25] overcomes the gain limitation of spiral antennas and extraordinarily extends the bandwidth of MTS antennas with constant modulation period.

In addition to the efforts devoted to increase the aperture efficiency and the bandwidth of MTS antennas, other works have exploited the MTS capability of controlling the aperture fields to get shaped beams and multi-beam antennas. For instance, the design of an isoflux axially-symmetric antenna for low Earth orbit (LEO) communication at X-band was described in [17, 26] including measurements of a prototype. In turn, the sector isoflux antenna described in [17] achieved much higher gain and data rate, relying on azimuthal rotation to maintain the pointing towards the ground station. The measurements of the corresponding prototype at Ka-band (26.4 GHz) yielded 2% of relative bandwidth for a 2 dB ripple, as reported in [22].

Finally, a shared-aperture MTS antenna with simultaneous dual beam pattern and operating at 17 GHz was reported in [27] (see Figure 8.1). The authors of [27] showed that the dual beam can be obtained with a single point source or that independent control of the beams can be obtained by introducing multiple sources on the antenna aperture [28, 29]. This is an interesting feature offered by MTS antennas, and it could come very handy for some specific remote sensing science applications. The antenna shown in Figure 8.1 is a 22 cm diameter antenna providing a measured aperture efficiency of 47.6% for each beam at 17 GHz. Here, the beam
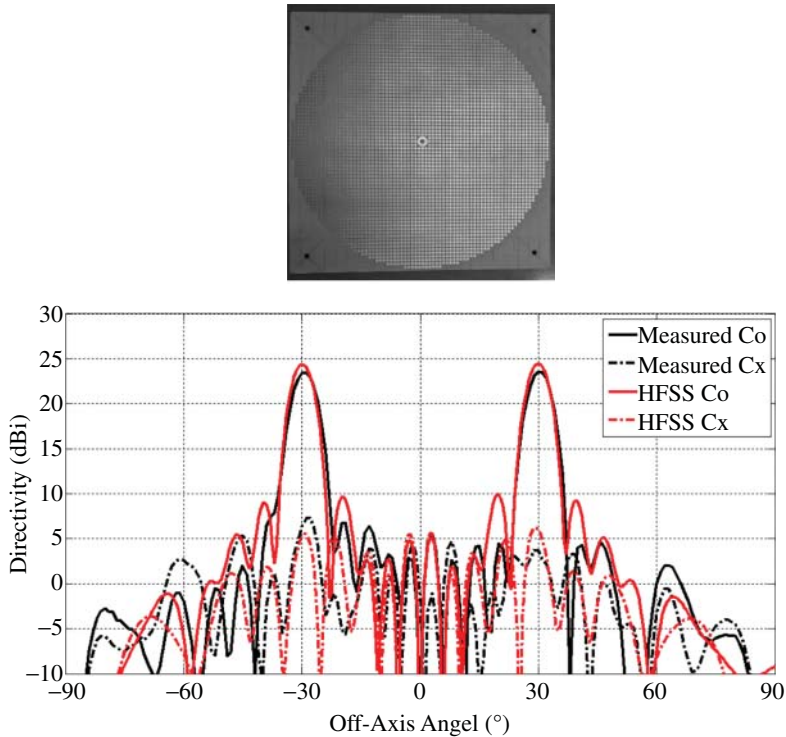
Figure 8.1   *Shared aperture metasurface antenna with dual beam pattern operating at 17 GHz and comparison between the simulated and measured directivity patterns. Sources: From Faenzi et al. [22]. © 2019 John Wiley & Sons and Gonzalez-Ovejero, et al. [27]. © 2017 John Wiley & Sons.*

efficiency is defined as $NG/[\cos(\theta_0)(k_0R)^2]$ where G is the beam gain, N is the number of beams and $\cos(\theta_0)(k_0R)^2$ is the maximum gain provided in the direction θ_0 by a uniformly illuminated circular aperture of radius R. Table 8.1 summarizes the main characteristics of the modulated MTS antennas reviewed above.

All the MTS antennas in Table 8.1 consist of sub-wavelength patches printed on a grounded dielectric substrate. Although this technology is valid for a wide range of terrestrial applications, the use of dielectric entails higher losses at high frequencies and makes the antennas susceptible to the space environment (thermal, radiation, and electrostatic discharge). The reader is referred to [14, 15, 22] and the references therein for an excellent review on modulated MTS antennas fabricated by printed patches. In this chapter, we will look into alternative design approaches to the traditional MTS printed on dielectric substrates and other recent developments at NASA's Jet Propulsion Laboratory (JPL) in collaboration with CNRS (IETR, UMR

Table 8.1 *Summary of modulated MTS antennas realized by printed patches.*

Ref.	Pattern type	Central frequency (GHz)	3 dB gain relative bandwidth	Aperture efficiency at f_0 (%)
[17]	RHCP broadside pencil beam	17	5.9% (16.25–17.25 GHz)	24.7
[19]	RHCP broadside pencil beam	7.165	4%	35.9
[19]	RHCP broadside pencil beam	8.425	2.4%	33.8
[22]	RHCP broadside pencil beam	29.75	4.7% (29.1–30.5 GHz)	70
[22]	RHCP tilted pencil beam	20	3.25% (19.65–20.3 GHz)	58
[17, 26]	Isoflux	8.6	8.5–8.6 GHz	n/a
[22]	Sector isoflux	26.4	2%	n/a
[27]	Dual-beam	17	5.9%	47.6

6164) and Queen's University. Over the last few years, JPL has introduced several innovative MTS antennas and performed some environmental tests to advance the technology readiness level (TRL) with the intention to fly these antennas on instruments for well-defined applications. In-house codes were developed to design and optimize these antennas and new fabrication methods were investigated as alternative solutions of dielectric-based antennas, e.g. silicon micromachining [30, 31] and additive manufacturing [32].

The antenna shown in Figure 8.2 is a spiral modulated MTS operating at 300 GHz and implemented using metallic cylinders with circular cross-section. The motivation to use a fully metallic structure was to minimize the losses at submillimeter wavelengths, compared to antennas that use conventional dielectric substrates at these frequencies. An innovative feeder was implemented to launch a cylindrical TM-SW on the metallic structure. Such feeder used an integrated transition to rectangular waveguide so that it is compatible with the rectangular waveguide output of solid-state frequency-multiplied sources. The MTS modulation was obtained by changing the radius or height of the cylinders in a unit cell with constant dimensions. This approach enabled the synthesis of a broad range of reactance values. This antenna was micro machined in silicon using deep reactive ion etching (DRIE) and then metallized by gold sputtering at the Microdevices Laboratory facilities at

(a)   (b)
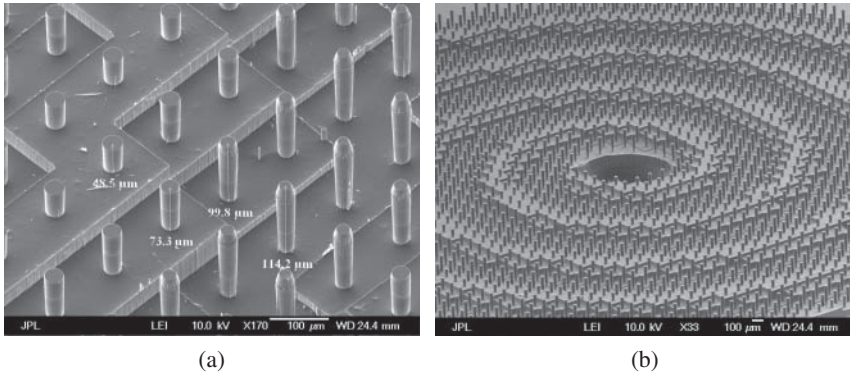
Figure 8.2   *SEM pictures of the circularly-polarized MTS antenna operating at 300 GHz and fabricated using silicon micromachining: (a) detail of the pins* [30]*; (b) central region of the antenna* [31].

JPL. Section 8.2.3 will provide more details regarding the design, fabrication, and testing of this antenna.

Along similar lines, a Ka-band MTS antenna entirely made of metal was designed, fabricated, and tested for telecommunication with NASA's Deep Space Network (DSN). As opposed to the previous design, which used cylinders with circular cross-section and isotropic response, this design employed elliptical cylinders to obtain an anisotropic response. Anisotropic surface reactances enhance the cross-polarization discrimination, which is critical for telecommunication antennas where circular polarization is required. The antenna used the orientation of the ellipses and the height of the elliptical metallic pins to get the MTS modulation [32]. The antenna, shown in Figure 8.3, was fabricated using additive manufacturing. It operates at the Ka-band downlink frequency band of the DSN (31.8–32.3 GHz). We will discuss this antenna with more detail in Section 8.2.4.

The rest of the sections on modulated MTS antennas in this chapter are organized as follows. First, we will briefly recall the design process, focusing on the metal-only realizations. Then, we will present in detail the two designs of metal-only MTS, briefly introduced in the two paragraphs above.

8.2.2   Design of Modulated Metasurface Antennas

To get a better understanding of radiation by modulated MTS, first, we will briefly recall the content of [33], one of the papers at the origin of modulated MTS technology. In absence of modulation, an average inductance X_0 supports the propagation of a TM-SW with wavenumber β_{SW} given by:

$$\beta_{SW} = k\sqrt{1 + \left(\frac{X_0}{\zeta}\right)^2} \qquad (8.1)$$

Figure 8.3 *Ka-band modulated metasurface antenna fabricated by metal additive manufacturing* [32].

with k and ζ being the free space wavenumber and impedance, respectively. The authors of [33] studied the canonical problem of an infinite inductance plane with a one-dimensional sinusoidal modulation along the x-direction:

$$X_s(x) = X_0 \left(1 + M \sin \left(\frac{2\pi x}{p} \right) \right) \tag{8.2}$$

where x is the direction of propagation, M the modulation factor, and p the period of the modulation. In presence of the modulation, the structure can gradually radiate the power carried by the SW. Indeed, the n-indexed mode in the Floquet mode expansion of this periodic problem presents a transverse-to-z wavenumber equal to:

$$k_{t,n} = \beta_{SW} + \beta_{\Delta} - j\alpha + \frac{2\pi n}{p} \tag{8.3}$$

where β_{Δ} and α are the perturbations in the phase and attenuation constants, respectively, due to the modulation. β_{SW} stands for the unperturbed value of k_t ($M = 0$) given by (8.1). Figure 8.4 shows the values of β_{Δ} and α computed for different average impedances X_0 and modulation indexes M. One can deduct from Figure 8.4 that the higher the modulation index and the average impedance, the higher the leakage factor α. This type of design curves is, hence, crucial to control the aperture efficiency of MTS antennas. On the other hand, β_{Δ} is a small factor with respect to β_{SW} and it can be neglected in the design of medium-gain antennas. However, in designs
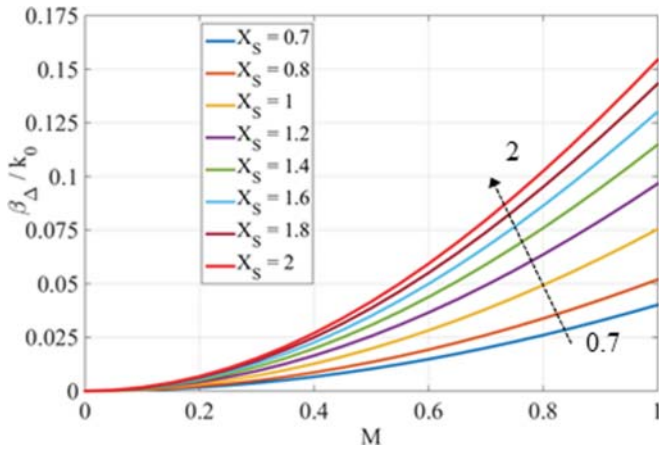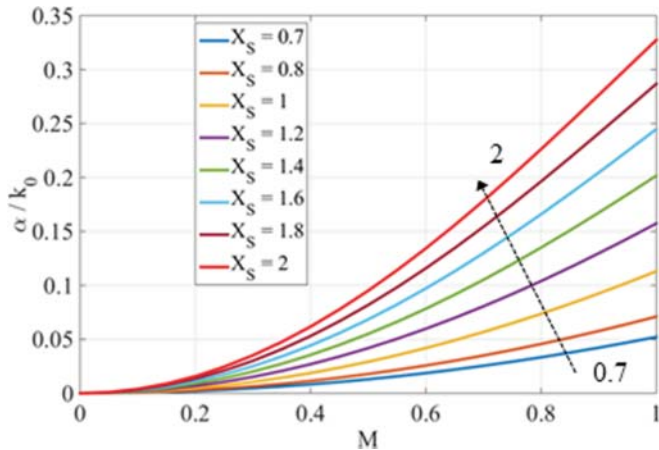
Figure 8.4   *Curves for: (a) β_{SW}; (b) α normalized to k as a function of the modulation index (M) and for different average impedance values (X_s).*

with strict specifications, one has to account for the deviation in the pointing direction induced by β_Δ. The same type of curves can be obtained for inductance tensor, as described in [34].

When $|\Re\{k_{t,n}\}| < k$, the corresponding mode enters in the visible region of the spectrum, becoming a leaky-mode. The $n = -1$ mode is the dominant leaky-mode and it radiates in a direction given by:

$$\beta_{SW} + \beta_\Delta - \frac{2\pi}{p} = k \sin \theta_0 \qquad (8.4)$$

where θ_0 is the angle with respect to the z axis. Hence, the value of X_0 and p required to obtain a single forward beam at an angle θ_0 can be related using (8.1) and (8.4). Given a free space wavelength λ and neglecting the effect of β_Δ, the period to obtain a single forward beam is:

$$p = \frac{\lambda}{\sqrt{1 + (X_0/\zeta)^2} - \sin \theta_0} \tag{8.5}$$

when $\overline{X}/\zeta > \sqrt{4 \sin \theta_0 (1 + \sin \theta_0)}$.

Although it is possible to use Oliner and Hessel's theory [33] directly to design one-dimensional MTS antennas as in [35], the more general case of planar apertures requires some additional effort. In the following, we will consider the design of circular antennas of radius R, which present a planar interface with free-space at the $z = 0$ plane of a Cartesian reference system with coordinates (x,y,z) and unit vectors $(\hat{\mathbf{x}}, \hat{\mathbf{y}}, \hat{\mathbf{z}})$. We will denote vectors by bold characters, unit vectors by bold characters with a caret, and tensors by bold characters underlined by double bars. A $\exp(j\omega t)$ time dependence, where ω is the angular frequency, is assumed and suppressed. For convenience, we define the observation point on the aperture as $\boldsymbol{\rho} = \rho \cos \phi \hat{\mathbf{x}} + \rho \sin \phi \hat{\mathbf{y}}$ in a cylindrical coordinate (ρ, ϕ) system with unit vectors $(\hat{\boldsymbol{\rho}}, \hat{\boldsymbol{\phi}})$.

Figure 8.5 shows the design flow of the circular modulated MTS antennas described in this chapter. The goal of the design process is to find a structure able to generate an objective aperture field $\mathbf{E}_A$, which one can either obtain in analytical form or retrieve numerically through the solution of an inverse problem [36]. We usually resort to the latter strategy in the synthesis of complex patterns, like isoflux or shaped beams. The calculation of $\mathbf{E}_A$ constitutes the *first step* in the design process, outlined in Figure 8.5.

In the *second step*, we compute the ideal IBC that, in presence of a TM-SW, reproduces the desired $\mathbf{E}_A$ on the antenna aperture. In our design approach, the desired aperture field is obtained by a periodically modulated IBC. This boundary condition is represented by the tensor $\underline{\underline{\mathbf{X}}}(\boldsymbol{\rho})$ and relates the total tangential electric and tangential magnetic fields on the MTS aperture as [17, 32]:

$$\mathbf{E}_t|_{z=0^+} = j \underline{\underline{\mathbf{X}}}(\boldsymbol{\rho}) \cdot \hat{\mathbf{z}} \times \mathbf{H}_t|_{z=0^+} \tag{8.6}$$

where we assume $\underline{\underline{\mathbf{X}}}(\boldsymbol{\rho}) = \underline{\underline{\mathbf{X}}}(\boldsymbol{\rho} + p\hat{\boldsymbol{\rho}})$, with p being the period of the modulation. It is important to note that the fields in (8.6) are evaluated at the upper interface and $\hat{\mathbf{z}}$ is the normal to the MTS plane. Equation (8.6) describes an impenetrable IBC [37]. In most reported papers on MTS antennas, penetrable boundary conditions are usually employed, since those MTS consists of printed patch elements on dielectric material.

In the calculation of $\underline{\underline{\mathbf{X}}}(\boldsymbol{\rho})$, we assume that the MTS antenna is fed by a source launching a cylindrical $\overline{\mathrm{SW}}$ with a wavenumber β_{SW}. The total aperture field $\mathbf{E}_t$ on
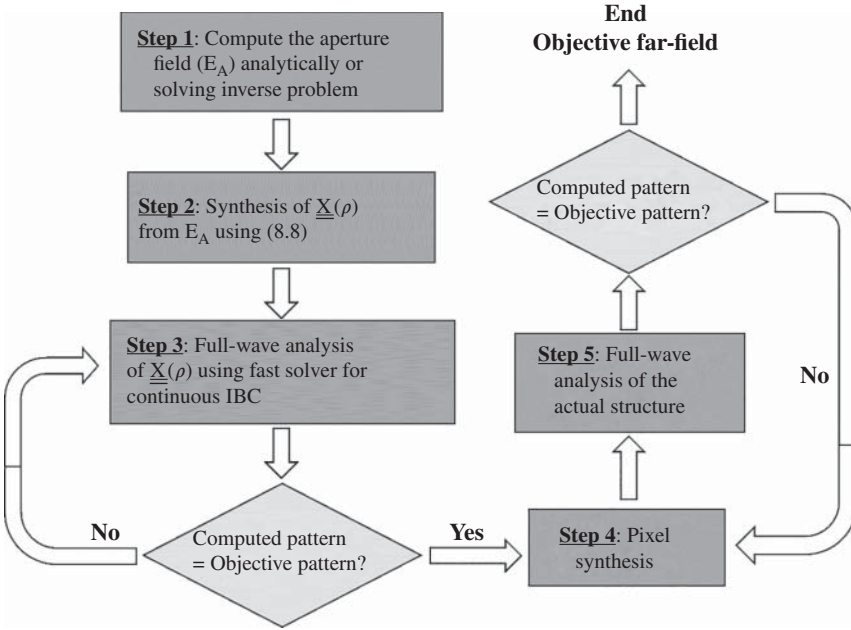
Figure 8.5   *Flow diagram for the design of modulated MTS antennas.*

the impenetrable boundary condition is then given by:

$$\mathbf{E}_t = I_{\mathrm{TM}}\mathrm{j}\underline{\underline{\mathbf{X}}}(\boldsymbol{\rho}) \cdot \hat{\boldsymbol{\rho}} H_1^{(2)}((\beta_{\mathrm{sw}} - \mathrm{j}\alpha)\rho) \tag{8.7}$$

where I_{TM} is the complex excitation coefficient of the SW, and $H_1^{(2)}(.)$ is the Hankel function of the second kind and first order.

In order to find $\underline{\underline{\mathbf{X}}}(\boldsymbol{\rho})$, we identify $\mathbf{E}_A$ with the -1 mode contribution of $\mathbf{E}_t$ in (8.7) which gives:

$$\underline{\underline{\mathbf{X}}}(\boldsymbol{\rho}) \cdot \left\{ \begin{matrix} \hat{\boldsymbol{\rho}} \\ \hat{\boldsymbol{\phi}} \end{matrix} \right\} = \left[X_0 \left\{ \begin{matrix} \hat{\boldsymbol{\rho}} \\ \hat{\boldsymbol{\phi}} \end{matrix} \right\} \pm 2\mathrm{Im}\left(\frac{\mathbf{E}_A}{I_{\mathrm{TM}}H_1^{(2)}(\beta_{\mathrm{sw}}\rho)} \right) \right] U_A \tag{8.8}$$

where the upper and lower signs correspond to the $\hat{\boldsymbol{\rho}}$ and $\hat{\boldsymbol{\phi}}$ components, respectively. The period p of the modulation is related to the SW wavenumber as $\beta_{\mathrm{SW}} = 2\pi/p$. The reader is referred to [17] for more details on the derivation of (8.8).

To better illustrate the calculation of $\underline{\underline{\mathbf{X}}}(\boldsymbol{\rho})$, let us assume that the objective aperture field ($\mathbf{E}_A$) is the one required to obtain a linearly polarized (LP) broadside pencil beam. Then, $\mathbf{E}_A$ is given by:

$$\mathbf{E}_A = E_0\,\hat{\mathbf{x}}\,\sqrt{\frac{2}{\pi\beta_{\mathrm{sw}}\rho}}\,\mathrm{e}^{-\alpha\rho}U_A \tag{8.9}$$

where E_0 is the field magnitude and U_A is a step function that equals one inside the aperture and 0 elsewhere.

Using (8.9) in (8.8) and projecting $\underline{\underline{\mathbf{X}}}(\boldsymbol{\rho})\cdot\hat{\boldsymbol{\rho}}$ along $\hat{\boldsymbol{\rho}}$ and $\hat{\boldsymbol{\phi}}$, gives the impenetrable reactance tensor which upon interaction with a cylindrical SW will generate the objective far-field. For instance, we can get the expression of the $X_{\rho\rho}$ component of the tensor $\underline{\underline{\mathbf{X}}}(\boldsymbol{\rho})$ as:

$$
\begin{aligned}
\underline{\underline{\mathbf{X}}}\cdot\hat{\boldsymbol{\rho}}\cdot\hat{\boldsymbol{\rho}} &= \left[X_0 + 2\mathrm{Im}\left(\frac{E_0[\hat{\mathbf{x}}\cdot\hat{\boldsymbol{\rho}}]\sqrt{\dfrac{2}{\pi\beta_{sw}\rho}}e^{-\alpha\rho}}{|I_{TM}|e^{j\psi}H_1^{(2)}(k_{sw}\rho)} \right) \right] U_A \\
&= \left[X_0 + 2Im\left(\frac{E_0\cos\varphi}{|I_{TM}|e^{j\psi}e^{-j\beta_{sw}\rho}} \right) \right] U_A \\
&= X_0\left[1 + \frac{2E_0}{I_{TM}X_0}\cos\varphi\sin(\beta_{sw}\rho - \psi) \right] U_A \qquad (8.10)
\end{aligned}
$$

where we can arbitrarily fix $\psi = 0$ and the term $2E_0/(I_{TM}X_0)$ corresponds to the modulation index. One can obtain the other components of the tensor carrying out similar operations, which leads to:

$$
X_{\rho\rho}(\boldsymbol{\rho}) = X_0\left[1 + M\cos(\phi)\sin\left(\frac{2\pi\rho}{p}\right) \right]
$$

$$
X_{\rho\phi}(\boldsymbol{\rho}) = X_{\phi\rho}(\boldsymbol{\rho}) = -X_0 M\sin(\phi)\sin\left(\frac{2\pi\rho}{p}\right)
$$

$$
X_{\phi\phi}(\boldsymbol{\rho}) = X_0\left[1 - M\cos(\phi)\sin\left(\frac{2\pi\rho}{p}\right) \right] \qquad (8.11)
$$

As anticipated in (8.5), the relation between X_0 and p is $p = 2\pi/(k\sqrt{1 + (X_0/\zeta)^2})$. Please note that (8.11) includes a modulation parameter M, which we assume constant. Although in the above expressions and in this chapter's examples we analyze cases with constant modulation index M, it can be used as a design parameter. A constant M implies that α is independent of $\boldsymbol{\rho}$ [17]. The use of a variable M leads to a control of α along $\boldsymbol{\rho}$, and can be used to taper the field amplitude to get a desired profile [17, 21]. Thus, by using a variable α one could increase the aperture efficiency as done in [20] and [21] with printed sub-wavelength patches.

In the *third step*, we employ the value of $\underline{\underline{\mathbf{X}}}(\boldsymbol{\rho})$ on the antenna aperture, obtained in the second step, to compute the far field. In many cases, especially when the aperture field corresponds to a pencil beam, the analytical form of $\underline{\underline{\mathbf{X}}}(\boldsymbol{\rho})$ in (8.8) already provides a simulation result that matches the objective far field within a very good agreement. If that is not the case, one can define some global variables to optimize

the profile of $\underline{\underline{X}}(\boldsymbol{\rho})$, as illustrated in the first loop in Figure 8.5. Expressions for $\underline{\underline{X}}(\boldsymbol{\rho})$ like the one in (8.11), allows one to optimize the impedance profile rewriting those simple equations as low-order polynomial functions of M and β_{SW} that depend on $\boldsymbol{\rho}$ smoothly.

Regarding the choice of solver, since the evolution of $\underline{\underline{X}}(\boldsymbol{\rho})$ is typically smooth, it is reasonable to expect that the currents on the impedance plane be also smooth. Therefore, these currents can be represented with a number of basis functions drastically lower than the ones needed for the actual patches printed on the substrate. Moreover, in the framework of this homogenized problem, one may also use ad-hoc basis functions [38, 39] to reduce further the computational cost at each iteration. For instance, [38] shows that Gaussian-ring basis with a closed-form spectrum enable the derivation of closed-form expressions for the method of moments (MoM) matrix entries. The analytical computation of the MoM matrix greatly reduces the computational burden. Owing to the use of closed-form entries and the small number of entire-domain basis functions, the formulation in [38] is particularly convenient to optimize $\underline{\underline{X}}(\boldsymbol{\rho})$ at a very low computational cost.

Once we have calculated the expression of the space-dependent tensor $\underline{\underline{X}}(\boldsymbol{\rho})$ on the antenna aperture, we must find a geometrical feature able to implement the entries of $\underline{\underline{X}}(\boldsymbol{\rho})$. Finding appropriate MTS elements is a fundamental step, since it will enable the realization of the actual antenna. This phase corresponds to the *fourth step* in the flow diagram, and is referred to as pixel synthesis in Figure 8.5. As a rule of thumb, the dimensions of MTS elements, or pixels, ranges from $\lambda/5$ to $\lambda/10$. The variation of impedance that is required to accomplish a specific design is achieved by changing their geometrical parameters. The element can either be isotropic (see Figure 8.6a) or anisotropic (see Figure 8.6b). To produce anisotropic impedances, the pixel geometry requires additional features in order to change the electromagnetic properties for propagation along different axis. Such features can be, for instance, the orientation and eccentricity of a printed elliptical shape like the one presented and analyzed by a quasi-analytical method in [40]. Printed elements are very well documented in the literature [14–29]. Therefore, in the following sections, we will focus on the metal-only elements also depicted in the bottom row of Figure 8.6.

After choosing the appropriate geometry for the MTS pixel, we must define a strategy to populate the antenna aperture with these elements. To that end, one can divide the circular area according to a regular lattice with unit-cells of dimension equal to the chosen pixel. Although triangular or hexagonal lattices may bring some benefits, Cartesian ones typically provide good results and have a simpler implementation. Thus, in this chapter, we will limit our analysis to square unit cells. Another important aspect is the local periodicity in MTS planes. As already mentioned above, the variation of $\underline{\underline{X}}(\boldsymbol{\rho})$ is quite smooth, i.e. the geometry of a given pixel and its neighbors will be similar. This feature legitimates the use a local periodicity condition (see Figure 8.7a). Under this assumption, we can use a full-wave periodic
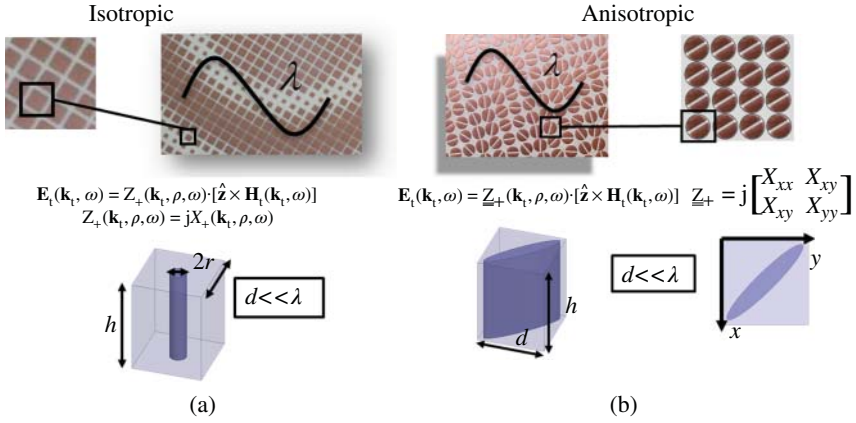
Figure 8.6 *Examples of (a) isotropic printed MTS elements and their three-dimensional metallic pin equivalent and (b) anisotropic printed MTS pixels and their three-dimensional elliptical cylinder equivalent.*

solver to map the pixel geometry to the relevant impedance tensor. Second, we will construct maps (or databases) that link an elliptical geometry to impedance tensor values for a given SW incidence direction (see Figure 8.7b). Then, the ideal tensor $\underline{\mathbf{X}}(\boldsymbol{\rho})$ is sampled on the regular Cartesian lattice, with unit-cell size equal to the pixels used to build our database (see Figure 8.7c). Finally, each impedance sample is implemented using a MTS pixel inside the corresponding cell in the sampled aperture (see Figure 8.7d).

In the *fifth and final step*, we must simulate the actual antenna geometry (obtained as output of the fourth step) using a full-wave solver. This step is time consuming and requires non-negligible computational resources. However, the far-field patterns computed in the third and fifth steps are usually very similar, and this simulation constitutes just a final check. This good agreement will typically hold, provided that in the third step (pixel synthesis) we have chosen elements geometries and unit-cells sizes that respect the homogenization of $\underline{\mathbf{X}}(\boldsymbol{\rho})$ within a sufficiently good approximation. Of course, the development of ad-hoc simulation techniques to overcome the computational burden in this step are of great interest, since they could enable alternative optimization strategies. In this regard, fast iterative techniques (like fast multipole methods) and basis functions especially tailored for the pixel geometry represent a promising approach [14, 15, 22]. When the designer is limited to use commercial software, deviations in the objective far-field pattern may be corrected by accounting for aperiodicity effects in the pixel synthesis or by tuning the global variation of the pixel geometries.

Finally, although not treated in the design flow, one must bear in mind that an efficient coupling of the cylindrical TM-SW to the MTS aperture is crucial to get
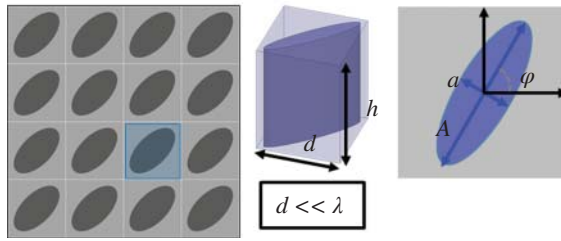
(a)
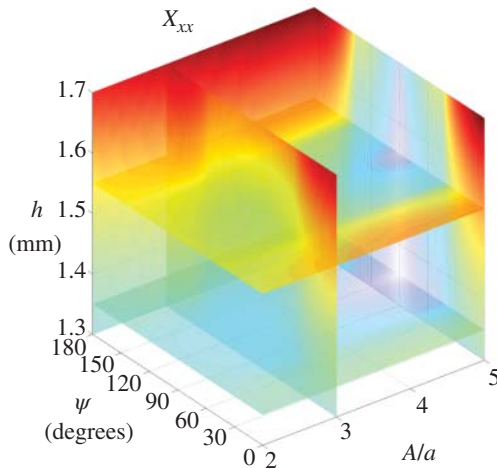
(b)
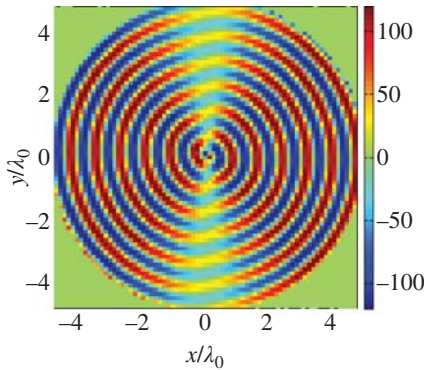
(c)
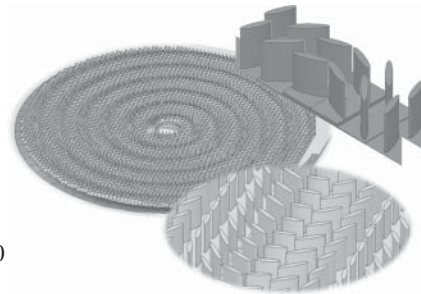
(d)

Figure 8.7   *Pixel synthesis: (a) MTS element and local periodicity assumption; (b) example of impedance map that relates the geometry of the MTS element with the X_{xx} entry of $\underline{\underline{X}}(\rho)$; (c) division of the antenna aperture in a Cartesian lattice and sampling of the values of $\underline{\underline{X}}(\rho)$ in the square unit-cells; (d) final antenna layout.*

the proper response from our antenna. In patch-based MTS antennas, we typically obtain this coupling by a coaxial pin connected to a ring-loaded central patch. In the two following sections, we will describe an alternative way of launching a cylindrical TM-SW using just waveguide circuits.

8.2.3   300 GHz Silicon Micro-Machined MTS Antenna

8.2.3.1   *Objective*

The objective of this work was to design a low-profile MTS based antenna operating at 300 GHz. It was imperative that the antenna is compatible with silicon micromachining based fabrication so that it can be effectively integrated with submillimeter wave front-end receivers also fabricated with the same method. The intent is to develop new generation of low-power, low-mass, and highly compact submillimeter wave instruments that could potentially be used on CubeSats or SmallSat platforms. While the JPL has extensive experience in submillimeter wave instruments, all of them employ traditional antennas such as arrays of horns or lenses, or parabolic reflector to achieve high directivity. Figure 8.8 shows an example of a Silicon micro-machined heterodyne receiver. To overcome the losses associated with conventional dielectric substrate based antennas at submillimeter waves, a fully metallic MTS based antenna is designed and developed.
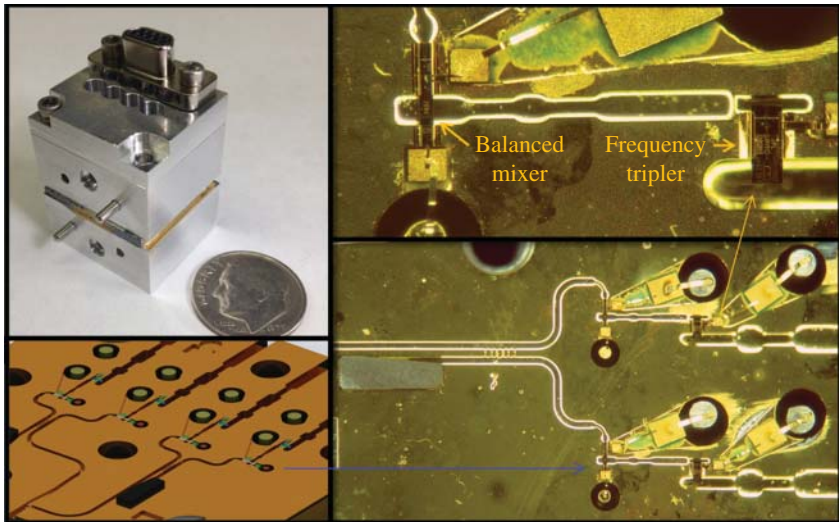
Figure 8.8   *Fully integrated Silicon micromachined receiver* [41].

8.2.3.2   *Design Methodology: Modulation*

This spiral modulated MTS antenna is designed at 300 GHz to provide RHCP medium gain. As explained in Section 8.2.2, the first steps consist in obtaining an aperture field that provides a RHCP broadside pencil beam with an isotropic IBC. Such field is given by:

$$\mathbf{E}_A = E_0 e^{j\varphi} \,\hat{\boldsymbol{\rho}} \sqrt{\frac{2}{\pi \beta_{sw}\rho}} \, e^{-\alpha\rho} U_A \tag{8.12}$$

Upon applying (8.12) in (8.8) one gets

$$X_s = X_0 \left(1 + M \sin\left(\frac{2\pi}{p}\rho - \varphi \right) \right) \tag{8.13}$$

where ρ and φ represent the position on the MTS plane in the polar coordinates. The derivation of (8.13) follows the reasoning in Section IV-A of [17]. A thorough discussion on the circularly-polarized radiation by the reactance distribution in (8.13) can be also found in [42].

8.2.3.3   *MTS Element*

The proposed MTS antenna consists of an array of metallic cylinders on a ground plane and arranged in a periodic lattice, like the one in the bottom side of Figure 8.6a. This unit-cell, often referred to as Fakir's bed of nails, has been used in the past for the synthesis of inductive artificial surfaces [1, 43]. Although we will only consider here the case of cylinders with circular cross-sections [31], elliptical sections can be used to obtain an anisotropic response as in [30, 32]. As we will discuss later, an anisotropic surface reactance is useful to enhance the cross-polar discrimination and, thus, the antenna efficiency.

The MTS modulation can be achieved by changing only the radius or height of the cylinders in a unit cell keeping the other dimensions the same. The later approach is preferred, since changing the height of the cylinder provides a broader range of reactances. To retrieve the inductance value associated with a cylinder's height, a local periodicity is assumed. We retrieve the frequency-β_{SW} pair of interest from the dispersion curves obtained with an eigenmode solver for a periodic problem made of cylinders with a constant height. Then, imposing the transverse resonance between jX and the free space TM impedance $(-j\zeta \sqrt{\beta_{SW}^2 - k^2}/k, \beta_{SW} > k$ for SWs), we obtain $X = \zeta\sqrt{\beta_{SW}^2 - k^2}/k$. Figure 8.9 shows the reactance values for a cylinder with varying height, a radius of 17.5 μm, and a 138.5 μm side square unit cell. The side of the unit cell was selected as $d = p/N$, where $N = 6$ cells per period and p has been obtained using (8.5) for $\overline{X}/\zeta = 0.7$ and a pointing angle $\theta_0 = 1°$.

To make sure the antenna can be reliably manufactured using DRIE, the ratio of height to radius (*h/r*) should always be smaller than 10. This constraint is imposed to the design.
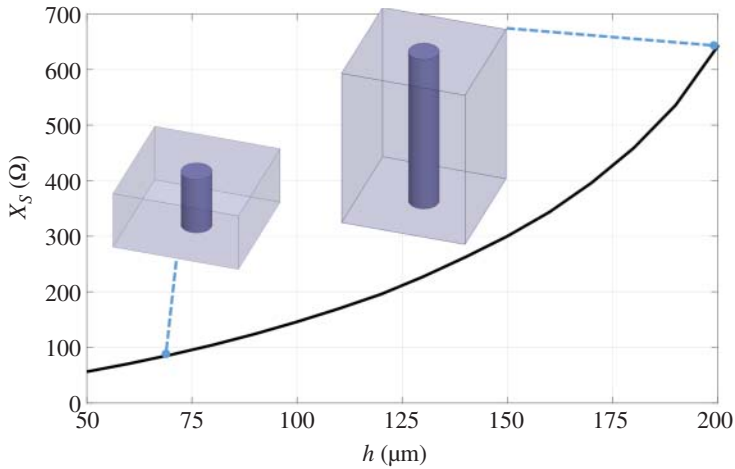
Figure 8.9 *Equivalent surface reactance of an infinite array of cylinders on a ground plane and arranged in a square lattice at 300 GHz as a function of the height h of the cylinders. The radius is fixed to r = 17.5 µm and the side of the unit cell is d = 138.5 µm.*

8.2.3.4   Antenna Design, Fabrication, and Test

The expression of the synthesized surface reactance is given by (8.13). The periodicity of the modulation along each radius is equal to $\lambda_{SW} = 2\pi/\beta_{SW} \approx 2\pi/\beta_0 = \lambda_0$. Therefore, two SW rays 90° out of phase give rise to circular polarization. For this design, we have chosen $X_0 = 0.7\zeta$, $N = 6$, $M = 0.65$, and $d = 138.5$ µm.

The overall antenna aperture is discretized in square unit cells with side a and the heights of the cylinders are obtained using (8.13) and the data in Figure 8.9. The discretization is illustrated in Figure 8.10. Each color
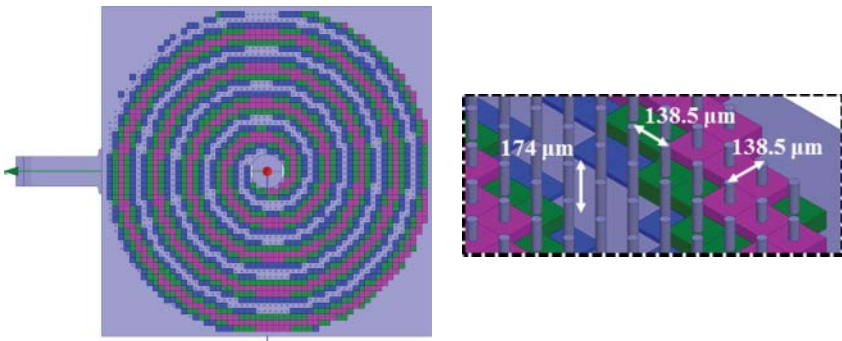
Figure 8.10 *Metasurface discretization on the aperture of the antenna.*
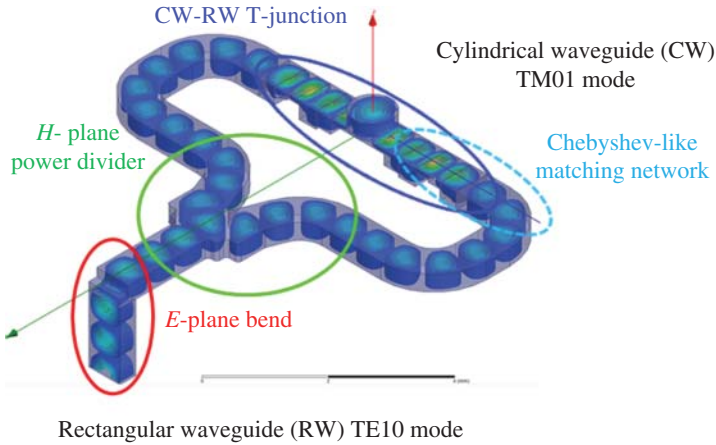
Figure 8.11   *Feed for the metasurface antenna with a rectangular waveguide input.*

represents a different height of the cylinders. In addition, it is important to note that the height of the cylinder is varied by changing the height of the ground plane. This was necessary due to fabrication challenges as it is easier to keep the top surface at the same height.

The antenna is designed assuming a center fed configuration and a rectangular waveguide input from the submillimeter instrument. The antenna is fed with an overmoded circular waveguide with only the TM_{01} mode propagating which offers optimum coupling to the TM-SW on the MTS plane. The feed shown in Figure 8.11 is located under the MTS. It transforms the TE_{10} mode of the input rectangular waveguide to the first higher-order TM_{01} mode in the circular waveguide. To get a good coupling to the SW mode and a low reflection coefficient, the feed must be designed in the presence of the MTS. The reflection coefficient was calculated using two different full-wave commercially available software: CST Microwave Studio and Ansys-HFSS. The agreement between both commercial simulation tools is excellent, and the return loss is above 20 dB at 300 GHz as illustrated in Figure 8.12. Figure 8.13 shows the radiation pattern calculated with Ansys-HFSS in the two principal planes.

The antenna was micro-fabricated at the Microdevices Lab of the JPL using DRIE. Figure 8.14 shows the scanning electron microscope (SEM) images of the fabricated MTS plane, including a table that summarizes the nominal and realized dimensions of the MTS pin elements (see Figure 8.14d). In turn, Figure 8.15 shows SEM pictures of the waveguide circuits used to feed the MTS, and the comparison between nominal and realized dimensions (see Figure 8.15d) of the steps used to match the MTS to a standard WR-2.8 rectangular waveguide. In both cases, the dimensions measured upon visual inspection of the fabricated samples were in
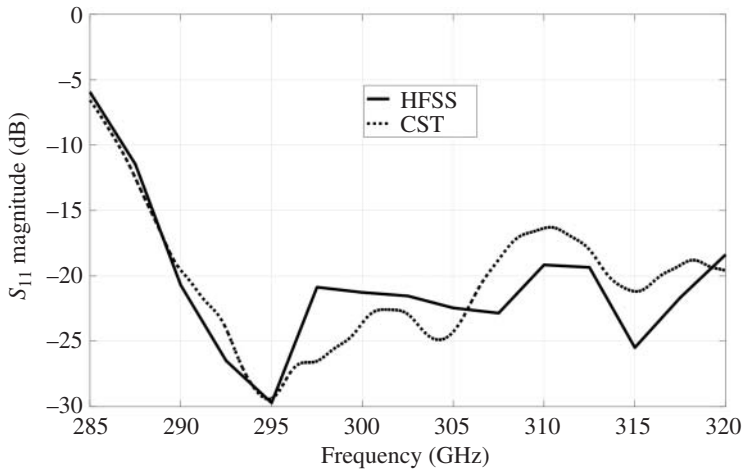
Figure 8.12 *Calculated reflection coefficient of the antenna using two full-wave commercially available software: Ansys-HFSS (solid black line) and CST MWS (dashed grey line).*
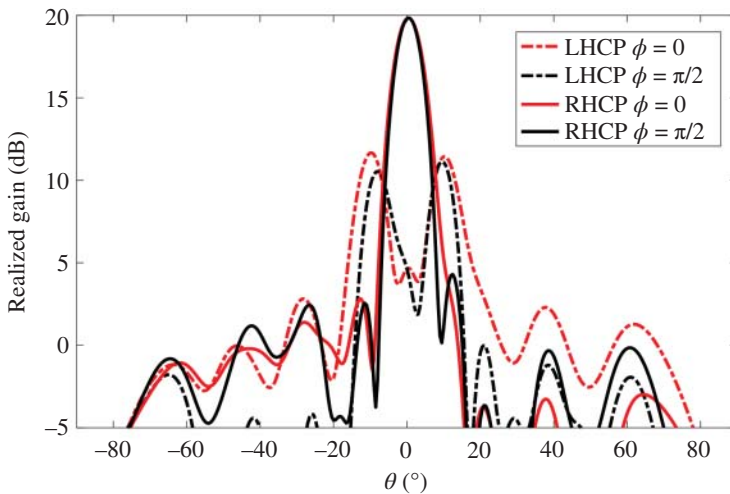
Figure 8.13 *Calculated gain pattern of the antenna in Figure* 8.10 *in the two principal planes, we use solid lines for the co-polar component and dashed ones for the cross-polar ones.*

(a)

(b)

(c)

Design value	Measured
174 μm	177 μm
159 μm	154 μm
110 μm	113 μm
72 μm	74 μm

(d)
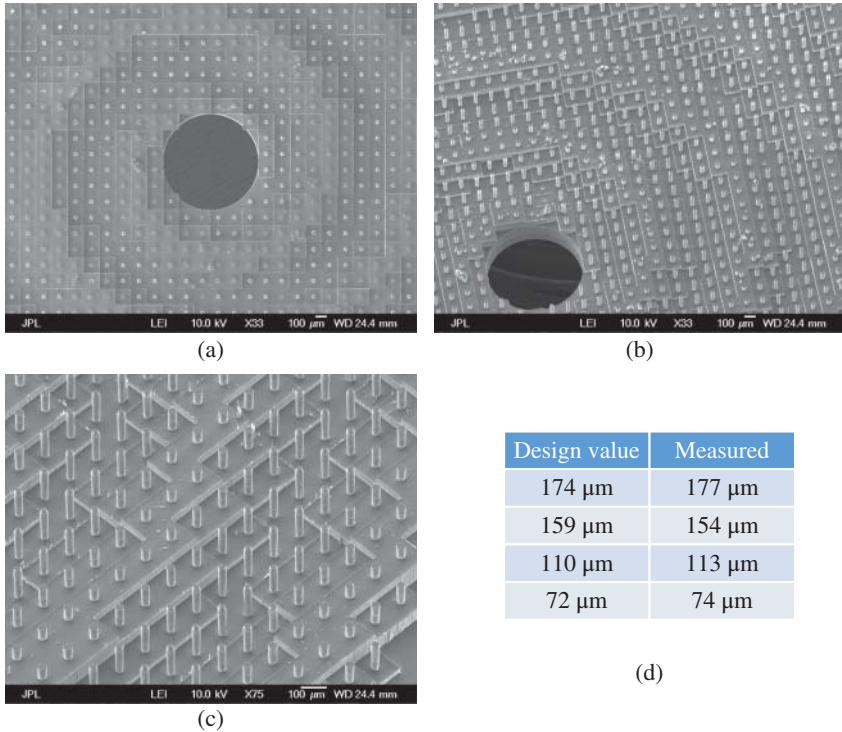
Figure 8.14 *SEM images of the 300 GHz MTS antenna realized with isotropic elements: (a) top; (b) perspective views of the MTS central region, including the circular waveguide; (c) perspective view of pins with variable height; (d) nominal and measured dimensions of the pins' heights.*

excellent agreement with the nominal ones. The antenna radiation pattern was also measured in a far-field measurement set-up at 295 GHz. Measured and calculated results are in good agreement, as one can see in Figure 8.16.

8.2.3.5   Improvement Using Anisotropic Surface

It was shown in [17] that, although the aperture efficiency of the isotropic antenna may be improved using amplitude synthesis, the cross-polarized fields are still quite high. Anisotropic antennas provide superior performance with lower cross-polarization and higher efficiency. To illustrate this point, we designed an antenna with identical radius as the one reported above using an anisotropic element, like the one shown in Figure 8.6b. Figure 8.17 shows the layout of this design, while the radiation pattern of the isotropic and anisotropic designs are shown in Figure 8.18a and b, respectively, for comparison. The improvement of the

Design value	Measured
355 μm	349 μm
192 μm	190 μm
126 μm	125 μm
61 μm	64 μm
50 μm	55 μm

(a)   (b)   (c)   (d)
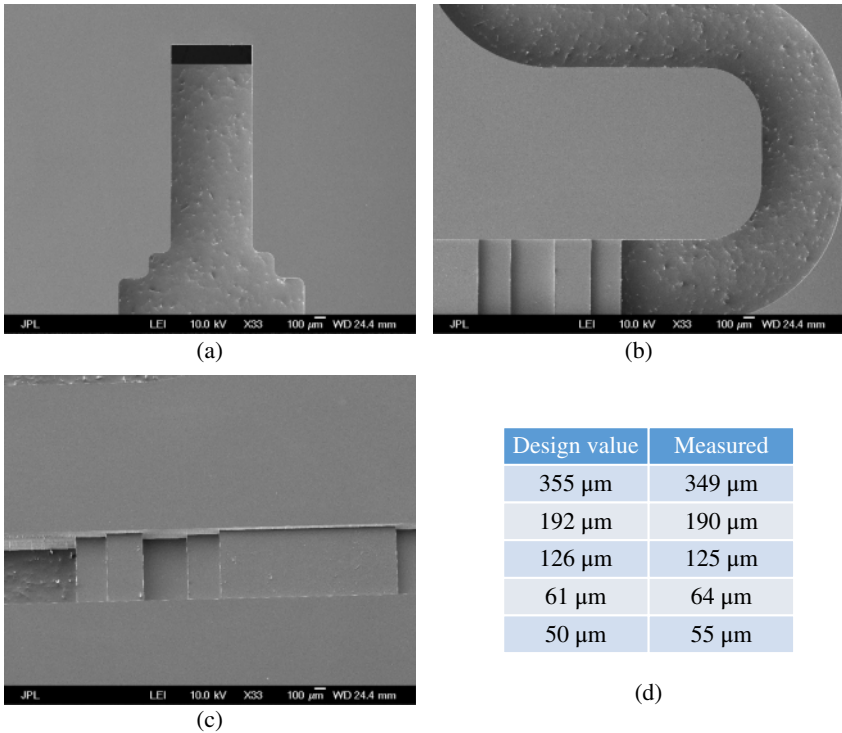
Figure 8.15 *SEM images of the 300 GHz feeder: (a) E-plane bend and H-plane power divider; (b) one of branches outputs of the Y-junction; (c) Chebyshev-like matching network; (d) nominal and measured dimensions of the steps in the matching network.*

cross-polar discrimination in the anisotropic design is evident, being significantly higher than in the isotropic one; the gain is also improved.

8.2.3.6 Conclusion

The proposed 300 GHz MTS antenna is a good alternative to current solutions for submillimeter wave planetary science instruments. The proposed structure avoids the losses in typical dielectric substrates above 100 GHz by using a metal-only MTS. The excitation of a TM-SW on the MTS plane is enabled by an innovative feed providing a cylindrical SW from a rectangular waveguide input. We have also shown that the use of anisotropic surfaces may lead to a more efficient control of the aperture fields improving the cross polarization and increasing the gain of the antenna. The next section will discuss with more detail the use of anisotropic elements in the design of metal-only modulated MTS antennas. Indeed, this design opens up to new possibilities at microwave frequencies and for any design where there is a
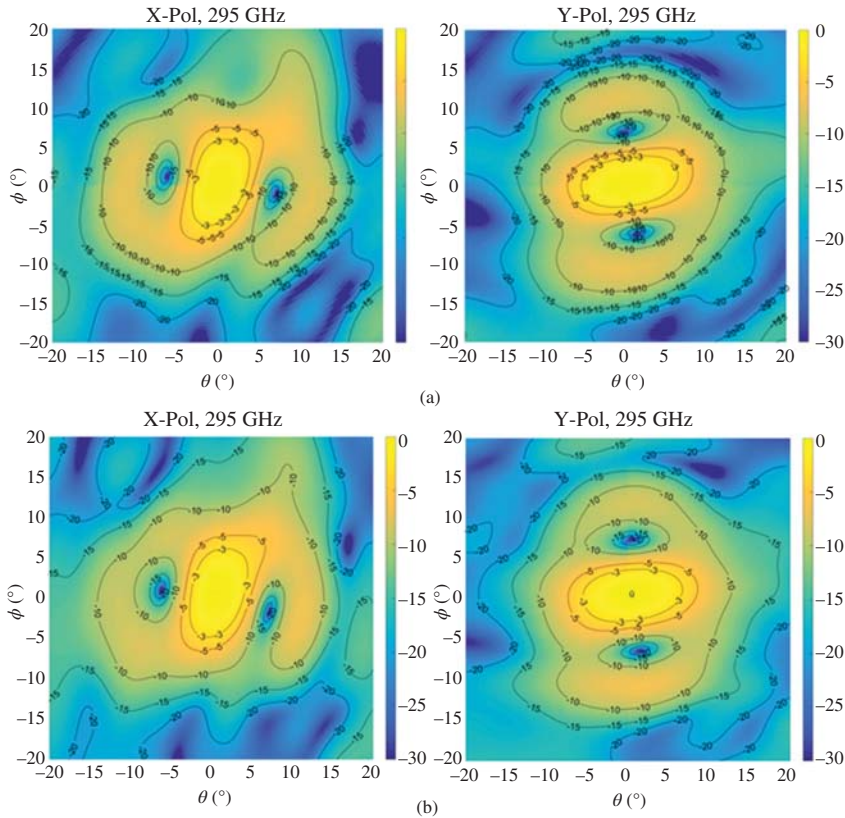
Figure 8.16   *(a) Calculated; (b) measured radiation patterns (linear components) at 295 GHz.*

clear need for all-metal design for deep space exploration [44]. The next sections provides more detail on anisotropic metal-only MTS design.

8.2.4   Ka-band Metal-Only Telecommunication Antenna

8.2.4.1   *Objective*

A novel low-profile antenna is introduced using metal-only sub-wavelength elements, well suited for fabrication using additive manufacturing. The MTS element consists in a metallic cylinder with elliptical cross-section, grown on a ground plane and arranged in a subwavelength square lattice. The proposed antenna is designed to operate at Ka-band at the DSN downlink frequency band (i.e. 31.8–32.3 GHz) with RHCP. A gain of 26 dBi is targeted, although antennas with higher gains are currently under development.
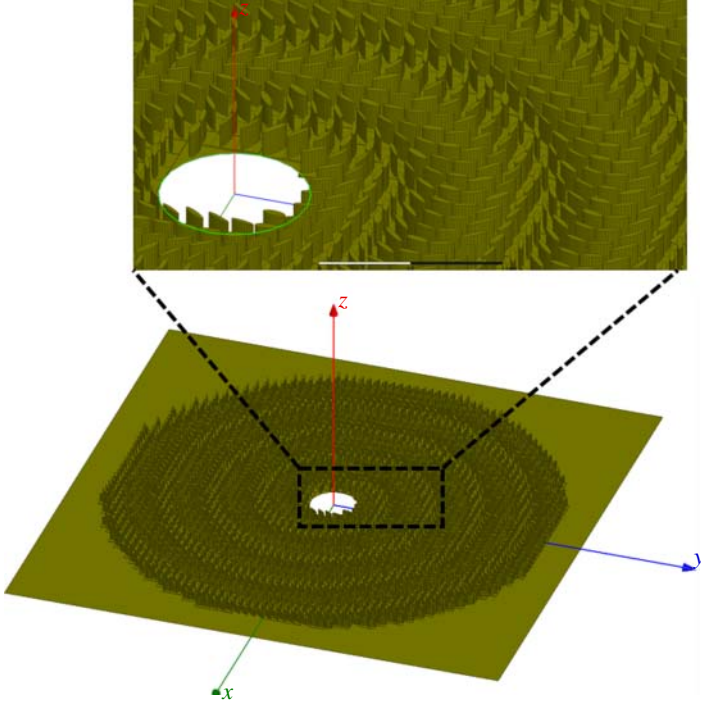
Figure 8.17 *Anisotropic MTS surface for the 300 GHz antenna with broadside RHCP beam.*

8.2.4.2 *Synthesis of the Modulated Metasurface Antenna*

The aperture field $\mathbf{E}_A$ required to obtain a RHCP broadside pencil beam with an anisotropic IBC is given by:

$$\mathbf{E}_A = E_0[\hat{\mathbf{x}} + j\hat{\mathbf{y}}] \sqrt{\frac{2}{\pi\beta_{\mathrm{sw}}\rho}} \, \mathrm{e}^{-\alpha\rho} U_A \tag{8.14}$$

where E_0 is the field magnitude and U_A is a step function that equals one inside the aperture and 0 elsewhere. Using (8.14) in (8.8) and projecting $\underline{\underline{\mathbf{X}}} \cdot \hat{\boldsymbol{\rho}}$ along $\hat{\boldsymbol{\rho}}$ and $\hat{\boldsymbol{\phi}}$, gives the impenetrable reactance tensor, which upon interaction with a cylindrical SW will generate the objective far field:

$$X_{\rho\rho}(\boldsymbol{\rho}) = X_0 \left[1 + M \sin\left(\frac{2\pi\rho}{p} - \phi\right) \right]$$

$$X_{\rho\phi}(\boldsymbol{\rho}) = X_{\phi\rho}(\boldsymbol{\rho}) = X_0 M \cos\left(\frac{2\pi\rho}{p} - \phi\right)$$
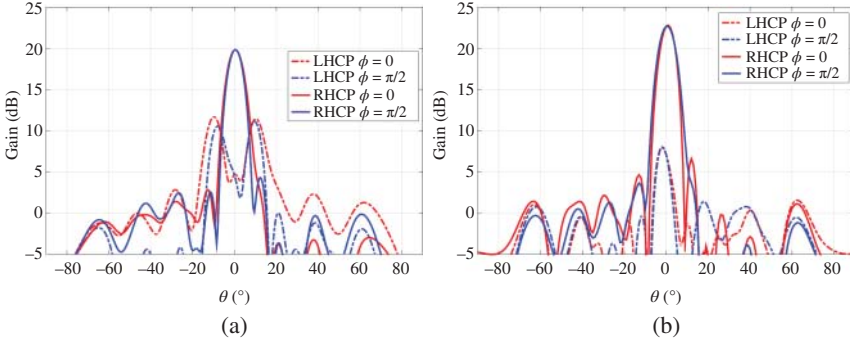
Figure 8.18 Comparison between the radiation patterns of (a) isotropic and (b) anisotropic metasurface antenna.

$$X_{\phi\phi}(\boldsymbol{\rho}) = X_0 \left[1 - M \sin \left(\frac{2\pi\rho}{p} - \phi \right) \right] \tag{8.15}$$

where the relation between X_0 and p is $p = 2\pi/(k\sqrt{1 + (X_0/\zeta)^2})$. The modulation parameter M in (8.15) is a design parameter assumed constant in this particular design.

8.2.4.3   Metallic Metasurface Elements

Once the expression of the space-dependent tensor $\underline{\underline{X}}$ has been computed on the aperture, we have to choose carefully a MTS element capable of implementing the entries of $\underline{\underline{X}}$. The selected MTS element consists in a metallic cylinder with elliptical cross-section placed on a ground plane (see right-hand side of Figure 8.19). The left-hand side of Figure 8.19 shows the iso-frequency dispersion ellipses for the unit cell at hand. These ellipses are obtained by using an eigenmode solver, which provides the propagation frequency of the fundamental mode for each pair of phase shifts ($\psi_x = \beta_{sw}^x d, \psi_y = \beta_{sw}^y d$). For a given design frequency, f_0, the equation of the iso-frequency ellipse can be written as $f_0 = f(\beta_{sw}^x, \beta_{sw}^y)$. Then, the corresponding reactance tensor can be computed by fitting, in the least square sense, the simulated iso-frequency ellipse with (19) in [45]. The reader is referred to Section III in [32] for further details. The elliptical cylinders exhibit different heights and elliptical cross-sections across the antenna aperture. By changing these geometrical features, one can synthesize the different values of the local inductance tensor on the antenna aperture. The parameters that define the geometry of these cylinders are: their height h, orientation angle ψ, and their elliptical cross section with a major axis A and minor axis a. The interface between the end point of the cylinder and free space remains planar, whereas the base the cylinder varies in height to manipulate the reactance profile.

   The entries of $\underline{\underline{X}}$ are retrieved using the eigen mode full-wave solver in CST Microwave Studio. The solution is obtained assuming local periodicity and by
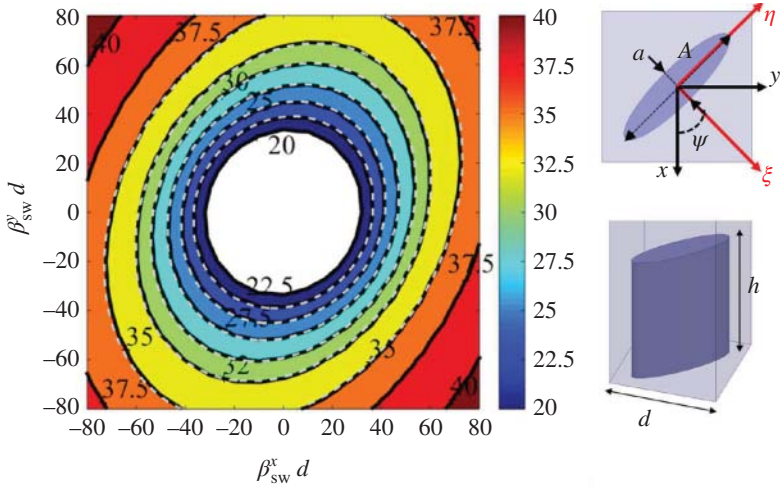
Figure 8.19   *Iso-frequency dispersion contours for the unit cell depicted in the inset where d = 1.235 mm, h = 1.525 mm, a = 240 μm, and A = 1.2 mm.*

imposing periodic boundary conditions. Using the methodology described in [32], one can build a data base which relates the surface reactance tensor with the geometry of the unit cell. Figure 8.20 shows the values of X_{xx}, X_{xy}, and X_{yy} as a function of the orientation angle ψ, the ratio A/a, and the height h of the cylinder.

8.2.4.4   Antenna Design

To implement (8.15), we used $X_0 = 0.8\zeta$, $M = 0.4$, $d = 1.235$ mm, and $p = 6d$. The antenna diameter is 10 cm or approximately $10\lambda_0$ at 32 GHz. When synthesizing the tensor in (8.15), the impedance surface is sampled on a regular Cartesian lattice with the same unit cell size d as the data base. Then, each impedance sample is implemented using a metallic pillar inside the corresponding lattice cell by retrieving its geometry from the data base.

Although (8.15) provides the entries of $\underline{\underline{\mathbf{X}}}$ in cylindrical coordinates, they can easily be transformed to a Cartesian reference system by a rotation matrix. Then, one can establish a direct link with the values in the database as seen in Figure 8.20.

The calculated radiation pattern at 32 GHz is shown in Figure 8.21. The peak gain of all-metal MTS antenna is 26.1 dBi, which implies an aperture efficiency of 40%. It is worthwhile to note that one may obtain larger aperture efficiencies by tapering the modulation index and, hence, the corresponding local attenuation constant α.

The antenna is fed by a circular waveguide excited in the TM_{01} first higher-order mode. The TM_{01} mode provides an efficient excitation on the MTS plane of a circularly symmetric TM-SW mode which matches (8.7) within satisfactory approximation. The structure is identical to the one introduced in Section 8.2.3 but its dimensions at Ka-band are shown in Figure 8.22c.

(a)

(b)

(c)
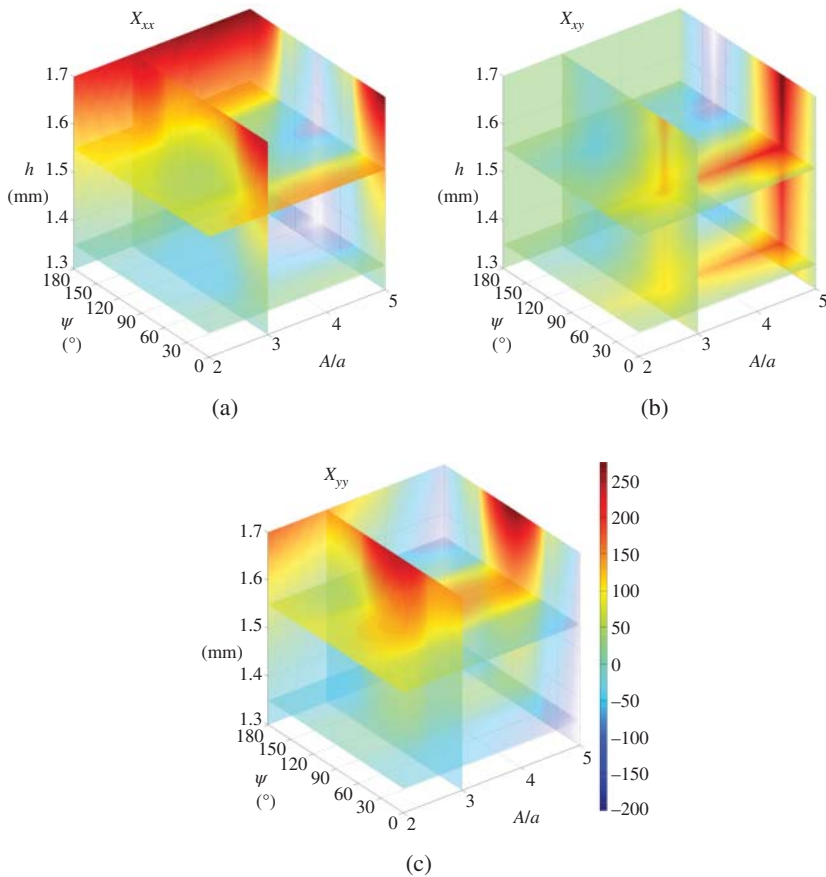
Figure 8.20   *Maps of (a) $X_{xx} - X_0$; (b) $X_{xy} - X_0$; (c) $X_{yy} - X_0$ as a function of the orientation angle ψ, the ratio A/a, and the height h of the cylinder. The simulation frequency is $f_0 = 32$ GHz, the unit cell side is d = 1.235 mm, and $X_0 = 0.8\zeta$.*

8.2.4.5   Fabrication

The antenna is composed of two blocks as shown in Figure 8.23. The antenna is fabricated by combining (1) metal additive manufacturing and (2) computer numerical control (CNC) milling in an aluminum base plate. The MTS elements are manufactured using laser beam melting (LBM) with LaserForm $AlSi_{10}Mg$ material on a ProX DMP320 metal printer. This additive manufacturing technique can guarantee a surface roughness of 10 μm. Once the 3D printing is completed, the waveguide in the back side are fabricated using CNC milling. The first fabricated prototype is
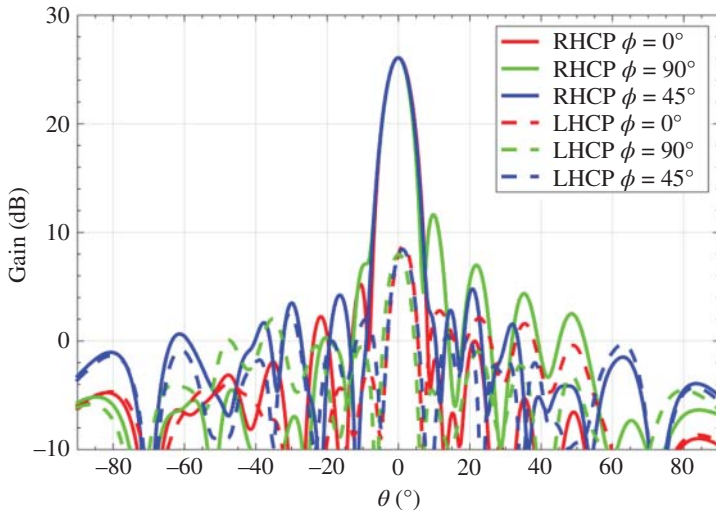
Figure 8.21   *Simulated radiation pattern for the Ka-band RHCP metal-only MTS antenna at 32 GHz in the principal and diagonal planes: solid lines show the co-polar components, while dashed ones represent the cross-polarized ones.*

shown in Figure 8.24. The 3D printed MTS elements can be seen in Figure 8.24a and c. The alignment tolerance is critical at Ka-band and that is why two alignment pins are used.

8.2.4.6   *Measurements*

The antenna performance has been assessed on the first fabricated prototype in terms of reflection coefficient and radiation pattern. The reflection coefficient is calculated using CST Microwave Studio. Good agreement is obtained between calculation and measurement. A small shift in frequency is observed which can be explained by the fabrication tolerance in the additive manufacturing process (Figure 8.25).

The radiation pattern of the antenna prototype has been measured and compared to calculation. Figure 8.26 shows the measured and calculated directivity. We can observe a 3% frequency shift toward lower frequencies in the measured peak directivity (solid gray line) with respect to the simulated one (dashed gray line). To understand better the origin of this frequency shift, we did run again the computer-aided design (CAD) model adding the effect of a 10 µm surface roughness in the 3D printed metallic elements. The solid black line with circular markers shows the new directivity versus frequency response. It is interesting to note that the simulator was

(a)

(b)

Variable	L_1	L_2	L_3	H_1	H_2	H_3
Value (mm)	6.255	5.771	3.910	0.056	3.233	1.053

(c)
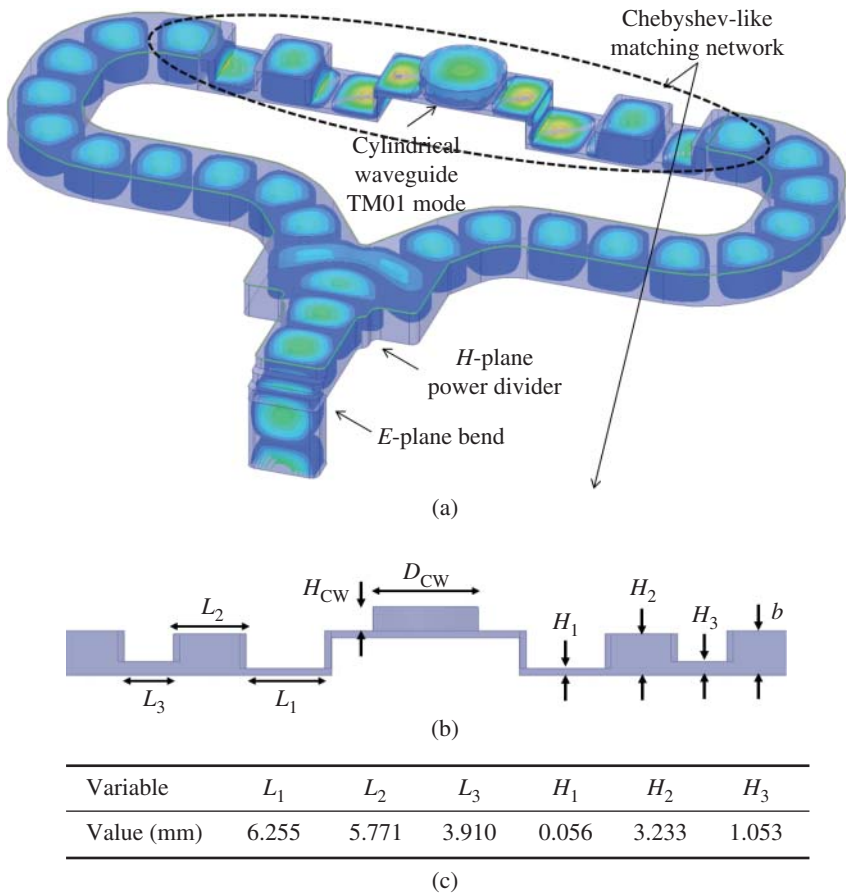
Figure 8.22   *(a) Feeding network for the metal-only MTS antenna at 32 GHz; (b) detail with the geometry of the Chebyshev-like matching network; (c) dimensions of the optimized feeder.*

able to predict the frequency shift after accounting for the surface roughness. The measured and calculated directivity patterns in the $\phi = 0$ plane at 31 and 31.5 GHz are compared in Figure 8.27a and b, respectively. Satisfactory agreement is obtained but the antenna performance could be improved by refining the fabrication process. The gain is 1 dB lower than expected due to additional loss in the MTS aperture caused by the element surface roughness.

Significant effort is on-going at the JPL to improve the fabrication of these antennas as they could address specific mission needs for all-metal and flat antennas capable of surviving harsh environment.
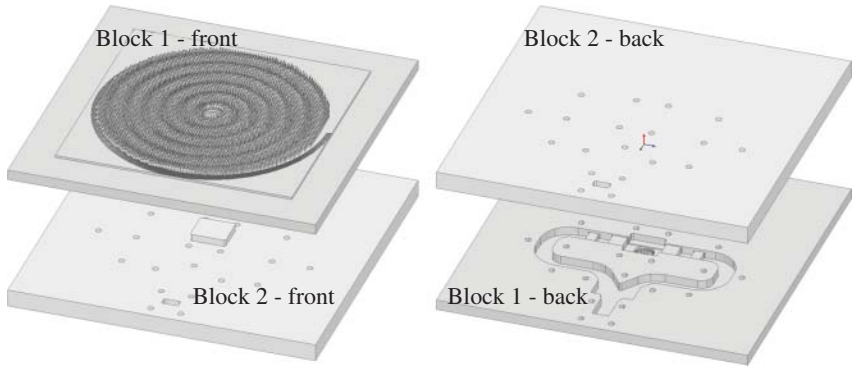
Figure 8.23 *Antenna mechanical description, with the 3D printed elements in the front of block 1. The back of block 1 and block 2 has been fabricated by CNC milling.*
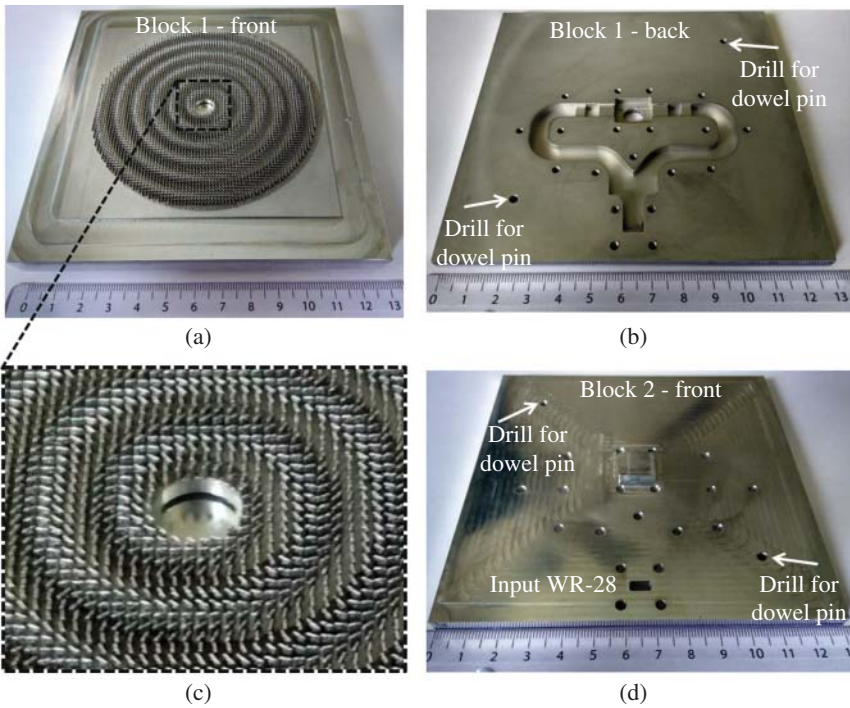
Figure 8.24 *Picture of the fabricated Ka-band all-metal metasurface antenna.*
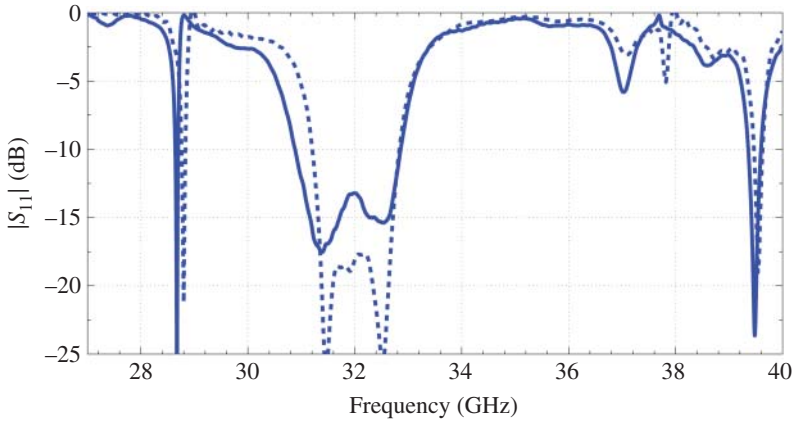
Figure 8.25 *Calculated and measured reflection coefficient of the Ka-band all-metal metasurface antenna. Solid line: measurement. Dash line: calculated.*
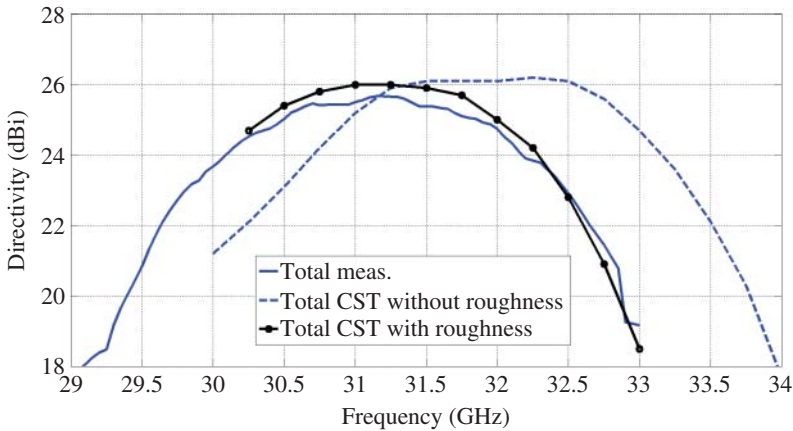
Figure 8.26 *Calculated and measured directivity of the Ka-band metal-only MTS antenna versus frequency. Solid line: measurement. Dashed line: calculated. Solid line with circular markers: calculated including the effect of surface roughness.*

8.2.4.7 *Toward a 20 cm Diameter Antenna*

Following this effort, a 20 cm diameter antenna was designed and fabricated. The design methodology is the same as previously reported. An emphasis was made in improving the fabrication process to remove the frequency shift that was observed (see Figure 8.26). The 20 cm metal-only MTS was fabricated using the same additive manufacturing technique. The MTS elements were purposely fabricated
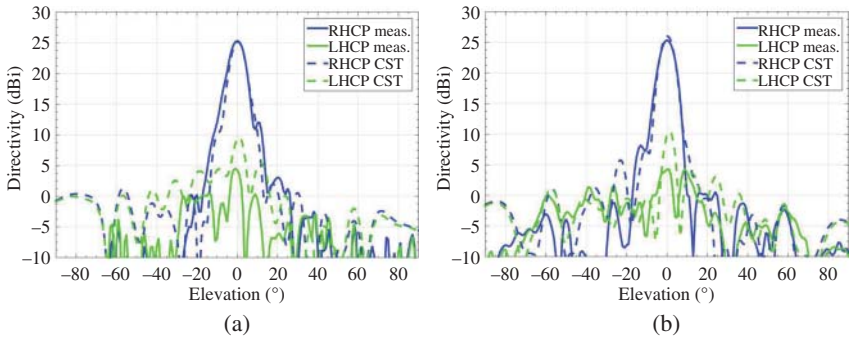
Figure 8.27   *Calculated and measured radiation pattern of the Ka-band metal-only metasurface antenna in the $\phi = 0$ plane at: (a) 31GHz; (b) 31.5GHz.*
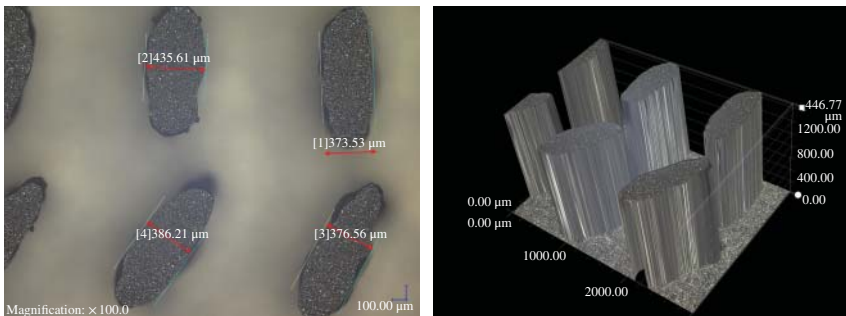
Figure 8.28   *Measurement of the metasurface elements of the 20 cm Ka-band metal-only antenna using a microscope at 100× magnification.*

with a larger height (i.e. 3.27 mm). Electrical discharge machining (EDM) was then employed to cut the MTS elements to the designed height (i.e. 1.43 mm). The MTS elements height was verified using a digital microscope (see Figure 8.28). The fabricated antenna is shown in Figure 8.29. The radiation pattern was measured in a planar near field chamber at the JPL. The radiation pattern at 31.6 GHz is shown in Figure 8.30. The agreement between calculation and measurement is very good confirming the improvement of the fabrication process. The measured gain and efficiency are shown in Figure 8.31. A peak efficiency of 48% was measured. Please note the efficiency is defined as the ratio of the realized gain of the antenna to its standard directivity. The standard directivity is $4\pi A/\lambda_0^2$, where A the area of the antenna aperture and λ_0 is the free space wavelength.

The demonstration of a 20 cm diameter metal-only MTS antenna with a reliable fabrication process is a big step forward toward seeing these antennas used in space. Our team is currently working toward implementing amplitude tapering to increase

Figure 8.29   *Fabricated 20 cm diameter Ka-band metal-only antenna.*
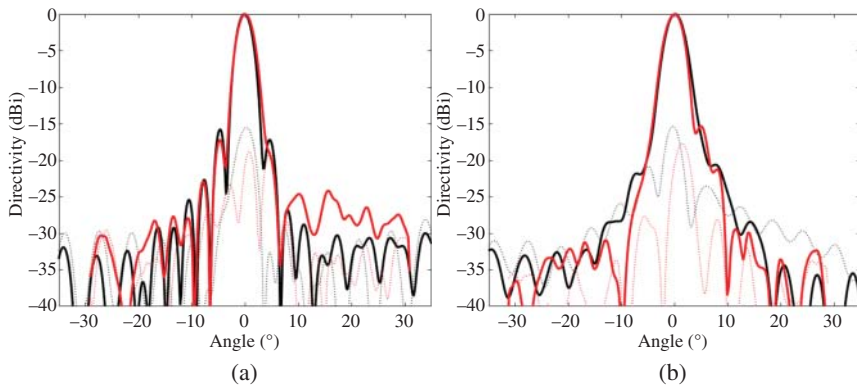
Figure 8.30   *Calculated (in black) and measured (in gray) radiation pattern measurement at 31.6 GHz: (a) $\varphi = 0°$; (b) $\varphi = 90°$.*

the efficiency of this antenna to 70%. Our team is also looking at building larger antenna using deployable panels.

8.3   Beam Synthesis Using Holographic Metasurface Antennas

8.3.1   Introduction

A MTS can be considered as an artificial aperture synthesized using an array of subwavelength-sized meta-elements (or meta-atoms) distributed across a planar
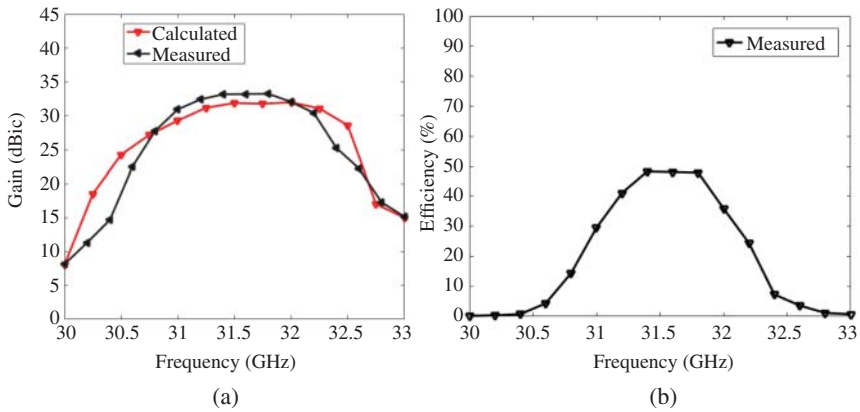
Figure 8.31   *(a) Measured and calculated realized gain; (b) measured efficiency of the 20 cm metal-only metasurface antenna.*

surface [1–3, 46]. Holography is an extremely powerful concept and has been well-reported in the literature, especially within the field of optics [47–51]. Combining the holography concept with MTS antennas has recently gained traction as a means of controlling the antenna radiated wavefronts with applications ranging from beam-synthesis [52–59] to compressive sensing and millimeter-wave imaging [60–63]. To understand the application of holography to beam synthesis and MTS aperture design, let us consider a one-dimensional (1D) microstrip transmission line loaded with an array of subwavelength, slot-shaped meta-elements as depicted in Figure 8.32. The microstrip transmission line shown in Figure 8.32 is essentially a 1D MTS aperture.

For the 1D MTS aperture illustrated in Figure 8.32, two important definitions can be given: (1) reference wave exciting the MTS aperture and acting as the reference-wave of a hologram, and (2) desired aperture field distribution, which is
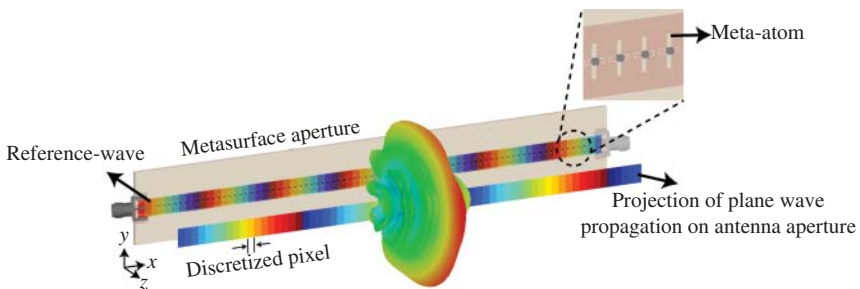
Figure 8.32   *1D holographic metasurface aperture synthesized from a microstrip transmission line loaded with an array of subwavelength, slot-shaped meta-atoms.*

the projection of a plane-wave in the radiation direction onto the aperture of the antenna.

From antenna theory, it is known that a slot shaped radiator can be considered as a complementary version of a metallic radiator, such as an electrical dipole, and hence its radiation can be modeled as a magnetic dipole. Therefore, in Figure 8.32, the holographic guided-mode reference exciting the meta-elements across the MTS is the magnetic field launched by the quasi-transverse electromagnetic mode (TEM) feeding port. Using the coordinate definition of Figure 8.32 and discretizing the aperture at a subwavelength limit, this holographic guided-mode reference can be expressed as follows:

$$\vec{H}_{\text{ref}} = H_0 e^{-\gamma x} \hat{y} \tag{8.16}$$

where γ is the propagation constant given by $\gamma = \alpha + j\beta$, where α denotes the attenuation due to transmission line losses (conductive loss, dielectric loss, and radiation loss), β is the wavenumber within the dielectric, and H_0 is an amplitude term. At this point, we note that the beam fidelity is mostly governed by the phase information [53], and therefore, we consider the phase distribution of (8.16) for the MTS aperture synthesis process.

For the 1D MTS aperture shown in Figure 8.32, beam-steering can be achieved only along the x-direction and the array factor (AF) can be defined as follows:

$$\text{AF}(\theta) = \sum_{i=1}^{N} \alpha_i e^{-j\beta x_i} e^{-jk_0 x_i \sin\theta} \tag{8.17}$$

In (8.17), uniform amplitude is assumed, and amplitude dependency is dropped while only the phase information is considered. θ is the radiation angle with respect to the broadside direction (z-axis), k_0 is the wavenumber in free-space, x_i is the element position with the index i denoting the meta-atom element number across the synthesized aperture, and N is the number of discretized sub-wavelength pixels across the MTS aperture. Considering (8.16) and (8.17), the total phase advance across the MTS antenna steering in θ direction can be expressed as follows:

$$\Psi(i) = \angle e^{-j\beta x_i} e^{-jk_0 x_i \sin\theta} \tag{8.18}$$

In order to steer the beam in a given θ direction, it becomes necessary to maximize the exponential function in (8.17), which can be achieved by defining a MTS with the meta-atom weights defined as follows:

$$\alpha_i = e^{j\beta x_i} e^{jk_0 x_i \sin\theta} \tag{8.19}$$

Interacting (8.19) with (8.17) maximizes the AF of the antenna in the θ direction, suggesting that the beam is steered in the θ direction. The interaction of (8.19) and (8.17) to calculate a phase grating to be applied to the holographic guided-mode reference is essentially a modulation problem. The modulation of the holographic

guided-mode reference into the desired aperture wavefront can be achieved using several modulation schemes, including amplitude modulation and phase modulation [52]. In this work, we leverage the amplitude modulation technique, suggesting that only the points where the phase of (8.19) is below a certain threshold contribute to radiation whereas the meta-elements at other points across the aperture do not contribute to radiation.

It should be mentioned at this point that, whereas, for a regular array antenna, the antenna aperture is synthesized at the Nyquist limit in free space, $\lambda_0/2$, for the MTS antenna shown in Figure 8.32, the aperture is synthesized at a much smaller, subwavelength scale, typically $d < \lambda_g/10$, where λ_g is the guided wavelength. This enables the MTS aperture to sample the guided-mode reference as a continuous hologram. Although, as opposed to a conventional array antenna, a holographic MTS antenna requires a finer sampling of the aperture, it should be emphasized that beam-synthesis using this technique does not require any phase shifting circuits, significantly simplifying the physical hardware architecture and reducing the power consumption requirements.

While the example provided in Figure 8.32 is useful to visualize the design process of a holographic MTS antenna, beam-synthesis is generally needed for a three-dimensional (3D) space, which requires synthesizing a 2D aperture. Similar to the 1D MTS shown in Figure 8.32, the design process of a 2D MTS antenna begins with the choice of a holographic reference-wave to excite the MTS. In Figure 8.33, a 2D MTS antenna excited by a coaxial probe in the center of the aperture is illustrated.
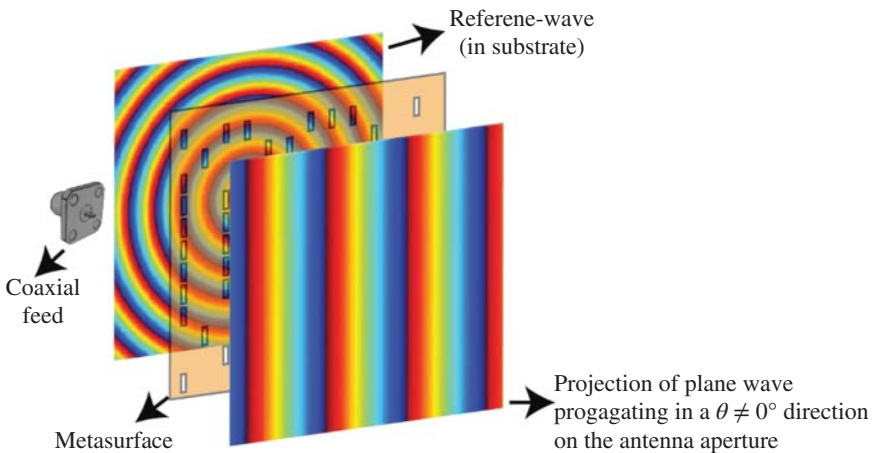
Figure 8.33 *Design of a 2D holographic metasurface antenna. For the presented example, the metasurface antenna is excited using a coaxial feed at its center and beam-steering is performed at $\theta \neq 0°$ (off-axis).*

Discretizing the MTS aperture at a subwavelength limit, the magnetic field launched by the center feed in Figure 8.33 can be modeled using Hankel functions as follows:

$$\mathbf{H}_{\mathrm{ref}} = \begin{cases} H_0^1(k_g\mathbf{r})\cos\varsigma, & x\text{-polarization} \\ H_0^1(k_g\mathbf{r})\sin\varsigma, & y\text{-polarization} \end{cases} \tag{8.20}$$

where bold font is used for vector-matrix notation, H_0^1 is the Hankel function of the zeroth order and first kind, and $\mathbf{r}$ and ς denote the distance vector and angle between the discretized pixels across the MTS aperture and the central feed point. For the MTS aperture depicted in Figure 8.33, the slot-shaped complementary meta-elements are oriented along the y-axis, suggesting that the y-polarization component of the magnetic field is considered as the holographic guided-mode reference exciting the meta-elements. Due to the 2D structure of the MTS in Figure 8.33, it is possible to achieve beam-synthesis in both θ and φ dimensions, with the AF definition of the antenna given as follows:

$$\mathrm{AF}(\theta,\phi) = \sum_{a=1}^{N}\sum_{b=1}^{N}\alpha_{a,b}H_0^1(k_g r_{a,b})\sin\varsigma\, e^{-jk_0 x_a \sin\theta\cos\phi}e^{-jk_0 y_b \sin\theta\sin\phi} \tag{8.21}$$

where a and b denote the element numbers of the meta-atoms in the x- and y-axes, respectively, while the x_a and y_b are the positions of the meta-atoms across the MTS. The total phase advance on the MTS aperture steering in (θ, φ) can then be given as follows:

$$\Psi(a,b) = \angle H_0^1(k_g r_{a,b})\sin\varsigma\, e^{-jk_0 x_a \sin\theta\cos\phi}e^{-jk_0 y_b \sin\theta\sin\phi} \tag{8.22}$$

Similar to the 1D MTS aperture described earlier, to steer the beam in a given (θ, φ) direction, it is necessary to define a set of meta-atom weights that compensate for the total phase advance in (8.22) as follows:

$$\alpha_{a,b} = H_0^1(k_g r_{a,b})^* \sin\varsigma\, e^{jk_0 x_a \sin\theta\cos\phi}e^{jk_0 y_b \sin\theta\sin\phi} \tag{8.23}$$

where symbol * represents the complex conjugate operator. Substituting (8.23) in (8.21) indeed maximizes the AF definition in the direction of (θ, φ), suggesting that beam-steering at (θ, φ) is achieved.

8.3.2   Examples Holographic Metasurface Antennas

Leveraging the holographic beam-forming concept, various MTS antenna designs can be realized. As an example, in Figure 8.34, two different types of holographic MTS antenna designs are shown. A 3D printed MTS antenna radiating a focused electric-field (or E-field) pattern in near-field is illustrated in Figure 8.34a. The MTS

on the left achieves beam-focusing in broadside direction while the MTS on the right-hand side of Figure 8.34a performs off-axis focusing. The measured E-field patterns shown in Figure 8.34b confirm the focusing operation. In Figure 8.34c, a dual-polarized printed-circuit-board (PCB) MTS antenna radiating a multi-beam far-field pattern is illustrated together with the radiation pattern of this antenna, which is shown in Figure 8.34d.

(a)

(b)
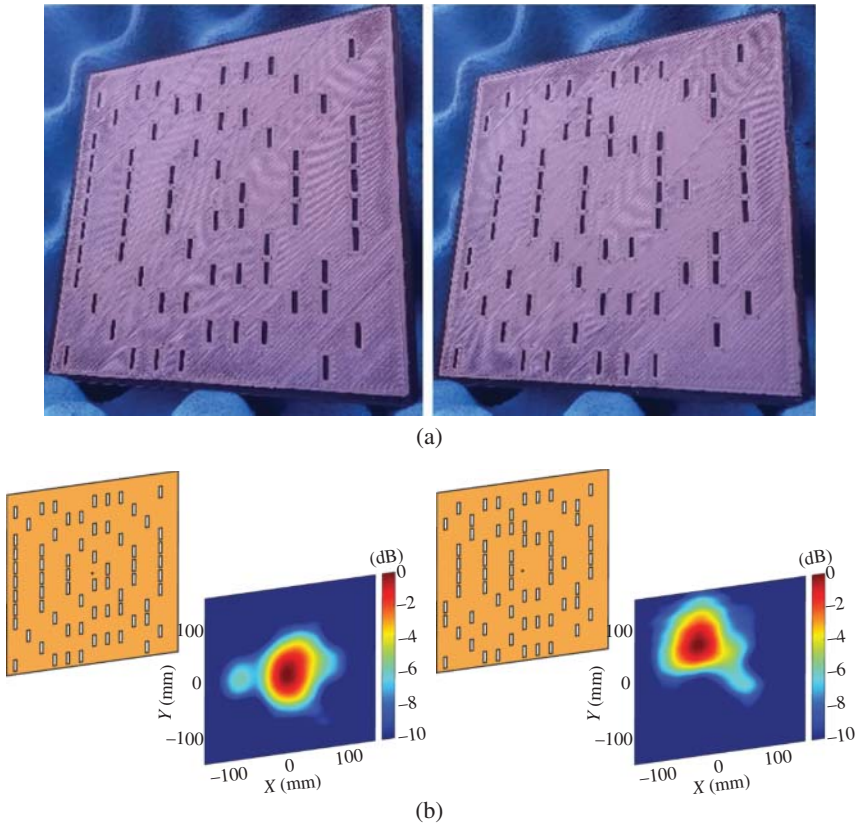
Figure 8.34 *2D holographic metasurface antenna examples: (a) 3D printed near-field focusing holographic metasurface antenna, left: on-axis focusing, right: off-axis focusing; (b) measured E-field patterns at the focal plane, left: on-axis focusing, right: off-axis focusing; (c) polarimetric holographic metasurface antenna to generate a multibeam far-field radiation pattern; (d) simulated and measured radiation pattern of the multibeam metasurface antenna. Source: Modified from Yurduseven and Smith [58]. © 2017 John Wiley & Sons.*

(c)

(d)
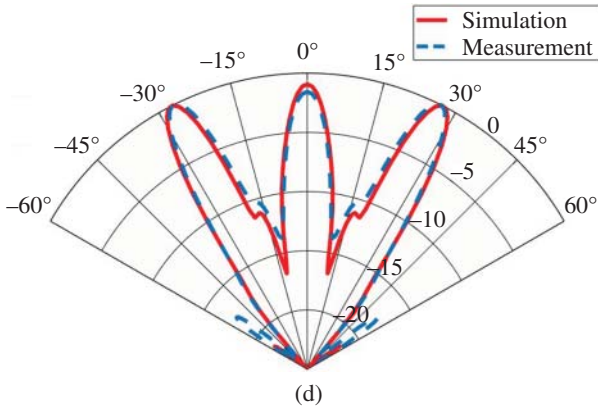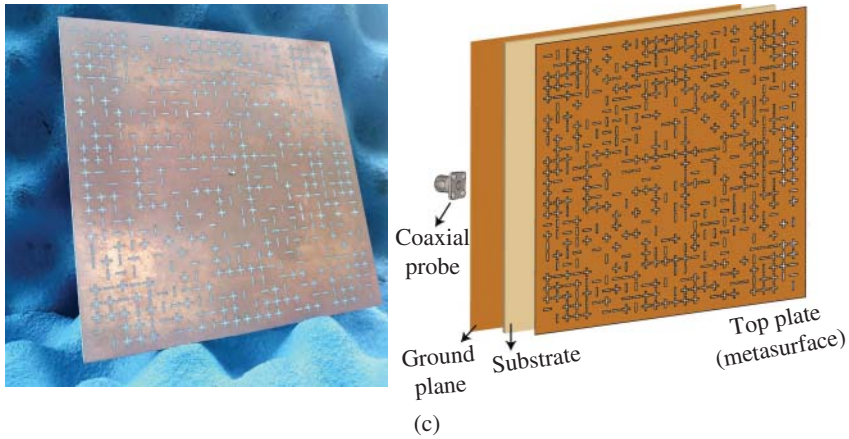
Figure 8.34   *(Continued)*

The examples shown in Figure 8.34 are a testament to the capability of the holographic beam-forming concept to engineer any waveform of interest producing the desired radiation response in the near-field and in the far-field of the aperture.

For the 1D and 2D MTS antennas illustrated in Figures 8.32–8.34, beam-synthesis is achieved in a static manner. This suggests that each time a different steering angle is needed, a new aperture design is required. For most practical applications, however, dynamic reconfigurability is desired. The coupling response of the metamaterial elements across a MTS aperture can be controlled dynamically using various mechanisms, including liquid crystal substrates [64] and semiconductor elements, such as varactors [65] and PIN diodes [53, 60].

In Figure 8.35, a dynamically reconfigurable 1D MTS antenna is demonstrated for electronic beam-steering applications. Leveraging the developed dynamic reconfigurability technique, three beam-steering cases are studied, $\theta = -30°$, $\theta = 0°$,
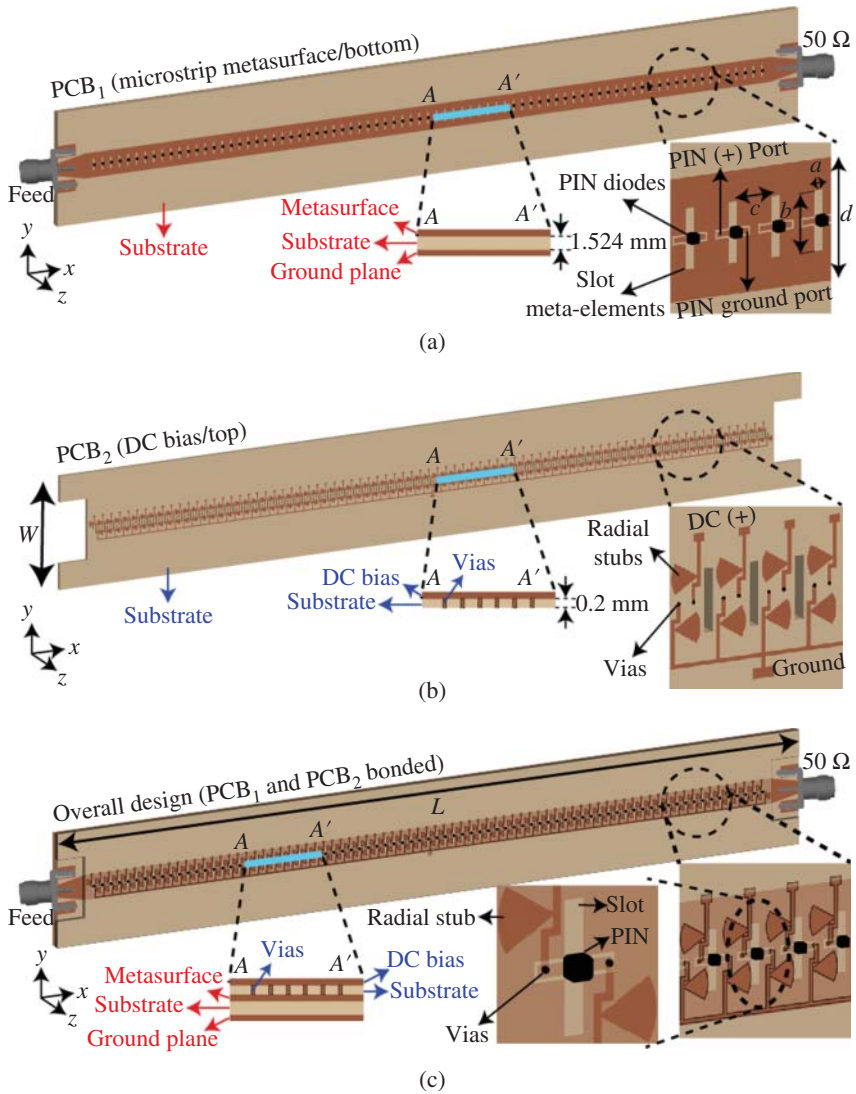
Figure 8.35 *1D dynamically reconfigurable holographic metasurface antenna for electronic beam steering: (a) bottom layer; (b) top layer; (c) combined architecture. Source: From Yurduseven et al. [60]. © 2018 The Optical Society.*
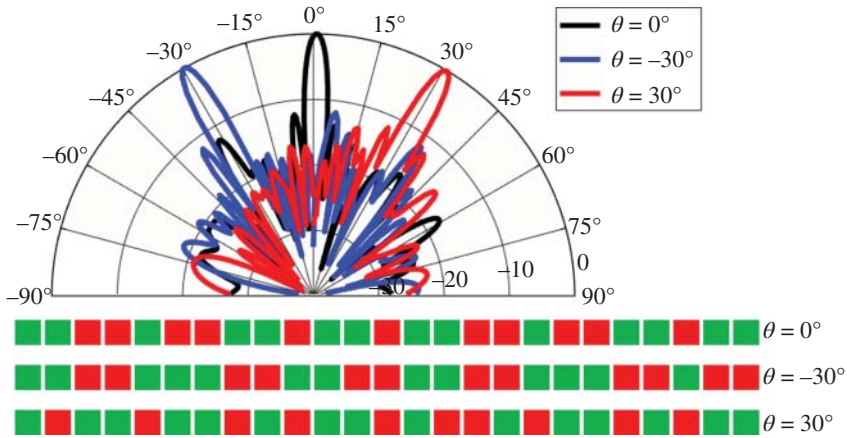
Figure 8.36 *Electronically steered radiation patterns of the reconfigurable metasurface antenna. Corresponding ON (light grey) /OFF (black) mask states are also depicted.*

and $\theta = +30°$. For each configuration, the AF of (8.17) and its interaction with the guided-mode reference of (8.16) are calculated. As depicted in Figure 8.35, the meta-atoms across the MTS aperture have PIN diodes, controlling the coupling characteristics of the meta-atoms to the holographic guided-mode reference. When the PIN diode is forward-biased, it can be considered that the meta-atom is short-circuited, effectively shifting its resonance to a higher frequency band that is out of interest. As a result, the slot-shaped meta-atoms with forward biased PIN diodes do not couple to the holographic guided-mode reference and, therefore, do not radiate. On the other hand, when the PIN diode is reverse-biased, it exhibits high impedance (ideally an open circuit), ensuring that the corresponding meta-atoms are not short-circuited and preserve their intended electrical length, coupling to the guided-mode reference and radiating into free-space. The dynamically reconfigured radiation patterns of the 1D MTS antenna depicted in Figure 8.35 are shown in Figure 8.36. In Figure 8.36, the ON/OFF mask states of the meta-atoms across the MTS aperture are also demonstrated.

8.3.3   W-Band Pillbox Beam Steering Metasurface Antenna

It is worthwhile to note that implementing the architecture shown in Figure 8.31 onto a 2D version would be very challenging and would require too many bias lines. Hence, to achieve a dynamic beam forming in a 3D space, metal strips would be preferable in the configuration shown in Figure 8.37.

For the 2D MTS aperture, a further simplification in the system architecture can be achieved using a more advanced feeding mechanism, known as the
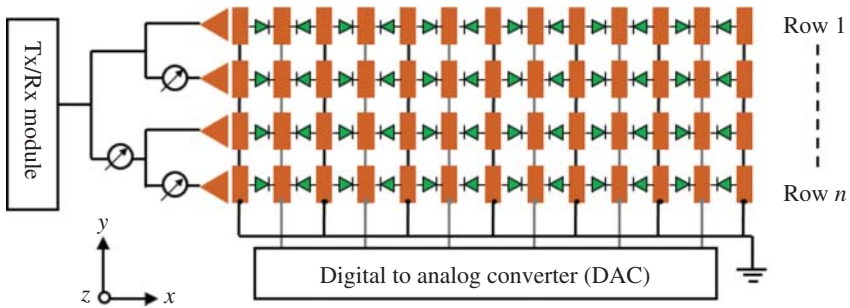
Figure 8.37 *2D dynamically reconfigurable holographic metasurface antenna for electronic beam steering.*

"pillbox" quasi-optical beamformer [66]. The pillbox feeding structure operates in a quasi-optical manner and steers the beam in the elevation direction by switching among multiple feeding ports while it is possible to achieve beam-steering in the azimuth direction by tuning the ON/OFF states of the meta-atoms. Such an architecture has the advantage of using a single biasing line for all the meta-atoms in the same column. This pillbox design would replace the phase shifter in the implementation shown in Figure 8.37.

A W-band beam steering antenna is currently under development at the JPL. The feeding structure of the MTS antenna is a quasi-optical pillbox design as shown in Figure 8.38. The pillbox feeding structure in this MTS antenna design enables the radiating elements of the antenna to be excited by a planar phase-front [66]. This feature makes the analytical modeling of the holographic guided-mode reference extremely simple. The pillbox design employs three feed horns to achieve a beam-steering.

As shown in Figure 8.38, the pillbox feeding network consists of two layers; a silicon (Si) layer ($\varepsilon_r = 11.9$) with a thickness of 350 µm and a gallium arsenide (GaAs) layer ($\varepsilon_r = 12.8$) with a thickness of 175 µm. Both the Si and GaAs layers are highly resistive, and hence exhibit low loss tangent. The pillbox design has a reflector rim that is etched all the way in between the top conductive plane (above GaAs) and the bottom ground plane (below Si). In between the Si and GaAs semiconductor layers, a middle conductive plane lies, into which a coupling slot is etched. As shown in Figure 8.38, the pillbox structure is fed using multiple grounded co-planar waveguide (CPW) ports, each exciting a substrate-integrated-waveguide (SIW) horn antenna embedded within the Si layer. The aperture width of the SIW horn antennas is optimized to have an E-field tapering of -12 dB at the reflector edges.

The proposed MTS antenna consists of a 2D MTS layer as shown in Figure 8.39. Because the phase-front of the guided-mode reference-wave within the GaAs layer is planar and the meta-atom element distribution in each row is identical, the derived polarizability distribution in (8.19) holds and it can be extended for all the rows of the 2D MTS layer.
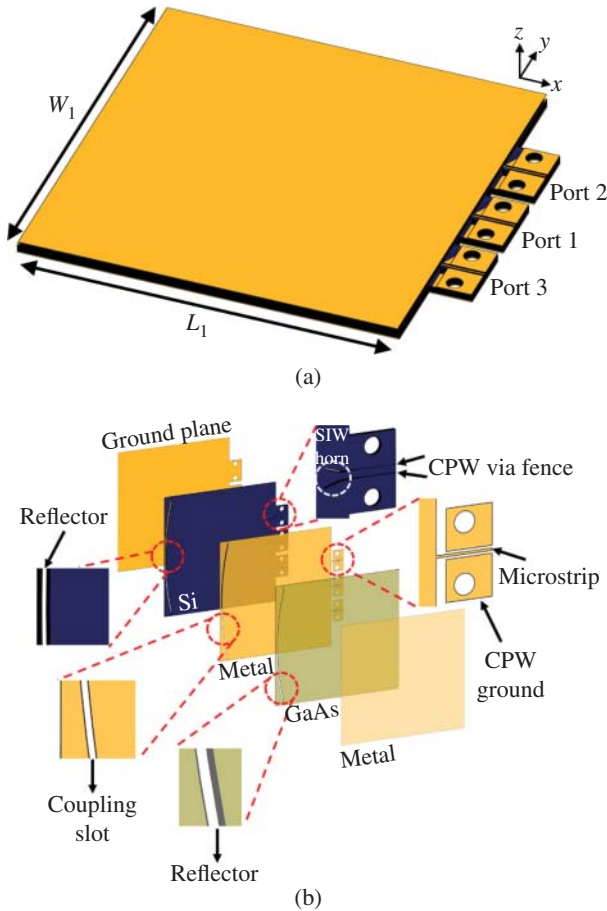
Figure 8.38 *Pillbox feeding structure of the Si/GaAs metasurface antenna: (a) actual Pillbox structure; (b) layers of the pillbox separated for visualization. Dimensions:* $W_1 = L_1 = 50$ *mm.*

In order to optimize the aperture efficiency and ensure that the guided-mode reference is attenuated by the time it reaches the end of the propagation direction across the MTS layer, the length of the slot-shaped meta-atoms is tapered along the x-axis, increasing from 0.38 to 0.4 mm, corresponding to an electrical length $\lambda_g/2.45 - \lambda_g/2.3$. In turn, the width of the meta-atoms is 0.085 mm, corresponding to an electrical size $\lambda_g/11$, where λ_g is the guided-mode wavelength.

The first building block of the pillbox feeding architecture of the MTS antenna is the design of the CPW-SIW conversion structure to feed the antenna. The proposed CPW-SIW conversion technique is shown in Figure 8.40. The CPW input is fed

(a)

(b)
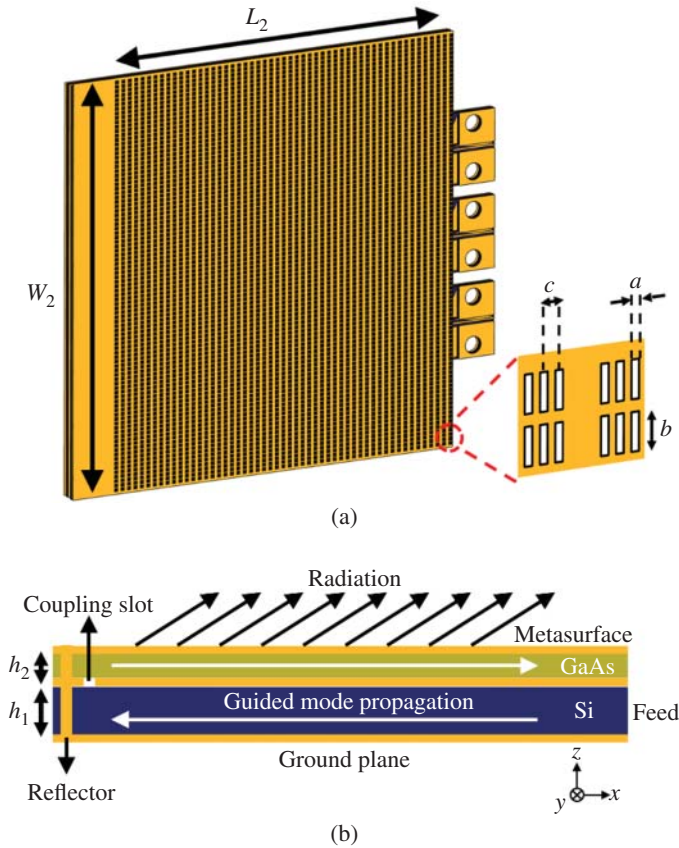
Figure 8.39 *Developed Si/GaAs quasi-optical holographic metasurface antenna: (a) depiction of the metasurface antenna structure; (b) propagation of the guided-mode reference wave inside the pillbox structure (x-z plane shown). $L_2 = 44.5$ mm, $W_2 = 49$ mm, a = 0.085 mm, b = tapered from 0.38 to 0.4 mm, c = 0.17 mm, $h_1 = 350$ μm, $h_2 = 175$ μm.*

through a 1.00 mm end-launch connector, launching a quasi-TEM mode into the Si substrate, which then excites the SIW horn antennas embedded within the Si substrate. Upon excitation, the re-radiated wavefront from the SIW horn antennas has a cylindrical wavefront as shown in Figure 8.41.

The aperture width of the SIW horn antenna is optimized to be 2 mm, resulting in an E-field tapering of −12 dB at the reflector edges. The reflection coefficient of the CPW-SIW transformation is shown in Figure 8.42. The S_{11} remains below −40 dB at 94 GHz.
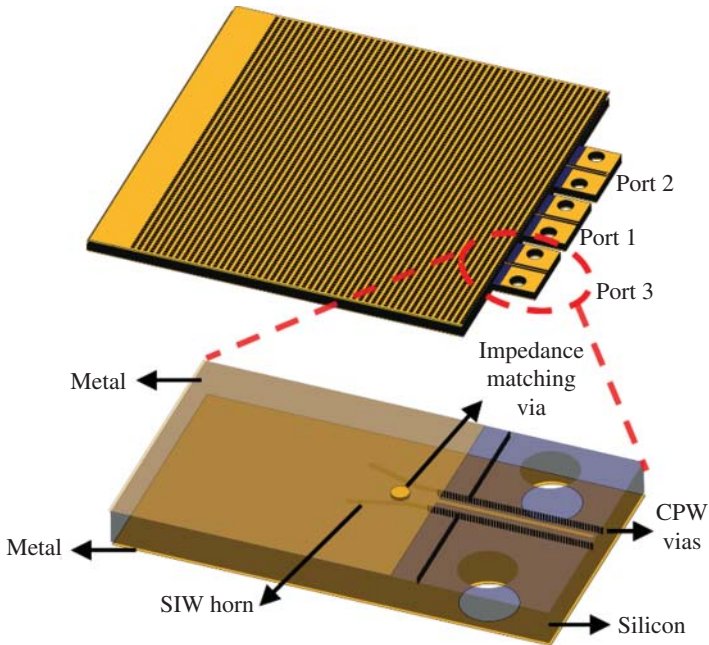
Figure 8.40 *CPW-SIW conversion at the feeding port (all ports are identical and only port 3 is shown). For visibility, top metal and Si layers are shown transparent. The impedance matching via is 50 μm wide and 85 μm long. Feeding ports are embedded within the Si layer, therefore, only the Si layer with top and bottom metals are shown in the close-up view.*

Following the optimization of the CPW-SIW feeding ports, the entire pillbox feeding structure with the MTS is analyzed. Figure 8.43 demonstrates the conversion from the cylindrical wavefront launched by the SIW horn within the Si substrate to the planar wavefront within the GaAs substrate, which excites the meta-atoms within the MTS aperture.

In Figure 8.43, the pillbox structure is excited through the first port (central feed). The cylindrical wavefront launched by the SIW horn antenna in the Si layer is reflected by the reflector rim and, upon reflection, couples to the top GaAs layer, where the phase-front of the guided-wave is planar. It is this planar phase-front excitation of the meta-atoms across the MTS layer that enables the weights of the meta-atoms in each column to be identical, which can be calculated using the (8.16), ensuring that each column can be biased using a using a single biasing line. This advantage significantly simplifies the required biasing circuit to achieve dynamic reconfiguration. The W-band MTS antenna shown in Figure 8.40 consists of 16,536 slot-shaped meta-atoms etched across the MTS layer. While biasing each individual meta-element would require the same number of biasing lines, which is not feasible,

(a)

(b)
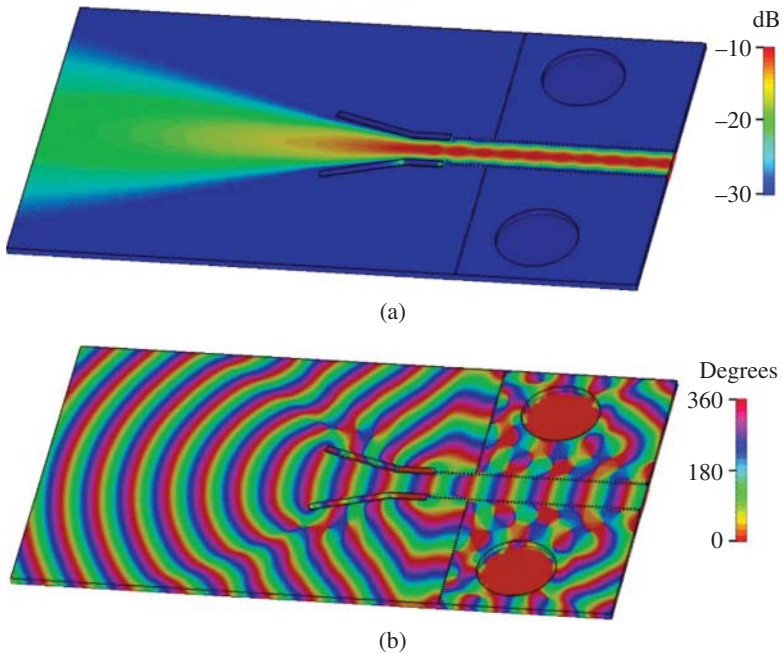
Figure 8.41 *SIW horn launched wavefront within the Si substrate: (a) amplitude pattern; (b) phase pattern. Phase pattern clearly shows a cylindrical phase front launched by the SIW feed horn. Magnetic field as the guided-mode reference is shown.*

the quasi-optical pillbox feeding structure reduces the number of required biasing lines down to 159.

A fabricated prototype of the W-band Si/GaAs beam-steering holographic MTS antenna is shown in Figure 8.44.

The calculated S-parameters of the MTS antenna are shown in Figure 8.45. The reflection coefficient of the MTS antenna at port 1 is around −15 dB while at port 2 and port 3, it is below −20 dB. The antenna impedance is well matched at all the three input ports. The cross-coupling levels between the input ports remain below −20 dB for S_{21} and S_{31} (and hence S_{12} and S_{13} due to reciprocity) as shown in Figure 8.45b. Although remaining below −10 dB at 94 GHz, the coupling between the second and third ports (S_{23} and S_{32}) is relatively higher than the other cross-coupling combinations, due to the specular reflection at the rim of the reflector. However, it should be mentioned that, for the developed MTS antenna, the input ports are not to be activated simultaneously, ensuring that the isolation between the input ports is not a challenge.

The radiation pattern is shown for each of the three ports in Figure 8.46. When fed through port 1, the MTS antenna forms a beam at ($\theta = 15°$, $\varphi = 0°$) with an antenna
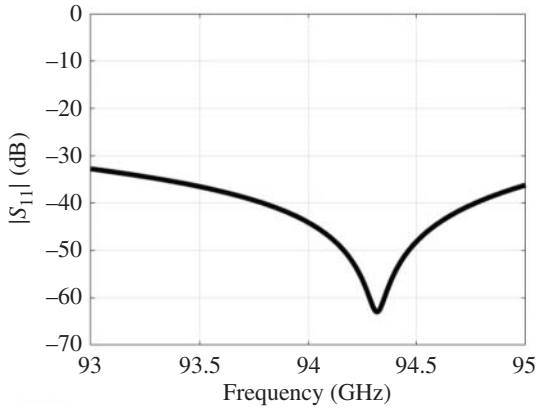
Figure 8.42   *Reflection coefficient of the CPW-SIW feeding port.*

(a)   (b)
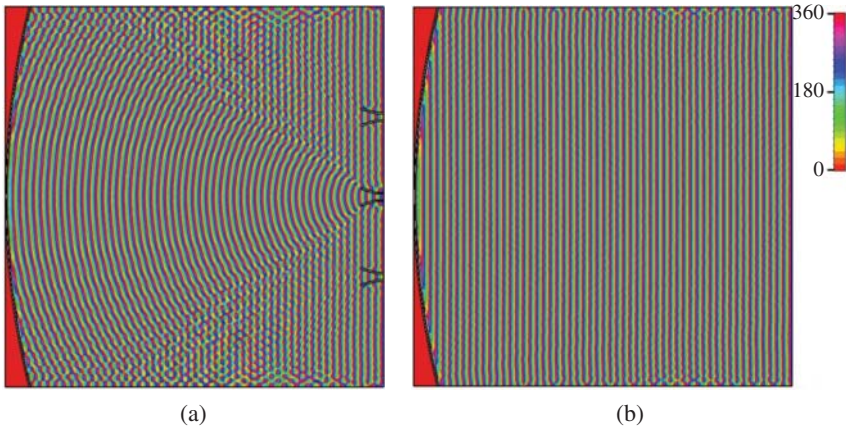
Figure 8.43   *Conversion from (a) the SIW horn launched cylindrical wavefront within the Si substrate to (b) the planar wavefront within the GaAs substrate. Phase of the magnetic field as exciting mechanism for the slot-shaped meta-elements is shown.*

directive gain of 31.9 dBi, resulting in an aperture efficiency of 59%. Switching to port 2 and port 3 enables the MTS antenna to steer the beam in the elevation direction to ($\theta = 45°$, $\varphi = 90°$) and ($\theta = 45°$, $\varphi = -90°$), respectively, with the directive gain of the antenna being equal to 28.7 dBi. The beam steering is clearly demonstrated as can be seen in Figure 8.46. It should be mentioned that for the design of the MTS, the choice of the beam angles is arbitrary and any other pointing direction can be chosen.

The prototype shown in Figure 8.44c was measured in a planar near field chamber. As a misalignment was noticed after fabrication, the calculated results were updated to account for this misalignment. The fabrication process will be improved to insure an alignment of 2 μm in *x*- and *y*-directions. The agreement between calculated and measured results is good (Figure 8.47). This design demonstrates passive beam steering capabilities by switching from one port to another.

Please note, this design can easily be scaled to frequencies up to 600 GHz. A similar concept was published in [67] for an antenna operating from 220 to 300 GHz with a single feed (i.e. no passive steering).

(a)

(b)
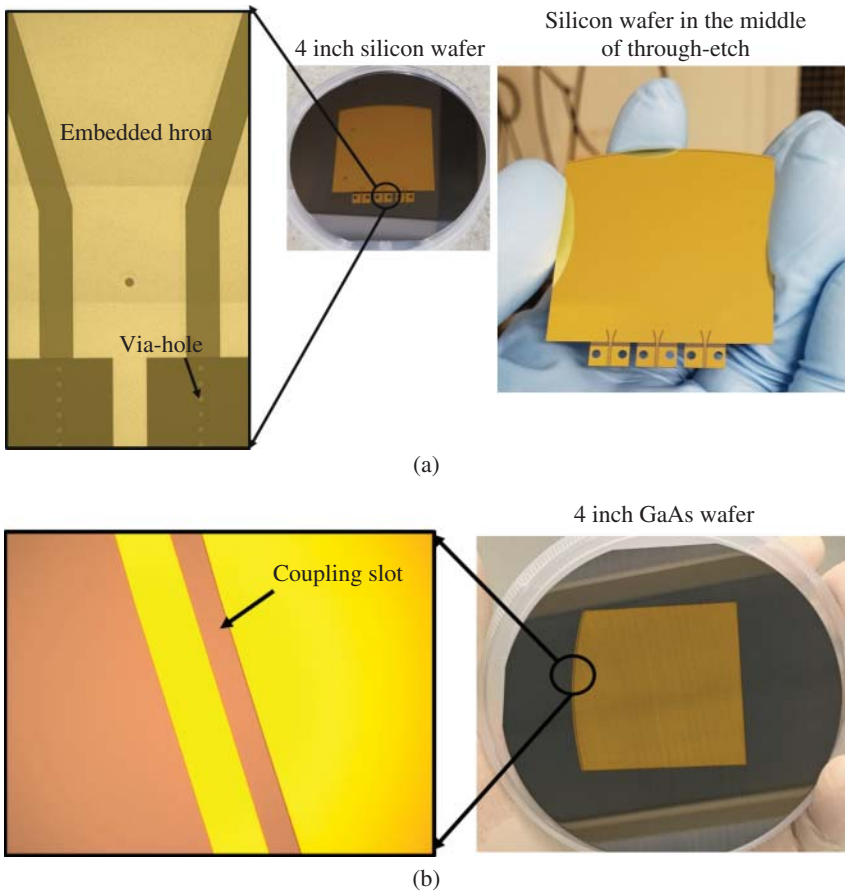
Figure 8.44 *Photography of: (a) the Si layer; (b) the GaAs layer of the fabricated Si/GaAs metasurface antenna before bonding; (c) metasurface antenna fully integrated.*
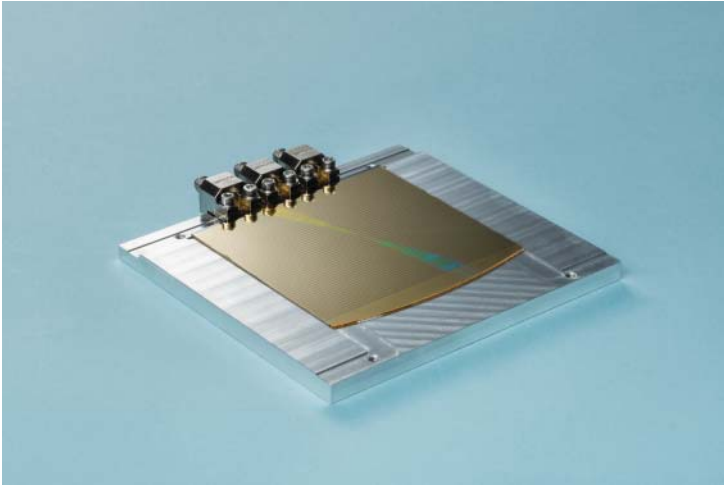
(c)

Figure 8.44   *(Continued)*

8.3.4   Toward an Active Beam Steering Antenna

The design introduced in Section 8.3.3 can hardly be implemented with diodes. Therefore, we have also designed an antenna that is fully compatible with the implementation of diodes. The antenna consists of three main parts sketched in Figure 8.48.

1. The pillbox quasi-optical beamformer constitutes the first element in the design; it includes three *H*-plane horns (one per beam) in the focal plane of a reflector in a parallel plate waveguide (PPW). The horns and reflector have been implemented by SIW technology, micromachining the via in a 350 μm thick high resistivity silicon (Si) wafer ($\varepsilon_r = 11.7$, $\tan\delta = 0.00016$). The beam launched by the horn is collimated by the reflector and transmitted to the upper PPW GaAs layer ($\varepsilon_r = 12.9$) by the coupling slots etched in the top metallization (M2) of the Si wafer. In the previous design we used a single slot. Using multiple matching slots improves the isolation between the three ports and improve the matching of all ports. The S-parameters are shown in Figure 8.49.
2. The transition that transforms the TEM mode in the GaAS PPW to a TM-SW that excites the MTS antenna, matching slots are used as shown in Figure 8.48.
3. The MTS antenna, which gradually radiates the power coupled to the TM SW by sinusoidally modulating an equivalent IBC. In this case, the impedance modulation is achieved by changing the width of metallic strips spaced 290 μm. In
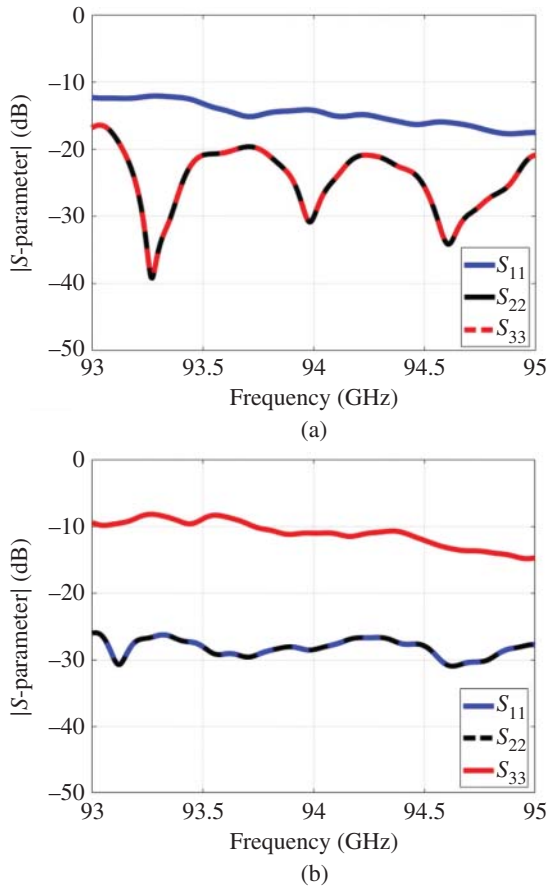
Figure 8.45 *Simulated S-parameter results for the W-band metasurface antenna: (a) reflection coefficient at the input ports; (b) cross-coupling patterns between the input ports.*

this particular case, we have also introduced amplitude tapering to increase the antenna aperture efficiency. The directivity and gain are summarized in Table 8.2.

The beam pointing in φ and θ direction is given for different horn position ranging from 0 to 10 mm in Figure 8.50.

Using metallic strips makes this antenna easily compatible with an active design where biasing Schottky diodes is required. Our team is currently working on the active steering antenna. The impedance modulation will be achieved by changing
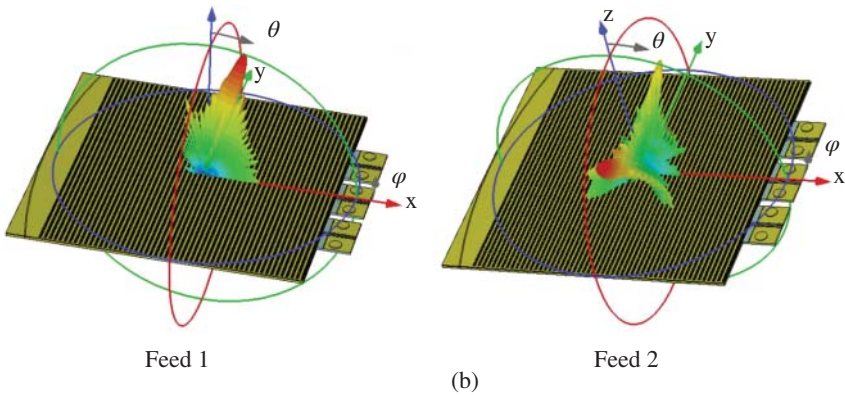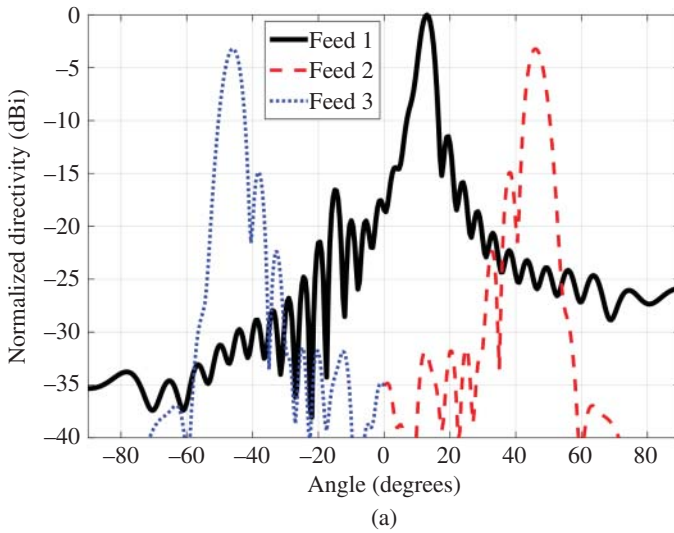
Figure 8.46   *Radiation patterns for each feed showing the desired beam steering: (a) antenna radiation pattern (solid line: E-plane for port 1, dashed line: H-plane for feed 2, dotted line: H-plane for feed 3); (b) 3D plot for feed 1 and feed 2.*

the states of diodes rather than changing the width of metallic strips. The width and spacing will remain identical.

8.4   Conclusion

MTS antennas are extremely attractive for space applications. They present clear advantages over reflectarray antennas or parabolic reflector antennas for platforms with limited stowage volume such as CubeSats, Smallsats, Rovers, or Landers.
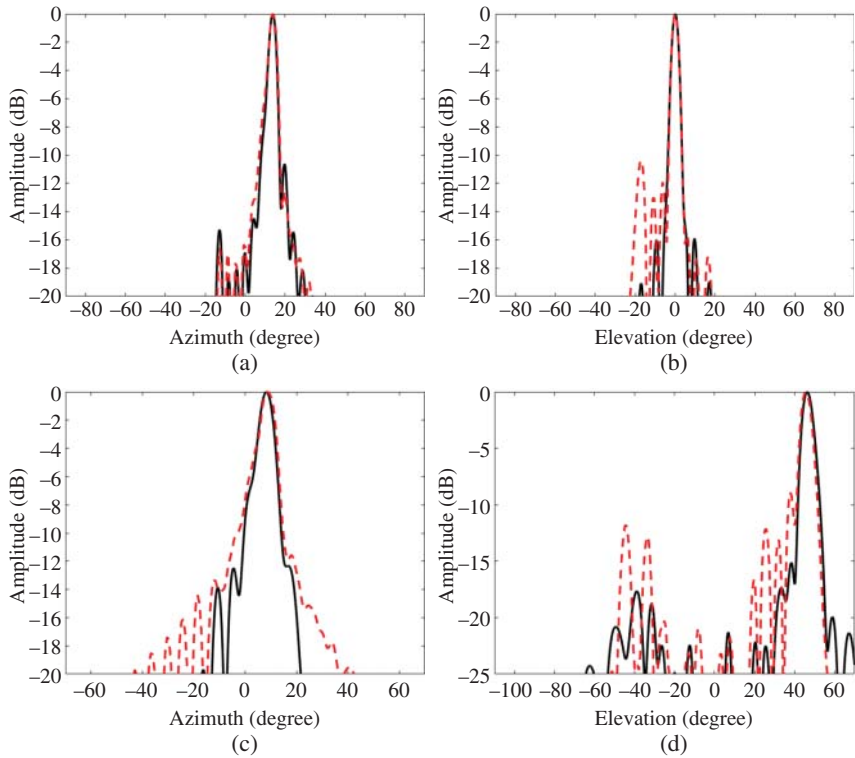
Figure 8.47 *Calculated and measured radiation patterns for feed 1: (a) E-plane; (b) H-plane; and for feed 2: (c) E-plane; (d) H-plane.*

Table 8.2 *Performance of improved passive metasurface antenna using metal strips as metasurface elements.*

	Port 1	Ports 2 and 3
Directivity (dBi)	33.6	33.0
Gain (dBi)	31.0	30.3

They are low-profile with their feed being located at the center of the antenna as opposed to at the focal point for a reflectarray antenna or a parabolic reflector. This is a significant advantage when it comes to deployable antennas as the complexity of the deployment is drastically reduced by removing the feed deployment.

In addition, we proposed solutions in this chapter for metal-only antennas fabricated using additive manufacturing. These antennas are of interest for space
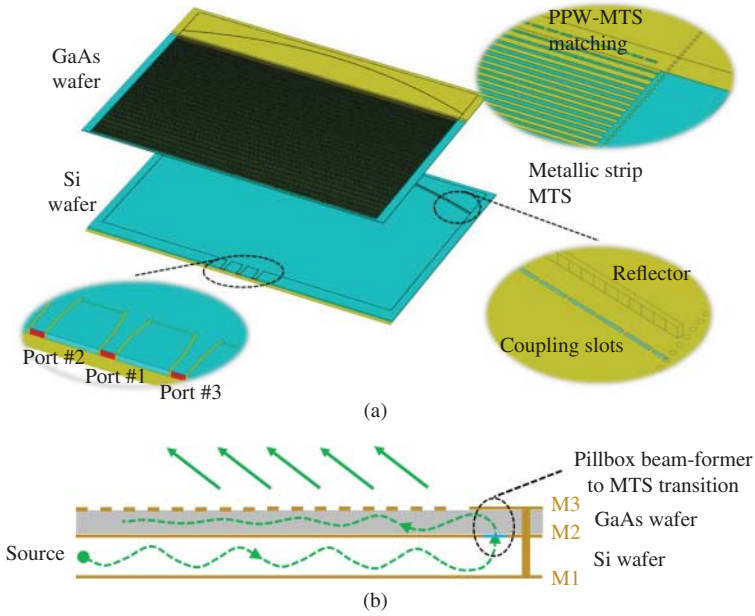
Figure 8.48   *(a) 3D view of the antenna with a description of the pillbox, PPW-to-MTS transition and modulated MTS; (b) section view of the antenna (not to scale).*
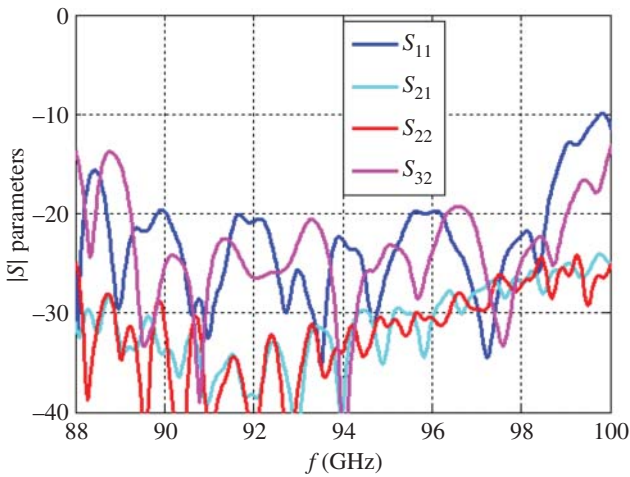
Figure 8.49   *S-parameters of the improved passive metasurface using metal strips as metasurface elements.*
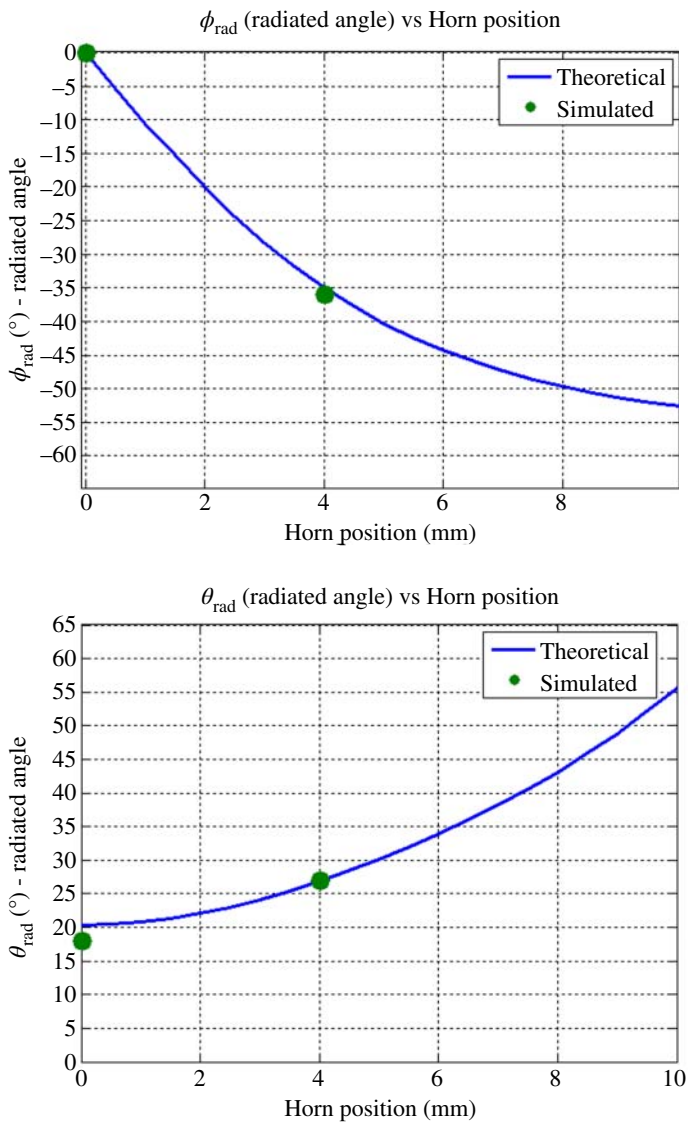
Figure 8.50   *Beam pointing for different horn position.*

exploration in harsh environment with high radiation levels and extreme temperatures. Moreover, these antennas could be fabricated at lower cost by using micro-fabrication techniques or additive manufacturing.

A 300 GHz MTS was fabricated using Silicon micro-machining. This antenna is designed as a fully metallic structure to overcome the losses of conventional dielectric substrates and can be fabricated at high frequencies (i.e. W-band to submillimeter-wave frequencies).

A circularly-polarized Ka-band MTS was fabricated using additive manufacturing and successfully tested at 32 GHz for deep space communication. We are currently developing larger version of this antennas (20 cm-diameter) with the objective of increasing their TRL (i.e. TRL = 6) for future missions.

We also introduced in this chapter a W-band beam steering antenna, currently under development at the JPL. The pillbox feeding structure operates in a quasi-optical manner and steers the beam in the elevation direction by switching among multiple feeding ports. It is possible to achieve beam-steering in the azimuth direction by tuning the ON/OFF states of the meta-atoms. Such an architecture has the advantage of using a single biasing line for all the meta-atoms in the same column. This concept can be extended to submillimeter-wave frequencies due to fabrication methodology.

While the TRL of these MTS antennas is still low (i.e. TRL 4), the JPL is actively maturing this technology to fly the first prototypes in the next few years.

Acknowledgments

References

1. S. Maci, G. Minatti, M. Casaletti, and M. Bosiljevac, "Metasurfing: addressing waves on impenetrable metasurfaces," *IEEE Antennas and Wireless Propagation Letters*, vol. **10**, pp. 1499–1502, 2011.
2. C. Holloway, E. F. Kuester, J. Gordon, J. O'Hara, J. Booth, and D. Smith, "An overview of the theory and applications of metasurfaces: the two-dimensional equivalents of

metamaterials," *IEEE Antennas and Propagation Magazine*, vol. **54**, no. 2, pp. 10–35, Apr. 2012.

3. S. B. Glybovski, S. A. Tretyakov, P. A. Belov, Y. S. Kivshar, and C. R. Simovski, "Metasurfaces: from microwaves to visible," *Physics Reports*, vol. **634**, p. 1, 2016.

4. C. Pfeiffer and A. Grbic, "Metamaterial Huygens surfaces: tailoring wave fronts with reflectionless sheets," *Physical Review Letters*, vol. **110**, no. 19, p. 197401, May 2013.

5. N. Yu, P. Genevet, F. Aieta, M. A. Kats, R. Blanchard, G. Aoust, J.-P. Tetienne, Z. Gaburro, and F. Capasso, "Flat optics: controlling wavefronts with optical antenna metasurfaces," *IEEE Journal of Selected Topics in Quantum Electronics*, vol. **19**, no. 3, p. 4700423, May 2013.

6. R. Quarfoth and D. Sievenpiper, "Artificial tensor impedance surface waveguides," *IEEE Transactions on Antennas and Propagation*, vol. **61**, no. 7, pp. 3597–3606, July 2013.

7. A. Patel and A. Grbic, "Transformation electromagnetics devices based on printed-circuit tensor impedance surfaces," *IEEE Transactions on Microwave Theory and Techniques*, vol. **62**, no. 5, pp. 1102–1111, May 2014.

8. M. Mencagli, E. Martini, D. González-Ovejero, and S. Maci, "Metasurfing by transformation electromagnetics," *IEEE Antennas and Wireless Propagation Letters*, vol. **13**, pp. 1767–1770, Oct. 2014.

9. M. Mencagli Jr., E. Martini, D. González-Ovejero, and S. Maci, "Metasurface transformation optics," *Journal of Optics*, vol. **16**, no. 12, p. 125106, 2014.

10. E. Martini, M. Mencagli, D. González-Ovejero, and S. Maci, "Flat optics for surface waves," *IEEE Transactions on Antennas and Propagation*, vol. **64**, no. 1, pp. 155–166, Jan. 2016.

11. C. Pfeiffer and A. Grbic, "A printed, broadband luneburg lens antenna," *IEEE Transactions on Antennas and Propagation*, vol. **58**, no. 9, pp. 3055–3059, Sep. 2010.

12. M. Bosiljevac, M. Casaletti, F. Caminita, Z. Sipus, and S. Maci, "Non-uniform metasurface luneburg lens antenna design," *IEEE Transactions on Antennas and Propagation*, vol. **60**, no. 9, pp. 4065–4073, Sep. 2012.

13. A. Epstein, J. P. S. Wong, and G. V. Eleftheriades, "Cavity-excited Huygens metasurface antennas for near-unity aperture illumination efficiency from arbitrarily large apertures," *Nature Communications*, vol. **7**, p. 10360, 2016.

14. G. Minatti, M. Faenzi, M. Mencagli, F. Caminita, D. González-Ovejero, C. Della Giovampaola, A. Benini, E. Martini, M. Sabbadini, and S. Maci, "Metasurface antennas," in *Aperture Antennas for Millimeter and Sub-Millimeter Wave Applications*, A. Boriskin and R. Sauleau, Eds., Cham: Springer, 2017.

15. G. Minatti, D. González-Ovejero, E. Martini, and S. Maci, "Modulated metasurface antennas," in *Surface Electromagnetics: With Applications in Antenna, Microwave, and Optical Engineering*, F. Yang and Y. Rahmat-Samii, Eds., Cambridge: Cambridge University Press, June 2019. ISBN: 9781108556477.

16. B. Fong, J. Colburn, J. Ottusch, J. Visher, and D. Sievenpiper, "Scalar and tensor holographic artificial impedance surfaces," *IEEE Transactions on Antennas and Propagation*, vol. **58**, no. 10, pp. 3212–3221, Oct. 2010.

17. G. Minatti, M. Faenzi, E. Martini, F. Caminita, P. De Vita, D. Gonzalez-Ovejero, M. Sabbadini, and S. Maci, "Modulated metasurface antennas for space: synthesis, analysis and realizations," *IEEE Transactions on Antennas and Propagation*, vol. **63**, no. 4, pp. 1288–1300, Apr. 2015.

18. D. Sievenpiper, J. Colburn, B. Fong, J. Ottusch, and J. Visher, "Holographic artificial impedance surfaces for conformal antennas," *Proceedings of IEEE Antennas and Propagation Society International Symposium*, vol. **1B**, pp. 256–259, 2005.

19. M. Faenzi, F. Caminita, E. Martini, P. De Vita, G. Minatti, M. Sabbadini, and S. Maci, "Realization and measurement of broadside beam modulated metasurface antennas," *IEEE Antennas Wireless Propagation Letters*, vol. **15**, pp. 610–613, 2016.

20. G. Minatti, E. Martini, and S. Maci, "Efficiency of metasurface antennas," *IEEE Transactions on Antennas and Propagation*, vol. **65**, no. 4, pp. 1532–1541, Apr. 2017.

21. G. Minatti, F. Caminita, E. Martini, M. Sabbadini, and S. Maci, "Synthesis of modulated-metasurface antennas with amplitude, phase, and polarization control," *IEEE Transactions on Antennas and Propagation*, vol. **64**, no. 9, pp. 3907–3919, Sep. 2016.

22. M. Faenzi, G. Minatti, D. González-Ovejero, F. Caminita, E. Martini, C. D. Giovampaola, and S. Maci, "Metasurface antennas: new models, applications and realizations," *Scientific Reports*, vol. **9**, p. 10178, 2019.

23. G. Minatti, M. Faenzi, M. Sabbadini, and S. Maci, "Bandwidth of gain in metasurface antennas," *IEEE Transactions on Antennas and Propagation*, vol. **65**, no. 6, pp. 2836–2842, June 2017.

24. M. Faenzi, D. González-Ovejero, F. Caminita, and S. Maci, "Dual-band self-diplexed modulated metasurface antennas," *12th European Conference on Antennas and Propagation*, London, 2018, pp. 1–4.

25. M. Faenzi, D. González-Ovejero, and S. Maci, "Wideband Active Region Metasurface Antennas," in *IEEE Transactions on Antennas and Propagation*, vol. **68**, no. 3, pp. 1261–1272, March 2020.

26. G. Minatti, S. Maci, P. De Vita, A. Freni, and M. Sabbadini, "A circularly-polarized isoflux antenna based on anisotropic metasurface," *IEEE Transactions on Antennas and Propagation*, vol. **60**, no. 11, pp. 4998–5009, Nov. 2012.

27. D. Gonzalez-Ovejero, G. Minatti, E. Martini, G. Chattopadhyay, and S. Maci, "Shared aperture metasurface antennas for multibeam patterns," *11th European Conference on Antennas and Propagation*, Paris, 2017, pp. 3332–3335.

28. D. Gonzalez-Ovejero, G. Chattopadhyay, and S. Maci, "Multiple beam shared aperture modulated metasurface antennas," *Proceedings of IEEE Antennas and Propagation Society International Symposium*, Fajardo, 2016, pp. 101–102.

29. D. González-Ovejero, G. Minatti, G. Chattopadhyay, and S. Maci, "Multibeam by metasurface antennas," *IEEE Transactions on Antennas and Propagation*, vol. **65**, no. 6, pp. 2923–2930, June 2017.

30. D. González-Ovejero, T. J. Reck, C. D. Jung-Kubiak, M. Alonso-DelPino, and G. Chattopadhyay, "A class of silicon micromachined metasurface for the design of high-gain terahertz antennas," *Proceedings of IEEE Antennas and Propagation Society International Symposium*, Fajardo, 2016, pp. 1–4.

31. D. González-Ovejero, C. Jung-Kubiak, M. Alonso-delPino, T. Reck, and G. Chattopadhyay, "Design, fabrication and testing of a modulated metasurface antenna at 300 GHz," *Proceedings of 11th European Conference on Antennas and Propagation*, Paris, France, 2017, pp. 3416–3418.

32. D. González-Ovejero, N. Chahat, R. Sauleau, G. Chattopadhyay, S. Maci, and M. Ettorre, "Additive manufactured metal-only modulated metasurface antennas," *IEEE Transactions on Antennas and Propagation*, vol. **66**, no. 11, pp. 6106–6114, Nov. 2018.

33. A. Oliner and A. Hessel, "Guided waves on sinusoidally-modulated reactance surfaces," *IRE Transactions on Antennas and Propagation*, vol. **7**, no. 5, pp. 201–208, Dec. 1959.

34. F. Caminita and S. Maci, "New wine in old barrels: the use of the Oliner's method in metasurface antenna design," *44th European Microwave Conference*, Rome, 2014, pp. 437–439.

35. A. M. Patel and A. Grbic, "A printed leaky-wave antenna based on a sinusoidally-modulated reactance surface," *IEEE Transactions on Antennas and Propagation*, vol. **59**, no. 6, pp. 2087–2096, June 2011.

36. O. Bucci, G. Franceschetti, G. Mazzarella, and G. Panariello, "Intersection approach to array pattern synthesis," *Proceedings of the IEEE*, vol. **137**, no. 6, pp. 349–357, 1990.

37. E. F. Kuester, M. Mohamed, M. Piket-May, and C. Holloway, "Averaged transition conditions for electromagnetic fields at a metafilm," *IEEE Transactions on Antennas and Propagation*, vol. **51**, no. 10, pp. 2641–2651, Oct. 2003.

38. D. González-Ovejero and S. Maci, "Gaussian ring basis functions for the analysis of modulated metasurface antennas," *IEEE Transactions on Antennas and Propagation*, vol. **63**, no. 9, pp. 3982–3993, Sep. 2015.

39. M. Bodehou, D. González-Ovejero, C. Craeye, and I. Huynen, "Method of moments simulation of modulated metasurface antennas with a set of orthogonal entire-domain basis functions," *IEEE Transactions on Antennas and Propagation*, vol. **67**, no. 2, pp. 1119–1130, Feb. 2019.

40. M. Mencagli, E. Martini, and S. Maci, "Surface wave dispersion for anisotropic metasurfaces constituted by elliptical patches," *IEEE Transactions on Antennas and Propagation*, vol. **63**, no. 7, pp. 2992–3003, July 2015.

41. G. Chattopadhyay, T. Reck, A. Tang, C. Jung-Kubiak, C. Lee, J. Siles, E. Schlecht, Y. M. Kim, M.-C. F. Chang, and I. Mehdi, "Compact terahertz instruments for planetary missions," *9th European Conference on Antennas and Propagation (EuCAP)*, Lisbon, 2015, pp. 1–4.

42. G. Minatti, F. Caminita, M. Casaletti, and S. Maci, "Spiral leaky-wave antennas based on modulated surface impedance," *IEEE Transactions on Antennas and Propagation*, vol. **59**, no. 12, pp. 4436–4444, Dec. 2011.

43. R. King, D. V. Thiel, and K. Park, "The synthesis of surface reactance using an artificial dielectric," *IEEE Transactions on Antennas and Propagation*, vol. **31**, no. 3, pp. 471–476, May 1983.

44. N. Chahat, B. Cook, H. Lim, and P. Estarbook, "All-metal dual frequency RHCP high gain antenna for a potential Europa lander," *IEEE Transactions on Antennas and Propagation*, vol. **66**, no. 12, pp. 6791–6798, Dec. 2018.

45. H. Bilow, "Guided waves on a planar tensor impedance surface," *IEEE Transactions on Antennas and Propagation*, vol. **51**, no. 10, pp. 2788–2792, Oct. 2003.

46. P. Joseph, S. Wong, M. Selvanayagam, and G. V. Eleftheriades, "Design of unit cells and demonstration of methods for synthesizing Huygens metasurfaces," *Photonics and Nanostructures - Fundamentals and Applications*, vol. **12**, p. 360, 2014.

47. D. Gabor, "A new microscopic principle," *Nature*, vol. **161**, p. 777, 1948.

48. D. Gabor, "Theory of communication," *Journal of Institution of Electrical Engineers*, vol. **93**, p. 329, 1946.

49. E. Leith and J. Upatnieks, "Reconstructed wavefronts and communication theory," *JOSA*, vol. **52**, pp. 1123–1128, 1962.

50. E. N. Leith and J. Upatnieks, "Wavefront reconstruction with continuous-tone objects," *JOSA*, vol. **53**, p. 1377, 1963.

51. J. Goodman, *Introduction to Fourier optics*, New York: McGraw-Hill, 2008.

52. D. R. Smith, O. Yurduseven, L. P. Mancera, P. Bowen, and N. B. Kundtz, "Analysis of a waveguide-fed metasurface antenna," *Physical Review Applied*, vol. **8**, no. 5, p. 054048, 2017.

53. O. Yurduseven, D. L. Marks, J. N. Gollub, and D. R. Smith, "Design and analysis of a reconfigurable holographic metasurface aperture for dynamic focusing in the Fresnel zone," *IEEE Access*, vol. **5**, pp. 15055–15065, 2017.

54. A. Grbic and G. V. Eleftheriades, "Leaky CPW based slot antenna arrays for millimeter-wave applications," *IEEE Transactions on Antennas and Propagation*, vol. **50**, p. 1494, 2002.

55. D. F. Sievenpiper, "Forward and backward leaky wave radiation with large effective aperture from an electronically tunable textured surface," *IEEE Transactions on Antennas and Propagation*, vol. **53**, p. 236, 2005.

56. S. Pandi, C. A. Balanis, and C. R. Birtcher, "Design of scalar impedance holographic metasurfaces for antenna beam formation with desired polarization," *IEEE Transactions on Antennas and Propagation*, vol. **63**, p. 3016, 2015.

57. S. Sun, Q. He, S. Xiao, Q. Xu, X. Li, and L. Zhou, "Gradient-index meta-surfaces as a bridge linking propagating waves and surface waves," *Nature Materials*, vol. **11**, p. 426, 2012.

58. O. Yurduseven and D. R. Smith, "Dual-polarization printed holographic multibeam metasurface antenna," *IEEE Antennas and Wireless Propagation Letters*, vol. **16**, pp. 2738–2741, 2017.

59. D. R. Smith, V. R. Gowda, O. Yurduseven, S. Larouche, G. Lipworth, Y. Urzhumov, and M. S. Reynolds, "An analysis of beamed wireless power transfer in the Fresnel zone using a dynamic, metasurface aperture," *Journal of Applied Physics*, vol. **121**, no. 1, p. 014901, 2017.

60. O. Yurduseven, D. L. Marks, T. Fromenteze, and D. R. Smith, "Dynamically reconfigurable holographic metasurface aperture for a Mills-Cross monochromatic microwave camera," *Optics Express*, vol. **26**, no. 5, pp. 5281–5291, 2018.

61. O. Yurduseven, P. Flowers, S. Ye, D. L. Marks, J. N. Gollub, T. Fromenteze, B. J. Wiley, and D. R. Smith, "Computational microwave imaging using 3D printed conductive polymer frequency-diverse metasurface antennas," *IET Microwaves, Antennas & Propagation*, vol. **11**, no. 14, pp. 1962–1969, 2017.

62. J. N. Gollub, O. Yurduseven, K. P. Trofatter, D. Arnitz, M. F. Imani, T. Sleasman, M. Boyarsky, A. Rose, A. Pedross-Engel, H. Odabasi, and T. Zvolensky, "Large metasurface aperture for millimeter wave computational imaging at the human-scale," *Scientific Reports*, vol. **7**, p. 42650, 2017.

63. O. Yurduseven, V. R. Gowda, J. N. Gollub, and D. R. Smith, "Printed aperiodic cavity for computational and microwave imaging," *IEEE Microwave Wireless Components Letters*, vol. **26**, no. 5, pp. 367–369, May 2016.

64. M. C. Johnson, S. L. Brunton, N. B. Kundtz, and J. N. Kutz, "Sidelobe canceling for reconfigurable holographic metamaterial antenna," *IEEE Transactions on Antennas and Propagation*, vol. **63**, no. 4, pp. 1881–1886, Apr. 2015.

65. D. F. Sievenpiper, J. H. Schaffner, H. J. Song, R. Y. Loo, and G. Tangonan, "Two-dimensional beam steering using an electrically tunable impedance surface,"

IEEE Transactions on Antennas and Propagation, vol. **51**, no. 10, pp. 2713–2722, Oct. 2003.

66. M. Ettorre, R. Sauleau, and L. Le Coq, "Multi-beam multi-layer leaky-wave SIW pillbox antenna for millimeter-wave applications," *IEEE Transactions on Antennas and Propagation*, vol. **59**, no. 4, pp. 1093–1100, Apr. 2011.

67. A. Gomez-Torrent, M. García-Vigueras, L. Le Coq, A. Mahmoud, M. Ettorre, R. Sauleau, and J. Oberhammer, "A low-profile and high-gain frequency beam steering sub-THz antenna enabled by silicon micromachining," *IEEE Transactions on Antennas and Propagation*, vol. **68**, no. 2, pp. 672–682, Feb. 2020.

Index